

Development of a Micromegas Time Projection Chamber in Xe-based Penning Mixtures for Rare Event Searches

Memoria Presentada por

Diana Carolina Herrera Muñoz

para optar al Grado de Doctor en Física

por la Universidad de Zaragoza

Directores de tesis Doctoral

Igor García Irastorza

Susana Cebrián Guajardo

Laboratorio de Física Nuclear y Astropartículas

Área de Física Atómica, Molecular y Nuclear

Departamento de Física Teórica

Universidad de Zaragoza

Noviembre de 2014

*A mi madre,
por su amor, sacrificios e inmensa sabiduría
a mi padre,
por enseñarme la importancia del conocimiento*

Contents

Preface	vii
Agradecimientos	ix
1 Introduction	1
1.1 Gaseous Xe Detectors	2
1.1.1 Physical Properties of Xe	2
1.1.2 Particle Interaction	3
1.1.3 Transport of Electrons	6
1.1.4 Electron Multiplication	8
1.1.5 Micro-pattern Gas Detectors	9
1.1.6 Simulation of Avalanche Multiplication in Micromegas	11
1.1.7 Energy Resolution	12
1.1.8 Xe-based Penning Mixtures	14
1.2 Ultra-low Background Conditions	17
1.3 Neutrinoless Double Beta Decay	19
1.3.1 Overview of Neutrino Physics	19
1.3.2 Double Beta Decay	21
1.3.3 Experimental Situation of $0\nu\beta\beta$ Decay Searches	23
1.3.4 NEXT- Neutrino Experiment with a Xenon TPC	25
1.3.5 NEXT-Micromegas and the T-REX Project	27
1.4 Dark Matter Searches	28
1.4.1 Overview	28
1.4.2 Direct Detection	29
1.4.3 Directional Dark Mater Searches	32
I PART I: Characterization of Micromegas in Xe and Xe+Ne mixtures	35
2 Characterization of Micromegas in Xe, and Xe+Ne Mixtures	37
2.1 Experimental Setup	38
2.1.1 Time Projection Chamber	38
2.1.2 Gas System	40
2.1.3 Vacuum System	41
2.1.4 Recovery System	42
2.2 Measurements of α -particles in Xe and Xe+Ne Mixtures	44
2.2.1 Experimental Procedure	44
2.2.2 Data Analysis	45
2.2.3 Electron Transmission	46

2.2.4	Risetime vs Pulse-height Distributions	48
2.2.5	Energy Resolution variation on drift field	51
2.2.6	Drift Velocity	54
2.2.7	Gain	57
2.2.8	Energy resolution dependence on the amplification field . . .	60
2.2.9	Discussion	62
2.3	Energy Resolution for γ -rays in pure Xe	64
2.3.1	Experimental setup and procedure	64
2.3.2	Spectrum from γ -rays of an ^{241}Am source in pure Xe	64
2.3.3	Analysis and results	65
2.3.4	Discussion	66
2.4	Conclusions	69
II	PART II: Xe-trimethylamine mixtures for $0\nu\beta\beta$ and directional dark matter searches	71
3	Mass Spectrometry system for Gas Analysis in HP Xe-based TPCs	73
3.1	Mass Spectrometry	74
3.1.1	Physical Principles	74
3.1.2	Omnistar TM Pfeiffer Quadrupole Mass Spectrometer	75
3.1.3	Data acquisition	77
3.2	System conditioning and optimization	79
3.2.1	Filament Outgassing	80
3.2.2	Measurements with Argon gas	81
3.2.3	Helium leak test	83
3.3	Calibration of Mass Spectrometer for Xe+TMA mixtures	85
3.3.1	Pure Xe and Xe+TMA mass spectra	85
3.3.2	Calibration Factor	88
3.3.3	Experimental Procedure	88
3.3.4	Results and Discussion	90
3.4	Conclusions	92
4	X-ray Measurements in Xe+TMA Mixtures	93
4.1	Experimental Setup and Procedure	94
4.1.1	Overview	94
4.1.2	Energy Spectrum of ^{109}Cd Source in Xe+TMA Mixtures	94
4.1.3	Experimental Setup	95
4.1.4	Experimental Procedure	97
4.2	Data Analysis	98
4.3	Results	101
4.3.1	Determination of optimum fraction	101
4.3.2	Measurements of gain	101

4.3.3	Variation with Pressure	108
4.3.4	Drift velocity	113
4.4	Towards Fano factor measurement in NEXT-0-MM	113
4.5	Comparison between Ingrid and microbulk Micromegas readouts	115
4.6	Conclusions	116
5	Study of Recombination in Xe+TMA Mixtures	117
5.1	Recombination Theory	118
5.2	Experimental Setup and Procedure	120
5.2.1	Overview	120
5.2.2	Drift field cage	120
5.2.3	Micromegas readouts	122
5.2.4	Gas mixture	122
5.2.5	Data acquisition	123
5.2.6	Measurements	124
5.3	Analysis and Results for the Coincidence Mode	125
5.3.1	Electron lifetime	127
5.4	Analysis for the Independent Mode	128
5.4.1	^{241}Am γ energy spectrum in Xe+TMA mixtures	128
5.4.2	PSA for α signals: charge and track angle	129
5.4.3	Ion mobility	135
5.5	Electronic Properties	136
5.5.1	Drift Velocity and Longitudinal Diffusion Coefficient	136
5.5.2	Gain for α -particles and γ -rays	137
5.6	Recombination Dependence on Drift Field	138
5.7	Columnar Recombination of Charge Collected from α -particles	139
5.7.1	Charge vs. $\cos\varphi$	139
5.7.2	Figure of merit: Q_0/Q_{90}	140
5.7.3	Discussion	144
5.8	Conclusions and Outlook	145
	Conclusions	147
	Resumen y Conclusiones	151
	Appendices	163
A	Assessment of material Radiopurity for Rare Event Experiments by γ-spectrometry	165
A.1	Overview	165
A.2	Measurements and results	167
A.3	Summary	171

B	Measurements with InGrid Micromegas readout	173
B.1	Experimental Setup	173
B.2	Experimental Procedure	173
B.3	Electron Transmission	174
B.4	Gain Measurements	175
B.5	Single electron spectra	176
C	Characterization of Micromegas readouts in Ar+2%ⁱC₄H₁₀ mix- tures.	179
C.1	Experimental Setup and Procedure	179
C.2	Results	180
C.2.1	Gain	180
C.2.2	Energy resolution	181
C.3	Conclusions	182
	Bibliography	187

Preface

This thesis has been done within the frame of the T-REX project [1], whose objective is to develop Time Projection Chambers (TPCs) for Rare Event Searches by using Micromegas readouts. The neutrinoless double decay ($0\nu\beta\beta$) and the dark matter are probably the most important [2, 3, 4], within the Rare Event Searches; because a positive result for either of them would have great implications in Particle Physics and Astrophysics. On one hand, the detection of a positive signal for neutrinoless double beta decay implies that neutrino has mass and is a Majorana particle, thereby Physics beyond of the Standard Model. On the other hand, from the detection of dark matter, it could be possible to explain the composition and influence of the 26.8% of the universe's mass.

For both searches good energy resolution and tracking capabilities for background rejection are highly appreciated conditions. In this context, the T-REX project is developing TPCs using Micromegas readouts to detect the ionization generated by a particle. As part of the R&D within the project, this work focused on the study of a high pressure Xe gas detector, because during the last years they have shown to be very competitive mainly due to its better energy resolution and pattern recognition in comparison with liquid xenon detectors.

However, as the energy resolution and the drift properties should be improved as much as possible, in this work two additives acting as a secondary gas have been studied. Specially the additives studied have the characteristic to have the ionization potential near to the first metastable level of Xe. This allows to enhance the gain and improve the energy resolution; there are the so called Penning mixtures. Motivated by this, two Xe-based Penning mixtures were studied experimentally in a small TPC prototype of 2.4l of volume: a xenon+neon (Xe+Ne) and a xenon+trimethylamine (Xe+TMA) mixture.

The focus in the first part of the work was the measurement of the energy resolution at high pressure, mainly towards the $0\nu\beta\beta$ decay searches as part of R&D within The Neutrino Experiment with a Xenon TPC (NEXT) [5]. In the second part, motivated by the good results of energy resolution and operational conditions with the Xe+TMA mixtures, it was studied the columnar recombination in Xe+TMA mixtures as a tool for directional dark matter detection [6, 7]. This thesis is divided in two parts, and 5 chapters, description of each chapter is given below:

Chapter 1 presents a brief introduction about the physical processes involved in the studies carried out in this work. The interaction, the ionization, the drifting and the multiplication processes are described. Finally the status of $0\nu\beta\beta$ and dark matter searches is presented.

In Chapter 2 the study of several Xe+Ne mixtures and pure Xe mainly with α -particles is presented. Measurements of electron transmission, drift velocity, gain and energy resolution are shown.

The description of commissioning of a mass spectrometer system used for gas analysis is presented in chapter 3. The installation and the measurements carried out to establish the optimum conditions for measuring are drawn. The experimental procedure to calibrate the instrument to determine the concentration of TMA is also described.

The systematic study of Xe+TMA Penning mixtures in a HP TPC with microbulk-Micromegas readouts is presented in chapter 4. The experimental procedure followed to work with these mixtures is given. The measurements of gain and energy resolution in the pressure range between 1 and 10 bar to determine the optimum TMA fraction are shown. Variation with pressure with a fixed mixture within the optimum range found is presented. Preliminary measurements of drift velocities after a modification of the setup are finally described.

Chapter 5 describes the study of recombination in Xe+TMA mixture carried out with a novel drift configuration formed by two symmetric drift regions equipped with two microbulk-Micromegas readouts. The recombination of the collected charge from α -particles and γ -rays -emitted in coincidence by an ^{241}Am source- is studied. The main focus in this chapter is the study of columnar recombination, as a tool towards the directional dark matter detection.

Agradecimientos

Estas páginas han sido escritas durante el proceso de redacción de esta tesis, en aquellos momentos en los que me sentía emotiva y agradecida con Dios por haberme dado la oportunidad de hacer mi doctorado en España.

Primero, quiero agradecer a mi director de tesis Igor García por brindarme la oportunidad de realizar el doctorado en el grupo de Física Nuclear y Astropartículas. Su capacidad de motivar a quienes estamos empezando en la investigación es increíble. Destaco la confianza brindada, lo cual permitió que pudiese sentir esa pasión por la Física Experimental, y entrega por mi trabajo, y por el grupo. Gracias porque siempre estuvo abierto, apoyándome en todo, con alegría y entusiasmo como es su costumbre. Su calma y sabiduría para manejar aquellas situaciones complicadas son dignas de admirar. Que afortunada me siento de ser parte de este grupo.

En segundo lugar, agradezco a Susana Cebrián, quien durante estos años ha estado pacientemente apoyando mi proceso de formación. Para ella dedico mi más profunda admiración como investigadora y principalmente como persona. Con ella empecé mi proceso de formación en la investigación durante la realización del Máster, y hoy cuan agradecida estoy porque este trabajo no hubiese sido posible realizarlo sin su constante apoyo. Solo puedo agradecer profundamente todo su apoyo incondicional en todo momento, y su dedicación y su interés por mi trabajo. Muchas gracias Susana.

Quiero agradecer también a Francisco Iguaz, ya que todo el trabajo presentado en esta tesis no es más que una consecuencia del duro trabajo previo que realizó (junto con Alfredo Tomás) en el montaje y desarrollo del software. Desde Francia solía llegar con sus regalos (artículos), siempre pendiente e interesado en ayudarme en todo lo referente a mi trabajo. Finalmente, de vuelta en Zaragoza, su apoyo en la realización de las últimas medidas para las medidas de Xe+TMA fue muy importante. Destaco su emotividad y su practicidad que sin duda han aportado mucho a mi formación.

A Diego González, también agradezco su importante aporte al trabajo desarrollado en esta tesis, aunque muchas veces no fue fácil aceptar las críticas y hoy soy consciente que todo aquello sin duda aportó rigurosidad al trabajo presentado.

A Theopisti y Gloria, un especial agradecimiento porque fueron también parte fundamental en mi formación. A Theopisti, parte imprescindible del grupo que con su sabiduría hace que todo se vea de una forma más clara. Siempre me brindaron su apoyo y confianza y son dignas de admiración como investigadoras y mucho más como personas. A Esther un especial agradecimiento porque, desde la distancia, siempre estuvo pendiente y respondía rápidamente a nuestras inquietudes. Here, I would like to express my acknowledgments to Ioannis Giomataris, even I could not have the opportunity to share with him a lot -there is no doubt that his support to the group is essential. I express my greatest sincere admiration for your scientific

work.

A Juan Castel y Angel Lagraba, un muy especial agradecimiento porque gracias a su eficiencia y disposición para realizar los cambios en el setup, muchas de las medidas aquí presentadas fueron posibles.

Quiero agradecer el apoyo por parte de JuanAn, Miguel Angel y María, en software, ya que en aquellos momentos en los que no sabía como continuar ¡ellos siempre tenían la solución! chicos gracias por su ayuda. Y no sin más agradecer a todos los investigadores del de grupo Física y Astropartículas -Jose Angel Villar, Eduardo García, Jorge Puimedon, María Luisa y Juan Carmona- a todos ellos gracias por su apoyo y soporte no es fácil estar lejos de casa y tener siempre el apoyo de ustedes fue muy importante. A Alfonso quiero agradecer su apoyo, sobre todo hacía que los viajes a Canfranc para visitar a *Paquito* fuesen muy agradables. También agradezco a la colaboración de NEXT, por el interés en el trabajo durante la realización, el aporte en reuniones de la colaboración fue muy importante.

Durante estos casi 5 años, he tenido la oportunidad de compartir con muchos colegas. En una primera etapa tuve la oportunidad de compartir con Alfredo, y Javi Galan, quienes siempre me mostraron su apoyo y además compartían su conocimiento ¡que grandes Físicos sois chicos! y por supuesto que grandes personas, les deseo todo lo mejor. Por otra parte, a mis compañeros: JuanAn, Javi, Carlos Laura, Clara, Patricia y Elisa; juntos fuimos creciendo como investigadores y muchos ya han partido para seguir su propio camino, a ellos muchas gracias porque siempre recibí su apoyo en cuestiones académicas y personales.

During my short stay in the Lawrence Berkeley Laboratory, I had the great opportunity to work in the *High Pressure Xenon Group*. All the group welcomed me and made me feel at home, giving me support and collaboration in all aspects. I am very grateful to Azriel Goldschmidt and Dave Nygren, they opened the group to me. What a great opportunity to work with them, I have had, I only can say thanks a lot. Although the time was short, I really grew a lot in wisdom, mainly in the scientific area and also as person. Carlos and Josh who helped me and shared with me their knowledges without restrictions, great physicists. I really like to expressing my deep admiration for all them. Luis and Carlos made my stay more friendly, their patience to help me to look a good place out for staying and to learn how to arrive at the Lab, and so on. I can not forget to my American mom Beberly, who gave me all her love. She and her son Carlos were a great support for me, they helped me a lot in my American experience.

A mi madre Alicia, a quien dedico esta tesis, agradezco todo su amor, todo el camino recorrido hasta aquí ha sido gracias a ti madre. No sabes cuan orgullosa estoy de ti madre, tu fortaleza, sabiduría y tu apoyo incondicional han permitido que pueda hoy tener el privilegio de ser Doctora. A mi padre a quien admiro por su amor al trabajo y responsabilidad, agradezco sus enseñanzas ya que gracias a él aprendí la importancia del conocimiento. Agradezco a toda mi familia -pero en especial a Tita, Julio y Gilda- quienes durante todo este tiempo, me han animado siempre y me han mostrado su cariño, confianza y apoyo.

Introduction

Contents

1.1 Gaseous Xe Detectors	2
1.1.1 Physical Properties of Xe	2
1.1.2 Particle Interaction	3
1.1.3 Transport of Electrons	6
1.1.4 Electron Multiplication	8
1.1.5 Micro-pattern Gas Detectors	9
1.1.6 Simulation of Avalanche Multiplication in Micromegas	11
1.1.7 Energy Resolution	12
1.1.8 Xe-based Penning Mixtures	14
1.2 Ultra-low Background Conditions	17
1.3 Neutrinoless Double Beta Decay	19
1.3.1 Overview of Neutrino Physics	19
1.3.2 Double Beta Decay	21
1.3.3 Experimental Situation of $0\nu\beta\beta$ Decay Searches	23
1.3.4 NEXT- Neutrino Experiment with a Xenon TPC	25
1.3.5 NEXT-Micromegas and the T-REX Project	27
1.4 Dark Matter Searches	28
1.4.1 Overview	28
1.4.2 Direct Detection	29
1.4.3 Directional Dark Mater Searches	32

Since high pressure xenon was proposed as medium of detection in 1980, this technique has become very competitive with respect to conventional liquid xenon detectors. Historically, the advantages of liquid noble gases for radiation detection were first recognized than for high pressure gas detectors. However, the development of Micro-Pattern Gas Detectors and the understanding of the concept of the TPC as well as the observation that xenon gas phase offers better energy resolution than the liquid phase [8], lead to high pressure xenon detectors to be considered a good option to many applications.

A schematic representation of a gaseous detector, illustrating the working principle of a drift chamber is shown in Fig. 1.1. An ionizing particle e.g. α -particle or γ -particle interacts with the atoms/molecules through a process that depends

on the nature of the particle, its energy and also the properties of the filling gas (see Sec. 1.1.2). As a result the atoms of the gas are excited or ionized, producing electron-ion pairs (charge mode), and after the decay of excited atoms light is emitted (*primary scintillation*). When the particle is highly ionizing one, the passage through the gas leaves behind a very defined track; by contrast, low ionizing particles produce a cloud of primary charge. Under the application of an electric drift field -hereinafter called drift field (E_d)- the electrons drift towards a readout plane (see Sec. 1.1.3), where a higher electric field is applied -the amplification field (E_a)- which allows that electrons can ionize the atoms producing avalanches of charge (see Sec. 1.1.4). In the scheme, it is not represented the *primary scintillation* process, however, it must be noted that using appropriated readouts this signal can be used as trigger for the determination of the so-called t_0 of the event. When the readout can record the time differences between the several signals generated by a track of an event, the detector evolve into a TPC, the first concept was proposed by D. Nygren in 1974 [9, 10]. TPCs provide three-dimensional event imaging, energy measurement, and particle identification. If the TPC is equipped with an appropriated readout plane e.g. Micromegas [11] (see Sec. 1.1.5), this detector allows to discriminate between the true signal and the background through pattern recognition.

The experiments using High Pressure Xenon TPCs (HPXe TPCs) as detectors have good prospects to reach excellent sensitivity for the next generation of Rare Event Searches. Further the modern technology of purification of noble gases, specially for Xe, will allow that detectors in the tons range present good conditions for particle detection. In addition, xenon offers the possibility to work in charge and electroluminescence mode.

In this chapter is discussed the physics involved in gaseous xenon (Xe) detectors in Sec. 1.1. The ultra-low background conditions for Rare Event Searches are summarized in Sec. 1.2. Finally, the status of neutrinoless double beta decay and the Dark Matter searches are respectively presented, in Sec. 1.3 and 1.4.

1.1 Gaseous Xe Detectors

1.1.1 Physical Properties of Xe

Within the noble gases, Xe has the highest atomic mass and highest light and ionization yield except for radon which has not been studied for radiation detection so far. Xe exists in the air with very small concentrations (lower than 0.1 ppm). The Xe has several isotopes, with odd spin component ^{129}Xe and ^{131}Xe . The Xe is obtained as a byproduct from liquefaction and separation of air. The cost of Xe is about \$1k/kg, more than for other noble gases, especially Ar, which is also employed in gaseous detectors [12], an extensive information about the physical properties in liquid and gas phase can be found in [13].

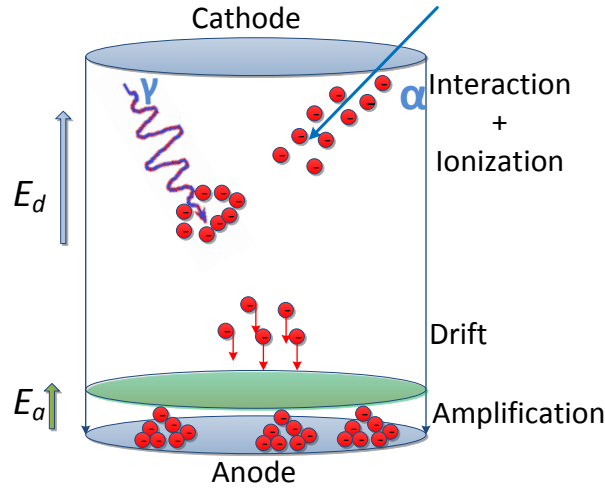


Fig. 1.1: Schematic representation of the working principle of a drift chamber is shown, in which three physical processes are involved: i) interaction together with the ionization, electron-ion pairs are created by the interaction with the atoms/molecules of the gas; ii) drift of electrons: the electrons move under the application of an drift field (E_d) towards the readout plane; iii) the electron multiplication, for which an amplification field (E_a) is applied to any special structure, the electrons gain enough energy to ionize new atoms, generating electron avalanches. The interaction of an α -particle and a γ -particle is illustrated. If the drift chamber is equipped by an appropriated readout and the time differences of several signals generated by the track of an event can be determined, the drift chamber evolves into a Time Projection Chamber (TPC).

1.1.2 Particle Interaction

The passage of an ionizing particle -such as α -particles, relativistic electrons, photons¹ and neutrons- through a Xe gas filled detector involves different mechanisms, as is widely discussed in [14]. In this section will be briefly drawn the most important aspects for the interaction of photons with matter.

1.1.2.1 Interaction of Photons with Matter

Soddy and Russel found in 1909 that a beam of photons - γ -rays- attenuates when it passes through the matter following an exponential law. A beam of photons of intensity I_0 passing through the Xe gas in a volume with length t , follows an exponential dependence with t [14]:

$$I = I_0 \exp^{-\mu_l t} \quad (1.1)$$

where μ_l is the linear attenuation coefficient, which represents the probability per

¹Photons includes γ -rays and X-rays radiation.

unit path length that photons are removed from the beam through three main physical processes: *photo-electric absorption*, *Compton scattering* and *pair production*.

1. *Photo-electric effect*: the photon is absorbed by an interaction with an atom of the gas generating an electron with most of the photon energy.
2. *Compton scattering*: the photon interacts elastically with an electron of the atom, transferring only part of its energy.
3. *Pair production*: the photon traversing the electromagnetic field of a nucleus creates an electron-positron pair.

Other possible interaction mechanisms include Rayleigh and Mie processes. The cross-sections of the photon interactions depend on the photon energy, the atomic number and the density of the material. The attenuation of a photon beam passing through the matter is calculated from the photon interaction cross sections. For most of the energies involved in this work (a few keV), the main process of interaction is the photoelectric absorption. Above this, Compton scattering becomes important. On the other hand, pair production can happen only for a photon energy larger than 1.02 MeV.

The propagation of the photons through the matter is described by the attenuation coefficient. In Fig. 1.2, the photoelectric mass attenuation coefficient is presented, this is proportional to $E^{-3.5}$, where E is the photon energy. The peaks observed correspond to the binding energies of K- and L-shells. For energies slightly lower than each edge, only electrons of lower bound shells can be removed from the atom. But, for energies larger than the binding, the electrons of the following shell can now be removed and therefore the probability of attenuation increases abruptly.

It must be noted that during the formation of the primary charges atoms can be excited, as a result photons are emitted in the range between VUV and Vis-IR, so-called here in after as light; this signal called *primary scintillation* can be used as trigger allowing the determination of the t_0 of each event.

In the photo-electric effect, the photon interacts with the atom inelastically producing an electron to be ejected from one of the shell of the atom, being the probability for K- and L- shells the largest one. The electron is ejected with a kinetic energy E_e , which is given by the difference between the incoming photon energy, $h\nu$, and the binding energy of the shell where the photo-electron was originated, E_b :

$$E_e = h\nu - E_b \quad (1.2)$$

In the non-relativistic limit ($E \ll m_e c^2$) and at photon energies higher than the K-shell, the cross section for the photo-electric effect is proportional to

$$\sigma_{pe} \propto Z^5 \left(\frac{m_e c^2}{E_0} \right)^{7/2} \quad (1.3)$$

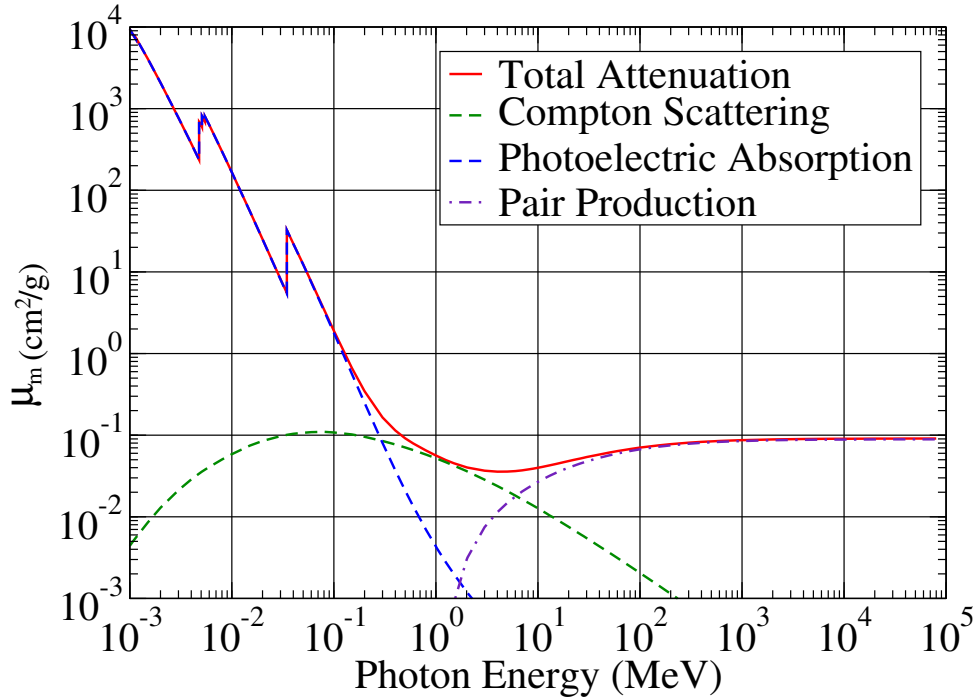


Fig. 1.2: Total mass attenuation coefficient of Xe for γ -rays plotted against their energy, the partial coefficients for *photoelectric absorption*, *Compton scattering* and *pair production* are presented as well, data extracted from [15].

where Z is the atomic number of the material, m_e the electron mass and E_0 the photon energy. This formula shows the strong dependence on the Z number, this explains the fact that the mean free path for lighter noble gases is much larger than for Xe. The emission of the electron, leaves a vacancy in its shell. When the vacancy is filled by an electron of an outer shell two processes can occur: *fluorescence* or *Auger transition*. In the fluorescence the energy is liberated in form of a characteristic X-ray, and in the Auger transition the difference energy is transferred to an electron of the same atom that has the probability to be ejected if the binding is lower than the transferred energy.

The Compton scattering dominates for energies between 0.3 and 6 MeV. Part of the energy of the photon is given to an electron of the outer shells of the atom; since the electron energy after the interaction depends on the angle of interaction, its spectrum of the Compton is a continuous. For energies above twice the rest mass of electron (1.02 MeV) an electron-pair can be produced, by the interaction of the photon with the Coulomb field of an atom's nucleus. As a consequence the photon disappears, and the energy is converted into kinetic energy of the electron and positron. The positron rapidly is thermalized and annihilated, yielding two γ -photons in opposite direction, each one with an energy of 511 keV.

1.1.2.2 W -value and Fano Factor

The result of the interaction of particles with atoms, is the generation of ionization or light. In the first case, a certain number of electrons, -the primary charge- are yielded. For practical reasons, the value of interest is the mean energy necessary to remove an electron from a shell of an atom, this is the W -value; in this way the number of primary electrons yielded with an energy E is given by

$$N_e = \frac{E}{W} \quad (1.4)$$

The ionization process is governed by statistics, which implies that N_e does not take always the same value. In 1947 it was introduced by U. Fano [16], a factor that accounts for the ratio between the observed variance, σ_e^2 and the predicted number of primary charges by the Poisson statistics model:

$$F = \frac{\sigma_e^2}{N_e} \quad (1.5)$$

Typically the values of the Fano factor are between 0.13 and 0.17 for Xe, and for Ar in the range 0.17-0.23 [17, 18, 19]. For a medium gas formed by various components, the number of primary electrons N_e can be calculated as a weighted average of the value N_e of the pure gases. The weighting factors are related with the relative concentration C_i and the ionization cross-section of each component σ_i .

$$W_{AB} = \frac{W_A W_B}{C_A \sigma_A W_B + C_B \sigma_B W_A} \quad (1.6)$$

Experimental studies on the Fano factor of binary mixtures have shown that the values are within the values of the two components [20, 21, 22, 23].

The variation of the number of primary charges created by the interaction introduced the first contribution to the energy resolution, this is an intrinsic value related to the medium gas. Energy resolution will be discussed in Sec. 1.1.7.

1.1.3 Transport of Electrons

The kinetic equation for the velocity distribution function of gas presented by Boltzmann in 1872 led to the understanding of charged particles motion in gases; special work dedicated to theory of transport of charged particles can be found in [24, 25, 26, 27]. The knowledge of the drift and diffusion of electrons and ions in gases is essential for the understanding of the operational characteristics of gaseous detectors, specially the macroscopic properties. The kinetic theory based on statistical mechanics is the branch that provides the connection between the microscopic and macroscopic properties. Here, it will be discussed only the main macroscopic transport properties of electrons in gases subject to an external electric field, thus drift velocity, diffusion, recombination and attachment are presented. The recombination will be discussed in detail in Chapter 5.

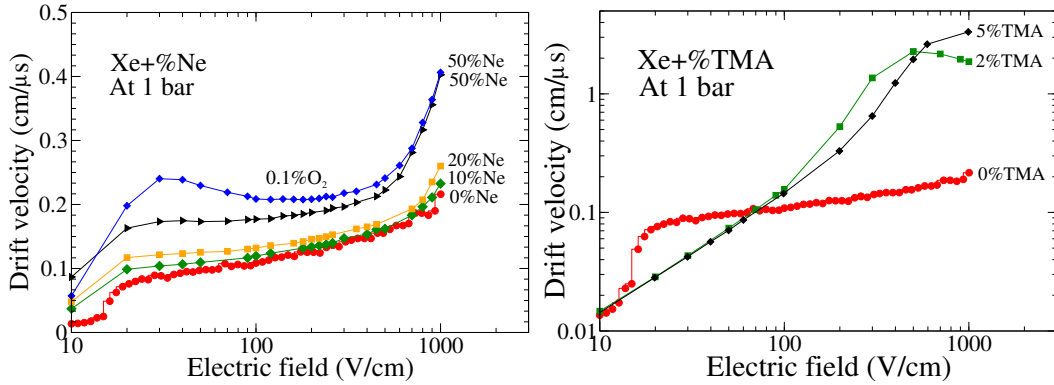


Fig. 1.3: Dependence of electron drift velocities versus electric field in Xe+Ne (left) and Xe+TMA mixtures. For Xe+50%Ne mixture, a curve of drift velocity with a concentration of 0.1% of oxygen (O_2) was added. Values obtained with Magboltz simulations [30].

1.1.3.1 Drift Velocity

The electrons move following the field lines under the effect of an external electric field E_d , in opposite direction to the drift field (drift of electrons)². The average velocity (v_d) acquired by electrons is traditionally called drift velocity, and it can be written as:

$$v_d = \frac{eE}{m} \tau \quad (1.7)$$

where τ is the average collision time between collisions.

The ions follow the direction of the drift field, and as they are very heavy particles, its drift velocity is typically 1000 times lower than for the electrons. This is the reason why most of applications use the signal of electrons. During the last decades, dedicated experimental works have measured the drift properties of a large variety of gases.

Drift properties have been studied in many gas mixtures used for filling gaseous detectors. Magboltz is a tool developed by S. F. Biagi [28, 29] to calculate the drift properties of different gases. This tool has shown an accuracy better than 2% in cases where the cross-sections are well known. Fig. 1.3 shows the drift velocity for Xe+Ne (left) and for Xe+TMA (right) mixtures, including in both graphs the curve for pure Xe (indicated as 0%Ne and 0%TMA). As seen, the addition of either of the admixtures (Ne, TMA) makes that drift velocity increases, for Xe+Ne mixtures in all the range (10-1000 V/cm), and for Xe+TMA mixtures from 70 V/cm. Typically the addition of molecular admixtures generates great increase in the drift velocity as observed with TMA. The increase of the drift velocity through the addition of a secondary gas facilitates the operation conditions of gaseous Xe detectors.

²In the drift region the electric field applied is low to avoid the ionization of the gas.

1.1.3.2 Diffusion, Recombination and Attachment

As mentioned, the electrons follow in average the drift field lines, however due to the scattering off with gas atoms/molecules the direction changes. Under the effect of an uniform electric field, a point-like primary electron cloud spreads out into a Gaussian spatial distribution. This process is called transverse and longitudinal diffusion. The projected standard deviation into an arbitrary axis, increases with time, t as;

$$\sigma = \sqrt{2Dt} \quad (1.8)$$

where D is the diffusion coefficient. Due to the so-called electric anisotropy, the longitudinal diffusion differs from the transverse one. As in the case of the drift velocity, the addition of appropriated admixtures to Xe, may reduce the diffusion in gaseous Xe detectors.

During the drift the electrons can be captured back by ions, they recombine with atoms/molecules, therefore at the end the charge collected decreases. The recombination strongly depends on the drift field, at very high drift field the recombination decreases. It can be distinguished two types of recombination: *initial* or *columnar*, which will be described in Chapter 5.

The electrons can also be captured by electronegative substances, this occurs when the electron energy is very low thus during the collision with this type of substances they are attached. This happens with atoms/molecules with large electron affinities, the halogenides, and above all the oxygen, are the most problematic substances. The oxygen can enter to the chamber by outgassing, internal leaks in the system or real leaks produced by manufacture defects. The outgassing is produced by the release of gas molecules -oxygen (O_2) and water vapor- from the inner walls of the chamber or from materials used in the field cage. To reduce attachment in gaseous Xe detectors, systems of recirculation are installed, which continuously remove the oxygen generated by outgassing. A summary of the different mechanisms of attachment can be found in [30].

Both attachment and recombination lead to the loss of charge of the final signal; however, when the level of impurities is very low (level of ppb) both contributions can be suppressed by using high drift field voltages.

1.1.4 Electron Multiplication

For most of the applications, the number of primary charges created after the interaction of the particle in the gas, is not enough to obtain a good signal, for this reason amplification is needed. For gaseous detector, it is possible to distinguish between two types of amplification: *Townsend avalanches* (charge amplification) and electroluminescence (light amplification) [31]; here is only discussed the charge amplification.

When the electric field applied is sufficiently high, electrons can acquire an energy above of the ionization potential, between collision with atoms. This produces

new charges -secondary electrons- through collisions between the electrons and the components of the gas (atoms or molecules), which in turn yields new electrons and so on. At the end, it is obtained a cascade of charge, a *Townsend avalanche*.

The fraction of electrons generated, per unit path length, x , is described by the Townsend equation:

$$\frac{dN}{N} = \alpha dx \quad (1.9)$$

where α is the first Townsend coefficient, defined as the number of ionizations generated per unit of length by a single electron in the direction of the applied field. Then the total electrons created in a length l , is given by

$$N = N_e \exp\left(\int_0^l \alpha(x) dx\right) \quad (1.10)$$

In this way, the factor of multiplication, G is defined as:

$$G = \frac{N}{N_e} = \exp\left(\int_0^l \alpha(x) dx\right) \quad (1.11)$$

where N is the number of charges at the end of the multiplication stage. The multiplication (amplification) factor -hereinafter called gain- is of central interest in the operation of gaseous detectors, for most of the applications a high gain is required. Each primary electron that enters into the amplification field region undergoes a process of multiplication that ends in the anode. The final charge is different for each avalanche, therefore the variance in the pulse-height can be written as:

$$\left(\frac{\sigma_Q}{Q}\right)^2 = \left(\frac{\sigma_e}{N_e}\right)^2 + \left(\frac{\sigma_G}{G}\right)^2 = \frac{F + f}{N_e} \quad (1.12)$$

where $\sigma_G^2 = \sigma_A^2/N_e$ which is obtained applying error propagation, considering that each avalanche is independent of the others. The parameter f provides the single-electron multiplication fluctuations.

1.1.5 Micro-pattern Gas Detectors

Since the late eighties the development of micro-strip gas chambers [32] generated great interest because its intrinsic rate capability was orders of magnitude higher than the precedent technology of multi-wire proportional chambers [33]. This new readout, manufactured on base of photolithographic technology on thin insulating supports, allows a granularity ten times better than with wires. The most important advantage is the improvement in the multi-track resolution capability.

However, this type of readouts present high spark-induced failures which produced damages on the detector, and fast aging; both problems could not be solved [34]. These circumstances led to development of several new technologies

more robust, the so-called Micro-Pattern Gas Detectors (MPGD). Within these technologies, two can be highlighted:

- MICRO-MEsh GASEous structure (MICROMEGAS [11], see Fig. 1.4-left), based on a parallel plate with a thin-gap, that collects and amplifies the charge.
- The Gas Electron Multiplier (GEM [35], see Fig. 1.4-right), consisting of a thin metalclad polymer foil, drilled by a high density of thin holes, each hole acts as an individual charge amplifier.

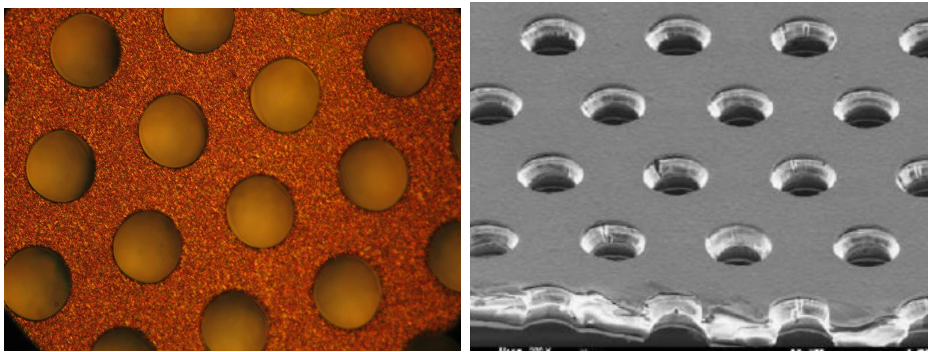


Fig. 1.4: The two main amplification structures of Micro-Pattern Gas Detectors (MPGDs): Micromegas of microbulk type (left) with geometric parameters of 50-90-45 μm corresponding to gap-pitch-hole diameter (image taken with an optical microscope of the University of Zaragoza J.J. Morales); and GEM (image extracted from [36]). Both structures built at CERN (R. de Oliveira).

The main advantages of these readouts are their high rate capability, higher than 10^6 ionizing tracks/ mm^2 , excellent space and multi-track resolution (50 μm for Micromegas and 500 μm for GEM) [37]. In addition, they are robust and the ageing is suppressed. For applications at high pressures it has been seen that the Micromegas are the most appropriated readout, as is seen in Fig. 1.5.

Within the Micromegas readouts different types are found: bulk [39], Microbulk [40], and InGrid [19, 41]. In the Bulk type the usual electroformed micromesh is replaced by a woven wire mesh by a simple process based on the printed circuit board technology; thus large surfaces areas ($2 \times 40 \text{ m}^2$) can be built. The low cost of fabrication together the robustness of the electrode materials make it extremely attractive for several applications. The InGrids [19, 41] readouts are structures precisely fabricated by wafer post-processing, they are integrated directly on top of silicon wafers. This technique produces an outstanding accuracy of mesh manufacturing and a very good alignment between grid holes and the pixel pads, achieving to maximize the detection efficiency and the fiducial detector area.

The microbulk type of Micromegas is the most recent one, which is produced thanks to the state-of-the-art of lithography techniques, particularly the etching of

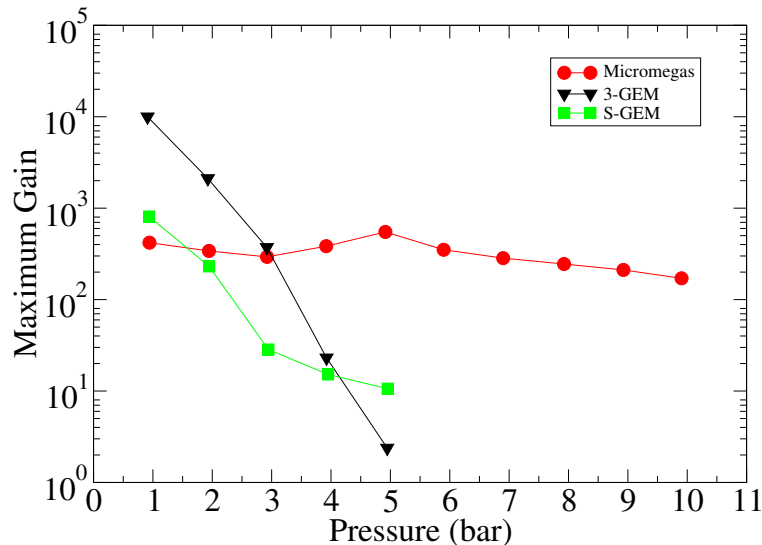


Fig. 1.5: Comparison of the maximum gain attained with Micromegas and two GEM micro-pattern gas readouts, for pressure ranged from 1 to 10 bar [38].

the kapton through the mesh holes to create the amplification volume. The homogeneity of the gap has $\sim 1 \mu\text{m}$ accuracy, thus the energy resolution is outstanding within the MPGD, and the whole detector is a robust block. Microbulks structures are more fragile than bulks to handle due to their delicate mesh, however more robust against continuous vibrations and tensions, and generally more stable. Another of the most important aspects in this device is the radiopurity confirmed by γ -spectrometry in Ref. [42].

1.1.6 Simulation of Avalanche Multiplication in Micromegas

Garfield is a program developed by R. Veenhof to perform detailed simulation of gaseous detectors [43, 31]. The knowledge of the electric field (\vec{E}) in each point of the electron trajectory is mandatory. Garfield has a Monte Carlo method to simulate the drift of electrons in real gases, this allows to track electrons at the atomic/molecular level by using cross-sections available in Magboltz. Specially in noble gases, each collision is classified as elastic, excitation or ionization. Although the application provides a library for analytically calculating electric fields, this has the limitation that is only for detectors that can be decomposed in equipotential planes, wires and tubes without intersections. However, during the last years it has incorporated interfaces for various Finite Element programs.

As part of this thesis, the development of a Toolkit to simulate the microphysics in Micromegas was initiated, based on open source tools Gmsh [44], Elmer [45] and Garfield++ [43]. The work was performed during a stay at Lawrence Berkeley Laboratory with the High Pressure Xenon group³. The simulation procedure con-

³We are specially grateful to D. Nygren, A. Goldschmidt, J. Renner and C. Oliveira.

sists in the creation of a geometry and the mesh (Gmsh), the resulting mesh is introduced to Elmer to solve the potential equations, and finally the field map is imported by Garfield through an interface developed by J. Renner [46]. The unit cell created in Gmsh is depicted in Fig. 1.6-top. The geometry simulated has 50 μm of gap thickness, 90 μm of pitch (distance between the holes centers) and 45 μm of hole diameter; these parameters can be changed easily allowing to study several geometries. The field map and the geometry are imported by Garfield++, where the desired periodicity is set (X-periodicity and mirror Y-periodicity), in this way Garfield++ repeats the field map in x and y as seen in Fig. 1.6-bottom (left). The equipotential surfaces are shown in Fig. 1.6-bottom (right). In Garfield the medium gas is added; further mixtures can be also simulated, indicating the concentration of each component. Other important aspect is that the program allows to study the Penning transfer, which is set as a probability.

Although in this thesis were not developed systematic studies, preliminary work focused in finding the best conditions of simulation. Various meshes distances were investigated, and the optimum number of primary electrons set in the simulation was changed. This work will allow the study of several Micromegas geometries, electron transmission, mixtures, among other characteristics. It must be noted that the work is being continued by the PhD. Student E. Ruiz-Chóliz, who presented recently a first communication, in which it was studied the electron transmission and the gain in Xe+TMA mixtures, including the Penning transfer [47].

1.1.7 Energy Resolution

Energy resolution represents the relative variance of the final signal, e.g. variance of the pulse-height. In each process, interaction, drift and multiplication, there is a contribution to the energy resolution. As a first approach, the processes can be considered as independent, thereby each contribution can be summed in quadrature. With the relative variation of the total signal, the energy resolution at Full-Width-at-Half-Maximum (FWHM) is defined as:

$$R(FWHM) = 2\sqrt{2\ln 2} \left(\frac{\sigma_Q}{Q} \right) \quad (1.13)$$

where the factor $2\sqrt{2\ln 2}$ comes from the relationship between the FWHM and the standard deviation (σ).

In a proportional counter or other a gaseous detector based on charge amplification, the fluctuations in the avalanche multiplication, are described by the parameter f and then, using Eqs. 1.4 and 1.12, the energy resolution of the final signal, including the primary (F) and the multiplication (f) fluctuations is given by:

$$R(FWHM) = 2.35\sqrt{\frac{W}{E}(F + f)} \quad (1.14)$$

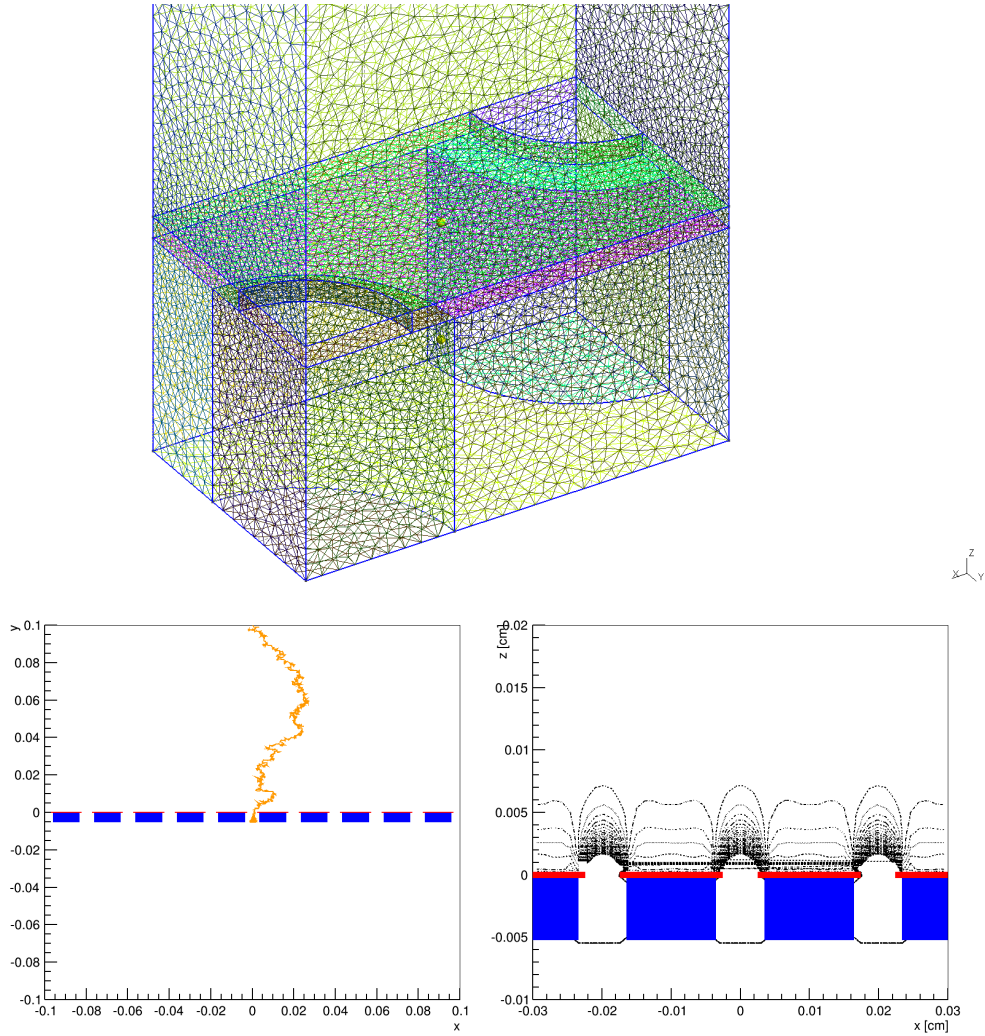


Fig. 1.6: Top: Unit cell of a Micromegas readout performed in Gmsh application, the mesh is seen. The Micromegas geometry simulated has $50 \mu\text{m}$ of gap thickness, $90 \mu\text{m}$ of pitch (distance between the holes centers) and $45 \mu\text{m}$ of hole diameter Bottom: Drift and multiplication of an electron simulated by Garfield with the imported field map from Elmer. Kapton ($45 \mu\text{m}$, blue) and the copper mesh ($45 \mu\text{m}$, red) can be distinguished (left). The equipotential surfaces are shown (right).

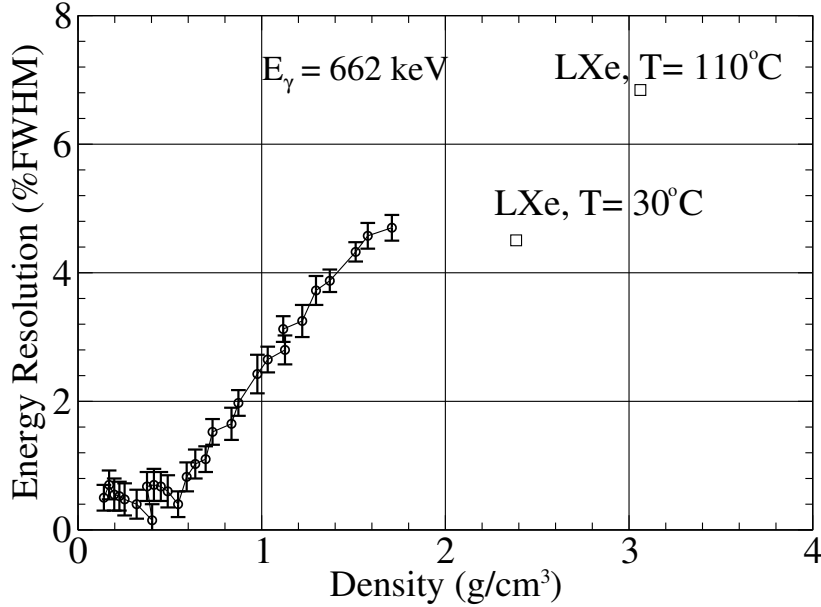


Fig. 1.7: Energy resolution at FWHM of the signal generated by γ -rays of 662 keV from a ^{137}Cs source, as a function of Xe density, adapted from [8].

Typically, the contribution in the amplification stage is larger than the intrinsic one given by the Fano factor. The energy resolution for pure Xe has been studied systematically with pressure in the work of A. Bolotnikov and B. Ramsay [8]. Results of this work showed that the energy resolution (for γ -rays of 662 keV) is practically constant until 0.55 g/cm^3 , as seen in Fig. 1.7. For larger densities the energy resolution deteriorates rapidly, approaching values of the liquid Xe phase. This work demonstrated the advantages of working in gas phase instead of liquid phase; the gas phase has become good option in applications where the energy resolution is an essential factor.

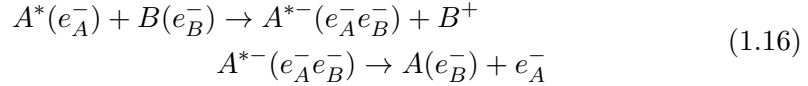
1.1.8 Xe-based Penning Mixtures

Penning effect was first investigated in 1927 by Frans Michel Penning [48], it occurs when excited gas atoms of the primary gas are able to ionize molecules of an additive gas. This can happen if the ionization potential of the secondary gas is very close to the first metastable level of the primary gas; at these conditions a resonance takes place producing collisions between the quench gas molecules and long-lived excited states of the main gas.

The most common transfer mechanism is the two-body collision of an excited atom A^* with an admixture molecule B , as a result it is produced the ionization of the admixture B :



For the ionization, two mechanisms have been proposed. In the first during the exchange reaction, an electron tunnels from B into A^* filling a hole, then an electron is ejected from an excited level of A^* [48]:



The second process consists in a direct transfer of a pair of optical transitions: A^* returns to its ground state while an electron from B is ejected [49]:



As a result of this transfer mechanism the ionization increases substantially. Various studies of Penning mixtures suggest that in the creation of the primary charge the related fluctuations can be reduced by the Penning effect. This means that the intrinsic energy resolution given by the Fano factor F may be reduced.

Experimental work in Ar and Xe Penning mixtures has shown that if the ionization potential of the additive deviates, in either direction, from the Ar or Xe metastable potential, the Penning effect decreases rapidly [50]. Specially, various admixtures were studied by B.D . Ramsey and P. C. Agrawal, in Table 1.1 some of the mixtures studied together with the last reported value of the ionization potential are shown. Measurements of gain and energy resolution were done, as a result the TMA admixture showed the best conditions of operation. These results can be explained by the fact that this molecule presents the ionization potential closer to the first metastable level of Xe (8.3 eV, see Table 1.2) than the other molecules. The gain curves for various TMA fractions and some admixtures tested are illustrated in Fig. 1.8. As seen the best conditions of operation are obtained for a Xe+2%TMA mixture. To demonstrate experimentally that the mechanism of transfer is due to Penning, is not an easy task. Typically the Penning transfer is attributed to the fact that at fix value of amplification field, the gain increases abruptly with the addition of the Penning admixture reaching a maximum value and then drops rapidly, as was seen in a systematic work in Xe +2,3 dimethyl-2-butene mixture [51].

Motivated by these experimental results and by recent theoretical proposal by D. Nygren [52], in this thesis was studied the TMA as an additive to Xe. This molecule is an organic compound with the formula $N(CH_3)_3$. It is colorless, hygroscopic, and flammable. In low concentrations it has a strong fishy odor and an ammonia odor at high concentrations. Moreover, there are evidences that this admixture can be wavelength-shifter to Xe, which could allow to collect more efficiently the electroluminescence signal, enabling a TPC to work at both electroluminescence and charge mode.

On the other hand, Xe+Ne mixtures were also studied in this thesis; this mixture was recently mentioned to be a good option for neutrinoless double decay searches [53]. In these mixtures, it could be produced Penning effect, although in this case the Xe acts as the additive gas for Ne. The first metastable level of Ne

Quench gas	Ionization potential eV
Carbon dioxide (CO ₂)	13.8
Methane (CH ₄)	13.0
Propylene (C ₃ H ₆)	9.7
Isobutylene (i-C ₄ H ₈)	9.3
Diethylamine (C ₂ H ₅) ₂ NH	8.01 (8.01-851)
Dimethylamine (CH ₃) ₂ NH	8.23 (8.23-9.55)
Trimethylamine (CH ₃) ₃ N	8.32 (7.82-9.40)
2,3 Dimethyl-2-butene	8.30
Triethylamine (C ₂ H ₅) ₃ N	7.50 (7.50-7.84)

Table 1.1: Ionization potential of molecular additives tested in Ref. [50], some values have been updated. The full range of ionization potential values quoted up to now are also indicated.

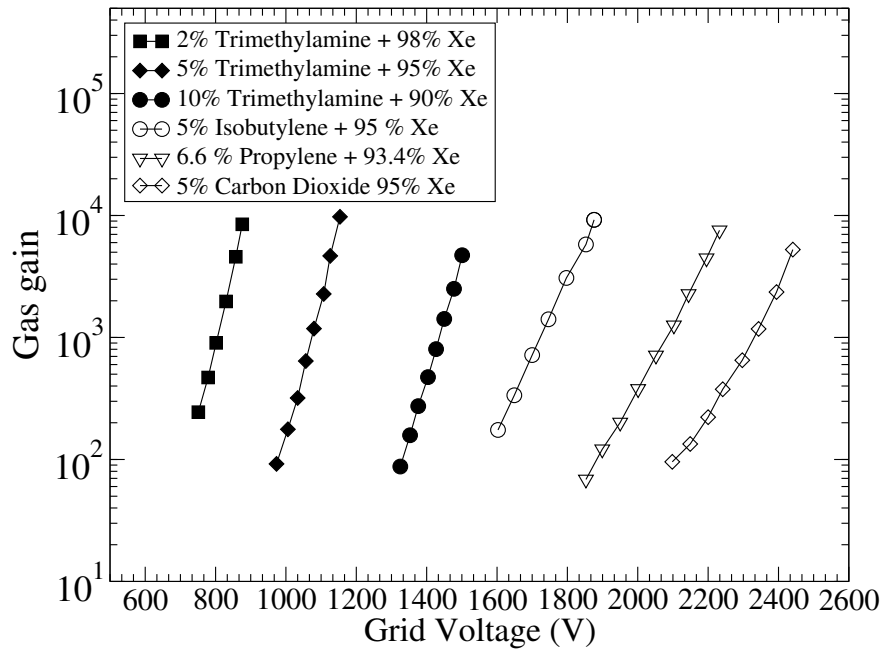


Fig. 1.8: Gain against the grid voltage in a parallel plate detector for different Xe-Penning mixtures, a modification from [50].

Gas	Ionization potential eV	First meta. level eV
Xe	12.12	8.3
Ne	21.56	15.1

Table 1.2: Ionization potential and the first metastable level of Xe and Ne are indicated. The ionization potential of Xe is below the first metastable level of Ne, therefore a Penning effect takes place; the excited energy of Ne is transferred into ionizations of Xe.

(15.1 eV) is above of the ionization potential of the Xe (12.12 eV) (see Table 1.2). Therefore Penning effect takes place; the excited energy of Ne is transferred into ionizations of Xe.

Previous experimental and simulation works have been performed in a Xe+Ne gas proportional scintillation counter. The Fano factor (F) and work function (W) were determined for low energy X-rays [23]. Results of intrinsic energy resolution R_{in} , FW values, and Fano factor for an energy of $E_x = 5.9$ keV, as a function of Xe concentration, improve as the concentration of Xe increases as illustrated in Fig. 1.9. Table 1.3 shows values of W and the Fano factor in Xe+Ne mixtures for α -particles. These results evidence that Xe+Ne mixtures can be a good option for a Xe-based gaseous detector, specially for soft X-rays detection because the addition of a lighter noble gas to Xe increases the absorption depth thus the bremsstrahlung and multiple scattering could be reduced [54, 55].

Gas mixture	W (eV)	$N_e \times 10^5$ e ⁻	F
100%Xe	22.40	2.41	0.21
80%Xe+20%Ne	22.86	2.36	
75%Xe+25%Ne	22.98	2.35	
70%Xe+30%Ne	23.16	2.33	0.27
60%Xe+40%Ne	23.81	2.27	
50%Xe+50%Ne	23.98	2.25	0.23

Table 1.3: Values of the mean energy for electron-ion pair generation (W) and the corresponding primary electrons (N_e) for an energy of $E_\alpha = 5.41$ MeV in Xe+Ne mixtures; these values were used to calculate the gain in this work (Chapter 2). In addition the Fano factor for some mixtures are presented. Data extracted from [23].

1.2 Ultra-low Background Conditions

A continuous challenge in Rare Event Searches, specially direct Dark Matter and neutrinoless double beta decay detection, is to minimize and characterize completely the background. The main background sources are environmental radioac-

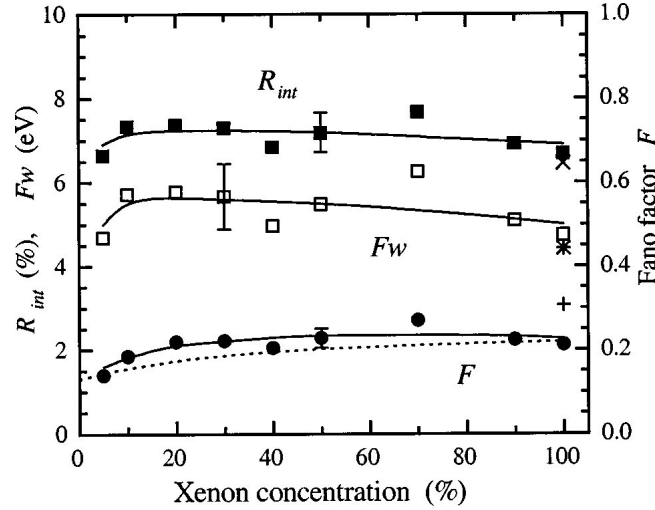


Fig. 1.9: Intrinsic energy resolution R_{int} , Fw values, and Fano factor for an energy of $E_x = 5.9\text{keV}$, as function of Xe concentration. For pure Xe, the respective values are represented by the symbols \times , $*$, and $+$. The plot has been extracted from [23].

tivity; radon and its daughters from radio-impurities in the materials of the detector and shielding, cosmic rays and their secondaries, activation of the detector material during the exposure at the Earth's surface. In Xe gas detectors, the intrinsic radioactivity from ^{85}Kr and the radon diffusion are particularly problematic [4, 56].

First results for the activity of Micromegas readout, specially for microbulk type produced at CERN, indicate that they are already comparable to the cleanest readout systems in low background experiments and it should be possible to further improve these levels after dedicated development [42]. These results set the Micromegas technique as a very attractive option for Rare Event Searches.

In this context, a material screening program based on gamma-ray spectrometry is underway for several years, and it has been included during the last years as part of the work developed in this thesis. All germanium spectroscopy measurements were carried out using a 1 kg ultra-low background HPGe detector from the University of Zaragoza (named Paquito) and operated at the Canfranc Underground Laboratory (see Fig. 1.10). The aim is to measure the activity levels of materials used in the Micromegas planes and also in other components involved in a plausible experimental set-up for Rare Event Searches: gas vessel, field cage, electronic boards, calibration system or shielding. Since the laboratory is located at a depth of 2450 m.w.e., the cosmic muon flux is about 5 orders of magnitude lower than at sea-level surface. This provides an ultra low background system essential for this type of measurements in which the levels of activity are very low (mB/kg or below). A description of the technique and results are briefly drawn in Appendix A (see Ref. [57] for a details).



Fig. 1.10: The germanium detector used for material screening, encapsulated in a copper cryostat and inside its lead shielding at LSC.

1.3 Neutrinoless Double Beta Decay

Evidence for Neutrino Oscillations was obtained from results of atmospheric, solar, reactor, and accelerator neutrino experiments [58, 59, 60]. These results are an impressive proof that neutrinos have a nonzero mass. The detection and study of neutrinoless double beta decay could answer the following problems of neutrino physics: i) lepton number non-conservation, ii) neutrino nature: Dirac ($\nu \neq \bar{\nu}$) or Majorana ($\nu = \bar{\nu}$), iii) absolute neutrino mass scale, iv) the type of neutrino mass hierarchy (normal, inverted, or quasidegenerate). For this reason, extensive experimental and theoretical activities have been carried out, recently summarized in [2, 61, 62]. This section starts with an overview of Neutrino Physics, then the phenomenology of neutrinoless double beta decay is presented and finally the current experimental situation is drawn.

1.3.1 Overview of Neutrino Physics

The interesting field of Neutrino Physics begins when the physicist Wolfgang Pauli in the year 1933, suggested the existence of a new particle to solve the problem of the violation of the principle of energy conservation, observed in the β decay experiments. After that, Enrico Fermi presented a phenomenological model for the β decay, in which hypothesized a new particle, calling it the “neutrino”. This particle should be emitted by the nuclei simultaneously with the electron, carrying the missing energy and momentum. The theory predicted that neutrino would not have charge and its estimated mass would be practically null. As the expected interaction cross section was very low ($\approx 10^{-44} \text{ cm}^2$), its detection was a challenge for the experimental physics of that moment, which was only solved two decades later, thanks to the progress in the Nuclear Reactor Physics.

Between 1953 and 1956, Frederic Reines and Clyde Cowen carried out an experiment for detecting the neutrino. The experiment consisted in yielding the inverse β decay ($\bar{\nu} + p \rightarrow e^+ + n$), for which a high flux of anti-neutrinos -from a nuclear reactor- interact into a target of 400l of heavy water and cadmium chloride. In this

process, a positron and a neutron are simultaneously produced, as a consequence a sequence of γ -rays are emitted; a pair of 511 keV photons from the positron annihilation and the other γ emissions to the neutron capture by the cadmium. The γ -rays were detected by means of liquid scintillators. The results confirming the detection of the neutrino were published at the end of 1956 year [63]. This experiment can be considered as a paradigm in the Neutrino Physics, and for the Rare Event Searches field.

The theoretical and experimental advances of the Neutrino Physics and the Particle Physics of the next years led to the formulation of the so-called Standard Model (SM). This theory identifies the fundamental particles and describes their interactions, establishing that the particles are classified in two basic types called quarks and leptons that interact interchanging particles named bosons. Each group consists of six particles, which are related usually in pairs or generations. Specially, the six leptons arrange in three generations, each one formed by a charge particle and another particle without charge: the “electron” (e) with “the electron neutrino” (ν_e), the muon (μ) with the “muon neutrino” (ν_μ), and the “tau” (τ) with the “tau neutrino” (ν_τ) [64].

The experimental studies of the next years confirmed most of the predictions of the SM. However, the measurements of ν_e from the Sun, since the mid of the 1960s showed that the quantity of measured neutrinos was lower than predicted. This was known as the “solar neutrino problem” which was solved in 2002, when the physicists of the Neutrino Sudbury Observatory [58] confirmed the hypothesis proposed by Gribove and Pontecorvo [65]. This theory sets that the neutrinos change of flavor during the travel from the Sun to the Earth, through a process denominated Neutrino Oscillations [66]. The main implication of the Neutrino Oscillations is that neutrinos must have mass. The three neutrino flavor eigenstates, $|\nu_{e,\mu,\tau}\rangle$ ($|\nu_l\rangle$), can be considered the superpositions of three mass eigenstates, $|\nu_{1,2,3}\rangle$ ($|\nu_i\rangle$):

$$|\nu_l\rangle = \sum_i U_{li} |\nu_i\rangle \quad (1.18)$$

where U_{li} is the unitary matrix that describes the mixture, the so-called Pontecorvo-Maki-Nakagawa-Sakata matrix. The present information on three-flavor Neutrino Oscillations is compatible with two different neutrino mass spectra: normal hierarchy and inverted hierarchy. As shown in Fig. 1.11, in the normal hierarchy the mass-squared difference between the two heavier states is much larger than the one between the two lighter states, conversely for the inverted hierarchy [67].

The results of oscillation experiments are outstanding, since they have provided the first evidence of Physics beyond the SM. But to fix the absolute scale of neutrino masses other kind of experiments are needed and only upper limits have been found up to date. Neutrino mass could be directly estimated analyzing the shape of the end of the beta spectrum in nuclei with a low transition energy like tritium. These experiments have given an upper bound of 2.2 eV for the observable related to the electronic neutrino mass; this result could be improved one order of magnitude in the KATRIN experiment, starting operation in Karlsruhe (Germany). Other limits

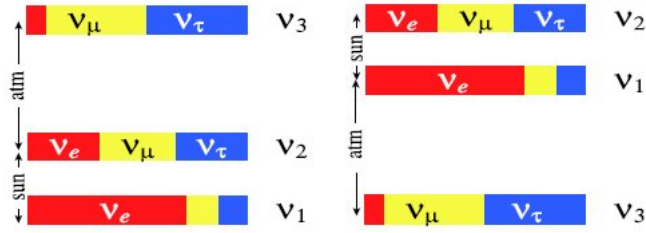


Fig. 1.11: Schemes of the normal (left) and inverted (right) neutrino mass hierarchy models according to the Neutrino Oscillation experiments. The area denotes the predicted content of electron (red), muon (yellow) and tau neutrino (blue), extracted from [62].

come from cosmological observations or analysis of supernovae emissions.

1.3.2 Double Beta Decay

The double beta decay is a process of second order which is produced only for even-even nucleus in which the β decay is forbidden energetically or strongly suppressed by the change of angular momentum. The parent nuclei (A, Z) decays into the daughter nuclei $(A, Z \pm 2)$ by emitting two electrons (or positrons) and other light particles ($L.P.$):

$$(A, Z) \rightarrow (A, Z \pm 2) + 2e^{\pm} + L.P \quad (1.19)$$

According to the emitted particles in the decay, the process can be classified in various modes, two are the most known: the double beta decay with emission of neutrinos ($2\nu\beta\beta$) and the neutrinoless double beta decay ($0\nu\beta\beta$).

For the $2\nu\beta\beta$ decay, the lepton number is conserved, therefore the process is allowed by the SM. The energy of the transition $-Q$ of the $\beta\beta$ decay ($Q_{\beta\beta}$ value)- is shared between the two electrons and the two neutrinos emitted. The experimental signal is the sum of energy of the two emitted electrons, then it is a continuous with mean value around $Q/3$ and finalizes at the $Q_{\beta\beta}$ energy, as shown in Fig. 1.12.

In the $0\nu\beta\beta$ decay the lepton number is not conserved and implies a Physics beyond the SM [68]. This process has become of great interest, due to the discovery of Neutrino Oscillations. The observation of the $0\nu\beta\beta$ decay implies that neutrino is a massive Majorana particle ($\nu = \bar{\nu}$, $m_{\nu} \neq 0$), as mentioned above. The predicted half-lives for this decay are above $T_{1/2}^{0\nu} > 10^{25}$ y. In this mode, the energy is totally carried by the electrons, hence the expected signal is a peak at $Q_{\beta\beta}$ value (see Fig. 1.12), whose width depends on the energy resolution of the detector. This process is relevant because would allow to determine the effective neutrino mass, since its decay probability is proportional to the square of this parameter. Due to the low event rate of this process, the main challenge of $0\nu\beta\beta$ decay experiment is to discriminate the signal from the radioactive background and the signal from the $2\nu\beta\beta$ mode. The $2\nu\beta\beta$ decay is an irreducible background for the $0\nu\beta\beta$ decay.

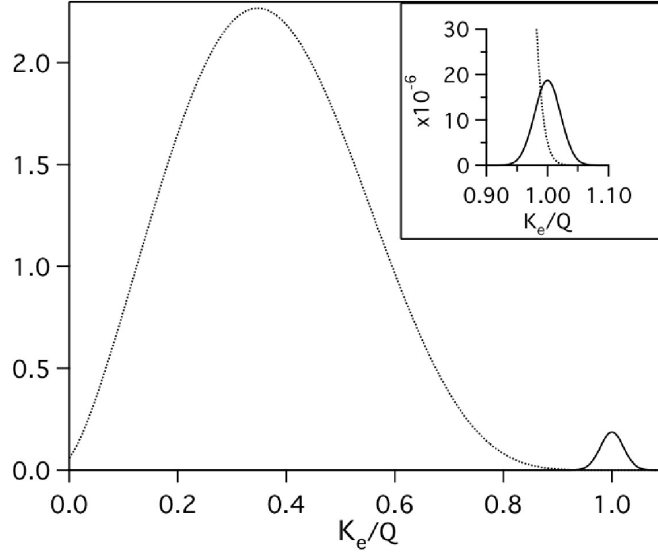


Fig. 1.12: Spectrum of the kinetic energy of the two electrons (divided by the transition energy Q_{bb}) for the two channels of double beta decay.

According to the neutrino mass mechanism of exchange light Majorana neutrinos, the inverse of the half-life $T_{1/2}^{0\nu}$ of the $0\nu\beta\beta$ decay process is directly related to the effective Majorana neutrino mass:

$$\frac{1}{T_{1/2}^{0\nu}} = G_{0\nu} |M_{0\nu}|^2 \left(\frac{\langle m_\nu \rangle}{m_e} \right)^2 \quad (1.20)$$

where $G^{0\nu}$ is the precisely calculable kinematic two-body phase-space factor including coupling constants (proportional to $Q_{\beta\beta}^5$), which has been recently revisited in Ref. [69]⁴. $M_{0\nu}$ the Nuclear Matrix Element (NME) and the term $\langle m_\nu \rangle$ is the observable effective neutrino mass of electron neutrino discussed below. Finally, m_e is the electron mass.

The determination of $M_{0\nu}$ still represents a challenge in theoretical study of the $0\nu\beta\beta$ decay. An accurate determination of this value is essential to calculate the neutrino mass $\langle m_\nu \rangle$ in case of the decay is measured. Further NME can provide a constraint on the upper limit for the effective neutrino mass based on the measured lower limit of $T_{1/2}^{0\nu}$; or from measured neutrino mass in other experiments, the NME allows the determination of lower limit on the half-life of the $0\nu\beta\beta$ decay. It must be noted that the determination of half-life for $2\nu\beta\beta$ has allowed the development of theoretical schemes for NME calculation for the two modes. The calculation of the NMEs requires to know the wave functions of the initial and final states, which have been calculated based on different nuclear models [70]:

⁴In this work, an improved calculation of phase-space factors for $2\nu\beta\beta$ and $0\nu\beta\beta$ is done, using exact Dirac wave functions with finite nuclear size and electron screening.

the configuration-interaction shell model (ISM) [71], recently calculated for the two modes of ^{136}Xe [72]; quasi-particle random phase approximation (QRPA) [73]; the interacting boson approximation (IBA) [74]; angular projected Hartree-Fock Bogoliubov (PHFB) [75]. Recently, it has been established a beyond mean-field covariant functional theory (BMF-CDFT), successfully applied to calculate the NMEs; showing to be consistent with previous results, except for ^{150}Nd [70].

The effective Majorana neutrino mass is therefore obtained directly from the measured half-life (Eq. 1.20) of the $0\nu\beta\beta$ decay as follows:

$$\langle m_\nu \rangle = \frac{m_e}{\sqrt{F_N T_{1/2}}} \quad (1.21)$$

where $F_N \equiv G^{0\nu} |M^{0\nu}|^2$, is obtained from nuclear structure calculations which is model dependent, as explained before. The $|\langle m_\nu \rangle|$ is obtained substituting the matrix U elements in Eq. 1.18:

$$\langle m_\nu \rangle \equiv \left| e^{i\alpha_1} |U_{e1}^2| m_1 + e^{i\alpha_2} |U_{e2}^2| m_2 + |U_{e3}^2| m_3 \right| \quad (1.22)$$

Here, $\alpha_{1,2}$ are the Majorana phases. The observable electronic neutrino effective mass contains the physics beyond the SM and is related with the eigenvalues of the neutrino's mass states and the mixing matrix elements of neutrino as shown in Fig. 1.11, providing information about the hierarchy.

1.3.3 Experimental Situation of $0\nu\beta\beta$ Decay Searches

The first searches of $\beta\beta$ decay were based on geo- and radiochemical measurements, which led to the observation of the process. The aim is to identify the accumulation of the decay isotope during geological time periods in samples enriched with a $\beta\beta$ decay isotope. Nowadays, the experiments only use the direct method, searching the signal on the energy spectrum emitted by the electrons (shown in Fig. 1.12). The $0\nu\beta\beta$ decay experiments using direct counting so far, have used several experimental approaches, which can be divided in two groups where: i) the $\beta\beta$ emitter is separated from the detector or ii) the $\beta\beta$ emitter is embedded in the detector. The main advantages in the first approach are the possibility to study several $\beta\beta$ emitters, and the potential to reconstruct the event topology using more sophisticated detector systems and then discriminate background from signal events. The drawbacks are the low energy resolution typically reached in tracking detectors and the difficulty to scale to larger masses. In the second approach large masses of $\beta\beta$ source can be accumulated with high detection efficiency; it has been applied using semiconductors, bolometers and liquid scintillators.

The sensitivity of experiments is quoted as the reciprocal of the expected half-life in years, this can be written as [62]:

$$(T_{1/2}^{0\nu})^{-1} \propto a\varepsilon \sqrt{\frac{Mt}{B\Delta E}} \quad (1.23)$$

where a is the abundance of the isotope, ε the efficiency of the detector, M the mass used, t the time of measurement, B the background counts (with units of counts/(keV·kg·y) and ΔE the energy resolution. From this relation, it is observed which are the important parameters for a $0\nu\beta\beta$ decay experiment. The exposure of the experiment given by Mt , is very important, indicating that with using larger masses of the emitter target in the detector with long periods of measurement, is achieved better sensitivity; in addition a higher abundance of $\beta\beta$ isotope emitter is desired. On the other hand, it is observed the direct effect of the background and the energy resolutions of the detector. In this way, it is desired to have a $\beta\beta$ target with an energy of $Q_{\beta\beta}$ large to avoid the natural background, which drops drastically above the highest relevant γ -line (at 2614 keV of ^{208}Tl from the ^{232}Th chain).

Experimental efforts of the first generation of $0\nu\beta\beta$ decay experiments, have allowed to measure the $2\nu\beta\beta$ first mode for 11 nucleus (with $T_{1/2}^{2\nu}$ in the range 10^{18} - 10^{24} y) [76]. These experiments used active masses of a few kg of $\beta\beta$ isotope, reaching to set half-life limits in the range 10^{23} - 10^{25} y, corresponding to explore effective neutrino masses between 250 and 1000 meV. In Table 1.4 are shown the $Q_{\beta\beta}$ values and the natural abundance of $\beta\beta$ emitter isotopes studied so far, as well as the lower limit on the half-life of the $0\nu\beta\beta$ decay ($T_{1/2}^{0\nu}$) at 90% C.L, together with the corresponding effective maximal and minimal limits of neutrino mass $\langle m_\nu \rangle$. It must be noted that a controversial claim for $0\nu\beta\beta$ decay has been done by the Heidelberg-Moscow Collaboration for ^{76}Ge , which has not been widely accepted by the scientific community [68], moreover, overruled recently by the constraints from cosmology observations and the latest data released by the EXO-200, KamLAND-Zen and GERDA collaborations [77, 78, 79]. As it can be seen the $0\nu\beta\beta$ decay of ^{136}Xe should give a signal at an energy of 2458 keV [80]. As the expected neutrino mass is between 0.001-0.1 eV, the half-life would be between 10^{27} - 10^{28} y, thus it is required 1-10 tons of the isotope to observe a few events in a period of 2 y [81].

The main challenge of the new generation of the experiments is to improve the sensitivity, using large scale detectors with isotope mass in the range of 100-1000 kg, and reducing as much as possible the background, with the aim to explore effective masses of a few eV. The most advanced experiments at present are shown in Table 1.5; information about the isotope of study is given together with the $T_{1/2}^{0\nu}$ sensitivity and the corresponding range of effective neutrino mass explored as well the status. MAJORANA [83] and GERDA⁵ [79] use semiconductor germanium. Super-NEMO is a continuation of NEMO-3 which [86, 87] achieved to measure the half-lives for $2\nu\beta\beta$ channel in several isotopes with a statistics without precedents. The CUORE experiment use bolometers [88].

EXO [77, 89, 90, 91] and KamLAND-Zen [92, 78] are the most advanced experiments within the liquid scintillators detectors, both investigating ^{136}Xe . The EXO experiment has 175 kg of liquid Xe, and it was the first in determining the

⁵The GERDA experiment uses the same crystals of Ge enriched that were used in Heidelberg-Moscow e IGEX [84, 85].

Isotope	$Q_{\beta\beta}$ (MeV)	Nat. ab. (%)	Experiment	$T_{1/2}^{0\nu}$ (yrs)	$\langle m_\nu \rangle_{min}^{lim}$ (eV)	$\langle m_\nu \rangle_{min}^{lim}$ (eV)
^{48}Ca	4.27	0.19	CANDLES (2)	5.8×10^{22}	3.55	9.91
^{76}Ge	2.04	7.8	HDM (2) IGEX (2)	1.9×10^{25} 1.6×10^{25}	0.21 0.25	0.53 0.63
^{82}Se	2.99	9.2	NEMO-3 (1)	3.2×10^{23}	0.85	2.08
^{96}Zr	3.35	2.8	NEMO-3 (1)	9.2×10^{21}	3.97	14.39
^{100}Mo	3.04	9.6	NEMO-3 (1)	1.1×10^{24}	0.31	0.79
^{116}Cd	2.81	7.6	SLOTVINO (2)	1.7×10^{23}	1.22	2.30
^{130}Te	2.53	34.5	CUORICINO (2)	2.8×10^{24}	0.27	0.57
^{136}Xe	2.47	8.9	DAMA (2)	1.6×10^{24}	0.83	2.04
^{150}Nd	3.37	5.6	NEMO-3 (1)	1.8×10^{22}	2.35	5.08

Table 1.4: $Q_{\beta\beta}$ value, natural abundance and experimental lower limit on the half-life of the $0\nu\beta\beta$ decay ($T_{1/2}^{0\nu}$) at 90% C.L., together with the corresponding effective maximal and minimal limits of neutrino mass $\langle m_\nu \rangle$. The maximal and minimal limits on $\langle m_\nu \rangle$ (taken from [82]), have been calculated using recent NMEs. For each experiment is indicated with (1) when the source \neq detector and (2) when the source = detector.

half-life for $2\nu\beta\beta$ decay for ^{136}Xe ($T_{1/2}^{2\nu} = 2.17 \times 10^{21}$ y). The main drawback of the liquid phase is the limited energy resolution. For this reason, a good option is to use a gaseous Xe TPC, in which an improved energy resolution could be reached and event topology information can be obtained, as proposed in NEXT (discussed in detail below).

1.3.4 NEXT- Neutrino Experiment with a Xenon TPC

The Neutrino Experiment with a Xenon Time-Projection Chamber (NEXT) [93, 94], will be installed in the Canfranc Underground Laboratory (Spain). This experiment will use the electroluminescence technique in a TPC, filled with 100 kg of Xe enriched in the double beta emitter ^{136}Xe ; in principle, pure Xe is considered, although currently investigation in admixtures is being performed. Part of the work in this thesis, is motivated by the possible use of Xe+TMA mixtures in NEXT.

The detector design combines the measurement of the topological signature of the event for background discrimination with the energy resolution optimization. As shown in Fig. 1.13, separate energy and tracking readout planes are based on different sensors: photomultiplier tubes for calorimetry and silicon multi-pixel photon counters for tracking [95]. The prompt primary scintillation light emission is detected through photo-detectors behind a transparent cathode. The t_0 time is determined with this signal, which is used for the event position along the drift distance. The charge created is drifted towards the opposite anode under the application of an electric field.

Three prototypes have been developed as part of R&D tasks, NEXT-MM,

Experiment	Isotope	Mass (kg)	Sensitivity $T_{1/2}^{0\nu}$ (yrs)	Sensitivity $\langle m_\nu \rangle$, meV	Status
GERDA	^{76}Ge	40	2×10^{26}	80-190	in progress
		1000	6×10^{27}	15-35	R&D
CUORE	^{130}Te	200	2×10^{26}	50-130	in progress
MAJORANA	^{76}Ge	30-60	1.5×10^{26}	90-200	in progress
		1000	6×10^{27}	15-35	R&D
EXO	^{136}Xe	200	4×10^{25}	100-240	in progres
		5000	2×10^{27}	14-33	R&D
SuperNEMO	^{82}Se	100-200	$1-2 \times 10^{26}$	44-140	R&D
KamLAND-Zen	^{136}Xe	320	2×10^{26}	44-105	in progres
		1000	6×10^{26}	25-60	R&D
SNO+	^{150}Te	800	10^{26}	50-130	in progres
		8000	10^{27}	16-40	R&D

Table 1.5: Information about the seven most advanced experiments in searching the $0\nu\beta\beta$ decay (apart from NEXT), the isotope of study is given together with the $T_{1/2}^{0\nu}$ sensitivity at 90% C.L and the corresponding range of effective neutrino mass explored as well the status (A modification from [76]).

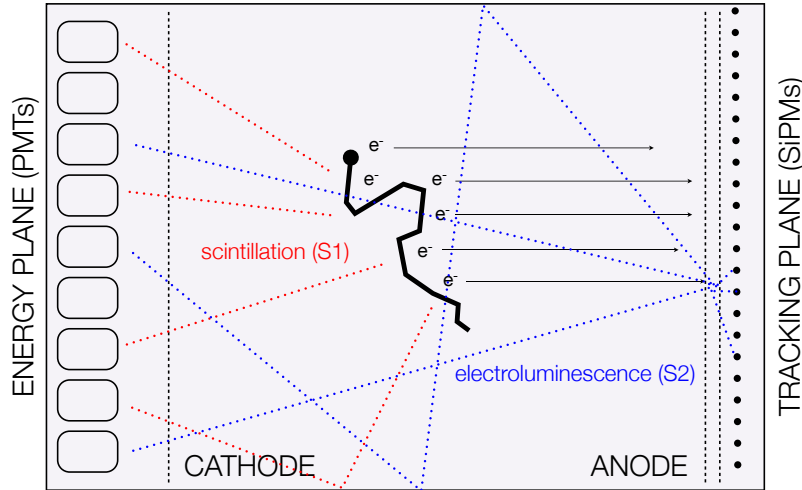


Fig. 1.13: Concept of the NEXT experiment: light from the Xe electroluminescence generated at the anode, is recorded both in the photosensor plane right behind it for tracking and in the photosensor plane behind the transparent cathode for a precise energy measurement.

NEXT-DBDM, and NEXT-DEMO, the two last are briefly described and the first one is discussed in detail in next section.

- NEXT-DBDM: This prototype is placed at Lawrence Berkeley Laboratory. The main objective has been to demonstrate the capability to obtain good energy resolution in HPXe using electroluminescence. In this detector, only 1 plane of PMTs is used, which is located in the cathode and used for calorimetry. First results showed an energy resolution of $\sim 1\%$ FWHM for 662 keV at 10 bar, which extrapolates to 0.5% at $Q_{\beta\beta}$ value [96]. Recently this prototype is also working towards directional Dark Matter searches. In this context, the ionization and scintillation for nuclear recoils in xenon is being studied, results recently presented in [97]. They show that nuclear and electronic recoil can be distinguished via the scintillation to ionization ratio.
- NEXT-DEMO (NEXT demonstrator): It is located at IFIC in Valencia. It has been developed to show both good energy resolution and tracking capabilities with two planes of photodetectors (PMT and SiPM). The drift region is only 30 cm. First tracks reconstruction has been presented, showing visible blobs at the extremity of the tracks. Latest results give an energy resolution of 5.5% FWHM at 30 keV, which extrapolates to 0.6% FWHM at the $Q_{\beta\beta}$ value of ^{136}Xe [98].

1.3.5 NEXT-Micromegas and the T-REX Project

The Micromegas technology is a very promising readout for applications in rare event searches with HPXe TPCs; specially, the microbulk type technology thanks to its very low radioactivity content as mentioned before [42, 1, 99]. Furthermore, Xe gas detectors offer improved energy resolutions and event topology recognitions. The goal of the T-REX project (TPCs for Rare Event eXperiments) is to explore this potential [1].

The commissioning and first data-taking with the NEXT-MM prototype (see Fig. 1.14) this prototype was presented in [100], this work includes measurements with bulk and microbulk technology in Ar+2% $i\text{C}_4\text{C}_{10}$ benchmark mixture, and very preliminary measurements in Xe+2%TMA mixture. The tracking capabilities of the system were demonstrated in this work. This work is pioneer using microbulk technology in a large system at high pressure. Recent results for Xe+TMA mixture were published [101]; energy resolution of 10.6% (1 bar) and 12.5% (2.7 bar) at ~ 30 keV with inter-pixel calibration were obtained. It must be noted that the use of Xe+TMA mixtures in this prototype was motivated by results performed within the context of this thesis, presented in chapter 4 and published in [102, 103]. The tracking capabilities showed with the larger prototype reinforce results presented in this thesis.

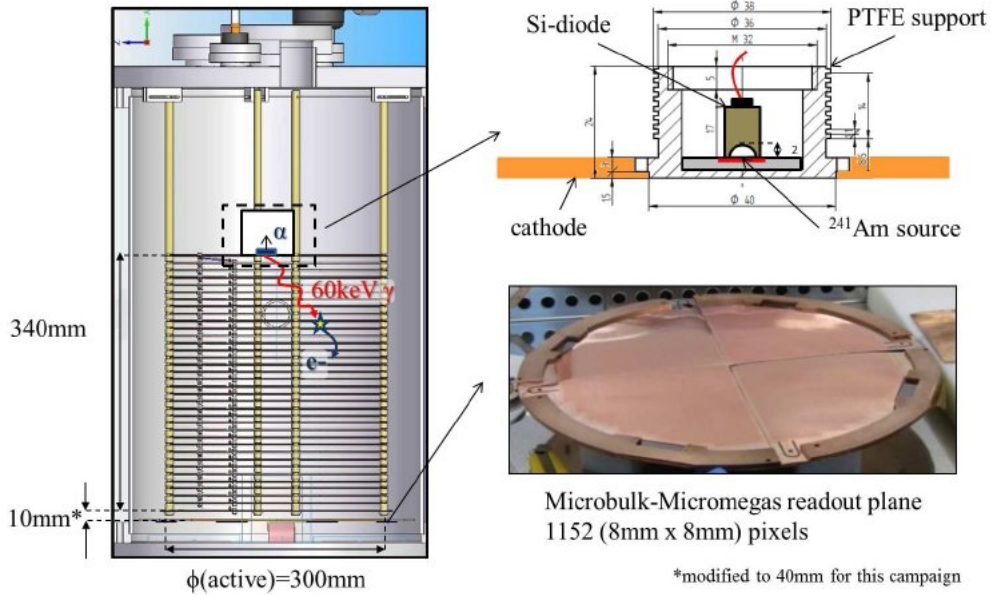


Fig. 1.14: Left: Schematic representation of the NEXT-MM prototype, transverse section showing the field cage, source position and readout plane. Right-up: ^{241}Am source and Si-diode detector in its PTFE enclosure. Right-down: Microbulk-Micromegas readout plane, formed by four separate quadrants, extracted from [101].

1.4 Dark Matter Searches

1.4.1 Overview

Diverse astrophysical and cosmological observations show that the universe is formed by a dominant non-baryonic matter, the so-called Dark Matter, since Fritz Zwicky in 1933 measured a velocity dispersion of the members of the Coma galaxy cluster, very large to be supported by the luminous matter [104]. Afterwards, measurements of the rotation curves of spiral galaxies performed in 1970s by Vera Rubin and Albert Bosma also gave evidence for non-luminous matter [105, 106]. Apart from these classic results, at present the evidence has been supplemented from weak and strong lensing [107, 108], hot gas in clusters [109], the Bullet Cluster [110], Big Bang nucleosynthesis (BBN) [111], the cosmic microwave background (CMB) [112] among others. These observations have allowed to measure the abundance of primordial elements, to obtain the precise mapping of anisotropies in the cosmic microwave background, as well as to study the distribution of matter on galactic and extragalactic up to the largest scales observed. These studies have led to establish a precise cosmological model of the Universe, the Standard Cosmological Model (Λ CDM). The Λ CDM model establishes that the universe is spatially flat and composed by $\approx 5\%$ baryonic matter, $\approx 27\%$ non-baryonic Dark Matter and

$\approx 68\%$ dark energy [113].

Furthermore, observations lead to establish that Dark Matter is stable, compound by weakly interacting particles [114]. Weakly Interacting Massive Particles (WIMPs) are a generic class of Dark Matter candidates, which must be looked beyond the SM. These should have been in thermal equilibrium with quarks and leptons in the hot early Universe, and decoupled when they became non-relativistic [114]. Examples of these generic particles are the lightest supersymmetric particle in many supersymmetric theories with R-parity conservation, the neutralino [115], and the lightest Kaluza-Klein particle in theories of extra dimensions [116]. In addition, axions and axions-like particles (ALPs) represent another type of well motivated Dark Matter candidates [117]. Axions from the Sun are searched using the axion helioscope technique, which exploits the predicted couplings of those particles with photons and electrons [118, 119, 120].

WIMP's can be detected following three different approaches: at particle colliders, indirectly by astrophysical observations, or directly in the laboratory by appropriated detectors. The production and detection of WIMPs at the LHC can provide information about their microscopic and interactions properties, however, it would not demonstrate that these particles are the Dark Matter of the Universe [121]. On the other hand, the astrophysical indirect detection attempts to search the products of WIMP annihilation within the Milky Way and beyond, as γ -rays or other secondary particles. Recent works have studied the Galactic center, mainly because it is predicted that it could contain very high densities of Dark Matter, according to many theoretical models; this may lead to very high rate of Dark Matter annihilation and hence high luminosity of γ -rays, antimatter and neutrinos. Specially, anomalous abundance of positron by PAMELLA Collaboration [122] and γ -rays by the Fermi Gamma Ray Space Telescope (FGST) [123, 124] have been measured. These measurements have achieved the level of precision required to probe thermal Dark Matter particle candidates with masses between ~ 10 -100 GeV [125]. However, the WIMP signal will need to be distinguished from astrophysical background and it is strongly dependent on the model for the Dark Matter distribution, the annihilation process and the propagation of charged particles in the Milky Way's magnetic field and the Galactic Center [126]. This section will focus on the third option: direct detection, specially concerning the search with sensitive detectors to the directionality of the WIMP signal.

1.4.2 Direct Detection

The aim of direct detection Dark Matter experiments is to measure the energy deposited in the nuclear recoil produced by WIMP elastic scattering off interaction with target nuclei in the laboratory detector. As the WIMPs interaction probability with matter is very small, predicted interaction cross section of the WIMP ranges typically between 10^{-6} and 10^{-10} pb ($1 \text{ pb} = 10^{-36} \text{ cm}^2$). The nuclear recoil rate expected is very small, for instance $\sim 1 \times 10^{-4}/(\text{kgd})$ in a LXe target [81]. Moreover, the energy of the recoils is significantly below ~ 10 -100 keV. The main challenge

of the direct Dark Matter detection is to discriminate between background and signals, typically orders of magnitude larger; specially, hardest task is to distinguish the nuclear recoils produced by the interaction of neutrons with target nuclei from those induced by WIMPs. Background from cosmic rays is minimized by working deep underground, and environmental backgrounds are reduced by using radiopure components and by shielding the detectors. Three potential identifying signatures could be generated: the time modulation of detection rates, the direction and target nucleus dependence of the energy spectrum of the recoils. The yearly movement of the Earth around the Sun yields an annual modulation of the nuclear recoil rate [127]. On the other hand, the motion of the Sun with respect to the Galactic halo, introduces directionality in the WIMP event rate.

The nuclear recoil produced by a WIMP interaction can produce at the detector medium: ionization, phonons (heat) and scintillation (light). Actually, most of the current experiments exploit this fact, using several techniques which register one or two of the signal channels. Typically the use of two channels allow to improve the background discrimination power. Since the 1980s there have been experiments with the aim to detect Dark Matter, the detectors and techniques have continuously improved.

The DAMA/LIBRA Collaboration has found evidence of an annual modulation in the interaction rate, with results progressively upgraded. After 14 cycles of measurements with 9.3σ of statistical significance (results obtained combining with the previous phase experiment, DAMA/NAI) a modulation amplitude of the single-hit events in the energy range of 2-6 keV was obtained [128]. Even though the ample statistics, the amplitude modulation, the frequency, and phase are in agreement with the expectations for Galactic Dark Matter, the results have not been widely accepted by the community, mainly because this modulation may be produced by an annual background modulation, rather than by WIMP interaction [126]. The main goal of the ANAIS experiment, to be operated at the Canfranc Underground Laboratory, is to confirm or refute the DAMA/LIBRA result using the same target and technique [129]. In addition, the CDMS II (Si) [130], CoGeNT [131], CRESST-II [132] have also found excess of events.

There are current experiments that use Xe as target. The Xe is a particularly suitable Dark Matter target due to its high atomic number and because it contains odd and even isotopes which allows to study both spin-dependent and spin-independent interactions. Current Xe-based Dark Matter experiments are in single-phase (liquid) detectors or dual-phase (liquid/gas) TPCs. In a dual-phase TPC, the prompt light signal is observed with two arrays of photosensors, and the free electrons are drifted away from the interaction place towards the vapor phase above the liquid and detected through an amplified, proportional scintillation signal (see Fig. 1.15). Simultaneous detection of both ionization and scintillation signals provides information allowing a larger potential of discriminations. Four collaborations are currently using or developing LXe detectors for Dark Matter: XENON [133], ZEPLIN [134] and LUX Collaborations [135] which selected the dual-phase TPC approach, while XMASS [136] Collaboration uses a single-phase

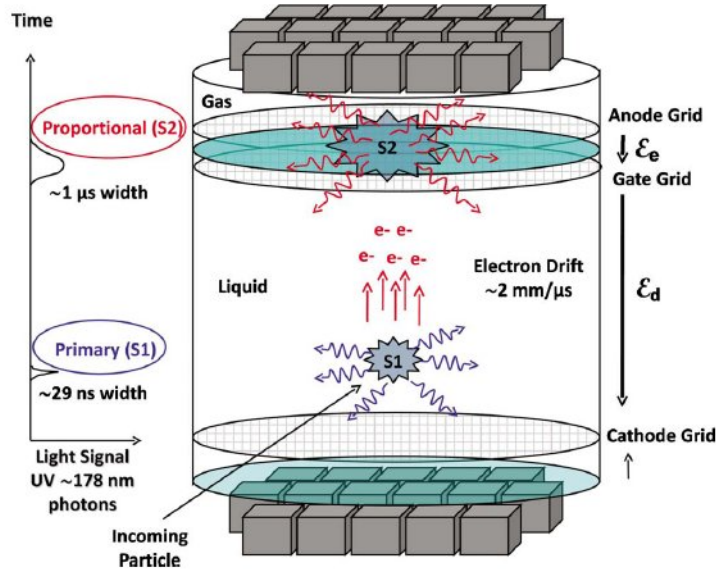


Fig. 1.15: Double phase TPC LXe detector used for Dark Matter detection in XENON [133], ZEPLIN [134] and LUX Collaborations, extracted from [81].

detector (scintillation signal) [81].

Specially, LUX experiment [135] has set the most stringent spin-independent WIMP-nucleon cross-section exclusion for the experiments working with Xe as target, with a minimum upper limit of $7.6 \times 10^{-46} \text{ cm}^2$ at a WIMP mass of $33 \text{ GeV}/c^2$ with 90% C.L., from the analysis for 85.3 live days of data with a fiducial volume of 118 kg. On the other hand, XENON experiment is a program consisting in a series of dual-phase TPCs: XENON10, XENON100, and XENON1000; numbers refer to the order of magnitude of the fiducial target mass in kg. The XENON100 detector is an upgrade of XENON10 [137], presently is operating underground at the Gran Sasso National Laboratory. Main feature is the improvement in the background respect to the previous phase. A blind analysis of 224.6 live days \times 34 kg exposure has yielded no evidence for Dark Matter interactions [133], constraining the spin-independent elastic WIMP-nucleon scattering cross section for WIMP mass above $8 \text{ GeV}/c^2$, with a minimum limit of $2 \times 10^{-45} \text{ cm}^2$ at a WIMP mass of $55 \text{ GeV}/c^2$ with 90% C.L., limits on spin-dependent WIMP-nucleon cross sections are also presented in Ref. [138].

These results from direct detection so far, together with the possible indirect detections of anomalous γ -rays spectrum of the Galactic center [124] could be consistent with a WIMP mass in the $6\text{-}30 \text{ GeV}/c^2$ range. However, these results are difficult to be reconciled with recent negative searches of SuperCDMS [139] or Xe experiments.

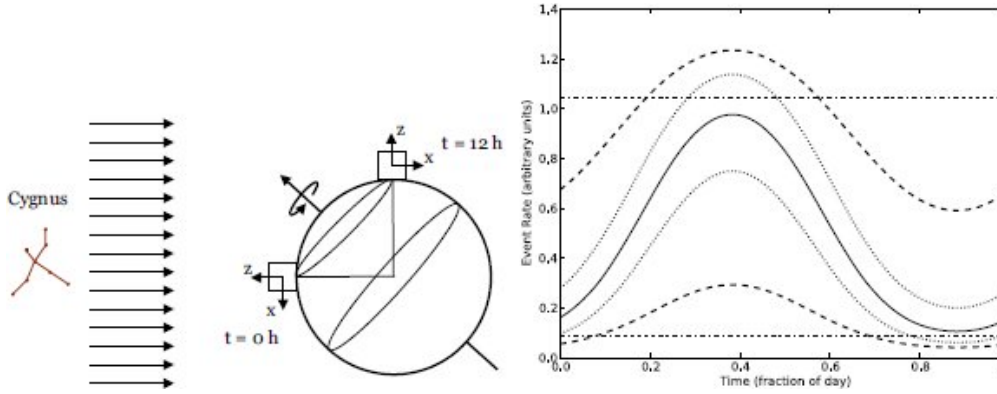


Fig. 1.16: Left: Scheme of how daily rotation of the Earth yields a modulation in recoil angle measured in the laboratory frame. Right: Magnitude of the daily modulation in event rate for seven lab-fixed directions, specified as angles with respect to the Earth's equatorial plane (figure taken from [126]).

1.4.3 Directional Dark Matter Searches

Directional Dark Matter detection is based on the fact that the motion of the Sun with respect to the Galactic halo with a velocity of around 220 km/s, introduces directionality in the WIMP event rate, and then in the nuclear recoils produced by the interaction of those particles in detectors [140]. The Earth is moving towards the constellation Cygnus, it is expected a modulation in nuclear recoils that peaked strongly in the opposite direction. Works have estimated that an anisotropic set of recoils may be discriminated from isotropic background with as few as 10 events [141, 142]. The peak recoil direction could also be measured, reaching to confirm the Galactic origin of the particle scattering, with around 30-50 events [143] (see Fig. 1.16).

Typically the directional event rate is written as follows [142]:

$$\frac{d^2 R}{dE d\Omega_q} = \frac{\rho_0 \sigma_N}{4\pi m_\chi \mu^2} F^2(E) \hat{f}_{lab}(v_{min}(E), \hat{q}) \quad (1.24)$$

where R is the event rate per unit time per unit mass of detector, expressed as a function of the direction and energy of the recoiling nucleus in the laboratory frame, and $d\Omega_q$ is the solid angle element around the direction of the recoil momentum q . The total Dark Matter density is ρ_0 , σ_N the WIMP-nucleus scattering cross section, m_χ the WIMP mass and $\hat{f}_{lab}(v_{min}(E), \hat{q})$ the transformation of the local WIMP velocity distribution in the lab frame. The minimum speed at which a scatterer can create a recoil of energy E is v_{min} , this depends on the WIMP-nucleus reduced mass $\mu = m_\chi m_N / (m_\chi + m_N)$ and on the nucleus mass m_N . $F(E)$ is the nuclear form factor, which is the Fourier transform of the nuclear density distribution that accounts for the decrease in the effective cross section for scattering events with non-zero momentum transfer. The WIMP-nucleus cross section σ_N is written in terms of the experiment-independent WIMP-nucleon cross section $\sigma_{p,n}$.

Gaseous detectors offer the best conditions for detecting directionality. After the interaction between a WIMP and the nuclei, the recoiling nuclei leaves an ionization track in the gas. A detector measuring the nuclear recoil momentum vector in three dimensions, (axis and direction of recoil) and with good angular resolution could distinguish the WIMP signal from the background with less statistics than in the annual modulation. In this case the direction changes by 90° every 12 hours, there is not background known that can mask this signal [126].

It is concluded that if a moderately high density WIMP flux is present in the Solar neighborhood, hence there are good prospects for its detection using directional dark matter detectors.

Directional detection is a recent field of investigation, it counts actually with prototypes in early stages. The main experiments search for the directionality by using TPCs, containing low pressure gases, such as CF_4 , CS_2 , C_4H_{10} or ^3He . (For a detailed description see Ref. [126]). Current experiments include DMTPC [144], DRIFT [145], MIMAC [146] and NEWAGE [147]. First evidence for the so-called head-tail directional signature of neutron-induced nuclear recoil tracks was presented by DRIFT-II [148].

In this scenario, a new concept for directional dark matter was recently proposed by D. Nygren [6]. The idea is based on the fact that columnar recombinations in high pressure xenon gas could be used as a tool for distinguishing the direction of nuclear recoils produced by the interaction of a WIMP in the detector. The measure of directionality for each event could be done comparing the recombination R signal to the surviving ionization signal I, thereby for each event the ratio R/I may provide the information of the angular direction of the recoil.

The concept is being evaluated through experimental and simulations work. As first step in this thesis is shown a preliminary study in Xe+TMA mixtures with α -particles in chapter 5. The columnar effect was observed: charge collected for parallel tracks is lower than for perpendicular ones, these results have been published in [149]. This result is a first step in evaluating this idea; further work will be done with neutrons, to see if the columnar effect remains for nuclear recoils.

Part I

**PART I: Characterization of
Micromegas in Xe and Xe+Ne
mixtures**

Characterization of Micromegas in Xe, and Xe+Ne Mixtures

Contents

2.1	Experimental Setup	38
2.1.1	Time Projection Chamber	38
2.1.2	Gas System	40
2.1.3	Vacuum System	41
2.1.4	Recovery System	42
2.2	Measurements of α-particles in Xe and Xe+Ne Mixtures	44
2.2.1	Experimental Procedure	44
2.2.2	Data Analysis	45
2.2.3	Electron Transmission	46
2.2.4	Risetime vs Pulse-height Distributions	48
2.2.5	Energy Resolution variation on drift field	51
2.2.6	Drift Velocity	54
2.2.7	Gain	57
2.2.8	Energy resolution dependence on the amplification field	60
2.2.9	Discussion	62
2.3	Energy Resolution for γ-rays in pure Xe	64
2.3.1	Experimental setup and procedure	64
2.3.2	Spectrum from γ -rays of an ^{241}Am source in pure Xe	64
2.3.3	Analysis and results	65
2.3.4	Discussion	66
2.4	Conclusions	69

The first experimental goal of this thesis was to perform measurements in a high pressure Micromegas TPC in pure Xe. Afterwards, the experimental efforts were focused on the study of Xe+Ne mixtures, the motivation to study this mixture was mentioned in Chapter 1 .

The setup used for measurements carried out in this thesis was built to characterize Micromegas readouts at high pressure and for testing different gases, mainly noble gases or mixtures whose base gas is a noble gas. A description of the design and commissioning of the chamber, denoted hereinafter by NEXT-0-MM TPC, and

the gas system is presented in F.J Iguaz PhD thesis [30]. Good performance of the TPC, vacuum and gas system, was demonstrated through γ -measurements in Ar+iC₄H₁₀ (Ar-Isobutane) up to 10 bar. In addition, α -measurements in pure Xe showed the potential capabilities in terms of energy resolution of Micromegas read-outs for double beta decay searches, even though the measurements were done in sealed mode (without removing oxygen). The best values of energy resolution at 4 bar were 2.5% FWHM (1.8% FWHM), for all α tracks (selecting parallel tracks respect to the drift field direction); these values extrapolate to 3.7% FWHM (2.7% FWHM) at the $Q_{\beta\beta}$ value of ¹³⁶Xe. The energy resolution obtained for parallel tracks (2.7% FWHM), -value that would be closer to the one in ideal conditions- fulfills the requirements of a $2\beta\beta$ decay experiment, showing that this technology is very competitive for this application [150, 151].

Measurements in pure Xe using α -particles and γ -rays were done up to 8 bar and 5 bar, respectively. A cryopumping recovery system was installed into the setup (gas system) allowing to reclaim the Xe from the system. This provided flexibility to carry out other experimental tasks, as to the systemic study of several Xe+Ne mixtures and Xe+TMA mixtures. In this chapter is presented the study of several Xe+Ne mixtures (Ne fraction 10%-50%) using different Micromegas, systematic measurements of electronic properties up to 7 bar with α -particles were carried out.

The chapter is organized as follows: the description of the experimental setup is explained in Sec. 2.1, focusing on the new systems installed. Then the α -measurements in pure Xe and Xe+Ne are presented in section 2.2. Following in section 2.3, γ -measurements in pure Xe at high pressure are described and finally the conclusions are drawn in section 2.4.

2.1 Experimental Setup

The experimental setup consists of a small Time Projection Chamber TPC (NEXT-0-MM TPC), a gas system, a vacuum system and a recovery system. The location of the complete system is in the *Laboratorio de Astropartículas* whose installation is in the Universidad de Zaragoza¹. A schematic view is shown in Fig. 2.1, below it will be described in detail each system.

2.1.1 Time Projection Chamber

The chamber was constructed with ultra-high vacuum specifications by the company Telstar and rated for operation up to 15 bar. It has an active volume of 2.4 l, having 10 cm in height and 16 cm in diameter (see Fig. 2.2). The chamber includes 10 circular outlets with different diameters (1 CF160, 4 CF40 and 5 CF16) which are closed by copper joints, allowing either ultrahigh vacuum or high pressure performance.

¹Laboratory is located in an external building of the Facultad de Ciencias in the campus of *San Francisco*.

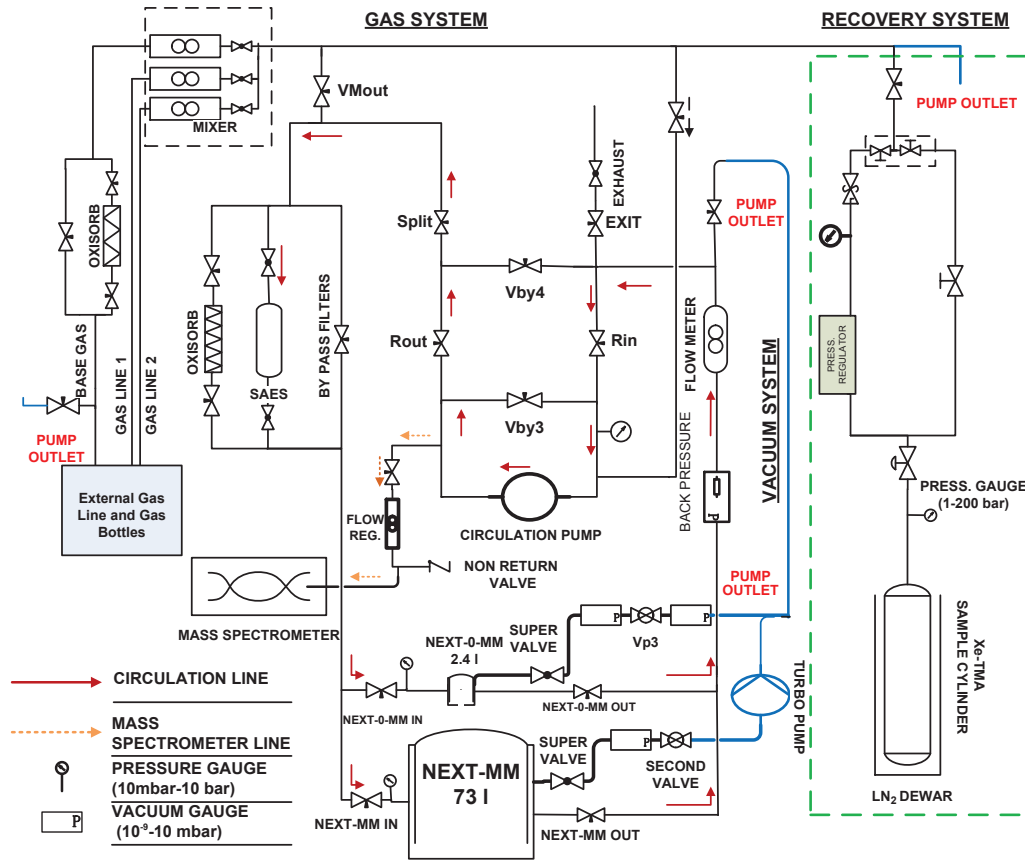


Fig. 2.1: Schematic view of the experimental setup. At the bottom/center, the TPC employed for these measurements (dubbed ‘NEXT-0-MM’) is shown. A medium-size TPC (NEXT-MM), central to this system, is also shown.

The outlet (CF160) is the main chamber access to the inside of the chamber, which is used for making all the necessary changes. One of the CF40 outlet is the access to the pumping system, during the measurements an all-metal pressure valve is used to isolate the chamber of the vacuum system; this allows to work at higher pressures and ultrahigh vacuum is ensured. Vacuum feedthroughs were installed in two of the CF40 outlets for establishing electronic connections, 4 SHV feed-throughs were installed in one of them, and in the another 3 BNC feed-throughs. The last CF40 outlet remained unused for most of the measurements presented in this thesis.

The drift field cage is formed by means of three peek-plastic columns that support two copper foils (cathode and anode with 10 cm in diameter) and six copper rings (see Fig. 2.3). Six resistors of 33 M Ω are connected successively from the cathode to the anode. On the center of the cathode was machined a circular reduction with a hole in its center to place radioactive sources. Meanwhile, in the anode foil a circular hole in the center was made to place the Micromegas readout by means of two delrin-plastic pieces.

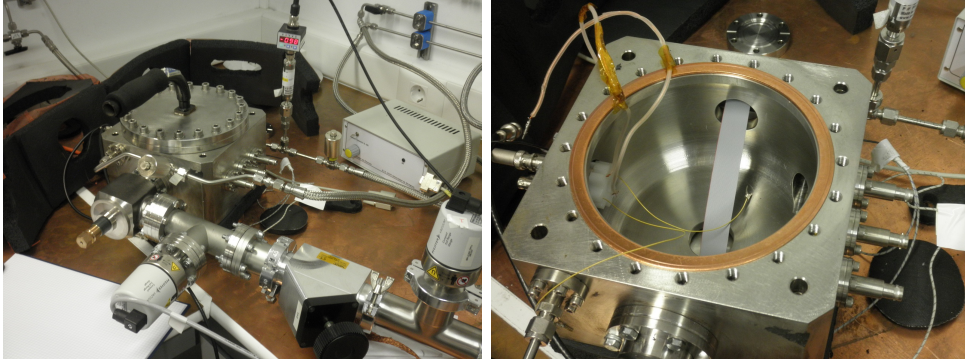


Fig. 2.2: Pictures of the Time Projection Chamber (NEXT-0-MM TPC) used for all the measurements carried out in this thesis.

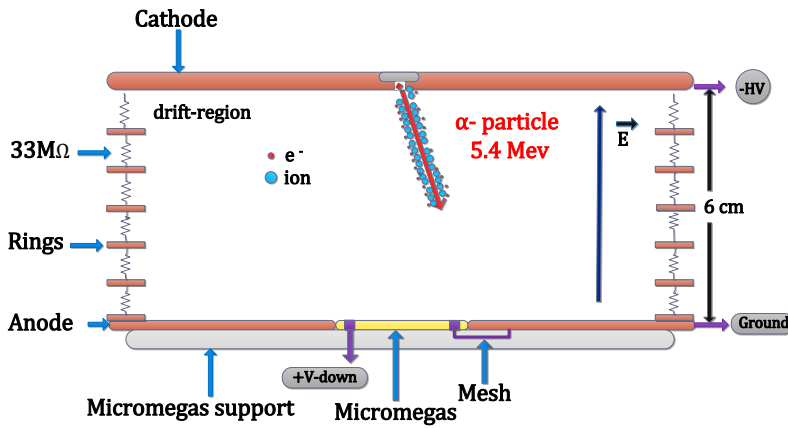


Fig. 2.3: Scheme of the drift field cage used for α measurements in Xe and Xe+Ne mixtures. The voltage configuration is also shown.

2.1.2 Gas System

The gas system consists in two subsystems: the external and the recirculation subsystem. It must be noted that the gas system has been subject to modifications in the course of this thesis, mainly to adapt it to the new needs. Specially, for these measurements a cryo-pumping system was added, explained in detail in section 2.1.4.

The gas system was designed for making mixtures of up to three components. For this reason, the external subsystem was conditioned to connect three gas bottles by means of three gas lines. Each line has a purge nitrogen line, used for removing the air in the system, for instance, when a new bottle is installed. One of the gas lines is used for the base gas, for this work was Xe. The other two lines are used to connect the gas bottles of the quencher gases. For measurements presented in this chapter, the first quencher gas line was connected to a Ne bottle.

The three gas lines are directly connected to a gas mixer, except the base line

that enters into the system through of a bypass valve or by a gas line with an Oxisorb purifier. The mixer allows to obtain an homogeneous admixture by using a Bronkhorst mass flow controller for each gas line that ends in a volume where the gases mix completely. However, this functionality to prepare mixtures was not used, as the Xe used was always in the recovery bottle.

The gas from the mixer enters into the recirculation subsystem where it has the possibility to pass by: an Oxisorb purifier line, a SAES (702) purifier line or a bypass gas line (see Fig. 2.1). Thereafter the gas is brought to the TPC to fill it until the desired pressure is achieved. When the gas is recirculated to remove oxygen and homogenize the mixture, the TPC-in and TPC-out valves remain open. During the recirculation, the gas goes out by the TPC-out valve into a back pressure and a flow meter (see Fig. 2.1). The recirculation process is completed by means of an oil free membrane pump (KNF type PM23592-286.13), providing that the gas flows into the TPC through the same line for which enters into the TPC.

2.1.3 Vacuum System

The main component of the vacuum system is the turbomolecular pump. The outlet of the pump is connected to a CF-standard T flange that provides three outlets. Two of the outlets are connected to a CF40 flanges, the first one is connected to the small (NEXT-0-MM) and the second to the medium (NEXT-MM) size chambers by means of flexible vacuum tubes (see Fig. 2.1). At the end of the NEXT-0-MM flexible tube, a vacuum gauge (G1) followed by a valve (secondary valve) it was installed; and just before the connection to the high pressure valve of the NEXT-0-MM chamber, other vacuum gauge (G6) was connected. The configuration between the pump and the NEXT-MM chamber entrance is similar, however there is only one vacuum gauge (G5), which is placed just before the high pressure valve of the chamber. This configuration allows to measure independently the vacuum pressure for both chambers, and measure the outgassing rate using the G6 gauge for the small chamber and the G5 gauge for the medium chamber.

The materials used for the drift field cage were selected to have as much low outgassing rate as possible, further they were properly cleaned or conditioned before introduced it. Bake-out processes were frequently performed to reduce the outgassing rate. For this purpose, the four corners of the vessel are connected independently to four thermal resistors, which in turn are connected to a power supply (variable voltage generator). The temperature is increased up to values around 120°C, whose value is maintained by means of a thermal insulator that covers completely the vessel.

The outgassing measurement is usually carried out just before to start the measurements, after having baked-out and pumped the vessel and the gas system for a long time period, typically until the vacuum pressure is below 5×10^{-5} mbar l/s. For outgassing measurement, the vacuum pressure is measured as a function of the time during 2 min., thus the outgassing rate is calculated by:

$$q = V \frac{\Delta P}{\Delta T} \quad (2.1)$$

were V is the isolated volume and ΔP corresponds to the change of pressure in the interval of time ΔT . In the case of the measurement for the NEXT-0-MM chamber the volume would be 2.3l, while if the gas system is included the value volume is 2.7l. It must be noted that this calculation is true in first approximation, enough for the interest of this work.

2.1.4 Recovery System

Before the installation of the recovery system, the Xe gas was normally vented to atmosphere after the measurements had concluded. However, due to the cost of Xe has been increasing during the last years, hence it was necessary to look for a method to recover and recycle the Xe. A **cryopump** system was selected as the method to reclaim and store the Xe. Thus it was designed, installed and commissioned; in Fig. 2.1 (at right side) can be seen a schematic representation of it, and in Fig. 2.4 a picture of the recovery system at the present.



Fig. 2.4: Picture of the recovery system used to store the Xe. At the beginning, only one sample bottle was installed, recently two more bottles were added allowing to work at 10 bar in the medium size chamber.

The cryopump works as vacuum pump, capturing gases by condensing them inside a volume whose surface has been previously cooled by means of Dewar filled with LN₂, so temperatures below 77.3 K are reached. The cryocondensation occurs when the temperature of the cooled surface is able to maintain the saturation pressure below the desired vacuum pressure. Using LN₂ in the pumping process, gases whose boiling and melting points are below 77.3 K can be trapped; those satisfying the condition are captured inside the cooled volume, passing most of the

times directly from the gaseous to the solid phase without any liquid phase. The phase transition temperatures, specifically the boiling and melting temperatures for Xe and other interesting gases are shown in Table 2.1. It is seen that all the gases quoted have boiling points above the LN₂ temperature, except the Ne which has a lower value. This implies that during the recovery process this gas would therefore remain without being trapped [152, 153].

Gas	Boiling Point (K)	Melting Point (K)
Xe	165.02 ± 0.05	161.40
Ne	27.2 ± 0.3	83.8 ± 0.3
TMA	276 – 280	155.95
O ₂	90.2 ± 0.2	54.8 ± 0.2
N ₂	77.4 ± 0.3	63.3 ± 0.3
CO ₂	216.6 ± 0.3	194.7 ± 0.3
Ar	87.5 ± 0.3	83.8 ± 0.3

Table 2.1: Boiling and melting temperatures for certain gases of interest, extracted from [154].

The cryopump system designed consists of a stainless steel sample cylinder of 2.2l together with a Dewar flask of 5l, and two gas lines whose function is connect the sample bottle with the gas system. These two gas lines guarantee security conditions during the recovering and filling processes. One of the gas lines is used to recover the gas from the chamber and the gas system into the sample cylinder by a cryopumping; this line provides an anti-return valve which avoids that the gas returns to the gas system, in those cases where the valve has not been closed after the recuperation process. Meanwhile, the other gas line is used in the filling process, to introduce the gas from the sample cylinder to the TPC. As usually the pressure of the sample cylinder is above 25 bar, it was installed a pressure regulator to reduce the pressure to values below 10 bar; in order to control the pressure after the pressure regulator a gauge was also installed. An escape valve was introduced to guarantee that the gas system is never exposed to pressures larger than 15 bar, hence if the pressure is accidentally larger than 15 bar the valve opens.

One of the major features that offers this system is that the oxygen can be removed from the Xe during the recovery process. The oxygen can enter into the chamber or the gas system through leaks and outgassing. In the course of the commissioning of the system, it was demonstrated that oxygen could be removed, by pumping directly the sample cylinder just after all the Xe has been condensed. To optimize this process, the Dewar flask is completely or in some cases partially removed, so the temperature of the sample bottle surface increases due to the heat transfer from the outside. Consequently, the boiling oxygen inside the vessel evaporates making more efficiently its removal, by pumping it.

2.2 Measurements of α -particles in Xe and Xe+Ne Mixtures

In this section the characterization of Micromegas readouts in Xe and several Xe+Ne mixtures using α -particles is presented. Studies of the dependence of the energy resolution and gain on drift field, amplification field and pressure were performed. For these measurements an ^{241}Am radioactive source with an activity of 500 Bq was placed centered on the cathode; to allow the penetration of the α -particles, a 2 mm diameter hole was drilled in its center.

2.2.1 Experimental Procedure

2.2.1.1 Pure Xe Measurements

Previous to the data acquisition, the chamber was baked-out during 8 h to reduce the outgassing, and pumped (~ 48 h). The vacuum pressure and outgassing rate values measured were 1.1×10^{-5} mbar and 7.7×10^{-6} mbar l/s, respectively. The pressures studied were 2, 4, 6 and 8 bar, in this range the full containment of the α tracks is guaranteed.

For the first measurement, the Xe gas was introduced from the external gas line through Oxisorb filter, up to 2 bar. After the data acquisition at 2 bar, new gas from external bottle was added up to 4 bar, likewise the highest pressures were reached (6 and 8 bar). At the moment of the experiment, the circulation pump was not available, hence the measurements were done in sealed mode. For this reason, the measurements were carried out in the shortest possible time, to reduce the content of oxygen outgassing.

For each pressure, the characterization consisted in performing a drift field scanning, in which the amplification field is fixed to a value where the signal-to-noise ratio was sufficiently good to provide noise free pulses. Through this process the transmission curve was obtained, allowing to determine a drift field value at which the transmission reaches the maximum. Once the operating point was established, the amplification field was changed from the minimum possible value until the sparks limit is reached; this limit was established as the amplification field at which sparks occurred successively during a time period of 30 s.

2.2.1.2 Xe+Ne Measurements

The recovery system had already been installed before starting the Xe+Ne measurements, which allows to reclaim the Xe from the chamber and store it inside the sample bottle by means of cryopumping (see 2.1.4). To prepare a determined Xe+Ne mixture, for instance a mixture by a volume percent of $C_A\% \text{Xe} + C_B\% \text{Ne}$ at certain pressure P , firstly, the equivalent percentage in pressure of Xe ($C_A P$) was introduced from the sample bottle. Then, the fraction in pressure of Ne ($C_B P$) gas was added from the external bottle. Thereafter the input and output valves of the chamber were closed, taking the measurements in sealed mode. For

this reason, before the data acquisition, the chamber was pumped and most of the times beaked out to reduce as much as possible the vacuum pressure and the outgassing rate; in fact the data taking started only if the values of outgassing rate and vacuum pressure were below 7×10^{-6} mbar l/s and 1.1×10^{-5} mbar, respectively.

After the preparation of the mixture, the measurements started after 20 minutes to allow the homogenization of the mixture in the chamber, then the acquisition started which lasted approximately 2 h. For each mixture, the procedure followed is similar to the one explained for pure Xe; a drift voltage and then an amplification field scan were performed. At the end, the Xe was reclaimed condensing it by cryopump process inside the sample cylinder; during this process the Ne remains in gaseous phase; almost half of the volume in the chamber and the in the sample bottle. The Ne gas in the sample bottle moves to the cooled volume by difference of pressure up to equal pressures in all the system. The Ne gas was then pumped, and at the same time the oxygen was removed by means of cryopumping, as described in section 2.1.4. The cryopumping ended when the vacuum pressure in the system was above 10^{-3} mbar.

This procedure allowed to limit the effect of attachment because to for each measurement a new mixture is prepared, hence the oxygen in the gas is limited to the outgassing during the measurement. A simple estimation of oxygen concentration gives 45 ppm at 1 bar, after 3 h of measurement, value for an outgassing rate of 7.0×10^{-6} mbar l/s and a volume of 2.4 l (chamber volume). For simplicity, in this calculation it is considered that the attachment is only produced by the oxygen; however, in the outgassing other kind of electronegative molecules are released.

2.2.2 Data Analysis

For α -particles measurements, 15 k pulses were acquired for each voltage configuration and digitized by means of the oscilloscope (Tektronix TDSS5054B). For this analysis the interest is centered in the charge and temporal projection of the track, these parameters are estimated through the pulse-height and the risetime of the signal which are defined as

- **Pulse-height:** The height of the pulse, obtained subtracting the pulse baseline (offset voltage) from the maximum value obtained.
- **Risetime:** It is defined as the temporal distance between the time position at which the height reaches 90% and 10% of the pulse-height.

The determination of these parameters is done through a pulse shape analysis (PSA) that consists of two steps:

1. Pulses are smoothed to reduce noise fluctuations by applying a Fast Fourier Transform (FFT) that is implemented using the C library *ffw3* [155]. This procedure allows to substrate the high frequencies which are related with noise

fluctuations; the cut frequency is selected on base of the frequential domain, so only the main frequencies are included allowing to obtain the smooth pulse.

2. Pulse parameters are calculated taking into account the definition given above, an example of a typical smoothed pulse from α -particles generated by the preamplifier is shown in Fig. 2.5, where the pulse-height and the risetime definition are also depicted.

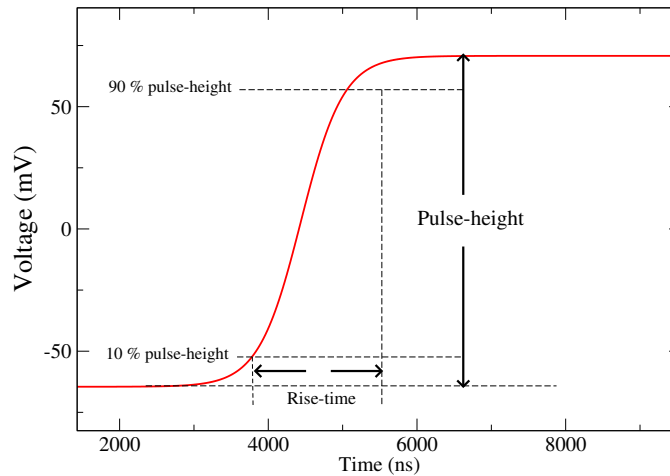


Fig. 2.5: Typical smoothed signal from α -particles. Pulse-height and risetime are shown, the definition of these parameters is given in the text.

2.2.3 Electron Transmission

The electron transmission curve is a measurement of the relative variation of electron collection efficiency on drift field. For each drift field, the electron transmission (ET) is calculated as the ratio of the charge collected to the maximum charge measured during the scanning of the drift field. This is given by the ratio of the corresponding peaks position at 5.4 MeV, which are calculated by fitting the peaks to a Gaussian function. In order to facilitate the analysis, the measurements with α -particles were organized in four groups. The description for each group of measurements is given in Table 2.2, in which the gas together with the geometric parameters of the Micromegas used (gap-pitch-hole diameter) are specified, as well as the range of pressure studied; and the Ne fraction is given when the filling gas was Xe+Ne.

For all measurements, the ET curves are shown in Fig. 2.6. In general for all curves, the electron transmission rises as the ratio of drift-to-amplification fields increases, reaching a maximum for most, in some cases the EL drops after the full transmission range.

Gas	Micromegas description label, gap-pitch-hole (μm)	Pressure range (bar)	Gas specifications
Xe	MM1, 50-60-30	2-8	-
Xe+Ne	MM2, 25-50-25	4-6	Ne range 20-50%
Xe+Ne	MM3, 50-75-45	3	Ne range 25-50%
Xe+Ne	MM3, 50-75-45	3-7	60%Xe+40%Ne mixture

Table 2.2: Description of the measurements with α -particles carried out in pure Xe and several Xe+Ne mixtures and pressures. The measurements are organized in four groups. The geometric parameters of the Micromegas together with the pressure are detailed for each group of measurements; and the Ne fraction is given when the filling gas is Xe+Ne.

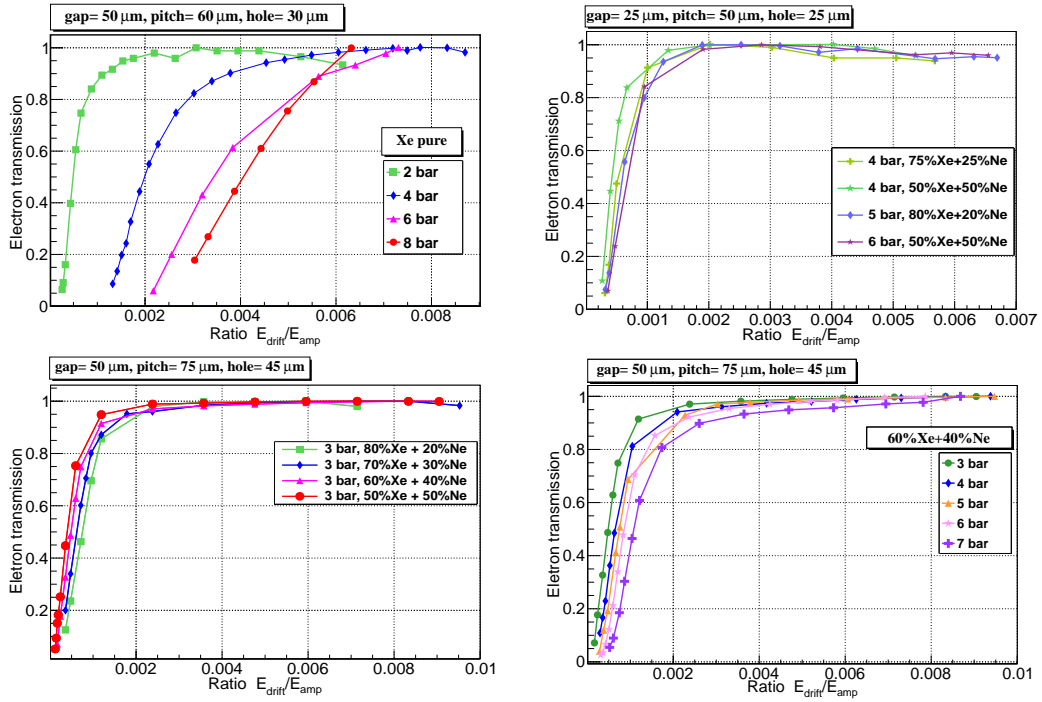


Fig. 2.6: Dependence of the electron transmission of Micromegas on the ratio of drift-to-amplification fields in pure Xe and Xe+Ne mixtures at different pressures. The specifications of gas and pressure for each curve are indicated in legends, as well as the geometric parameters of the Micromegas at the top of each graphic.

For pure Xe measurements, a Micromegas with geometric parameters of 50-60-30 μm (MM1) was used (see Table 2.2). The amplification voltages for each pressure were: 380 (2 bar), 440 (4 bar), 650 (6 bar) and 750 V (8 bar), Results for 2 and 4 bar show that the full ET is reached at ratios of drift-to-amplification fields of 0.004 and 0.0085; while at 6 and 8 bar the full transmission is not achieved. At higher pressure the drift field could no be increased due to the high voltage limit of the feedthrough used for these measurements (6 kV). The values of ET should have the

same value at a given value of the reduced drift field (E_d/P), so the representation of the ET as a function of the reduced drift field (E_d/P) is more appropriated (see Fig. 2.7-left). As the pressure increases, the ET is significantly lower than at 2 bar. This means that at higher pressure the charge collected is lower, which is a strong evidence of attachment for these measurements, as expected.

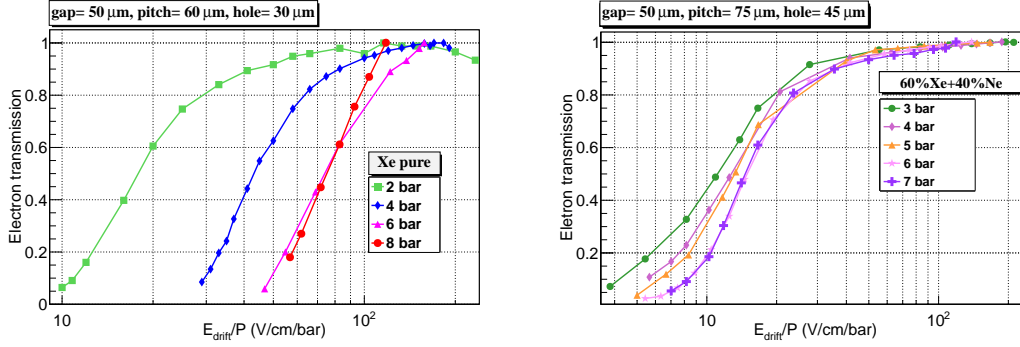


Fig. 2.7: Dependence of the electron transmission of Micromegas of $50 \mu\text{m}$ gap thickness on E_d/P in pure Xe and in $60\%Xe+40\%Ne$ mixture at different pressures. The specifications of the gas and pressure for each curve are indicated in the legends, as well as the geometric parameters of the Micromegas at the top of each graphic.

For Xe+Ne mixtures, the ET curves of Micromegas with geometric parameters of $25\text{-}50\text{-}25 \mu\text{m}$ (MM2) for several pressures and Ne fractions are shown in Fig. 2.6-above (right) and with $50\text{-}75\text{-}45 \mu\text{m}$ (MM3) in Fig. 2.6-bottom, varying the Ne fraction (20%-50%) at 3 bar (left) and ranging the pressure from 3 to 7 bar in a $60\%Xe+40\%Ne$ mixture (right). At 3 bar varying the Ne fraction (Fig. 2.6-bottom (right)), the amplification voltage was set at 350 V, thus the drift and amplification properties on Ne concentration was studied. As seen it seems that the ET at low drift field depends on the Ne fraction, further a systematic effect is observed, as the fraction of Ne increases the ET is higher; the same behaviour is seen in Fig. 2.6-top (right) at 4 bar. These results suggest that this is an effect of the Ne fraction, instead of the readout, indicating that recombination decreases with the addition of Ne. On the other hand, the ET as a function of E_d/P is shown in Fig. 2.7-right ($60\%Xe+40\%Ne$ mixture); it is seen that the ET decreases as the pressure increases, which is attributed to the attachment, however the variation is considerably less than the observed in pure Xe (see Fig. 2.7-left).

2.2.4 Risetime vs Pulse-height Distributions

The loss of electron transmission observed at low drift fields for pure Xe and Xe+Ne mixtures in Fig. 2.7-left can be explained by means of three physical phenomena (diffusion, recombination, attachment) or geometries defects. Previous works indicate that the diffusion has not substantial influence on the ET [156]. The influence of the recombination, specifically the columnar, and attachment on the ET at low drift fields can be evaluated by studding the risetime vs pulse-height distributions.

Therefore, it is possible to clarify, what of the two phenomena it is affecting the transmission (electron collection efficiency).

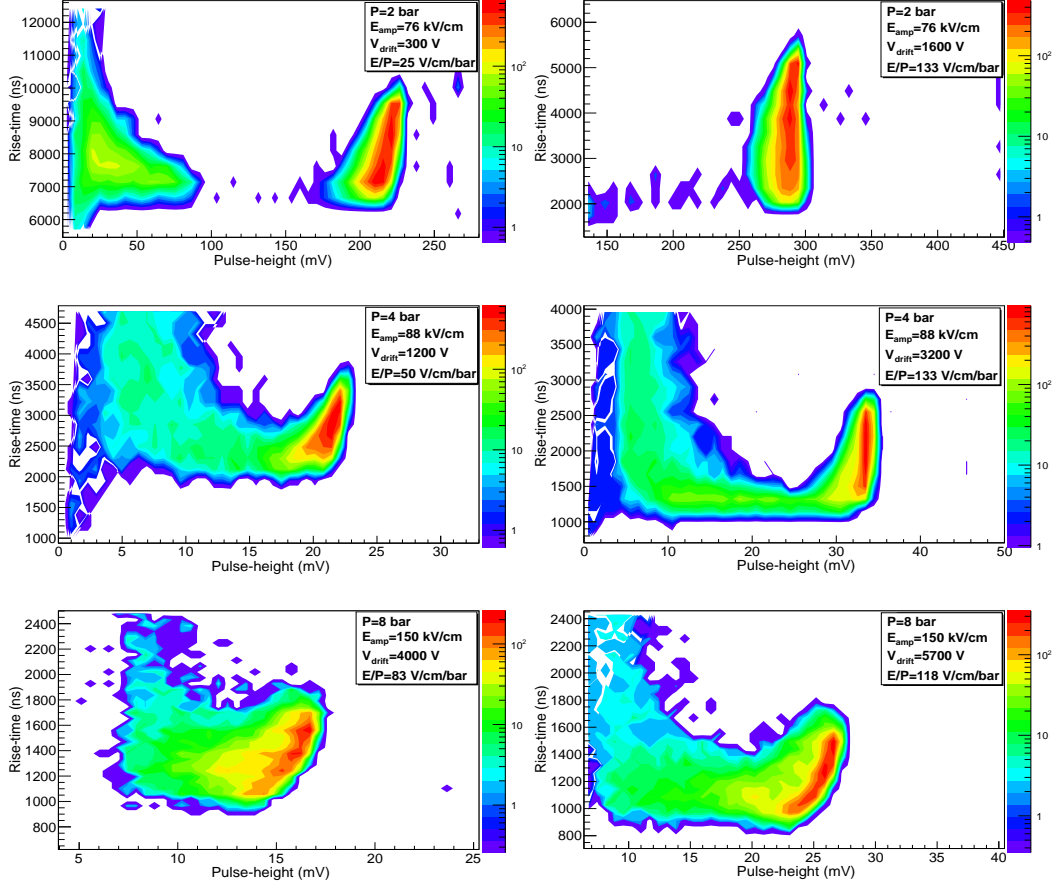


Fig. 2.8: Distribution of risetime vs pulse-height at low (left) and high (right) E_d/P , for pure Xe at 2 (top), 4 (middle) and 8 bar (bottom). The voltage configuration is indicated on each plot.

In Fig. 2.8 various risetime versus pulse-height plots are seen for pure Xe at 2, 6, and 8 bar, and in Fig. 2.9 in 60%Xe+40%Ne mixture at 3, 6 and 7 bar. For each pressure, it is shown a distribution for low (left) and high (right) E_d/P values. A dependence of the pulse-height on risetime is observed, as the pulse-height increases the risetime as well. This correlation is seen for all the low plots (Fig. 2.8-left) for pure Xe. However, at high E_d/P at 2 bar ($E_d/P=133$ V/cm/bar) this dependency disappears, but not at 4 and 8 bar, being more pronounced at the highest pressure. On the other hand, in 60%Xe+40%Ne mixture (see Fig.2.9) the correlation is not observed either at low or high E_d/P (55 and 138 V/cm/bar) at 3 bar. At higher pressures (5 and 7 bar), the correlation is observed at low E_d/P , (58 and 50 V/cm/bar) but substantially lower than in pure Xe at higher E_d/P (122 and 119 V/cm/bar).

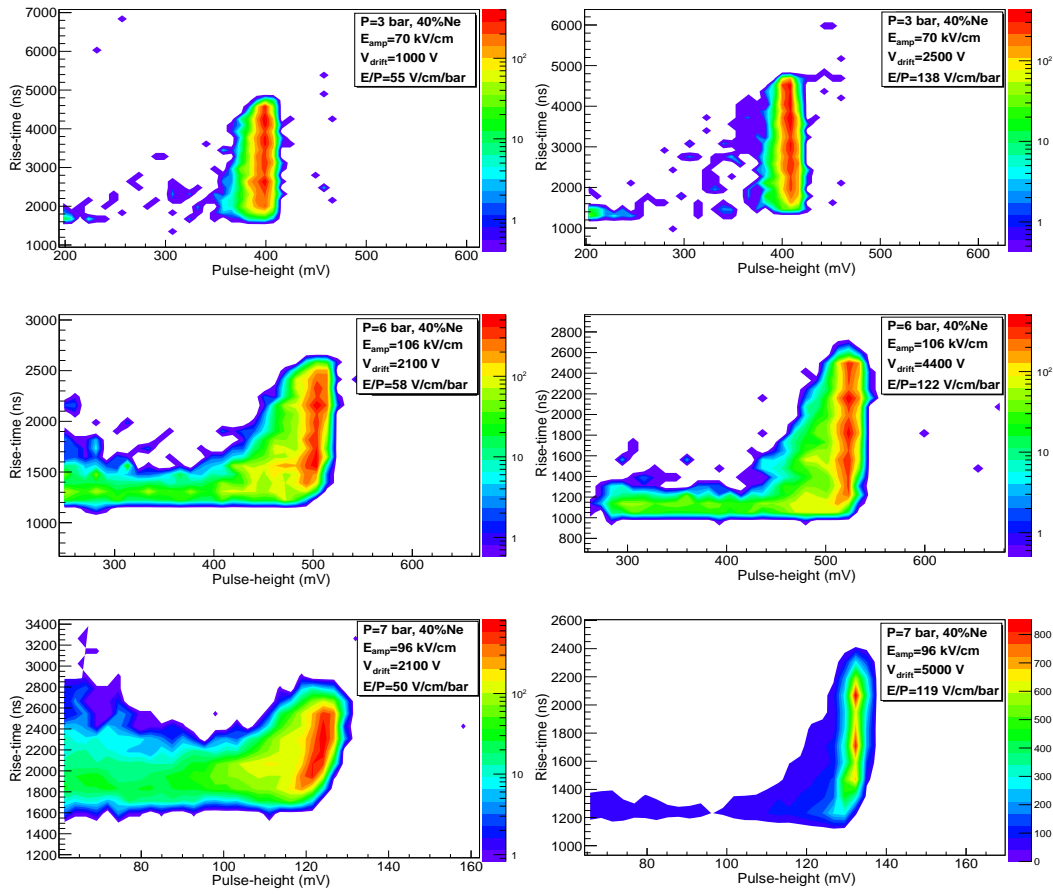


Fig. 2.9: As for previous figure, but in 60%Xe+40%Ne mixture at 3 (top), 6 (middle) and 7 bar (bottom). The dependence of risetime on pulse-height is substantially lower than the observed in pure Xe, indicating the lower attachment for these measurements.

This correlation between risetime and pulse-height is compatible with attachment instead of columnar recombination. To understand this, it is worthwhile remembering that the risetime is the temporal projection of the track over the drift field direction (see Fig. 2.10). Thus smaller risetime corresponds to α -tracks with larger tracks angles respect to drift field direction whereas larger risetimes to tracks with shorter α -tracks angles. The electrons produced by ionization of perpendicular α -tracks travel larger distances to arrive at Micromegas mesh, increasing the probability of being trapped by electronegative impurities, therefore, less charge is collected compared with electrons from parallel α -tracks for which the distances of drift are smaller.

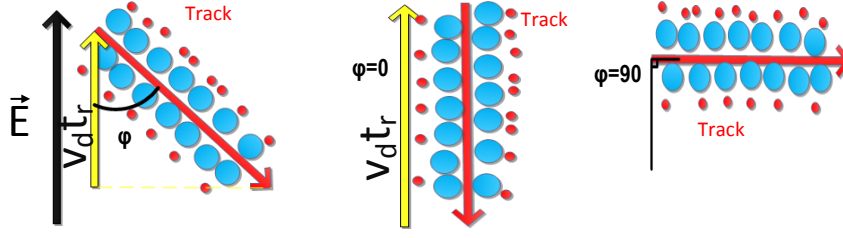


Fig. 2.10: Schematic representation of the α track in three different orientations together with its projection on the drift field direction. The strong dependence of risetime on pulse-height at high pressure is due to attachment.

2.2.5 Energy Resolution variation on drift field

Energy resolution measures how accurately it is possible to evaluate the energy deposited by a radiation particle. As explained in previous chapter, the main contributions to the energy resolution are the fluctuation in the primary number of electrons and the gain fluctuations. The dependence of the energy resolutions on the drift field provides information about the effect of loss of charge by electron transmission and recombination. Experimentally, the energy resolution at FWHM is determined through the following equation:

$$R(FWHM) = 2.35 \frac{\sigma_m}{M} \quad (2.2)$$

M is the mean of the distribution and σ_m its standard deviation. These parameters are extracted from Gaussian fit performed to the pulse-height distribution acquired for each configuration. It must be noted that most of the pulse-height distributions do not follow a Normal distribution, however, as first approximation the fit was performed at the left side of the peak.

In the previous section, it was seen that the measurements for pure Xe and Xe+Ne mixtures are dominated by attachment, mainly at the highest pressures. In order to obtain a better estimation of the energy resolution, cuts on risetime were applied to obtain the pulse-height distribution. Tracks with small angles and with larger ones were selected, in Fig. 2.11 and 2.12 are shown pulse-height distributions formed by α (^{241}Am source) interaction in pure Xe at 2, and 8 bar and in a 60%Xe+40%Ne mixture at 3 and 7 bar. For each pressure, two drift field configurations were selected, at low (Fig. 2.11- and 2.12-left) and high (Fig. 2.11- and 2.12-right) E_d/P ; the respective pressure, amplification field, drift voltage and E_d/P are indicated on each plot. For every figure, the pulse-height distribution for raw (rose), parallel tracks (green, larger risetime) and perpendicular tracks (blue, smaller rise times) are shown; in legends are indicated the respective cuts applied for each sample of events. The energy resolution at FWHM is indicated for raw and parallel α tracks pulse-height distributions, being obtained from Gaussian fit

of the right side of the α peak of the raw spectrum and the complete α -peak for parallel tracks.

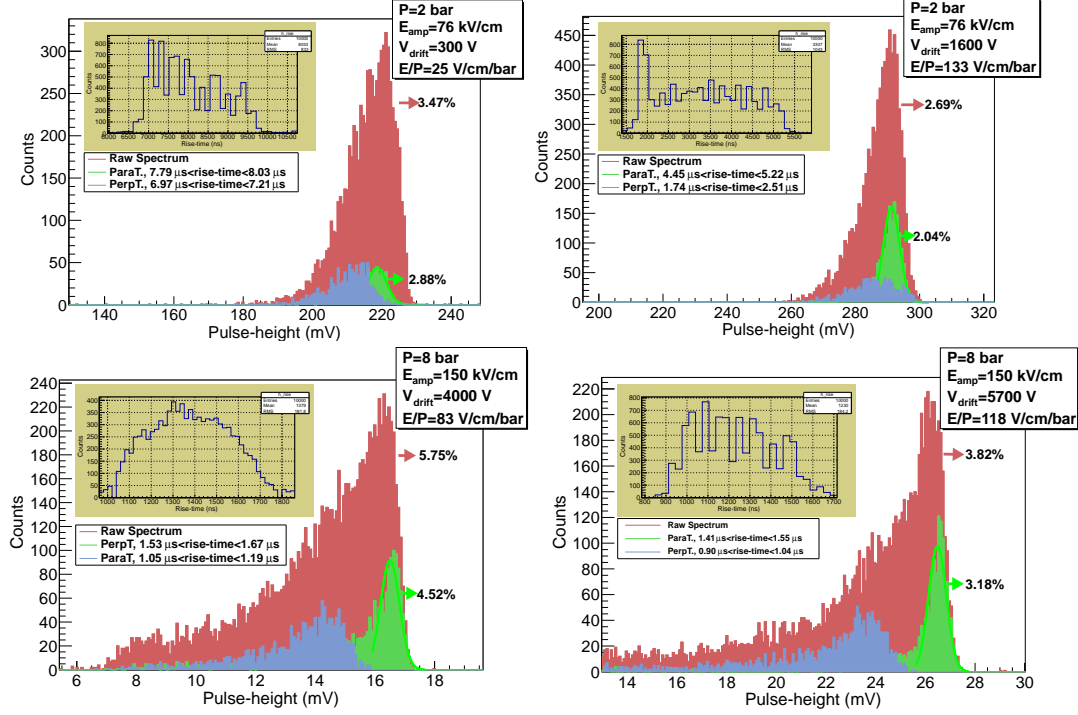


Fig. 2.11: Pulse-height distributions generated by the α -particles (5.4 MeV of an ^{241}Am source) interaction in pure Xe at 2 and 8 bar. For each pressure, distributions are presented at low (left) and higher (right) reduced drift field (E_d/P). The distributions are plotted for raw spectrum (rose) and tracks near to the parallel (larger risetime, green) and perpendicular (smaller risetime, blue) drift field direction. The energy resolution is indicated for raw spectrum and for parallel tracks at FWHM.

In general, for all the pure Xe and some Xe+Ne configurations shown the raw pulse-height distribution exhibit an asymmetric form, with a large tail on the left side. The tail is more pronounced for pure Xe at low E_d/P (< 100 V/cm/bar), reducing it at higher values. For 60%Xe+40%Ne mixtures the tail is seen at low E_d/P , but substantially decreases at higher values. The perpendicular pulse-height distributions (smaller risetime, blue spectrum) have a large tail for almost all the configuration either pure Xe and Xe+Ne mixtures with a mean value lower than the α -peak of the raw spectrum. By contrast the parallel pulse-height distributions have a Gaussian distribution with main value practically in the same position that for raw spectrum. This means that the tail observed for most of the raw pulse-height distributions is from perpendicular α -tracks, this indicates that loss of charge is due to attachment.

The energy resolution (%FWHM) for raw and parallel pulse-height distribution were determined following Eq. 2.2, for all the voltages configurations acquired with pure Xe and Xe+Ne mixtures, results are depicted in Fig. 2.13.

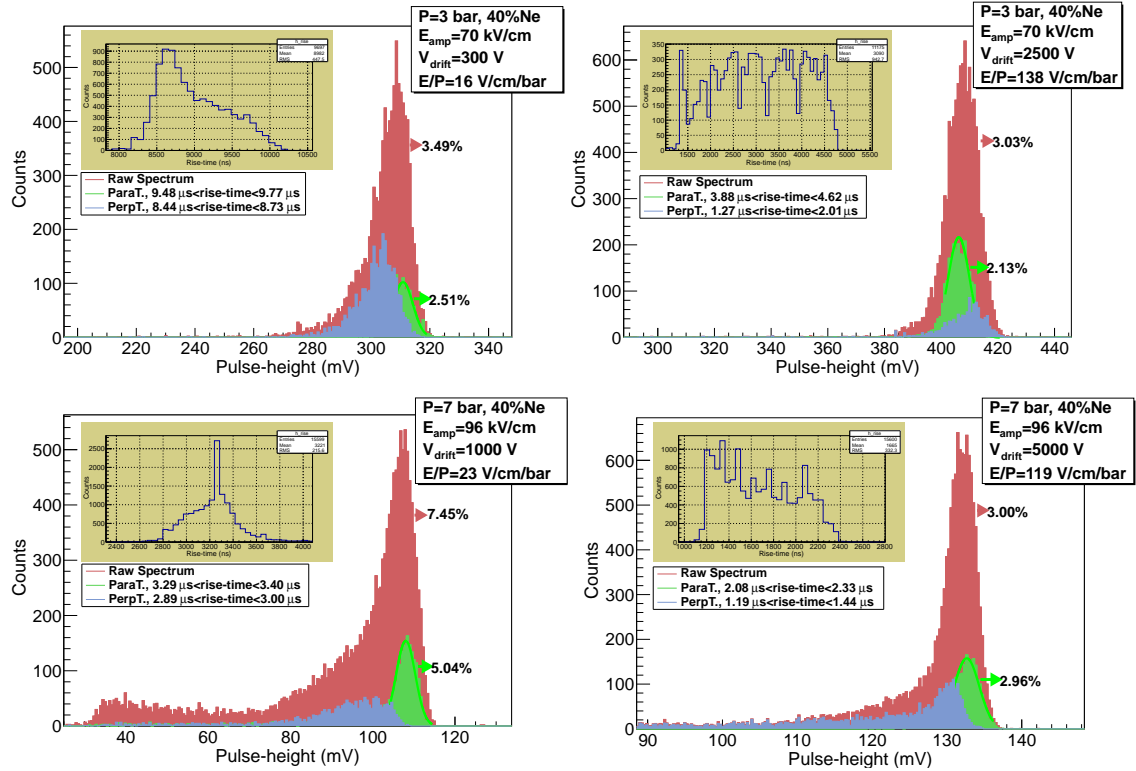


Fig. 2.12: As for Fig. 2.11 for Xe+Ne mixtures at 3 and 7 bar. The mean charge of perpendicular tracks is closer to the one of parallel tracks at high pressure, this implies that the attachment effect is lower than the observed in pure Xe.

From Fig. 2.13 the following observations can be done:

- The energy resolution improves rapidly with the increase of the drift field, from 100 V/cm/bar the value remains practically constant for all the configurations, except for pure Xe at 8 bar, which is explained by the high level of impurities present for these measurements.
- For each configuration (gas, pressure, Micromegas), the curve of raw energy resolution (open marks) is always above the parallel one (solid markers), except for some configurations in pure Xe. This fact is explained by the longer tail observed for these configurations, indicating that the Gaussian fit is not the most appropriated; a Landau fit is likely more adequate to fit the α -peak of the raw pulse-height distributions. However, the interest of these measurements was to calculate the energy resolution at the optimum conditions, thus the value of major interest is the energy resolution from parallel tracks.
- The best values of energy resolution from parallel for pure Xe are around 2% at FWHM for pressures in the 2-6 bar range, being 3% at 8 bar. For Xe+Ne mixtures, the best values of energy resolution are around 2% for Micromegas with a gap thickness of 50 μm (Fig. 2.13-bottom (left and right)), being a little

higher for Micromegas with $25\ \mu\text{m} \sim 2.25\%$ (top-right). Two configurations with higher oxygen contamination respect to the others are 80%Xe+20%Ne at 5 bar (Fig. 2.13-top (right), blue) and 60%Xe+40%Ne at 7 bar (Fig. 2.13-bottom (left), purple).

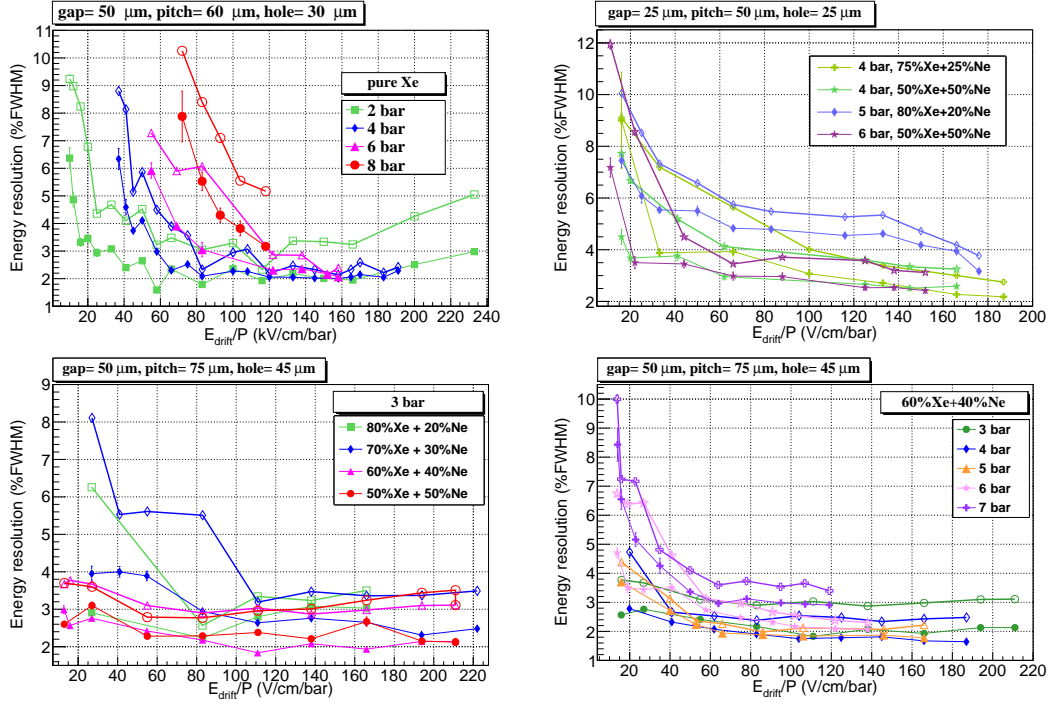


Fig. 2.13: Energy resolution dependence on E_d/P at 5.4 MeV for various pressures and Micromegas: for pure Xe (top-left); Xe+Ne mixtures with, gap= $25\ \mu\text{m}$ (top-right); in Xe+Ne mixtures with gap of $50\ \mu\text{m}$ (bottom), varying the Ne fraction at 3 bar (bottom-left) and varying the pressure in 60%Xe+40%Ne mixture (bottom-right). For each configuration, is indicated the energy resolution for all the tracks (open markers) and for parallel ones (solid markers). The geometric parameters of Micromegas are indicated on the top-left of each graph.

2.2.6 Drift Velocity

Drift velocity of pure Xe and Xe+Ne mixtures were determined from risetime distributions of α -particles. The risetime of α signals is related to the temporal projection on drift field direction. The risetime multiplied by the drift velocity provides the track length projection on drift field direction -the parallel component on the drift field direction- $l_{\alpha,\parallel} = v_d t_r$. A schematic representation of the α track is presented in Fig. 2.10, three different orientations together its projection on the drift field direction are shown. At left, a track forming an angle φ with the drift field is depicted, its projection is equal to $l_{\alpha,\parallel}^\varphi = t_r v_d$. At middle, it is represented a parallel track, the temporal projection would be $t_{r,max}$ -the maximum value of the risetime

distribution, so the track length is $l_\alpha = l_{\alpha,\parallel}^{\varphi=0} = t_{r,max}v_d$, where l_α corresponds to the track length of the α -particles. And finally at right, a track with a perpendicular orientation is depicted, in which the projection on the drift field direction is zero. Experimentally the minimum risetime ($t_{r,min}$) measured is different to zero ($t_{r,min} \neq 0$), due to diffusion of electrons and the electronic time response. Therefore the drift velocity at a given pressure P is given by

$$v_d = \frac{l_\alpha^1}{P} \frac{1}{\sqrt{t_{r,max}^2 - t_{r,min}^2}} \quad (2.3)$$

where l_α^1 is the track length at 1 bar. This value can be calculated by Geant4 simulations, a value of 2.20 cm was obtained for pure Xe [30] and it has been seen that the addition of small quantities of TMA does not introduce significant changes, as is expected. The minimum risetime $t_{r,min}$, is subtracted in quadrature to introduce the effect of diffusion and the electronic time response. To validate this method for measuring the drift velocity, the values obtained in this work for pure Xe and Xe+Ne mixtures are compared to Magboltz simulations. It must be noted that the results of Magboltz in the case of pure Xe are compatibles with previous experimental measurements, thus the comparison with Magboltz simulations gives a good check for the measurements presented in this work. A compilation of drift velocity measurements for pure Xe and Ne, as well as for Xe and neon mixtures can be found in [27]. Drift velocities in Xe+Ne mixtures have not been measured before, hence the comparison with simulations should be taken as a starting point. The drift velocity measurements are shown in Fig. 2.14, the results have been organized taking into account the classification given in Table 2.2.

Drift velocity measurements of pure Xe are shown in Fig. 2.14 (top-left). Experimental data points are systematically above Magboltz simulations values. The starting point of the saturation differs for each pressure, moving to right side as the pressure increases. This is explained by the fact that at higher pressure the oxygen content was larger because the gas was stored in the chamber for a longer time, hence the attachment is stronger. The behaviour at low drift fields indicates the high sensitivity of the Xe gas to the impurities, as is quoted in [27]. Meanwhile, the drift velocity curves are close in the saturation region at 2, 4 and 6 bar, compatible with the dependence on the reduced drift field E_d/P . The reason for which the drift velocity is higher than the simulations calculation may be that small quantities of argon could still be present in the chamber, because this gas was used before introducing the Xe to the system. As the drift velocity of the argon is higher than for Xe, at a given E_d/P value, the presence of small quantities can contribute to increase the drift velocity as it was seen in previous measurements in Xe with this setup in similar conditions [30].

Drift velocity measurements with Xe+Ne mixtures are presented in Fig. 2.14 in similar way than in previous results. Magboltz calculations are also presented for some Xe+Ne mixtures and pure Xenon. The experimental drift velocities curves

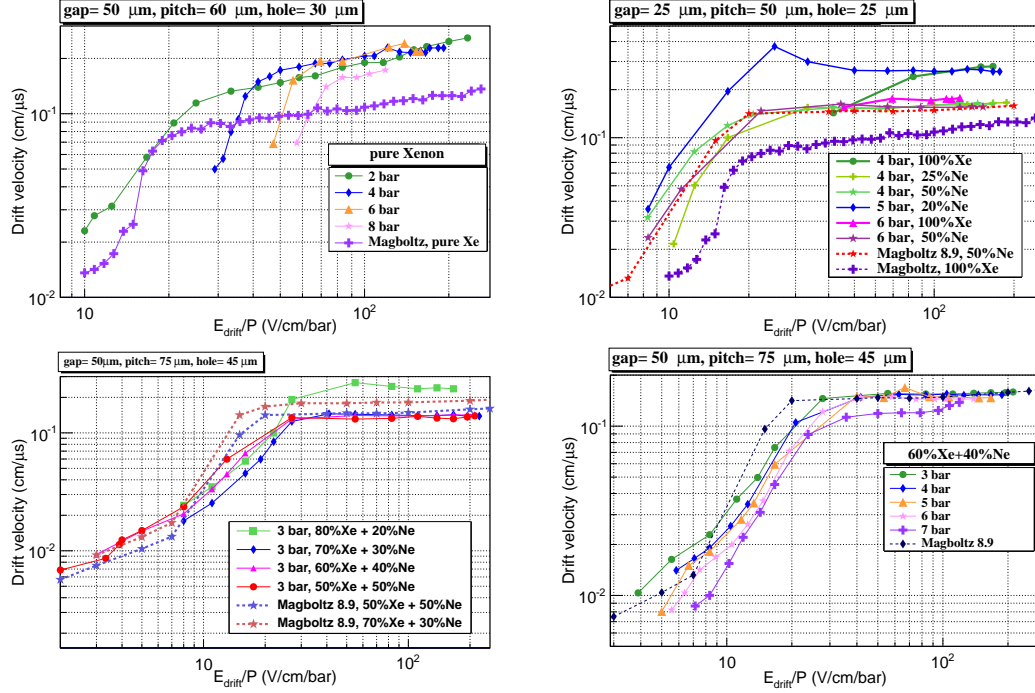


Fig. 2.14: Electron drift velocity as a function of E_d/P : for different pressures and Micromegas readouts: for pure Xe (top-left); Xe+Ne mixtures with gap $25 \mu\text{m}$ (top-right); in Xe+Ne mixtures with gap thickness of $50 \mu\text{m}$ (bottom), varying the Ne fraction at 3 bar (bottom-left) and varying the pressure in $60\%Xe+40\%Ne$ mixture (bottom-right). The geometric parameters of Micromegas are indicated on the top of each graph. Magboltz simulations for 20°C and 1 bar are also presented (dash lines).

for Xe+Ne mixtures follow the same tendency than the simulations: within the saturation region, it is seen a good agreement; while at low drift fields there are higher deviations. The variation with Ne fraction is studied in Fig. 2.14-top (right) and in Fig. 2.14-bottom (left). At 3 bar, where the variation of Ne is systematic (Fig. 2.14-bottom (left)), the measured values are systematically for the simulation. In principle, the drift velocity should increase with the addition of Ne, such it is seen for the simulations, however, results show that the drift velocity is constant within the saturation region, except for the Xe+20%Ne mixture. Similar behaviour is observed in Fig. 2.14-top (left). The high values in the Xe+20%Ne mixture at 3 bar could be explained by the presence of oxygen in this measurement. Considering the simulations presented in Fig. 1.3-left in a Xe+50%Ne mixture, the addition of $0.1\%O_2$ produces an slight increase in the drift velocity.

The behaviour of the drift velocity with pressure for Micromegas of $25 \mu\text{m}$ gap in Xe+Ne mixtures is observed in Fig. 2.14-top (right) and for a $60\%Xe+40\%Ne$ mixture in Fig. 2.14-bottom (right). The measured values at different pressures are compatibles according to dependence on E_d/P , and in good agreement with the simulation data. A systematic decrease in the drift velocity with the pressure is

seen at a given E_d/P value at low values, this is attributed to an overestimation of $t_{r,min}$ and $t_{r,max}$ because at higher pressures the risetime becomes smaller, yielding a loss in the resolution of the risetime, thus the determination could be wrong. This also explains the behaviour at 8 bar for pure Xe which is also systematically below than the curves for lower pressures (see Fig. 2.14-top (left)).

2.2.7 Gain

The multiplication of electrons can be quantitatively described by the multiplication factor (gain) as $G = N/N_e$, where N represents the total number of electrons that are readout at the anode (details in Sec. 1.1.4). Experimentally, this output signal is amplified by means of a preamplifier whose output generates a pulse-height distribution with a mean value that is proportional to the total electrons N , which in turn are proportional to N_e . The mean of the pulse-height distribution is equal to $H_p = N_e G R_{pre}$, therefore the gain can be calculated as follows:

$$G = \frac{H_p}{E/W \times R_{pre}} \quad (2.4)$$

where N_e has been replaced by E/W (see Sec. 1.1.2.2) and R_{pre} is the preamplifier conversion factor. The values of W for Xe+Ne mixtures are shown in Table 1.3, where the N_e is related to the energy of the α -particles $E = 5.41$ MeV. These values could be use for α -particles because previous works have shown that the variations of W with energy or kind of particle are negligible, thus its use is a good approximation for the gain calculations.

The preamplifier conversion factor, R_{pre} , was calculated by using a pulse generator connected into a test capacity ($Q = C_i V_{in}$), which in turn is fed to the input of a preamplifier. Both the input V_{in} and output voltage V_{out} are measured by means of an oscilloscope with an uncertainty below 5%. The value of the capacity was $C_i = 10$ pF. The calibration was performed with several input signals (V_i). The conversion factor is therefore calculated by:

$$R_{pre} = \frac{\sum_i^n \frac{V_{out,i}}{Q_i}}{n} \quad (2.5)$$

Measurements were performed with a Canberra preamplifier, whose conversion factors in the two modes are 3.2×10^{-5} and 1.6×10^{-4} mV/e⁻ with statistical errors lower than 2%. According to Eq. 2.5, R_{pre} must be in mV/e⁻ units, however, in Eq. 2.4 it has units of mV/C. Hence, Eq. 2.4 is multiplied by the electron's charge $e = 1.6 \times 10^{-19}$ C. It must be noted that the integration time of this preamplifier is short (30 μ s), however, as gain measurements were performed for $E_d/P > 50$ V/cm/bar, at these conditions ballistic effect is discarded.

Gain was studied as a function of amplification voltage (amplification field); the drift field was selected in such a way that the amplification-to-drift fields ratio

was constant for each amplification voltage configuration (gas and pressure), this guarantees similar electron transmission. In the cases where the full transmission region was not well defined (pure Xe at 6 and 8 bar), the drift field was set constant as its maximum possible value.

Measurements of the gain as a function of the amplification field are depicted in Fig. 2.15, for pure Xe (50 μm gap, top) and for pure Xe and Xe+Ne mixtures (25 μm gap, middle and 50 μm gap, bottom). Results for Micromegas of 25 μm gap include measured curves for pure Xe with the same Micromegas. The gain curves included for pure Xe in Fig. 2.15 (bottom) are the same that in Fig. 2.15 (top), some of them have been added for visual comparison, but they were not taken with the same Micromegas.

In gain curves for pure Xe with Micromegas readouts of gap thickness of 50 μm presented in Fig. 2.15-top an exponential behaviour with the amplification field is observed only for measurements at 2 bar, while at higher pressures, the exponential behaviour is lost at lower gains, more specifically above gains of 1. Previous pure Xe measurements carried out in the same setup with similar conditions have been included, after a correction of the calibration factor. In addition, measurements with Hellaz set-up are also included [30, 157].

For configurations with Micromegas of gap thickness of 25 μm (see Fig. 2.15-middle), the gain has an exponential behaviour with E_a , except at 5 bar in 80%Xe+20%Ne. At a given amplification field, the gain increases with the Ne fraction, for the three pressures studied (4, 5 and 6 bar). For instance at 4 bar, with $E_a = 120\text{ kV/cm}$, the gain goes from 4 to a value above 40, when the Ne fraction is varied between 0% and 50%. The same increase is obtained at 6 bar, for the same Ne fraction variation (extrapolating the gain curve for pure Xe at lower amplification fields).

Gain measurements for Micromegas with gap thickness of 50 μm are in Fig. 2.15-bottom. The exponential behaviour with the E_a is again not followed for most of the curves, from gains below 1, as for pure Xe and Xe+Ne mixtures with gap of 50 μm and 25 μm . The gain increases with the Ne fraction as well, approximately the same proportion as for Micromegas of 25 μm , one order of magnitude between 0% and 40%. This indicates that the effect on the gain is similar for both Micromegas geometries, which means that the improvement is due to the addition of Ne. This is clearly observed at 6 bar at $E_a = 100\text{ kV/cm}$, the gain increases from 1 (pure Xenon) to 10 (60%Xe+40%Ne). At 3 bar, the gradual increase of the gain at a given amplification field is observed, when the Ne is systematically varied between 20% and 50%.

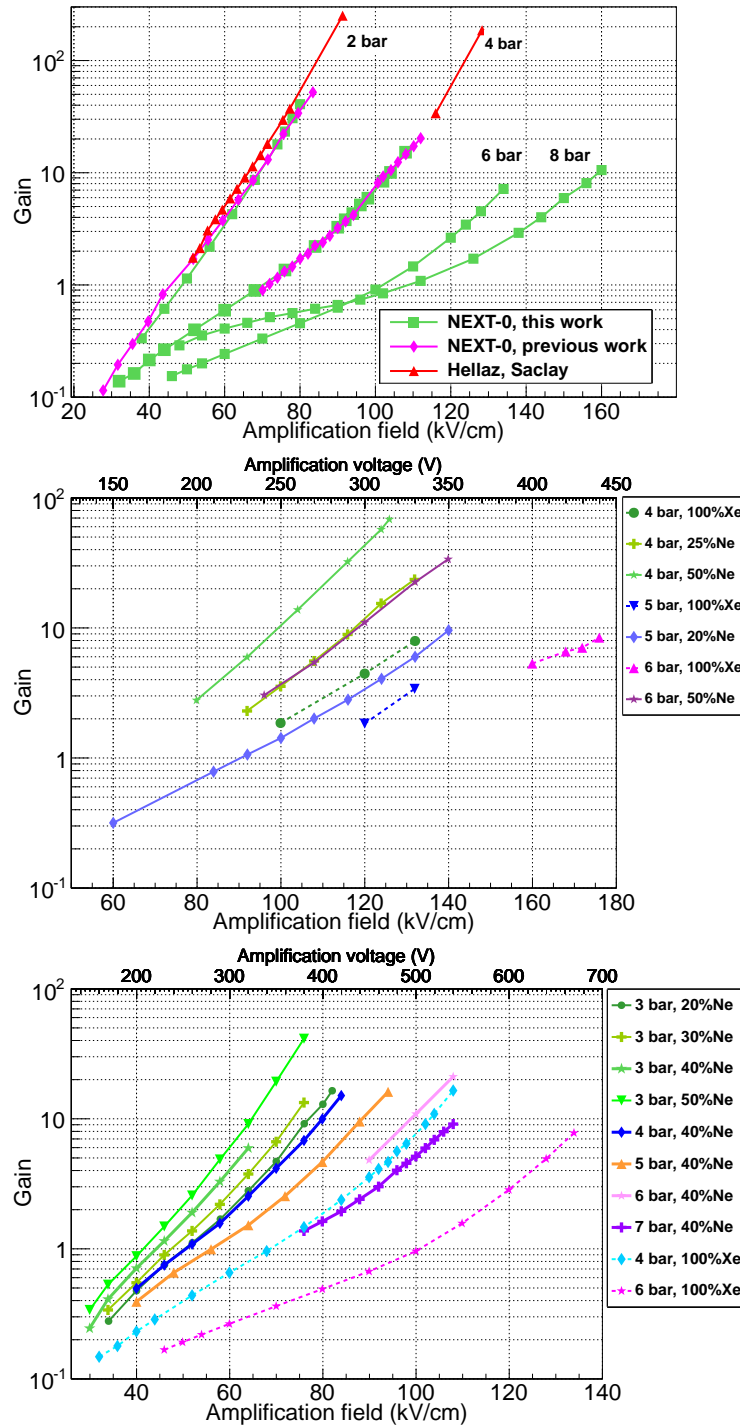


Fig. 2.15: Dependence of the gain on the amplification field at different pressures in pure Xe and Xe+Ne mixtures. Three different Micromegas readouts were used: for pure Xe with $50\ \mu\text{m}$ gap (top); for Xe+Ne mixtures with $25\ \mu\text{m}$ gap (middle) and $50\ \mu\text{m}$ gap (bottom). Details of geometric parameters of each Micromegas are shown in Table 2.2.

Considering the onset of breakdown for all the measurements, it is concluded that:

- For pure Xe measurements, with Micromegas of $50\ \mu\text{m}$ gap, it is observed a systematic decrease in the maximum gain, except at 6 bar where the value is slightly lower than at 8 bar. Between 2 and 8 bar there is a total reduction of the gain of a factor 4, going from 40 to 11.
- For measurements with a gap of $25\ \mu\text{m}$, it is seen that the addition of Ne allows to obtain larger maximum gains.
- By contrast, with a gap of $50\ \mu\text{m}$, there is no clear behaviour with the increase of Ne concentration or pressure. This could be because the Micromegas had been used, which avoids in most of the cases to know the real onset breakdown.
- When the pressure is varied, for a mixture of 60%Xe+40%Ne as shown in Fig. 2.15-bottom, the maximum gain does not show any systematic behaviour with pressure.

2.2.8 Energy resolution dependence on the amplification field

In previous chapter, it was seen that the two main contributions to the energy resolution in a gaseous detector are the fluctuations of the primary electrons and the gain fluctuations. The Fano factor quantifies the primary fluctuations and it is constant for a pure gas or gas mixture, thus varying the amplification field for a given drift field within the plateau region, it is possible to study the tendency of the energy resolution with the gain, that it is, to evaluate the gain fluctuations. This can be made because under these conditions the contributions due to the possible loss of ET, attachment or electron ion recombination are very small. The energy resolution was determined by Eq. 2.2; for Xe+Ne mixtures the fit to the pulse-height distribution was performed for the complete α -peak, and for pure Xe the fit has been realized in most of the cases for the right side of the α -peak, because the signal does not follow a Gaussian distribution. The energy resolution as a function of the gain for pure Xe and Xe+Ne mixtures is shown in Fig. 2.16. For all the configurations, the resolution decreases with the gain until the minimum value is reached, then it degrades in some cases, specially where the gain is higher than 40.

Values of the best energy resolution (%FWHM) are summarized in Table 2.3 at 5.4 MeV for raw and parallel tracks pulse-height distribution in pure Xe and Xe+Ne mixtures for pressures between 4 and 6 bar. The energy resolution of the α -peak for raw pulse-height distribution is in all the cases worse than the associated with parallel tracks. At 4 bar, it is clearly observed that the addition of Ne to Xe, improves the energy resolution, going from 3.8% (0% Ne) to 2.60% (50%Ne) for raw pulse-height distribution. While for parallel pulse-height distribution it goes from 2.97% (0% Ne) to 2.28% (50%Ne). The same trend is observed at higher pressures, the resolution improves with the addition of Ne. In principle, the energy resolution seems to remain practically constant as the pressure is increased.

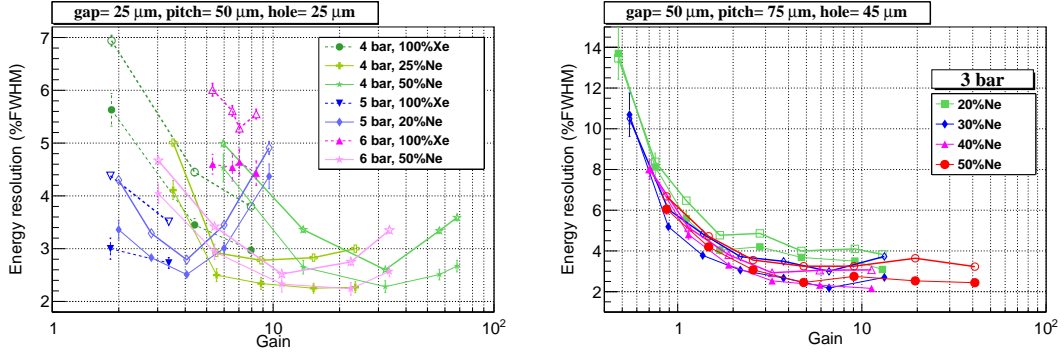


Fig. 2.16: Dependence of the energy resolution for α -particles (5.4 MeV) with the gain at different pressures in pure Xe and Xe+Ne mixtures. The energy resolution from Gaussian fit of the α -peak for the raw spectrum (open marker) and for spectrum formed with parallel tracks (solid marker) are shown for each set, for Micromegas with gap thickness of 25 μm (left) and 50 μm varying Ne fraction at 3 bar (right).

The systematic variation with the Ne concentration (20-50%) for a fix pressure can be seen in Fig. 2.16-right, between 20% and 50% at 3 bar. The best energy resolution from raw and parallel pulse-height distribution are depicted as function of the Ne concentration in Fig. 2.17-left. The major change in energy resolution is seen when the Ne concentration goes from 20% to 30%, between 30% to 50% it seems that the value remains stable.

Gas mixture	Pressure (bar)	Best En. Res. Raw (%FWHM)	Best En. Res. Parallel (%FWHM)
100%Xe	4	3.80 ± 0.06	2.97 ± 0.12
75%Xe+25%Ne	4	2.78 ± 0.04	2.34 ± 0.11
50%Xe+50%Ne	4	2.60 ± 0.04	2.28 ± 0.12
100%Xe	5	3.51 ± 0.05	2.73 ± 0.10
80%Xe+20%Ne	5	2.79 ± 0.06	2.51 ± 0.08
100%Xe	6	5.28 ± 0.09	4.43 ± 0.24
50%Xe+50%Ne	6	2.52 ± 0.05	2.33 ± 0.15

Table 2.3: Values of the best energy resolution (%FWHM) at 5.4 MeV from raw and parallel tracks pulse-height distributions in pure Xe and Xe+Ne mixtures for different pressures. The Micromegas readout used had geometric parameters of 25-50-25 μm , corresponding to gap-pitch-hole diameter, respectively.

The trend followed by the energy resolution with the pressure is observed in Fig. 2.18. The pressure was varied systematically in 60%Xe+40%Ne mixture from 3 to 7 bar and in pure Xe between 4 and 8 bar. The measurements were performed with two types of Micromegas both with gap thickness of 50 μm , but the pitch and hole diameter are different, being 75-45 μm (pitch-hole diameter) in 60%Xe+40%Ne

mixture and 60-30 μm (pitch-hole diameter) in pure Xe. The best values of energy resolution for each configuration are shown in Fig. 2.17-right for raw (open markers) and parallel (solid markers) pulse-height distributions.

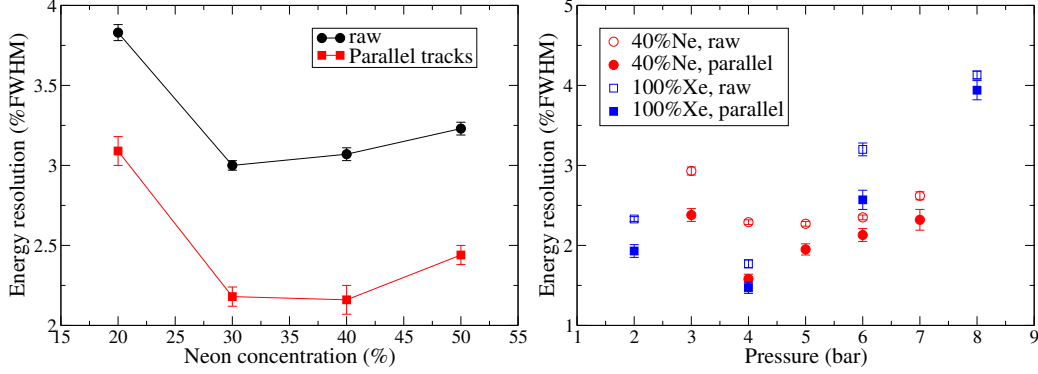


Fig. 2.17: Values of the best energy resolution (%FWHM) at 5.4 MeV for raw and parallel tracks pulse-height distributions in Xe+Ne mixtures at 3 bar (left) and in pure Xe together with 60%Xe+40%Ne mixtures varying the pressure (right). Micromegas with geometric parameters of 50-75-45 μm (gap-pitch-hole diameter) were used in Xe+Ne mixtures, with 50-60-30 (gap-pitch-hole diameter) in pure Xe.

In pure Xe the energy resolution deteriorates with pressure from 4 bar to 8 bar, going from 1.47% at 4 to 4.14% at 8 bar, for parallel tracks. While in 60%Xe+40%Ne mixture the values are almost compatibles between 3 and 6 bar, except at 4 bar where the values are a bit better and at 7 bar with a slight degradation. The degradation in pure Xe is due to the attachment caused by the high contamination in the gas. By contrast, the slight degradation in Xe+Ne mixtures is only seen from 6 bar, indicating that these measurements have not been strongly affected by the attachment, event though the measurements were done in sealed-mode.

2.2.9 Discussion

The strong loss of electron transmission at low drift fields, the dependency of the pulse-height with risetime and the dependence of the start of the saturation point in drift velocity curves with the pressure, confirm the strong effect of the attachment in pure Xe measurements.

By contrast, in Xe+Ne mixtures, good values of ET values are reached from 40 V/cm/bar for all the configurations studied. Drift velocities are in good agreement with Magboltz simulations, and there is no dependency of the pulse-height with risetime for most of the configurations, showing that the attachment has not a predominant effect in these measurements. The fact that drift velocity increases rapidly with the drift field in Xe+Ne mixtures, it could reduce the probability of attachment.

It must be noted that the columnar recombination could play an important role in the loss of transmission at low drift fields, however, for these measurements, this

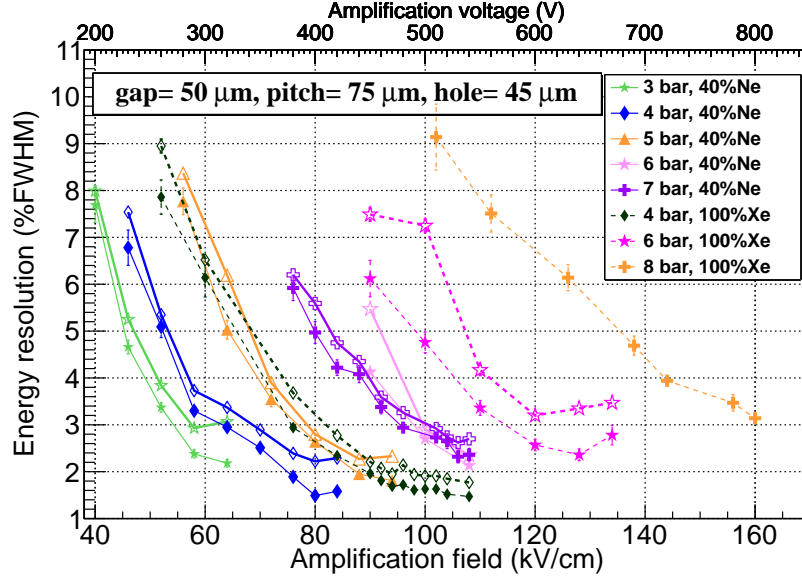


Fig. 2.18: Dependence of the energy resolution for alpha particles (5.4 MeV) on the amplification field at different pressures in pure Xe and Xe+Ne mixtures. The energy resolution from Gaussian fit of the α -peak for the raw spectrum (open marker) and for spectrum formed with parallel tracks (solid marker) are shown for each set, for Micromegas with geometric parameters of 50-75-45 μm (gap-pitch-hole diameter) in 60%Xe+40%Ne, and with 50-60-30 μm (gap-pitch-hole diameter) in pure Xe.

effect could not be seen for two reasons: the attachment masks the columnar effect and the collimation of the α -particles suppresses the tracks with larger tracks angles (respect to the drift field), tracks that should have stronger columnar recombination.

There is a clear improvement on the energy resolution when the Ne fraction increases from 20% to 30%, then the value remains practically constant. This result is compatible with the behaviour of the Fano factor and the intrinsic energy resolutions with the Ne concentration observed in Fig. 1.9 [23].

It is clear that the addition of Ne, improves the performance of a Micromegas-TPC detector, especially for pressures above 5 bar. This is clearly seen in the onset breakdown which is significantly higher for Xe+Ne mixtures than for pure Xe. Although for measurements carried out with Micromegas of gap 50 μm , it is not possible a direct comparison between pure Xe and Xe+Ne because the readout used for each set of measurements was different. However, the fact that the best value of energy resolution as function of pressure presents very low changes indicates the advantage of working with Xe+Ne mixtures.

2.3 Energy Resolution for γ -rays in pure Xe

2.3.1 Experimental setup and procedure

The experimental setup used for measuring γ -rays is the same than the used for α -particles (see Fig. 2.1). However, for these measurements, the recovery system had already been installed as for Xe+Ne mixtures, facilitating the operation and limiting the outgassing by reducing the content of oxygen in the gas since the gas could be reclaimed at the end of each acquisition. The measurements were also performed in sealed mode because the circulation pump was not available yet. Two types of Micromegas readouts were used, the geometrical characteristics of them and the different conditions of acquisition are described in Table 2.4. Two different ^{241}Am sources were used, one for measurements with Micromegas MM01 while for Micromegas MM02 it was replaced by another with a higher activity. In both cases the sources were flipped upside down, thus the α -particles are blocked by means of its own encapsulation.

Item	Micromegas description gap-pitch-hole (μm)	Pressures (bar)	Activity ^{241}Am (kBq)
MM01	50-60-30	2.0 and 3.5	0.5
MM02	50-70-35	3.0 and 5.0	11.4

Table 2.4: Description of the measurements performed in pure Xe with γ -rays from an ^{241}Am source. The Micromegas label and the corresponding geometric parameters together with the pressure of acquisition are indicated for each configuration.

The signal induced on the anode is fed to a Canberra electronic chain (preamplifier+amplifier: models 2005 and 2002, respectively), the amplifier with shaping time of $4\ \mu\text{s}$). The amplified pulse is digitized by means of a multi channel analyzer (MCA), thus the pulse height signals are converted into a number of ADC counts, which are saved on an histogram that can be analyzed afterwards.

Systematic measurements were not made as in the α -measurements, because the detector had damages caused by sparks occurred in previous tests. For γ -measurements at high pressure, it is necessary to apply higher amplification fields than in α -measurements, as it was needed to work at higher gains; for this reason, when Micromegas with previous damages were used the probability that sparks occur producing irreversible damages on them increases. Hence, it was only possible to take measurements up to 5 bar.

2.3.2 Spectrum from γ -rays of an ^{241}Am source in pure Xe

The ^{241}Am source emits γ -rays at 59.54 (intensity=35.90%) and 26.34 keV (intensity=2.40%) that interact inside the detector most of the times by photo-electric effect, being the Compton scattering less likely to occur and pair production im-

possible at these energies. In addition, X-rays at energies below than 22 keV are emitted by this source, however, they were not taken in consideration in this analysis. Because the gains (at which the measurements were taken) were not sufficient to observe these energies.

Type	Energy (keV)	EP ($E_\gamma - E_{X-r}$) (keV)	I (%)
Xe L_α	4.10	55.44	3.6
Xe L_β	4.49	55.05	2.16
Xe K_{α_1}	29.78	29.76	47.40
Xe K_{α_2}	29.46	30.08	25.60
Xe $K_{\beta_{1,3}}$	33.60	25.94	8.4-4.35
Xe $K_{\beta_{2-4}}$	34.43	25.11	2.54-0.49

Table 2.5: Xenon escape peaks (EPs) for 59.54 keV γ -rays ($E_\gamma - E_X$).

To have a better understanding of the energy spectrum formed with γ -rays from an ^{241}Am source, it was developed a GEANT4 [158] application based on the RESTsoft code, to simulate the interaction of radiation in TPC's detectors by A. Tomás [159]. Specifically, the geometry of NEXT-0 TPC was implemented in the RESTsoft application (see Fig. 2.19-left), and the detection efficiency for energy range between 10 and 100 keV was determined (see Fig. 2.19-right). For this, γ -rays placed on the top of the conversion volume are simulated to interact in the gas, and the detection efficiency at each energy is calculated from the simulated energy spectrum. In Fig. 2.19-right, it was also determined the photo-peak efficiency, which refers to the possibility that an event deposits completely the energy contributing thus to the photo-peak. As seen, both the detection and the photo-peak efficiency take similar values at low energies until the K-edge. Thereafter, the photo peak efficiency is considerably lower than the total one, since a secondary photon carries part of the total energy contributing to the EPs.

The detection efficiencies for both γ -emissions are very similar (see Fig. 2.19-right), however, the intensity for the low energy γ -emissions (26 keV) is almost 15 times lower (see Table 2.5), thus its contribution to the final energy spectrum is negligible. Hence, γ -rays at 59.54 keV were simulated, to properly analyze the final energy spectrum. The results of this simulation are depicted in Fig. 2.20, and in addition in Table 2.5 is specified the origin of each escape line.

2.3.3 Analysis and results

Typical energy spectra in pure Xe at different pressures and with two types of Micromegas are shown in Fig. 2.21. The specific information about the Micromegas readout used, pressure as well as the E_d/P and amplification voltage (V_a) for the acquisition are shown on the top of each spectrum. In all the spectra a very well

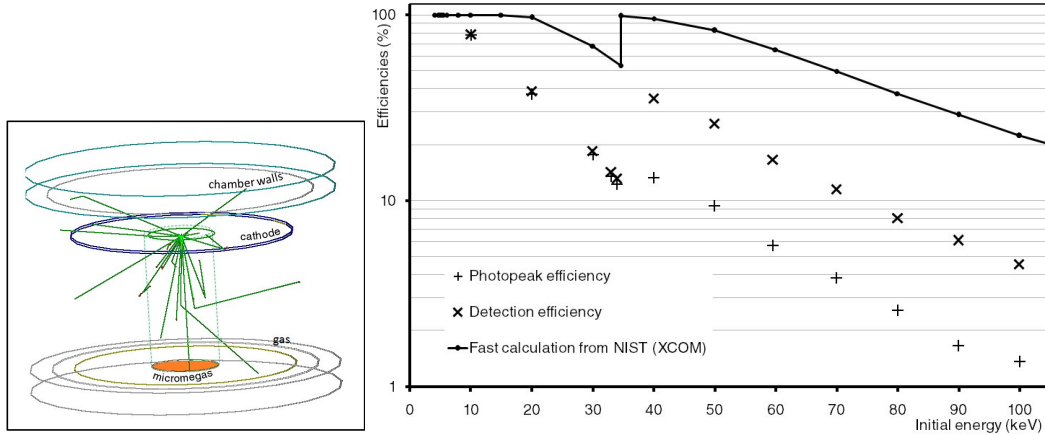


Fig. 2.19: Left: Geometry simulated in the RESTsoft GEANT4 application to model the NEXT-0 TPC. Right: Detection efficiency curve for γ -rays in NEXT-0-MM TPC. Both figures taken from A. Tomás PhD Thesis [159].

defined a peak is observed at the right the side of each spectrum, which corresponds to the γ -emission at 59.54 keV; while at lower energies the EPs associated with the K_{α} and K_{β} fluorescence Xe for 59.54 keV γ -emission are observed. In particular, the Xe $K_{\alpha,\beta}$ EPs can be distinguished for the energy spectrum at 2 bar (see Fig. 2.21-top,left). However at higher pressures a broader peak is seen. The energy resolution was calculated at 59.54 keV by fitting the peak to a Gaussian function over a linear background. On the other hand, the range of energy between 17 and 39 keV was fit using a routine in ROOT [160]. In a first step, a simple Gaussian fit is performed in the range. In the second step, the fit function consists of two Gaussian functions over a linear background, one of the function corresponds to the K_{α} Xe EP whose parameters are set from parameters determined in previous step. The relative height of the Gaussian function associated to the K_{β} Xe EP, the small peak, is set from simulation information. Results obtained in all the fits are shown in Fig. 2.21

The energy resolution as a function of the reduced drift field is shown in Fig. 2.22 for the four different configurations acquired. The energy resolution dependency with E_d/P is only observed for two configurations, while for the others only one voltage configuration was acquired. At 2 bar with Micromegas MM01, the values of energy resolution are compatible from 160 V/cm/bar. However at 3 bar, the energy resolution decreases more rapidly with E_d/P than for the other configurations.

2.3.4 Discussion

The best values of the energy resolution at 59.54 and 29.87 keV are shown in Table 2.6 together with the extrapolation of the energy resolution at $Q_{\beta\beta}$. In principle, the Micromegas readout MM02 presents better energy resolution than MM01, considering that the value measured at 3 bar (7.3%) is much better than at 3.5 bar

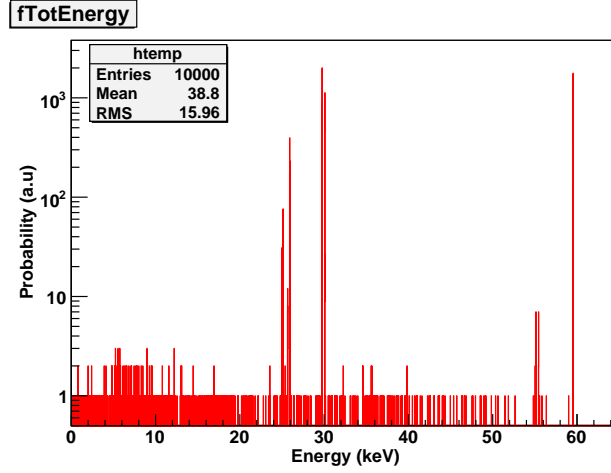


Fig. 2.20: Energy spectrum lines expected for the 59.54 keV γ -emission of an ^{241}Am radioactive source in pure Xe following GEANT4 simulation.

(9.5%) and even at 2 bar (7.6%). For this Micromegas both the pitch and the hole diameter are larger than for MM01, indicating that this geometrical parameters may decrease gains fluctuations.

Pressure (bar)	MM	Best. En. Res.	Best. En. Res.	En. Res. at $Q_{\beta\beta}$
		at 59.54 keV (%FWHM)	at 29.87 keV (%FWHM)	(2480 keV) (%FWHM)
2.0	MM01	7.6 ± 0.47	10.95 ± 0.30	2.36 ± 0.04
3.5	MM01	9.5 ± 0.25	12.94 ± 0.22	2.95 ± 0.03
3.0	MM02	7.3 ± 0.27	14.30 ± 0.30	2.27 ± 0.05
5.0	MM02	12.1 ± 0.55	19.63 ± 0.58	3.76 ± 0.09

Table 2.6: Best values of energy resolution at 59.54 keV γ -emission and at the corresponding 29.87 keV Xe K_{α} EP from an ^{241}Am source obtained in pure Xe, together with the value of the energy resolution extrapolated to the $Q_{\beta\beta}$ -value (2480 keV), taking into account that energy resolution has a dependency with $1/\sqrt{E}$.

With both Micromegas a degradation of the energy resolution with the pressure is observed. This effect can be produced by attachment or recombination. However, previous measurements in pure Xe with Micromegas in recirculation mode and with a lower drift distance (about 1 cm) also show a deterioration of the energy resolution with pressure [38], even though, the values acquired are a bit higher than the ones presented in this work. For instance at 5 bar, the energy resolution measured at 22.1 keV X-rays extrapolates to 4.73% at $Q_{\beta\beta}$ value [38], while in these measurements at the same pressure to 3.76%. This is a better result, although the measurements in this work were carried out in not-recirculation mode and with drift

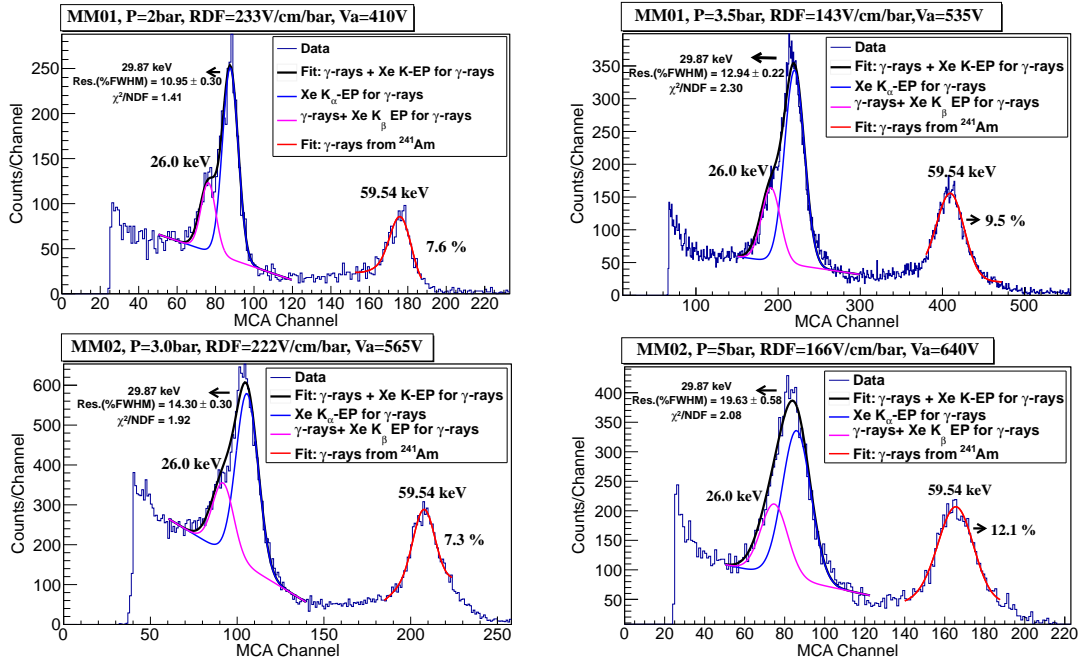


Fig. 2.21: γ -energy spectra from an ^{241}Am source acquired at 2, 3, 3.5 and 5 bar in pure Xe, for Micromegas MM01 50-60-30 μm (top) and MM02 50-70-35 μm (bottom), (gap-pitch-hole diameter). Results of the fits performed to evaluate the energy resolution are presented too.

distance six times larger. This indicates that the degradation observed is probably not only linked to attachment, but also the recombination.

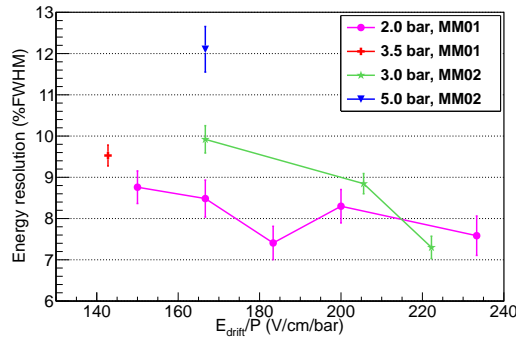


Fig. 2.22: Energy resolutions at 59.54 keV γ -emission from an ^{241}Am source as a function of the reduced drift field at 2, 3 and 5 bar in pure Xe.

2.4 Conclusions

The good performance of a Micromegas-TPC at high pressure in pure Xe and Xe+Ne mixtures was demonstrated through measurements with α -particles. Good operational conditions were reached in terms of gain and energy resolution, even though the experimental conditions were not the best, because the measurements were realized in sealed mode (without gas purification).

The method of selecting parallel tracks by the application of a cut on risetime distributions, allowed to obtain a better estimation of the energy resolution and gain. For pure Xe, the best value of energy resolution, extrapolated to the $Q_{\beta\beta}$ value was 2.2% at 2 bar. Meanwhile, maximum gains above 40 at 2 bar and 10 at 8 bar were measured.

The characterization of α -particles in Xe+Ne mixtures allowed to observe the good performance of this mixture for working at high pressures, reaching larger maximum gains and better energy resolutions. In addition, good agreement of the drift velocity measurements with Magboltz simulations was observed. The addition of Ne improves the gain, for instance, in a Xe+50%neon the gain increases one order of magnitude respect to pure Xe for Micromegas with gap thickness of 25 μm and 50 μm .

The behavior of the energy resolution in Xe+neon mixtures shows that from 20% to 30% of Ne fraction the energy resolution improves, remaining practically constant between 30% and 50%. Although at low pressures, there is not a strong improvement in energy resolution in comparison to pure Xe; at higher pressures a noticeable improvement is seen, which may indicate that the addition of neon probably decreases the gain fluctuations. This could be associated to the fact that the columnar recombination for this mixture may be much lower. The good performance of Xe+Ne mixtures at higher pressures in terms of gain and energy resolution opens the possibility to use this mixture in applications where high gains and good energy resolutions are needed. In addition, this admixture allows a reduction of

costs.

For γ -rays in pure Xe very good results in energy resolution were achieved at high pressures: at 3 bar the best value at 59.54 keV was 7.3%, with a steady degradation with pressure, being 12.1% at 5 bar; these values extrapolate to 2.27% and 3.76% at $Q_{\beta\beta}$ value. These are very promising results considering that there is still a wide range of improvement.

Part II

PART II: Xe-trimethylamine mixtures for $0\nu\beta\beta$ and directional dark matter searches

Mass Spectrometry system for Gas Analysis in HP Xe-based TPCs

Contents

3.1	Mass Spectrometry	74
3.1.1	Physical Principles	74
3.1.2	Omnistar TM Pfeiffer Quadrupole Mass Spectrometer	75
3.1.3	Data acquisition	77
3.2	System conditioning and optimization	79
3.2.1	Filament Outgassing	80
3.2.2	Measurements with Argon gas	81
3.2.3	Helium leak test	83
3.3	Calibration of Mass Spectrometer for Xe+TMA mixtures	85
3.3.1	Pure Xe and Xe+TMA mass spectra	85
3.3.2	Calibration Factor	88
3.3.3	Experimental Procedure	88
3.3.4	Results and Discussion	90
3.4	Conclusions	92

For the study of HP Xe-based TPCs for Rare Event Searches is essential to control the level of electronegative impurities and other impurities in the gas, because these impurities can produce loss of charge by attachment or introduce changes in the electronic properties. In addition, a quantitative analysis of the gas filling allows to know the concentration of each gas component, which is essential to find the optimum concentration of operation according to the applications.

Mass spectrometry has several attractive features as an analysis technique, because electronegative and non-electronegative impurities species can be detected, specially the O₂ and other problematic noble gases that contain radioactive isotopes [161]. Furthermore, by mass spectrometry the quantification of the gas composition of different mixture can be done.

In this way, a Quadrupole Mass Spectrometer (QMS) was added to the gas system. In this chapter the commissioning and the experimental procedure to find

the optimum conditions of measurement are described. In addition, the calibration procedure carried out for Xe+TMA mixtures is drawn (see Sec. 3.3). Finally, in Sec. 3.4 the conclusions are presented.

3.1 Mass Spectrometry

3.1.1 Physical Principles

A mass spectrometer system can be seen as an ionization vacuum-meter, that previously to the ions detection, has an additional facility to separate the various types of generated ions during the ionization process according to its mass-to-charge ratio (m/q). A simplified design showing the three main process involved is depicted in Fig. 3.1, where the ionization, the mass analyzer and the detection system are illustrated.

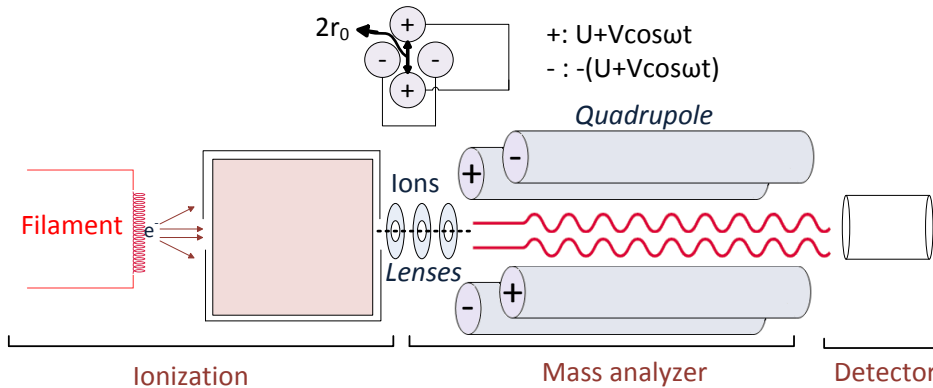


Fig. 3.1: Schematic representation of a quadrupole mass spectrometer made up of the ionization, mass analyzer and detection systems. Usually the rods of conventional systems are hyperbolic. A modification from [162].

In the *ionization*, the atoms or molecules in gaseous phase are bombarded by low energy electrons emitted by a heated filament, as a result ions are created. Depending on the electron energy and the size of the atom or molecule different processes of ionization or even molecular fragmentations could be held; hence single ionization, double ionization or a molecule and a new radical are created. The filament is connected to a potential; at low potentials the energy of the ejected electrons is lower than the molecule or atom ionization, in contrast at very high potentials the electrons wavelength becomes very small (as $\lambda = h/mv$), hence molecules or atoms become transparent to them. Typically the range of electron energy used is between 70 and 100 eV, since in this range it has been observed the maximum production of ions [163, 164].

The separation of ions is performed by means of the mass analyzer system. Different types of analyzers have been developed, which are based on different prin-

principles; in general they use static or dynamic electric and magnetic fields (described in detail in [163]). As the OmnistarTM QMS utilized a quadrupole mass filter, only this type of mass analyzer is described. The quadrupole mass analyzer was proposed by W. Paul [165], this consists of four rods with circular or hyperbolic sections placed parallel among themselves. Each opposing rod pair is electrically connected with each other, and a high-frequency alternating voltage ($V \cos \omega t$) together with superposed direct voltage (U) are applied between one pair of rods and the inverse between the other pair. In this way, for a given voltage configuration only ions with a certain m/q ratio will reach into the detector, while the other will collide with the rods; for a continue scanning of m/q the voltages are continuously changed [163]. In this stage is essential to work under high vacuum conditions, because this avoids that ions can collide with other gaseous molecules.

After the ions separation according to their m/e ratio in the mass analyzer, the ions are transformed into an electric signal by a detector. Detector generates an electric current proportional to the abundance of the incident ions. In mass spectrometry systems different detectors are used, reviewed recently in [163, 164, 166]. Here only the Faraday and Secondary Electron Multiplier (SEM) detectors are briefly described, as they are the used by the Omnistar^{TMA} QMS. The Faraday detector is the simplest system that consists of a flat electrode which collects the ions. The cup detector is enclosed -except for a small entrance aperture- to ensure that secondary electrons leading to erroneous readings could escape. The main drawback of this detector is the low sensitivity, minimum currents of about 10^{-14} A can be detected [166]; in contrast with this detector low systematics errors can be obtained being ideal for quantitative analysis [164]. On the other hand, SEM detector overcomes the limitations of the Faraday one, by adding an additional amplifying element [164]. The ions from the mass filter are accelerated by a strong electric field striking an electrode -called the conversion dynode which is connected to a HV- producing secondary particles as electrons, neutral or positive and negative ions. Secondary electrons are accelerated towards a second dynode generating further secondary electrons; this process is repeated until a large number of electrons are yielded striking finally the Faraday plate [163, 166].

3.1.2 OmnistarTM Pfeiffer Quadrupole Mass Spectrometer

An OmnistarTM Pfeiffer Quadrupole Mass Spectrometer was connected into the gas system for qualitative and quantitative gas analysis; the point of connection is observed in Fig. 3.2-top and a picture of the mass spectrometer in Fig. 3.2-bottom. The system consists of a gas sampling inlet system (capillary), a PrismaPlus mass spectrometer, a diaphragm vacuum pump and turbo pump. A valve and a flow regulator and a pressure gauge allows to control the gas inlet and the flow gas. During a measurement the inlet valve is opened through the user interface, thus the gas flows trough the capillary entering into the heated gas inlet chamber and then to the mass spectrometer (in ultra-high vacuum) system for gas analysis.

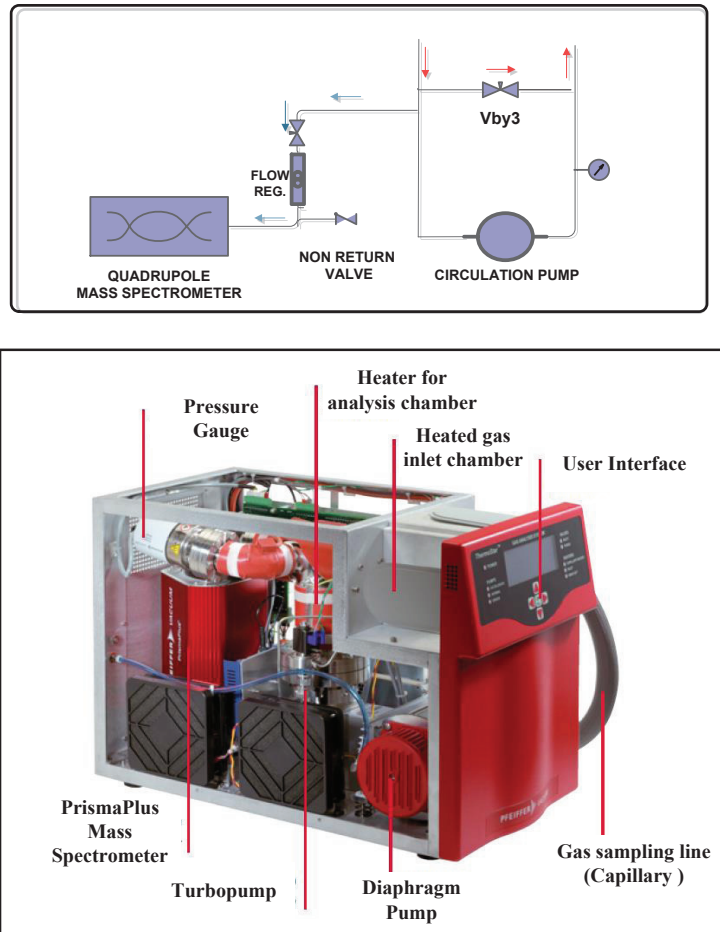


Fig. 3.2: Top: Representation of the location of the OmnistarTM Quadrupole mass spectrometer (QMS) connected into the gas system for gas analysis (zoomed view from gas system in Fig. 2.1). Bottom: Picture of the instrument with the main parts of the system: gas sampling line (capillary), the diaphragm pump the turbo pump, and the prismaPlus mass spectrometer (Quadrupole).

3.1.3 Data acquisition

The OmnistarTM QMS is controlled via a computer by Ethernet using the Quadrupole software (given by Pfeiffer). Quadrupole is a Windows application based on the Microsoft .NET Framework 2.0, which provides several ways of displaying and recording the data. This system allows to store and recall sets of tuning parameters as well as to tune the instrument automatically. It is possible to acquire an scanned mass spectrum where the peak shape can be examined and optimized; a bar chart in which the signal is recorded at each minimal mass is generated. The software also allows the measurements of selected masses.

For most of the gas analysis performed in this thesis, it was selected the analog scan mode, because it provides a complete information of the analyzed gas and it can be studied offline. On an analog scan, the x axis of mass spectrum corresponds to m/q , where q is given in multiples of the elementary charge of one electron in absolute value ($1 e = 1.602177 \times 10^{-19} \text{ C}$), and the mass is indicated in atomic mass units (amu), being $1 \text{ u} = 1.660540 \times 10^{-27} \text{ kg}$. Fig. 3.3 shows a typical mass spectrum acquired for nitrogen gas. The nitrogen was introduced from the external bottle into the gas system. The main peaks on the spectrum correspond to the nitrogen gas (N_2) contributions: the single and the double ionization at 28 and 14 amu respectively are seen. For this acquisition the external gas line system was not pumped enough, thus high content of air was expected, as is seen in the spectrum. The components of air together with its proportion in percent by volume are indicated in Table 3.1. In addition the peaks expected peaks for each component with the relative ion current are shown in Table 3.2. First and second contributions correspond to single and double ionization while the third one is due to new radicals.

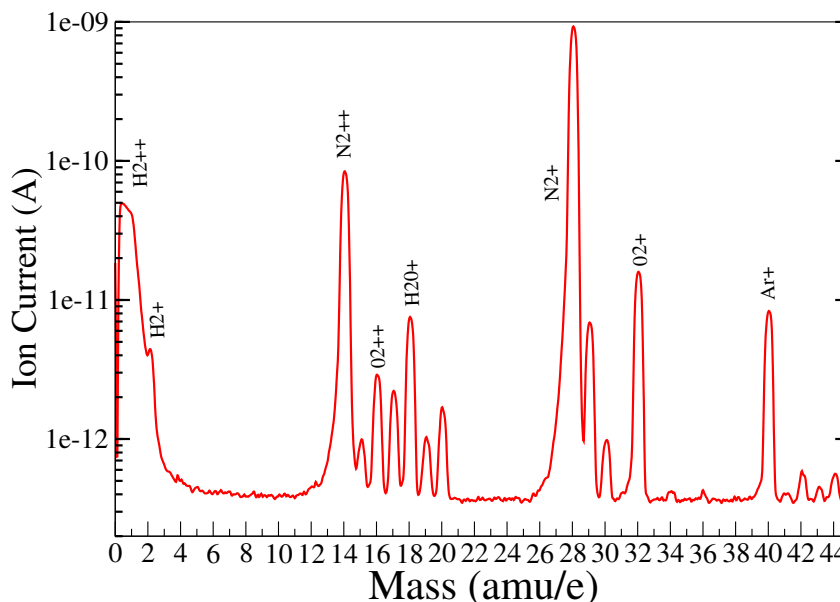


Fig. 3.3: Mass spectrum acquired for nitrogen gas (N_2) with an OmnistarTM Quadrupole Mass Spectrometer.

Percent by volume	
N ₂	78.1
O ₂	20.9
Ar	0.93
CO ₂	0.03
Ne	1.8×10^{-3}
He	5.2×10^{-4}
Kr	1.1×10^{-4}
Xe	8.7×10^{-6}

Table 3.1: Components of air together with the percent by volume [164].

Element or molecule	Peaks a.m.u/e		
	1st 100%	2nd-rel. i.c	3rd-rel. i.c
H ₂	2	1 - 3%	
He	3		
CH ₄	16	15 - 85%	14 - 16%
H ₂ O	18	17 - 26%	16 - 1.8%
Ne	20	22 - 10.2%	
N ₂	28	14 - 14%	29 - 0.7%
O ₂	32	16 - 18%	34 - 0.4%
Ar	40	20 - 18%	36 - 0.34%

Table 3.2: Element and molecular gas components in air with the expected peaks in mass spectrum. The main contribution is considered as 100%, and for the second and third contributions the relative value of ion current in percentage relative to the main is indicated [164].

Mass spectrometer must be calibrated for each gas to perform a quantitative analysis, this establishes the sensitivity for a determined gas. From this information, the concentration of each component can be calculated [164]. This is because for each component the probability of ionization is different, usually the mono atomic gases and the noble gases have low probability of ionization, while for molecular gases the probability of ionization is higher. Table 3.3 shows the relative probabilities of ionization of some gases of relevance for this work. The probabilities are given in terms of the molecular nitrogen, being assigned for it a value of 1.

Element or molecule	Rel. Prob	Element or molecule	Rel. Prob
He	0.15	CO	1.05
Ne	0.30	Ar	1.2
H ₂	0.44	NH ₃	1.3
N ₂	1.0	Xe	2.4
O ₂	1.0	CH ₄	1.6
H ₂ O	1.0	C ₄ H ₁₀	4.9

Table 3.3: Relative probabilities of ionization referred to molecular nitrogen (N₂) for an electron energy of 100 eV, values extracted from [164].

3.2 System conditioning and optimization

The first objective was to achieve the best measurement conditions and establish a procedure of operation for the QMS. As it is known the main limiting factor for reaching high sensitivity for oxygen qualitative or quantitative analysis, is the residual gas of the own mass spectrometer, caused by outgassing of the material of the instrument [163, 164, 166]. For this reason, a long measurement of 19 days was carried out to study the vacuum pressure and the partial pressure of the residual gases with the inlet valve of the mass spectrometer closed. Results are shown in Fig. 3.4, where the vacuum pressure is presented together with the ion current at 18 amu that corresponds to the main peak of water vapor.

Within this range of time, successive bake-out processes of different duration were performed, time is indicated on the plot at the starting time. During this time two power cuts occurred causing unexpected shut down of the instrument. The following procedure was carried out just after switch on the QMS:

1. Pump down is started.
2. When the vacuum pressure is below 10^{-6} mbar a bake-out is programmed, in particular for this study bake-out processes between 1 and 4 hours were programmed.
3. After the bake-out finished, the filament is switched on and the periodical acquisition mass spectrum is started using the SEM detector; the mass scanned was 1-40 amu.

It must be pointed out that during the bake-out the filament must be off, to avoid damages. As the vacuum pressure indicates the total pressure produced by the atoms or molecules inside the chamber, the sum of the ions currents of each component is proportional to the partial pressure of each specie. In this study for simplicity it is shown specifically for the 18 amu peak, however for the other residual

gases was observed similar behaviour. From the temporal evolution of the vacuum pressure and the ion current at 18 amu, the following observations can be done:

- Vacuum pressure shows a modulation with time, taking maximum value at night and minimum at mid day. The residual gases have the same modulation with time, as seen at 18 amu (water vapor) from 360 h. This behaviour can be related with the change of temperature during the day.
- After pump starts the pressure decrease exponentially, reaching values below 10^{-6} mbar after 5 minutes.
- The vacuum pressure increases rapidly during a short time period (lower than 1 h) at the beginning of the bake-out produces, thereafter the pressure starts to decrease. The increase in pressure is due to the outgassing emitted by the wall materials of the chamber.
- When the filament is switch on, the ion current and the vacuum pressure increase due to outgassing of the filament; detailed analysis of the effect on vacuum pressure of this outgassing is given in next section.

3.2.1 Filament Outgassing

The outgassing of the filament has been reported in several works [165, 167]; the aim of this measurement was to establish the time required to reach vacuum pressure values similar to those before the filament has been turn on. Fig. 3.5 shows the temporal evolution of the pressure during five days. In this range of time a power cut occurred (at the third night at 81 h), hence the mass spectrometer remained off for about 8 h. Thereafter the mass spectrometer was switched on and the pump started until vacuum pressure value was below 10^{-6} mbar (time required was less than 10 minutes), when the vacuum pressure was below of 10^{-6} mbar a bake-out of 3 h was programed. After the bake-out finished, the pressure decreases exponentially reaching values of 2×10^{-8} mbar after 18 h. At this pressure the filament and the SEM detector were switched on; this produces an increase in the pressure of the mass spectrometer due to the outgassing from filament, the pressure changes from 2×10^{-8} to 5×10^{-8} mbar. The necessary time to return to similar values of vacuum pressure is around 18 h.

On the other hand, the ion current of the main components of residual background components together with vacuum pressure are seen in Fig. 3.6 for another acquisition. The temporal evolution of ion current of H_2 (2 amu) Ar (40 amu), CO_2 (44 amu) and water vapor (18 amu) after the filament is switched on is observed. The ion currents of the components are above in more than one order of magnitude respect to the stable values, indicating that the partial pressure of these elements increases when the filament is turned on. The time required for a total stabilization is around 30 h.

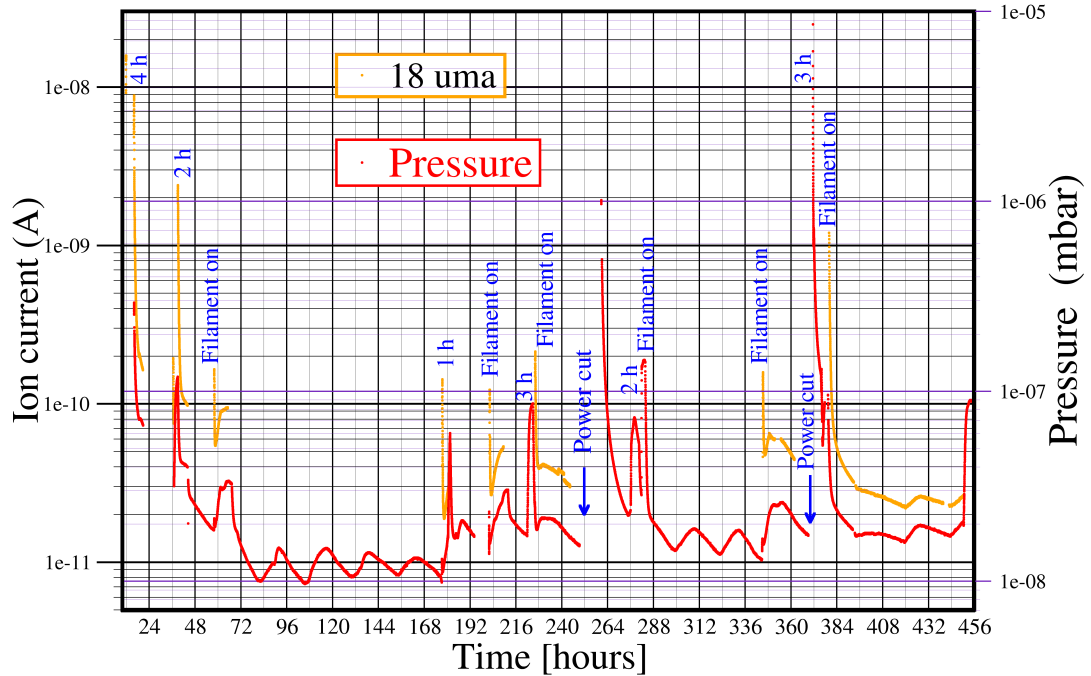


Fig. 3.4: Temporal evolution of the pressure and ion current of water vapor (from 18 amu peak). The effect produced by the filament outgassing and bake-out are observed.

After these previous studies optimum conditions of measurement were established. It was seen that the minimum vacuum pressure that can be achieved is between 1×10^{-8} and 2×10^{-8} mbar; this value is achieved more rapidly after a bake-out larger than 3 h. From initiation of the vacuum system, and after the bake-out and switching on the filament, around 30 h are required to reach the ultimate pressure and stability.

3.2.2 Measurements with Argon gas

In all the previous measurements the inlet valve was closed, because the main interest was focused on the study of the residual background gases. Argon gas was introduced into the system and SEM detector switched on for the measurement. For this measurement, it was not acquired an analog spectrum, selected masses were measured instead. Ion current at 40 (Ar), 18 (water vapor), 28 (N_2), 16 (O_2) and 44 (CO_2) amu are measured as a function of time in Fig. 3.7. The first measurements with the inlet valve open but no Ar flux, show the residual gas from the capillary and the gas system (in vacuum). In this condition, the

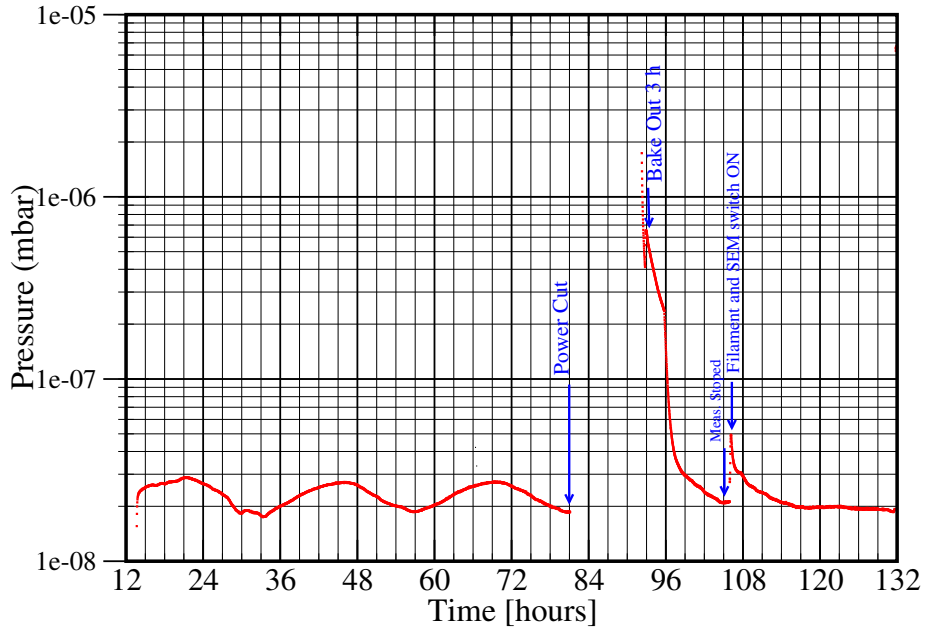


Fig. 3.5: Temporal evolution of the pressure during five days. In this range of time a power cut occurred in the third night (81 h), whereupon a bake-out of 3 h was programmed.

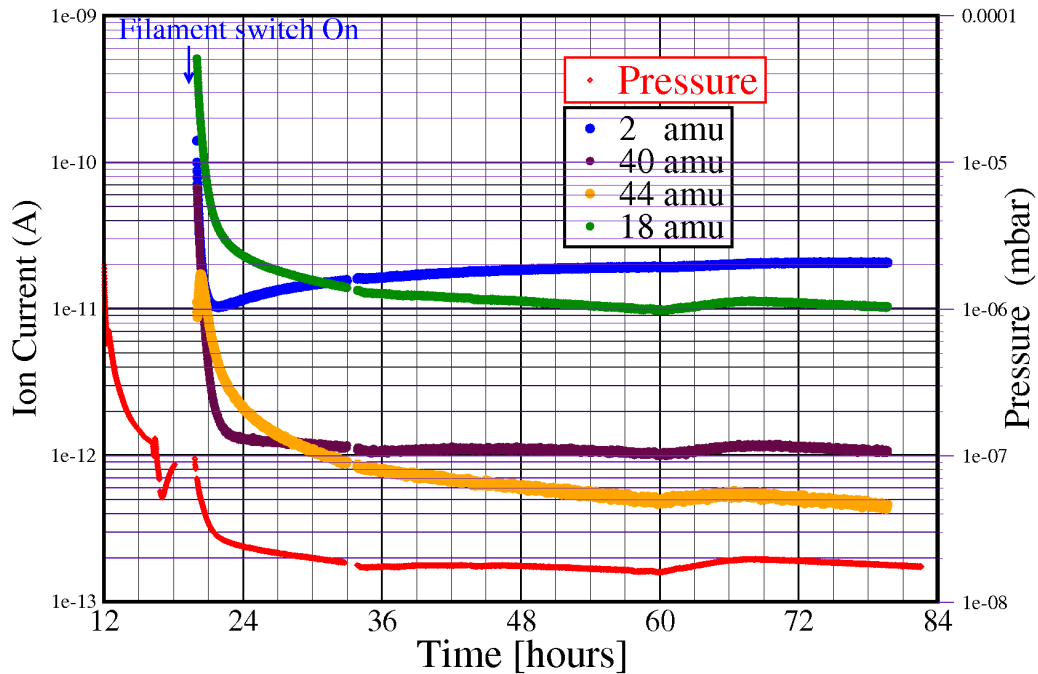


Fig. 3.6: Temporal evolution of the pressure and ion current of molecular H (2 amu) Ar (40 amu), CO₂ (44 amu) and water vapor (18 amu) after the filament has been switched on.

higher contribution was from nitrogen (28 amu). After setting an Ar flux of 0.41/h, the background component decreases immediately even below the values before including Ar gas. The stabilization of the Ar ion current is reached immediately, while for residual gases takes a few minutes. After 30 minutes of acquisition the inlet valve was closed, the ion currents dropped even below the initial values. This is interesting because indicates that the background level can be improved rapidly purging the QMS with the gas of study, instead of pumping for a long time period.

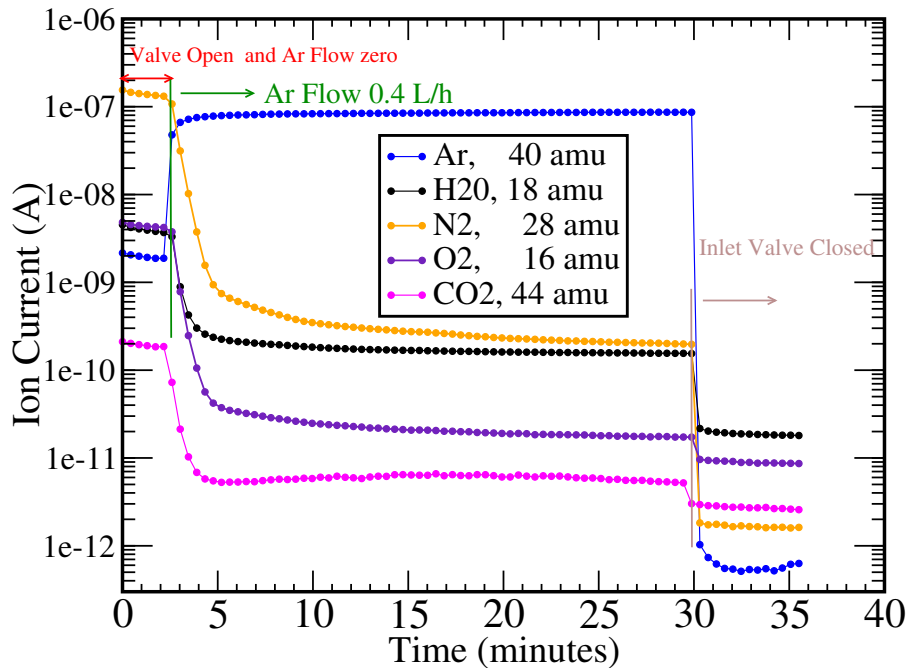


Fig. 3.7: Ion current Ar and some residual gases peaks as a function of time. Within the first region the residual gases from the gas system and the capillary tube are measured, then a flow of Ar gas is set, and finally the inlet valve is closed.

3.2.3 Helium leak test

Several weeks of pumping showed that the level of background pressure could not be better than 1.3×10^{-8} mbar. However, the analysis of the mass spectra indicated the presence of a leak into the mass spectrometer. On the spectrum of residual gases, it was observed that the ratio between the main peaks from N_2 (28 amu) and O_2 (32 amu) was around 4, as expected for air, which evidences a leak in QMS system. Hence, a SEM LeakTest Template in Quadera was used to localize the leak; with this option the mass spectrometer monitors only the peak at 4 amu, that corresponds to helium gas. In this way, small quantities of helium gas were spread on all the pipe connections, and finally it was found that the leak was inside, in the connection between the capillary and the outlet of the mass spectrometer. Mass spectrum acquired when the leak was in the system is observed in Fig. 3.8.

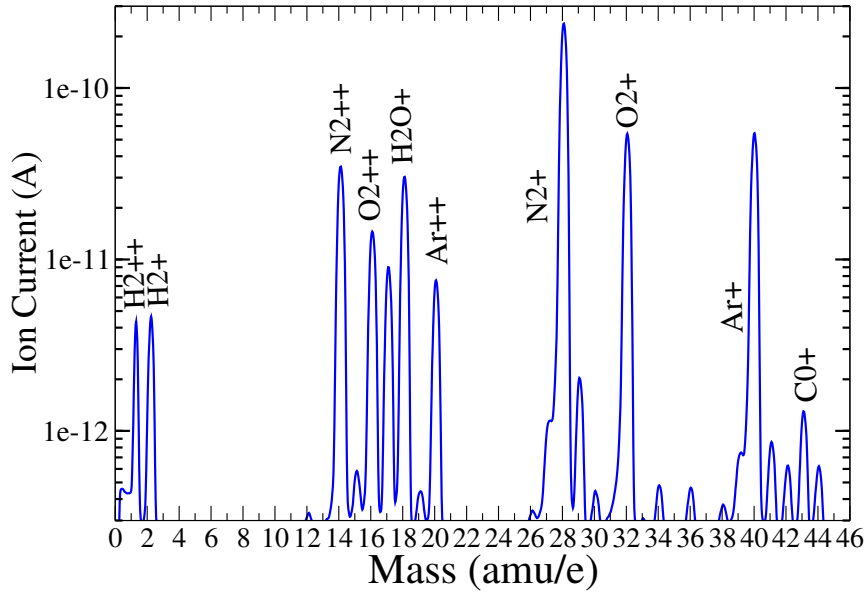


Fig. 3.8: Mass spectrum acquired when a leak was in the Quadrupole Mass Spectrometer System, the leak location was found within the connection of the capillary and the outlet of the internal system. The air components are clearly distinguished, the C_{N_2}/C_{O_2} ratio is about 4 which evidences the leak in the system.

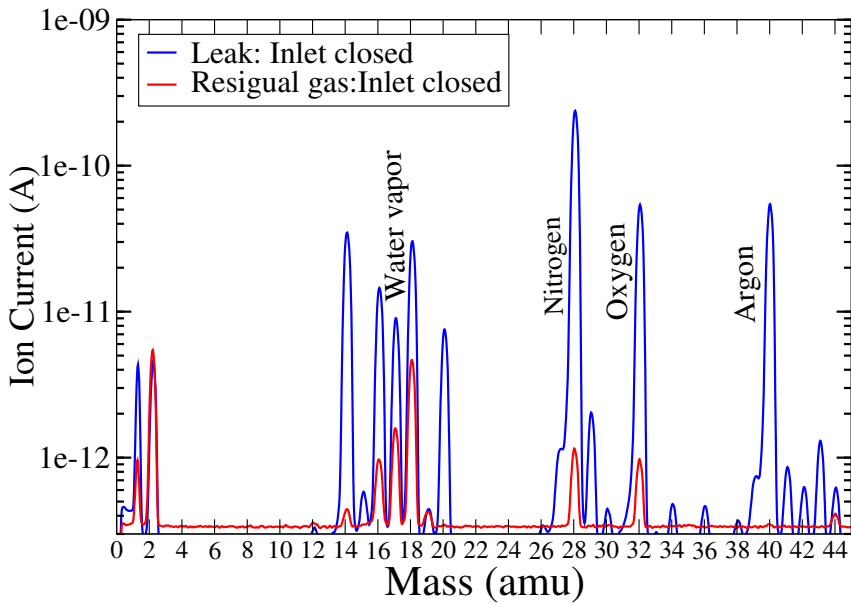


Fig. 3.9: Comparison of mass spectra acquired during the system with a leak and after the adjustment was performed.

After the connection was adjusted, the improvement on pressure was immediately observed. Comparison of mass spectra acquired during the leak was in the system and after solving the problem are depicted in Fig. 3.9. The following conclusions can be done from the residual mass spectra:

- With the leak in the system the higher component is at 28 amu, that corresponds to the N_2 , being about 4 the ratio between signals at 28 and 32 amu.
- After the leak was removed, the higher contribution is from water vapor at 18 amu, and the main peaks for N_2 and O_2 have practically similar ion currents.

3.3 Calibration of Mass Spectrometer for Xe+TMA mixtures

The focus in the second part of this thesis was the study of Xe+TMA mixtures for Rare Event Searches; measurements with several TMA concentrations were important in order to find the optimum concentration for energy resolution and gain for $0\nu\beta\beta$ decay experiments as well as for columnar recombination studies for directional dark matter searches. Thus the quantification of TMA was a requirement to perform systematic studies of the mixture, considering that the preparation of Xe+TMA mixtures is carried out in the laboratory.

A first calibration of Xe+TMA mixtures was done in 2011 after the measurements performed in Chapter 4 which were published in [102]. However, after a revision of the procedure carried out it was found that experimental and calculation mistakes were done. For this reason, new measurements were performed in 2013 for a new calibration and are reported here. These consisted in the preparation and analysis of several homemade mixtures following different experimental procedures.

3.3.1 Pure Xe and Xe+TMA mass spectra

Mass spectra acquired for pure Xe and Xe+TMA are depicted in Fig. 3.10 (top). The spectrum for pure Xe is illustrated in detail in Fig. 3.10 (bottom), divided in three regions: the low part where the contributions of the impurities and background are shown (0-46 amu), the middle part (60-70 amu) where the double ionizations related to the Xe isotopes are observed, and in the last region (>70 amu) the main contributions due to single ionizations from Xe isotopes are depicted.

For the acquisition of the pure Xe mass spectrum, the gas system was previously purged several times with the own Xe gas that is introduced from external bottle. After each purge the Xe was recovered into the recovery bottle by means of cryopumping. At the beginning of the procedure, the ion current at 32 amu was above 1×10^{-12} A, whose level was decreasing after each purge, reaching a stable value around 2.44×10^{-13} A. By a simple calculation the level of oxygen can be obtained.

This can be done considering that the relative probability of ionization of Xe and O₂ (2.4, see Table 3.3) is proportional to the calibration factor, thus concentration of O₂ is $c_{O_2} = C_{O_2} \times 2.6 / C_{Xe} = 2000$ ppm, where C_{O_2} and C_{Xe} correspond to the ion current at 32 and 132 amu. This result implies that levels of oxygen below this value can not be quantified because they are masked by the irreducible background of the own instrument, as is mentioned in [164].

The analysis of mass spectrum for gases with several fragmentation ions and isotopes, as Xe or TMA, is usually performed through the fragmentation factor or cracking pattern that is defined as:

$$f_i = \frac{I_i}{I_0} \quad (3.1)$$

where I_i is the signal at a mass number m_i , and I_0 the signal at main mass number peak m_0 . The fragmentation factors for TMA mass spectrum differs from those found in literature. This has been noted before and it is attributed to the fact that fragmentations factors depends on the operational parameters of the QMS [168].

Xe Peak (amu)	f_i (%)	TMA Peak (amu)	f_i (%)
62	1	15	8.14
64	13.2	17	1.29
65	29.3	18	1.64
66	17.8	27	3.63
67	6.9	28	4.78
68	6.1	29	5.86
124	3.5	30	15.51
126	3.4	32	1.07
128	7.1	41	5.16
129	98.4	43	8.7
130	15.2	56	2.82
131	79.4	57	5.82
132	100	58	99.99
134	37.8	59	43.57
136	32.0	60	1.78

Table 3.4: Expected peaks contributions to the mass spectrum analysis of Xe [154] and TMA [169], the values are given in percentage respect to the main contribution.

The expected peaks for Xe and TMA are shown in Table 3.4. Some peaks contributions for TMA are not shown due the low contribution (lower than 2%), however the lower contributions that overlap with O₂ (32 amu), water vapor (17 and 16 amu), and N₂ (28 amu) are seen. The single ionizations of Xe (from 124 amu) correspond to the Xe isotopes, and the peaks below to 124 amu come from

double ionization of the atoms. Most of the contributions to the TMA mass spectrum come from fragmentation molecules and its double ionizations [170]. In any case, these fragmentation factors have not been used for the determination of TMA concentrations in this work.

Even though the sensitivity of the instrument could be improved for oxygen and water vapor, a simple analysis for quantification of these impurities would be complicated. This is because the TMA has contributions at 32, 18 and 17 amu, as a consequence the contribution from water vapor (18 and 17 amu) and oxygen (16 and 32 amu) can not be singled out.

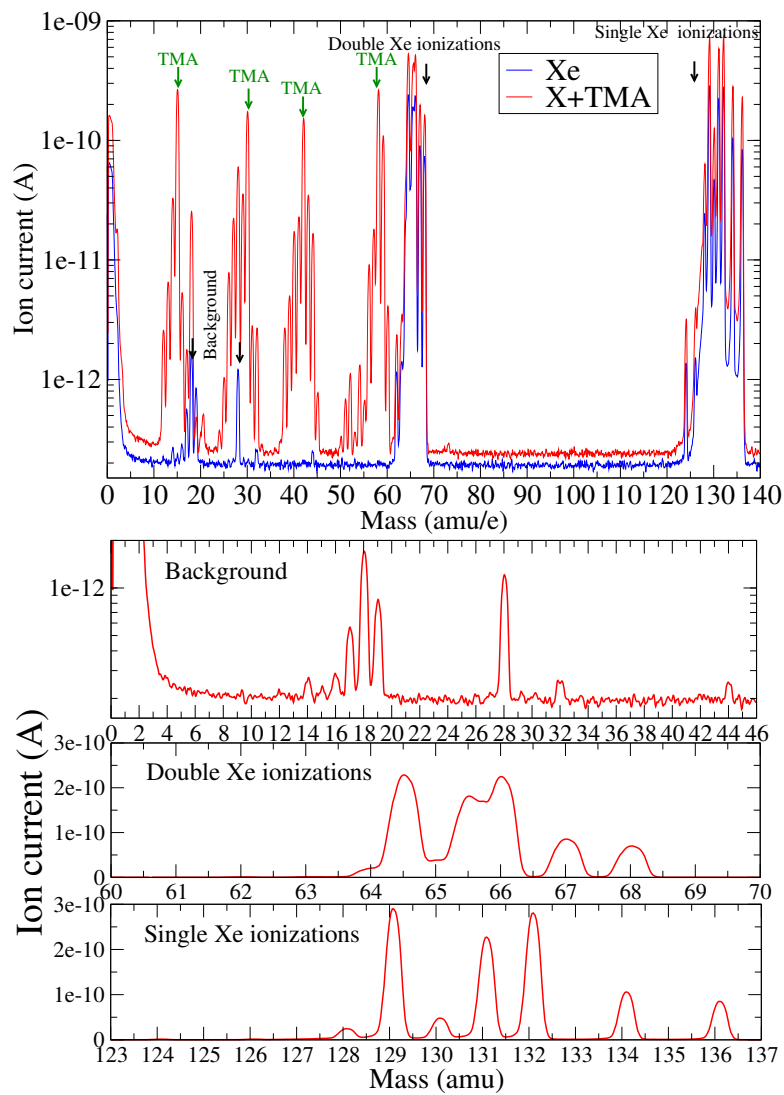


Fig. 3.10: Top: Mass spectra of Xe and Xe+TMA mixture acquired with the QMS. Bottom: Pure Xe spectrum divided in three regions: in the first region is shown the background, in the second the double Xe ionizations and in the third the single ionizations corresponding to the isotopes of Xe.

3.3.2 Calibration Factor

Calibration factor is determined considering that the sum of ion currents of each component is proportional to the partial pressure, which in turn is proportional to the concentration of each component. The calibration factor defined, α , can be obtained from:

$$\frac{P_{TMA}}{P_{Xe}} = \alpha \frac{C_{TMA}}{C_{Xe}} \quad (3.2)$$

where P_{TMA} and P_{Xe} are the total partial pressures, while C_{TMA} corresponds to the value of ion current at 58 amu and C_{Xe} at 132 amu. This relation is satisfied if the selected peaks for each gas do not overlap and impurities are very small. The first condition always satisfies and the second one for most of the measurements is fulfilled; only in cases of a highly contaminated mixture the quantification of TMA could give wrong values.

Once known the calibration factor, the relative percentage of pressure of TMA can be obtained as:

$$\%P_{TMA} = \frac{P_{TMA}}{P_{TMA}+P_{Xe}} = \frac{1}{1 + \frac{P_{Xe}}{P_{TMA}}} \quad (3.3)$$

Substituting Eq. 3.2 in 3.3:

$$\%P_{TMA} = \frac{1}{1 + \frac{1}{\alpha} \frac{C_{Xe}}{C_{TMA}}} = \frac{\alpha}{\alpha + r} \quad (3.4)$$

where r is the $\frac{C_{Xe}}{C_{TMA}}$ ratio. The related error of the TMA percentage is given by:

$$\sigma_{P,TMA} = \sqrt{\left(\frac{r}{(\alpha + r)^2}\right)^2 \sigma_{\alpha}^2 + \left(\frac{\alpha}{(\alpha + r)^2}\right)^2 \sigma_r^2} \quad (3.5)$$

Typically the gas analysis consists in the acquisition of 10 mass spectra, scanning the range between 1-140 amu with the SEM detector. For each spectrum the ratio r (C_{Xe}/C_{TMA}) and then the associated error from statistic deviations are calculated. The calibration factor is the value obtained at the end of this chapter and its error comes from the instrumental error of the pressure gauge (5 mbar). In this way, from Eq. 3.4 the TMA concentration by volume percent ($\%P_{TMA}$) is calculated and the related systematic error from Eq. 3.5.

3.3.3 Experimental Procedure

It was not available a certified Xe+TMA mixture, hence several Xe+TMA mixtures with a certain concentration were prepared inside the NEXT-0-MM TPC in order to calculate the calibration factor for each one through Eq. 3.2. At the beginning, pure TMA gas was introduced into the system from the external bottle to acquire mass spectra and observe the composition of the gas. It was observed that this

was highly contaminated, ion currents for peaks at 32 amu and 28 amu were above 10^{-10} A. For this reason, in order to remove the impurities of the TMA gas, a small pure TMA gas from the external bottle was introduced into the sample bottle; and then by cryopumping the gas was liquefied and then pumped to remove the impurities. Previously to this procedure, the Xe+TMA gas inside the sample bottle was moved into the NEXT-1-MM TPC by difference of pressure. The small quantity of gas remained in the sample bottle (less than 1 bar) was evacuated by pumping with the turbo pump.

Taking in mind this initial condition, the experimental procedure for the preparation of a mixture of Xe+ $X\%$ TMA at a certain pressure, was the following:

1. Both the TPC together with the gas system are pumped until the values of vacuum and outgassing rate are below 5×10^{-3} mbar and 5×10^{-4} mbarl/s.
2. The X percentage of TMA gas is introduced inside the vessel from the sample bottle, then the inlet and outlet valves are closed -isolating the TPC- in order to pump the gas system.
3. The $100 - X$ percentage of pure Xe is then introduced from the external bottle. To avoid that the TMA goes out, at the moment of opening the inlet valve of the TPC, it is only opened until the pressure in the gas system is above of the pressure in the TPC.
4. After the pure Xe is introduced, both the inlet and outlet valves are opened, thereafter the recirculation is started through bypass valve to homogenize completely the mixture. After 10 minutes the recirculation pump is stopped.
5. Then the mass spectrometer valve is opened and the flow is set to 0.1 l/h, starting the acquisition of the mass spectra until the vacuum pressure stabilize. Values between $1-2 \times 10^{-5}$ mbar are typical values of measurement, these values change depending on the gas system pressure. Usually, in order to obtain good statistics 10 mass spectra are acquired, in each one, it was scanned 0.5 ms per amu. A total time of 70 s is spent for each mass spectrum, covering a range of masses from 0 to 140 amu.

Detailed information for each mixture prepared is presented in Table 3.5. Six mixtures were considered (roman number) and for each one different conditions of measurement correspond to different runs (arabic number). The pressure of measurement is indicated for each run (Press. Meas.), this is the total pressure in the gas system and the chamber at the moment of the acquisition. The relative pressures of TMA and Xe in the chamber together with the TMA fraction calculated are also shown, as well as C_{Xe}/C_{TMA} ratio (ratio of ion current at 132 and 58 amu), currents for each peak are obtained calculating the maximum for each peak.

Although six mixtures were prepared, different conditions of measurement were used in order to quantify systematic errors that could affect the calibration factor. For some runs the standard procedure was modified:

mixture, run	Press. Meas. (bar)	Press. TMA (bar)	Press. Xe (bar)	Fraction TMA (%)	Current ratio TMA C_{Xe}/C_{TMA}	Calib. Factor α
I, 1	1.20	0.05	1.15	4.2	1.09	0.048
II, 2	1.5	0.16	1.34	10.7	0.38	0.045
II, 3	1.5	0.16	1.34	10.7	0.41	0.048
III, 4	1.5	0.05	1.45	3.4	1.46	0.050
III, 5	1.5	0.05	1.45	3.4	1.57	0.054
IV, 6	2.5	0.25	2.25	10	0.47	0.053
IV, 7	2.5	0.25	2.25	10	0.48	0.053
V, 8	1.7	1.25	1.25	50	0.059	0.058
VI, 9	2.5	0.03	2.97	1	6.031	0.060
VI, 10	1.7	0.03	2.97	1	5.27	0.053
VI, 11	1	0.03	2.97	1	4.93	0.050

Table 3.5: Details of each mixture prepared to calculate the calibration factor which allows to quantify the composition of Xe+TMA mixtures are shown. The total pressure of measurement, the relative pressure of each component and the related TMA fraction are indicated, as well as the average ratio between the ion current at 132 and 58 amu (C_{Xe}/C_{TMA}) obtained after the analysis of the mass spectra acquired (10 spectra) are presented together with the related calibration factor deduced.

- **Run 2:** The acquisition was started without recirculation of the mixture.
- **Run 3:** Measurement was realized with 1 h of recirculation through bypass valve -not by purifier- following the standard procedure.
- **Run 5:** After 10 minutes of recirculation the inlet and outlet valves were closed, then the gas system was pumped during 5 minutes, reaching vacuum values of less than 5×10^{-3} mbarl/s; after that the procedure of acquisition started, opening the mass spectrometer valve.
- **Run 6:** Acquisition was carried out after 20 minutes of recirculation, following the standard procedure.
- **Run 7:** The mixture remained stored during 12 h inside the chamber, then it was recirculated for 20 minutes, and before the acquisition the gas system was pumped as in Run 5.

3.3.4 Results and Discussion

From results of the calibration factor calculated for several TMA concentrations and different experimental procedures presented in Table 3.5, the following conclusions can be drawn:

- The change of the recirculation time shows that 10 minutes are enough to homogenize the mixture. The calibration factor for the mixture without recirculation presents a deviation of 10% respect to the value obtained when the mixture was recirculated.
- The discrepancies for the values from the run 1 to run 4 could be attributed to bad experimental conditions which were improved in the following measurements.
- The runs 5 and 6 have values of calibrations factors compatible although the total pressure is different and also the relative pressure of TMA. This is attributed to the improvements in the experimental procedure. This result implies that the calibration factor for TMA concentrations below 10% does not depend on TMA concentration and pressure, as expected.
- The high deviation of the calibration factor determined with mixture VI, for different pressures (2.5, 1.7 and 1 bar) is attributed mainly to the fact that the relative pressure of TMA (0.03 bar) is dominated by an instrumental error of 10% (5 mbar).

From values of Table 3.5 the calibration factor was estimated by averaging the values for each configuration, obtaining a value of $\alpha = 0.054 \pm 0.005_{sys}$. A mass spectrum of a mixture with a TMA concentration of 98%Xe+2%TMA ($2.00 \pm 0.05_{stat} \pm 0.19_{sys}\%$) is illustrated in Fig. 3.11, this value is deduced from the estimated calibration factor.

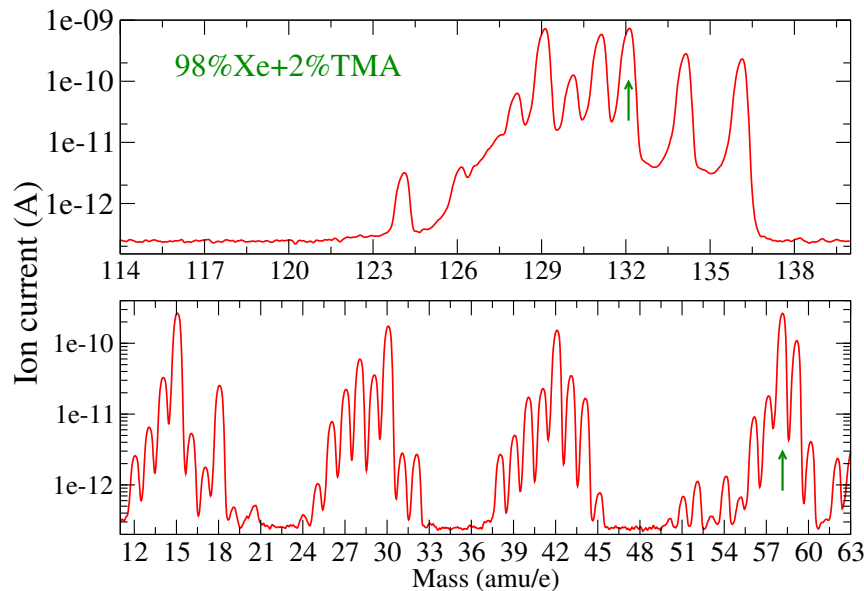


Fig. 3.11: Mass spectrum of a 98%Xe+2%TMA mixture, single ionizations of Xe are shown in the top spectrum and the TMA mass spectrum in the bottom. The peaks used for the determination of the TMA concentration are depicted, for Xe the peak used is 132 amu and for TMA the peak at 58 amu.

The concentration was calculated using Eq. 3.4, the statistical error from the standard deviation of the 10 measurements acquired and the systematic error from Eq. 3.5. Hereinafter the values of TMA concentration for simplicity are given without error. The spectrum only shows: the single ionizations from Xe (top plot) and TMA fragments (bottom plot) indicating the peaks at 132 and 58 amu which are used in the analysis for the quantification.

3.4 Conclusions

A Quadrupole Mass Spectrometer was installed successfully into the gas system of the HP Xe-based TPC (NEXT-0-MM) in order to perform precise gas analysis and find optimum conditions of operation. Several measurements of vacuum pressure and residual gas analysis were carried out, concluding that 30 h are required to obtain the ultimate vacuum pressure ($\sim 10^{-8}$ mbar) after the system is put into operation; this time includes the bake-out and the time necessary for degassing of the filament.

A calibration procedure for Xe+TMA mixtures was established, several mixtures of Xe+TMA were prepared with different TMA concentrations; as a result the calibration factor was estimated with a systematic error of 10%, error mainly related to the instrument used for measuring the pressure. This systematic error could be improved in a new calibration by using a better pressure gauge or preparing mixtures with higher content of TMA. This calibration procedure can be applied to different mixtures which will allow the systematic study of them.

Detailed analysis from Xe mass spectra allowed to confirm that with the Quadrupole Mass Spectrometer it is not possible to obtain sensitivity of oxygen at the order of ppm, due to the irreducible background from outgassing of the instrument. Levels of oxygen below 500 ppm can not be quantified with the system.

X-ray Measurements in Xe+TMA Mixtures

Contents

4.1	Experimental Setup and Procedure	94
4.1.1	Overview	94
4.1.2	Energy Spectrum of ^{109}Cd Source in Xe+TMA Mixtures	94
4.1.3	Experimental Setup	95
4.1.4	Experimental Procedure	97
4.2	Data Analysis	98
4.3	Results	101
4.3.1	Determination of optimum fraction	101
4.3.2	Measurements of gain	101
4.3.3	Variation with Pressure	108
4.3.4	Drift velocity	113
4.4	Towards Fano factor measurement in NEXT-0-MM	113
4.5	Comparison between Ingrid and microbulk Micromegas readouts	115
4.6	Conclusions	116

The measurements presented in this chapter are focused on exploring the possibility of improving the energy resolution of the Micromegas-TPC readouts, using Xe-TMA Penning mixtures. Early studies performed in this mixture using wire chambers at 1 bar [50] showed a great gain enhancement and improved energy resolution, as compared with pure Xe. An experimental study of the TMA mixture was performed at high pressure through measurements of electron transmission, gain and energy resolution at different conditions. All results presented in this chapter have been obtained with the NEXT-0-MM TPC, that was described in Chapter 2.

As the measurement of Fano factor is an important step to estimate the value of the intrinsic energy resolution, preliminary measurements with an InGrid readout were performed with the aim of evaluating the measurement of the Fano factor in a future experiment in the NEXT-0-MM chamber.

The content of the chapter is structured as follows: the experimental setup and procedure are presented in Sec. 4.1, then the Data Analysis in Sec. 4.2. The results of measurements are presented in Sec. 4.3. The evaluation of measuring the Fano

factor in Xe+TMA mixture with Ingrid readout is presented in Sec. 4.4, then the comparison between the microbulk and InGrid readouts is done in Sec. 4.5. Finally, in section 4.6 the conclusions are drawn.

4.1 Experimental Setup and Procedure

4.1.1 Overview

The first experimental goal of this study was to establish a range of TMA concentration for which it would be possible to obtain the best energy resolution and the highest gain for pressures between 1 bar and 10 bar. Therefore, a systematic variation of the TMA concentration was performed at four reference pressures: 1 bar, 5 bar, 8 bar and 10 bar (see section 4.3.1). Once the optimal TMA concentration range was established, a systematic study at several pressures ranged from 1 bar to 10 bar was done (see Sec. 4.3.3). These measurements were performed with a ^{109}Cd source, the energy spectrum generated by this source in Xe+TMA mixtures is discussed below.

4.1.2 Energy Spectrum of ^{109}Cd Source in Xe+TMA Mixtures

The ^{109}Cd nuclei decay by electron capture (EC) to a metastable state of the daughter, ^{109m}Ag ; this process occurs in K, L and outer shells with probabilities of 79%, 17% and 4%, respectively. After that, due to Ag fluorescence, the emission of K_α (22.1 keV), K_β (25.0 keV) X-rays or Auger electrons takes place. The daughter nucleus ^{109m}Ag decays with 4% of probability via γ -ray emission (88.0 keV), or via internal conversion (IC) with 45% and 48% of probability for K and L shells; as a result high-energy electrons are ejected, $e_k=62.5$ keV or $e_L=84.6$ keV, which in turn are also accompanied by the emission of Ag fluorescence X-rays K_α (22.1 keV) or K_β (25.0 keV). For shells higher than L the contribution of IC is 3% [171]. The decay scheme of the ^{109}Cd radioactive source is shown in Fig. 4.1, the EC is only represented for K-electron capture.

The charge spectrum emitted by the ^{109}Cd source in Xe+TMA mixtures is the same that in pure Xe, since the addition of TMA does not introduce any change. As it can be seen in Fig. 2.19 the photo-peak efficiency at 88 keV is very low in NEXT-0-MM chamber, therefore, instead of it the Xe escape peaks should appear on the spectrum. Three Xe EP are related to it, at energies of 84, 58 and 54 keV corresponding to Xe L_α , K_α , K_β Ag fluorescences. The detection efficiency continues to be low for these energies, certainly at low pressures the energy spectrum must be taken for a long time to obtain good statistics for these peaks. However, at higher pressures the detection efficiency increases, thus these peaks should appear with larger frequency.

The detection efficiency at energies of K_α (22.1 keV) and K_β (25.01 keV) Ag fluorescence X-rays is very high (see Fig. 2.19), hence, these peaks are the most important contribution, especially at low pressures. The corresponding Xe L_α EP

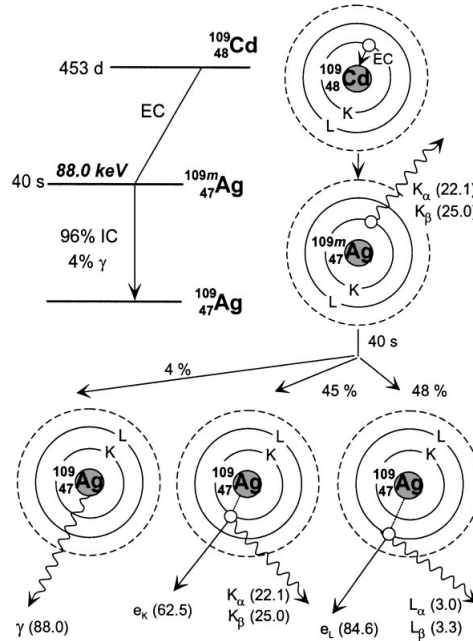


Fig. 4.1: Representation of the decay of a ^{109}Cd radioactive source, the numbers in parenthesis indicate the energy in keV. Figure taken from [171].

for each K peak should be seen with very low intensity. Table 4.1 summarizes in detail the energy and intensity of the γ -ray, and K X-rays emissions, and their corresponding EP's. The intensity referenced for X-rays has been calculated as the sum of all the respective α 's and β 's contributions. All the information about the energy and intensities have been taken from [172].

4.1.3 Experimental Setup

The experimental setup used for these measurements is the same that is described in Chapter 2. Some changes were applied, mainly to adapt it to the new needs. The main modification was the addition of a mass spectrometer; the installation of this system and its performance was explained in detail in previous chapter (see Chapter 3). This system allows to monitor the gas impurities and determine the TMA concentrations of the mixtures used, following a standard procedure which was also presented in previous chapter.

The other change introduced was the modification of the drift field cage. A reduction of the drift distance from 6 cm to 1 cm was carried out, this allowed to reach higher E_d/P values indeed at higher pressures by applying lower drift voltages. For this purpose, the copper rings together with the resistors were removed from the drift structure, thus the anode plate was shifted to the first slot of the PEEK pillars. A ^{109}Cd radioactive source (with an activity of $1 \mu\text{C}$) was placed on the center of the cathode, where a 2 mm diameter hole was done to collimate the radiation, allowing γ - and X-rays to reach the drift region. An schematic representation of the drift

Type	Energy (keV)	I (%)
γ -ray	88.0	3.61
K_α X-ray	22.1	85.20
K_β X-ray	25.0	16.81

Escape Peaks	X-ray energy (keV)	Escape Peak Energy (keV)	I (%)
Xe L_α -EP for γ -ray	4.24	83.76	5.76
Xe K_α -EP for γ -ray	29.87	58.13	47.40-25.60
Xe K_β -EP for γ -ray	33.76	54.25	4.35-8.40
Xe L_α -EP for K_α X-ray	4.24	17.86	5.76
Xe L_α -EP for K_β X-ray	4.24	20.76	5.76

Table 4.1: Detailed description of the γ - and X-ray emissions of a ^{109}Cd source (top) and the corresponding Xenon escape peaks (EP) (bottom) [172].

field cage can be seen in Fig. 2.1. The Micromegas used for these measurements is of the microbulk type, with geometric parameters of 50-45-90 (gap-pitch-hole diameter), in Fig. 4.2 are shown pictures taken with an optical microscope of the University of Zaragoza.

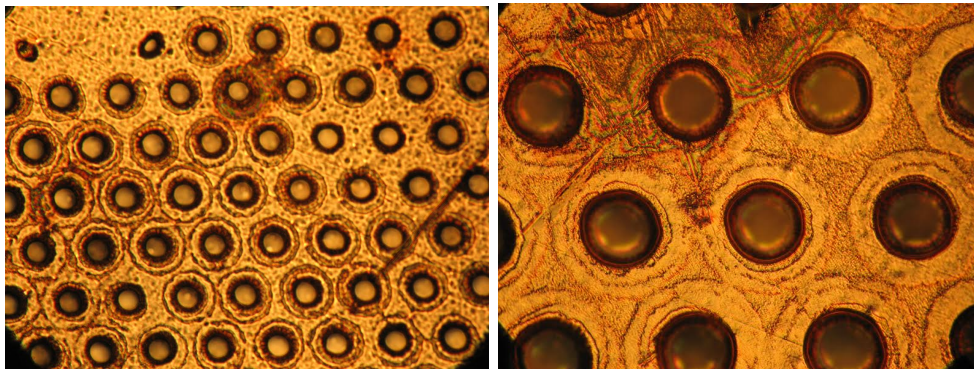


Fig. 4.2: Pictures of the microbulk Micromegas used for Xe+TMA measurements, with geometric parameters of 50-45-90 μm (gap-pitch-hole diameter). The Micromegas has a copper mesh with a gold deposition (image taken with an optical microscope of the University of Zaragoza by J.J. Morales).

The mesh of the Micromegas was connected to the anode plate and then grounded to the body of the chamber (see Fig. 4.3). A positive voltage is applied to the back-electrode. The signal is fed into a CANBERRA preamplifier+amplifier chain (model 2005 and 2022 respectively), the amplifier with a shaping time of 4 μs . The amplified signal is finally recorded by a multichannel analyzer (AMPTEK MCA 8000A), that produces the pulse height distribution.

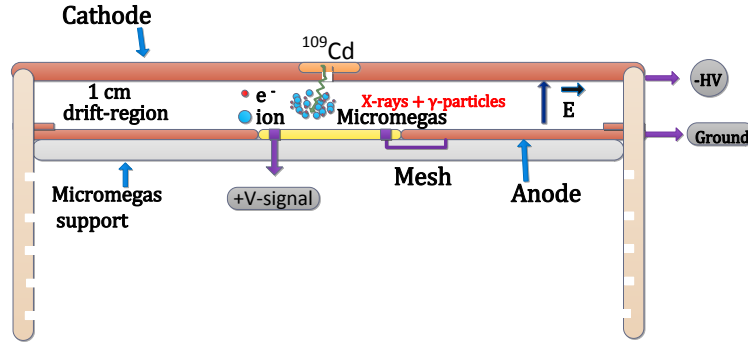


Fig. 4.3: Schematic view of the drift field cage for X-rays measurements and γ -rays in Xe+TMA mixtures.

4.1.4 Experimental Procedure

Prior to each set of measurements, the chamber and the gas system were pumped up to reaching values down to 10^{-6} mbar. The chamber was routinely baked out at temperatures above 100°C during approximately three hours, obtaining outgassing rates below 5×10^{-5} mbarl/s. After that, the chamber was filled at determined pressure and gas mixture; immediately after this, the circulation process started. Contrary to the specifications of the provider, it was observed that the SAES filter retains and releases TMA depending on the previous concentration employed. For instance, when the concentration of the new mixture is higher than the previous one used, the filter will retain TMA until an internal equilibrium is reached, therefore it is seen that the final TMA concentration reduces. Conversely, if the concentration of the new mixture is lower than the previous used, the filter will release TMA, obtaining that the TMA concentration increases. For this reason, a previous study of the gas composition was performed, by measuring the TMA concentration from the beginning of the recirculation; stable concentration of TMA was reached in approximately 30 minutes. Apart from that, the peak position and the energy resolution at 22.1 keV for a determined voltage configuration also showed to have constant values after 30 minutes. For each set of measurements, the described procedure was selected to confirm the equilibrium instead of measuring with the mass spectrometer, mainly to avoid the loss of gas.

After the stabilization of the mixture, the operation point was determined by obtaining the electron transmission curve and selecting a field ratio at which the electron transmission takes values above 98%. With this purpose, the amplification voltage was fixed for gains above 100 and the drift voltage was scanned within a range of 0.1 – 1 kV (1 bar) and 0.2 – 5 (1 bar). Electron transmission curves for pressures from 1 to 10 bar are shown in Fig. 4.4, using TMA concentrations around 1.5%.

. For all pressures is viewed that the electron transmission increases with the field ratio until reaching a maximum value, which corresponds to the maximum

collection efficiency for each configuration. Thereafter, the electron transmission drops. The field ratio at which the ET reaches the maximum moves to right side as the pressure is increased. It is also seen that the ET rises more slowly with increasing pressure; this behaviour is explained by the electron-ion recombination that is stronger at higher pressures, as it will be discussed in Chapter 5.

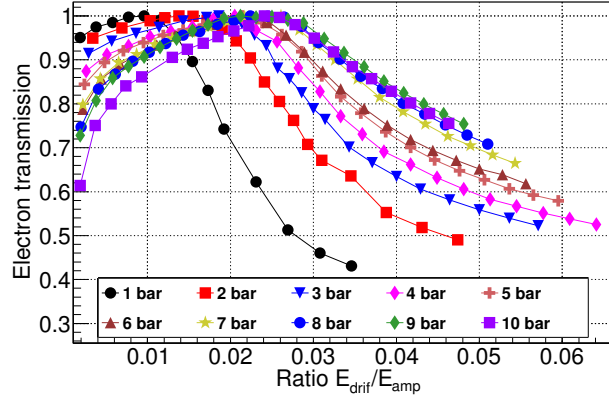


Fig. 4.4: Electron transmission of the Micromegas readout plotted against the ratio of drift-to-amplification fields in Xe+TMA mixtures, for pressures between 1 and 10 bar. The TMA concentration for each pressure is around 1.5 %.

Subsequently, gain measurements were performed increasing systematically the amplification voltage; the field ratio remained constant for each amplification value and configuration (mixture and pressure), ratios above 98% were selected to ensure good electron transmission. The increase was stopped until two consecutive sparks appeared within a short time period (30 s); typically the variations were between 34 (84) and 58 (114) kV/cm for 1 (10) bar. It must be noted that at the highest pressures the increase was until the first spark occurred to prevent irreversible damage to the Micromegas. At the end of each set of measurements, the TMA concentration was measured using the mass spectrometer, following the standard procedure explained in Chapter 3. Finally, the gas was removed from the chamber and the gas system by cryopumping process and then pumped with the turbomolecular pump to prepare the system for the next set of measurements.

4.2 Data Analysis

Typical energy spectra registered for a ^{109}Cd source at 1 bar in a Xe+1.2% TMA mixture (top) and 10 bar in a Xe+0.7% TMA (bottom) is shown in Fig. 4.5. In both spectra the K_α and K_β lines from the Ag fluorescence are clearly distinguished. The corresponding escape peaks from the L-shell in Xe are observed below the K_α and K_β line, placed at 17.9 keV and 20.8 keV. The Ag K_α , K_β lines (in blue) and the corresponding Xe escape peaks (in magenta) were fitted in the energy range between 14 keV and 30 keV using a 3-step routine (see Fig. 4.5).

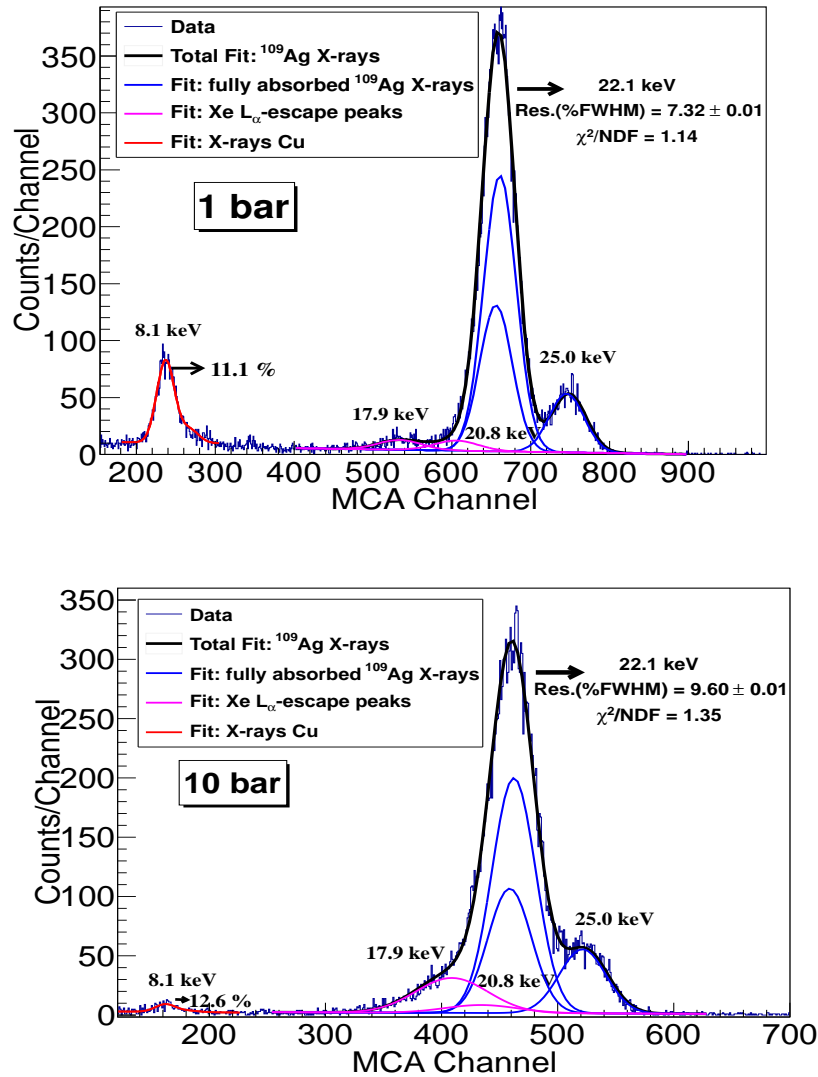


Fig. 4.5: X-ray energy spectra registered for ¹⁰⁹Cd source, in a Xe+1.2 % TMA mixture at 1 bar (top) and Xe+0.7% TMA at 10 bar (bottom). The fit performed to the overall Ag K-fluorescence lines consists in a 3-step routine. The Cu K-fluorescence peak at 8.1 keV is separately fitted to a single Gaussian function. Energy resolution (%FWHM) for 22.1 keV and 8.1 keV peaks is indicated.

The results of this procedure are shown in figure 4.5. In the first step, the complete range was fitted to one Gaussian function $K_{\alpha 1}$ (22.2 keV) over a linear background. In the second one, two Gaussian functions were considered which correspond to $K_{\alpha 2}$ (22.0 keV) and K_{β} (25.0 keV) lines. In the last step, two more Gaussian functions were added which correspond to the Xe X-rays escape peaks. The input parameters in the last two steps are the calculated ones at previous steps. On the other hand, the Cu K-fluorescence at 8.1 keV is also observed, this is

produced by the interaction of X-rays with the electrodes of the Micromegas. The Ag K_{α} peak parameters (position and width) at 22.1 keV are used for calculating the gain and energy resolution due to its higher statistics.

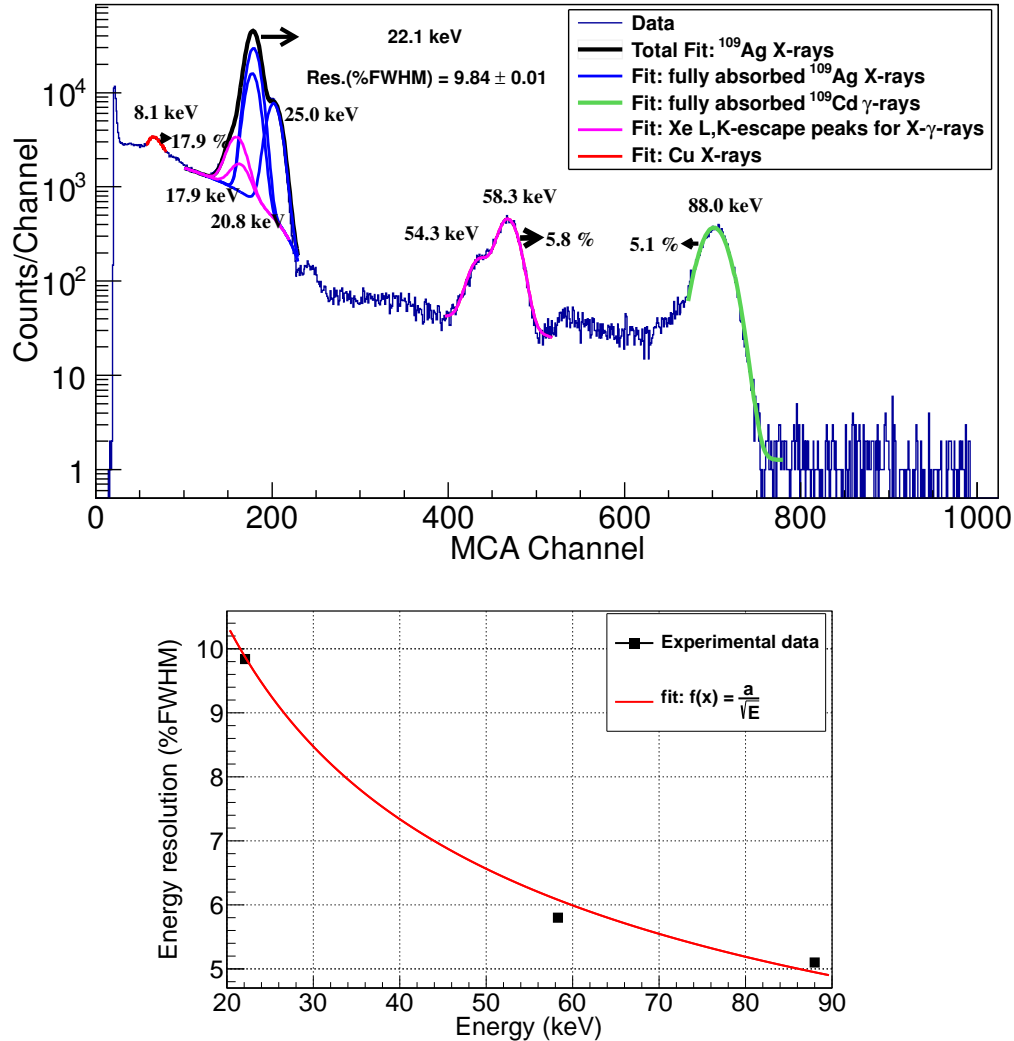


Fig. 4.6: Top: Energy spectrum from the ^{109}Cd source acquired at 8 bar in a Xe+0.8% TMA mixture, with $E/p = 245 \text{ V/cm/bar}$ in the drift region. The K-fluorescence emission and the γ -rays from ^{109}Ag with their related escape peaks of Xe can be distinguished. The fits realized for each peak are depicted and energy resolution (%FWHM) values are indicated. Bottom: Energy resolution of the main peaks is plotted against energy; the behaviour shows an approximate $1/\sqrt{E}$ scaling; even though only the peak at 88 keV is mono-energetic.

Energy spectrum acquired at 8 in a mixture of Xe+0.8% TMA, is shown in Fig. 4.6-top with a larger energy range than previous figure. It is interesting to

observe the γ -rays from ^{109}Cd source at 88.04 keV and two escape peaks located at 58.3 keV and 54.3 keV, related to K_α (29.7 keV) and K_β (33.7 keV) X-ray emissions of Xe, respectively. The energy resolution of the main peaks is indicated, with values of 9.8, 5.8 and 5.1 %FWHM at 22.1, 58.3 and 88.0 keV, respectively. As expected, the energy resolution shows a dependency with the inverse of the square-root of the energy (see Fig. 4.6), even though only the peak at 88 keV is mono-energetic, because the others come from various X-rays for 22.1 keV and various EP's for 58.3 keV.

It must be pointed out that the energy spectrum in Fig. 4.6 was not acquired under optimum fields for this mixture and the only interest was to observe the γ -rays of ^{109}Cd . The event containment and conversion probability of ^{109}Cd γ -rays is indeed only well suited for the highest pressures, making their study at low/medium pressure more complicated in our setup.

4.3 Results

4.3.1 Determination of optimum fraction

The variation in TMA concentration was performed in different ranges: at 1 bar (0.3% – 10.4%), 5 bar (0.3% – 3.8%), 8 bar (0.2% – 3.3%), and 10 bar (0.4% – 3.8%). The active response of the filter to TMA led in practice to slightly different families of mixtures for each pressure. The optimum range of TMA concentration was selected based on the dependences of the gain and the energy resolution on the TMA concentration.

4.3.2 Measurements of gain

A simple modification of the equation 2.4, presented in Chapter 2, was done to calculate the gain for these measurements. Since the signal is fed to a Canberra electronic chain (preamplifier+amplifier), the conversion factor R_{pre} was replaced by a factor that contains the two conversion factors ($R_{pre+am} = R_{pre} \times R_{amp}$). The conversion factors were determined following a procedure similar to the one explained in section 2.2.7. Thus, gain is given as

$$G = \frac{M \times f_{mca}}{E/w \times R_{pre+amp}} \quad (4.1)$$

where M is the peak position in channels at 22.1 keV, f_{mca} is the factor that converts channel to mV (5000 mV/1024), and E/w is the mean number of charges created by the X-ray interaction in Xe+TMA mixtures. The mean energy for formation of an ion pair (w) has not yet been measured for Xe+TMA mixtures, hence the w value for pure Xe at 22 eV was used for all gains calculations; the estimated error due to this assumption is below 10%.

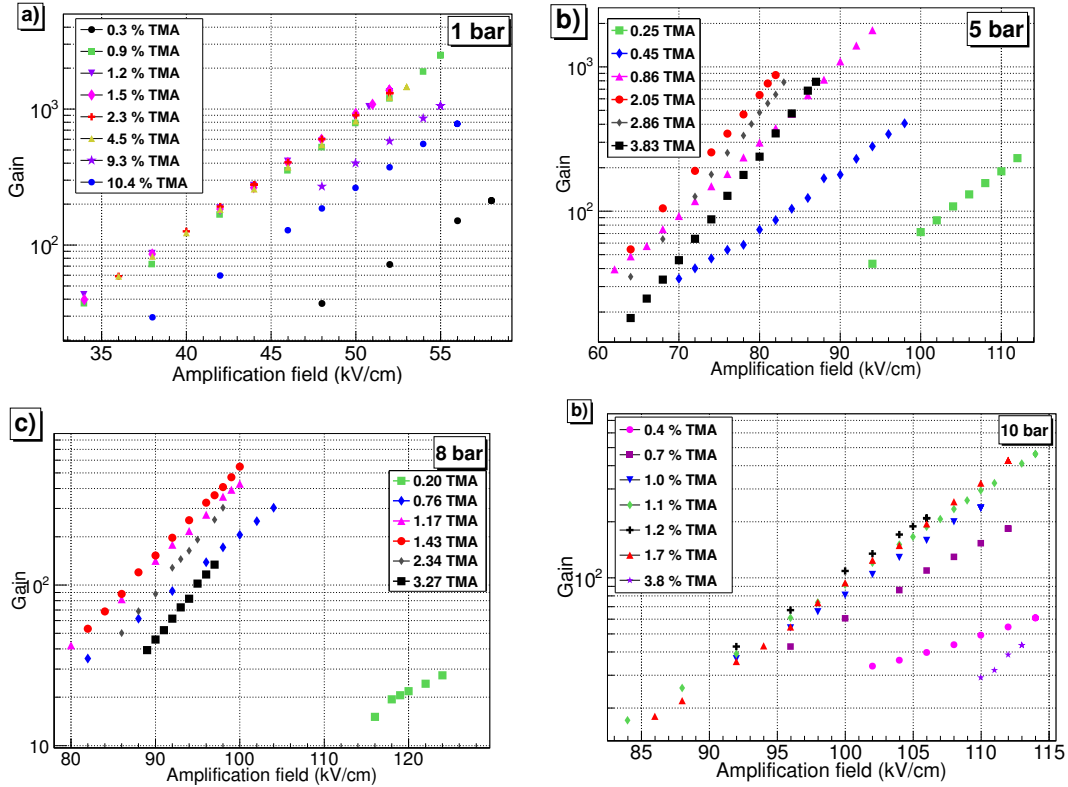


Fig. 4.7: Dependence of gain on amplification field for different TMA concentrations at 1 (a), 5 (b), 8 (c), 10 (d) bar. For each curve the TMA concentration is indicated.

The dependence of gain on the amplification field at four pressures is shown in Fig. 4.7: 1 bar (a), 5 bar (b), 8 bar (c), and 10 bar (d) bar. For all mixtures, the drift field was set to obtain the field ratio selected for each configuration (pressure and mixture), as was explained before. Based on the analysis of the Fig. 4.7, the following observations can be done:

- all the gain curves have a linear behaviour with the amplification field in semi-log plot, having correlation factors above 0.999, except in cases of lower statistics. This fact can be interpreted as indicative of negligible feedback.
- considering the plot at 1 bar (see Fig. 4.7a), it is seen that to reach same values of gain for each curve, lower amplification fields must be applied when the TMA percentage is increased between 0.3% and 0.9%. The curves within a concentration range from 0.9% and 4.5% TMA seem to overlap, suggesting that transfer mechanisms are already fully active while the avalanche dynamics remains largely unaffected.

The tendency changes above 4.5% TMA so that higher fields must be applied to obtain the same gain, this was also viewed in neon-based mixtures [173]. Similar behaviour is observed at high pressures (Fig. 4.7b-d). The increased

energy loss by inelastic collisions to TMA molecules is the most likely explanation for this change in tendency, therefore shattering the extra ionization obtained by Penning transfer.

- The onset of breakdown at each pressure presents a similar behaviour: by increasing the TMA concentration, the maximum gain increases up to maximal values within a TMA concentration range of 0.9% to 4.5% at 1 bar and 0.9% to 1.7% for pressures of 5, 8 and 10 bar; above these values, the maximum gain falls. Values of maximum gain below 60 are obtained for TMA concentrations lower than 1%, while within optimum range values gains above 2000 (400) at 1 (10) bar have been attained.

The increase of the maximum gain using the TMA concentration is an important advantage in comparison with the values in pure Xe, because this allows to work at higher gains with lower amplification fields in stable conditions. It must be pointed out that in some cases this trend is broken, this is attributed mainly to dust on the surface of the detector; this can limit the maximum gain, specially at high pressures. For this reason, the detector was routinely washed and then flushed with helium, observing that higher amplifications fields could be applied, and in consequence larger gains could be reached.

In order to do a better study of the optimum TMA concentration, it was performed a linear fits of the $\ln G$ versus amplification field data for a proper interpolation or extrapolation of the gain. The variation of the gain (at a constant amplification field) on the percentage of TMA is seen in Fig. 4.8-left.

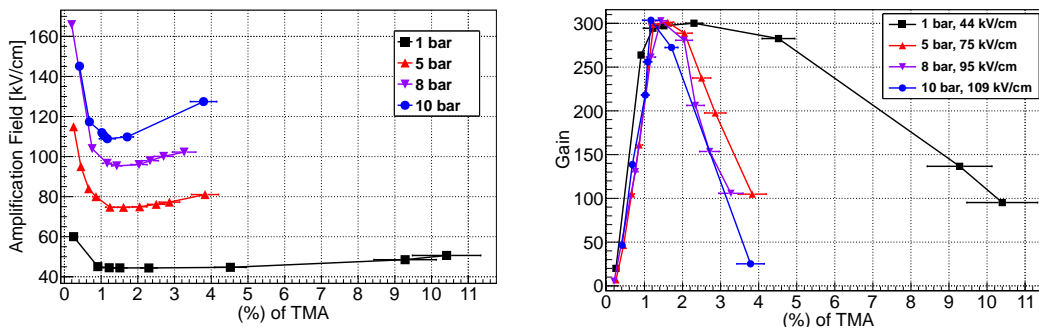


Fig. 4.8: Left: Amplification field needed to reach a gain of $G = 300$ as a function of the TMA percentage. Right: Gain plotted against of TMA concentration at a fix pressure and amplification field. For each data set, an optimum for Penning effect can be clearly observed, as the range of TMA concentration in which maximum values of gain are obtained, that corresponds to range where minimum values of amplification field are applied.

For each pressure the gain rapidly rises when small quantities of TMA are added until values around 1.2% TMA. Further, a range where the gain remains roughly constant occurs between 1.2% and 1.8% TMA, except for 1 bar where the gain remains constant in a larger range ($\sim 0.9\%$ - 3.0%). Thereafter, the gain drops sharply. At low pressures (up to 1 bar), the rapid rise in gain at constant amplification field has also been observed using Xe+2, 3 dimethyl-2-butene as Penning admixture, showing similar dependencies with the additive at 1 bar [51]. This great increase is an evidence that Penning effect takes place.

On the other hand, for each pressure studied Fig. 4.8-left, shows the dependence of the amplification field calculated to obtain gains of 300 versus the TMA concentration. In all pressures, by increasing the TMA concentration, the field needed to obtain the same gain decreases until values down to 44, 75, 95, 109 kV/cm at 1 bar, 5 bar 8 bar and 10 bar, respectively. The minimum value is reached for TMA concentration around 1%.

4.3.2.1 Townsend Coefficient

First Townsend coefficient (α) allows to describes the electron multiplication processes in Micromegas readouts. Taking into account a semi-empirical parameterization of this coefficient [174],

$$\alpha = AP \exp(-B/S) \quad (4.2)$$

where S is the reduced amplification field ($S = E_{amp}/P$), P is the gas pressure, and A and B are constants that depend on the gas. The logarithm of the gain of a Micromegas is the integral of the Townsend coefficient along the field lines from the mesh to the anode. By assuming a constant field, in first order, the electron multiplication G can be written as [175]:

$$\ln\left(\frac{\ln(G)}{P}\right) = \ln(Ad) - \frac{B}{S} \quad (4.3)$$

where d is mesh-anode distance and A and B can be obtained from a linear fit of the $\ln(\ln(G))$ vs. S^{-1} data. The values of parameters A and B obtained by fitting each set of data to Eq. 4.3 are shown in Table 4.2.

According to this simplified physical picture [176, 177], A and B are related with microscopic parameters: A corresponds to the inverse of the collision mean free path at the reference pressure P_0 ($A = 1/(\lambda_0 P_0)$), and $B = V_i/(\lambda_0 P_0)$, where V_i is the effective energy to produce an electron-ion pair. Under the physical picture in [176], the mean energy of the electron swarm between two collisions is given by $\bar{\epsilon} = E\lambda = E\lambda_0 P_0/P$. The ratio $\bar{\epsilon}/V_i = E\lambda/V_i$ gives hence a figure on how likely ionization can be occurred. Naturally, for large λ/V_i , ionization will occur at lower fields. This implies that $B \times P = V_i/\lambda$ can be seen as a characteristic field at which the probability of ionization becomes important.

%TMA $\pm 10\%$ syst.	Best Ene. Res. (% FWHM)	Gain [$\times 10^2$]	A ($\text{cm}^{-1}\text{bar}^{-1}$)	B (kV/cm/bar)
Pressure 1 bar				
0.25 ± 0.01	8.4	1.5	6986 ± 284	108.9 ± 2.0
0.91 ± 0.03	7.4	5.2	5007 ± 251	66.7 ± 2.1
1.22 ± 0.22	7.3	8.6	4507 ± 96	61.1 ± 0.8
1.51 ± 0.05	7.3	9.3	5073 ± 167	66.3 ± 1.4
2.30 ± 0.06	7.5	9.0	5058 ± 172	66.1 ± 1.4
4.52 ± 0.11	7.3	8.2	4974 ± 153	65.7 ± 1.3
9.28 ± 0.23	7.3	5.8	6020 ± 672	80.8 ± 5.6
10.41 ± 0.24	7.3	5.5	5714 ± 304	81.7 ± 2.5
Pressure 5 bar				
0.25 ± 0.01	8.9	2.3	1665 ± 81	45.5 ± 1.0
0.45 ± 0.01	8.6	4.1	988 ± 16	27.9 ± 0.3
0.66 ± 0.02	8.4	7.3	1182 ± 46	27.6 ± 0.6
0.86 ± 0.02	8.3	8.1	1144 ± 46	25.8 ± 0.6
1.24 ± 0.03	8.4	6.5	1228 ± 35	25.2 ± 0.4
1.61 ± 0.05	8.5	6.4	1492 ± 23	28.1 ± 0.2
2.05 ± 0.05	8.9	8.8	1772 ± 39	30.7 ± 0.3
2.50 ± 0.06	9.0	7.4	2008 ± 38	33.1 ± 0.3
2.86 ± 0.07	9.0	7.8	2246 ± 43	35.3 ± 0.3
3.83 ± 0.09	9.6	7.9	2783 ± 15	40.6 ± 0.1
Pressure 8 bar				
0.20 ± 0.02	27.3	0.2	708 ± 79	33.3 ± 1.7
0.76 ± 0.02	9.1	3.0	809 ± 58	22.7 ± 0.8
1.17 ± 0.03	9.0	3.6	1162 ± 99	25.3 ± 1.0
1.43 ± 0.04	9.4	5.4	1379 ± 42	27.0 ± 0.3
2.04 ± 0.06	9.8	4.5	1696 ± 41	29.6 ± 0.3
2.34 ± 0.06	10.4	3.0	2224 ± 90	33.6 ± 0.5
2.71 ± 0.07	11.4	1.7	2519 ± 59	35.7 ± 0.3
3.27 ± 0.08	12.0	1.3	3399 ± 222	40.2 ± 0.8
Pressure 10 bar				
0.41 ± 0.01	19.7	0.6	330 ± 25	15.9 ± 0.8
0.68 ± 0.04	9.6	1.8	772 ± 43	22.4 ± 0.6
1.02 ± 0.04	10.2	2.3	997 ± 45	24.3 ± 0.5
1.08 ± 0.03	10.2	4.6	1072 ± 13	24.7 ± 0.1
1.17 ± 0.19	10.1	2.0	1141 ± 54	25.0 ± 0.5
1.71 ± 0.04	10.4	4.2	1423 ± 29	27.6 ± 0.2
3.79 ± 0.09	47.0	0.4	4644 ± 1033	46.6 ± 4.7

Table 4.2: Values of the best energy resolution obtained at each TMA concentration for pressures of 1 bar, 5 bar, 8 bar and 10 bar, and the corresponding value of gain at which it was measured. The systematic error of energy resolution for all values is estimated to be less than 0.2% FWHM. In addition, in the last two columns the values of the parameters A and B are presented; these values were obtained by fitting the gain curves (properly transformed to the $\ln(\ln(G))$ vs. S_1 representation) to Eq. 4.3.

Hence, from results in Table 4.2 the following interpretation can be made:

- For small TMA concentrations B starts from a given value, asymptotically approaching the one in pure Xenon.
- As TMA increases, Penning transfers become active, allowing ionization takes place at lower fields. This process is mediated by excited atomic and molecular states; molecular states, require considerable less energy for being ionized than the parent gas, therefore B is reduced. The measurable consequence of this fact is that the gain increases with TMA concentration by factors up to $\times 16$ (50) at 1 (10 bar), with the electric field remaining unchanged.
- When TMA further increases, B becomes larger, probably caused by the TMA molecule cooling down the electron swarm. Thus larger fields are required to achieve identical gains.

As a conclusion a narrow operating range exists in Xe+TMA mixtures, where TMA is clearly advantageous over pure Xe for this kind of amplification structures. This happens within a TMA concentration range of $\sim 0.9\%$ - 4.5% and $\sim 0.9\%$ - 1.5% at 1 and from 5 to 10 bar, respectively. It has been known that quenched gases show a significantly reduced diffusion, improving the pattern recognition of pixelized readouts; this aspect is well studied in [178, 179].

4.3.2.2 Energy resolution

The energy resolution for 22.1 keV X-rays was determined through Eq. 2.2, using the width and the peak position of the peak at 22.1 keV taken from the results of applying the 3-step fit for each energy spectrum (see sec. ??). The energy resolution against the gain for different TMA mixtures is plotted in Fig. 4.9, for pressures: 1 bar (a), 5 bar (b), 8 bar (c) and 10 bar (d). For each mixture, the energy resolution improves as gain increases. The worse values of energy resolution at low gains are due the poor signal-to-noise ratio. To evaluate the electronic noise contribution at FWHM, a square pulse was injected at the preamplifier input by an AC-coupling between them; subtracting it in quadrature it was found that the energy resolution at low gains has compatible values with the ones for gains larger than 300. The noise contribution for gains above 300 was also measured, obtaining values lower than 1%. All values of resolution presented include the noise contribution.

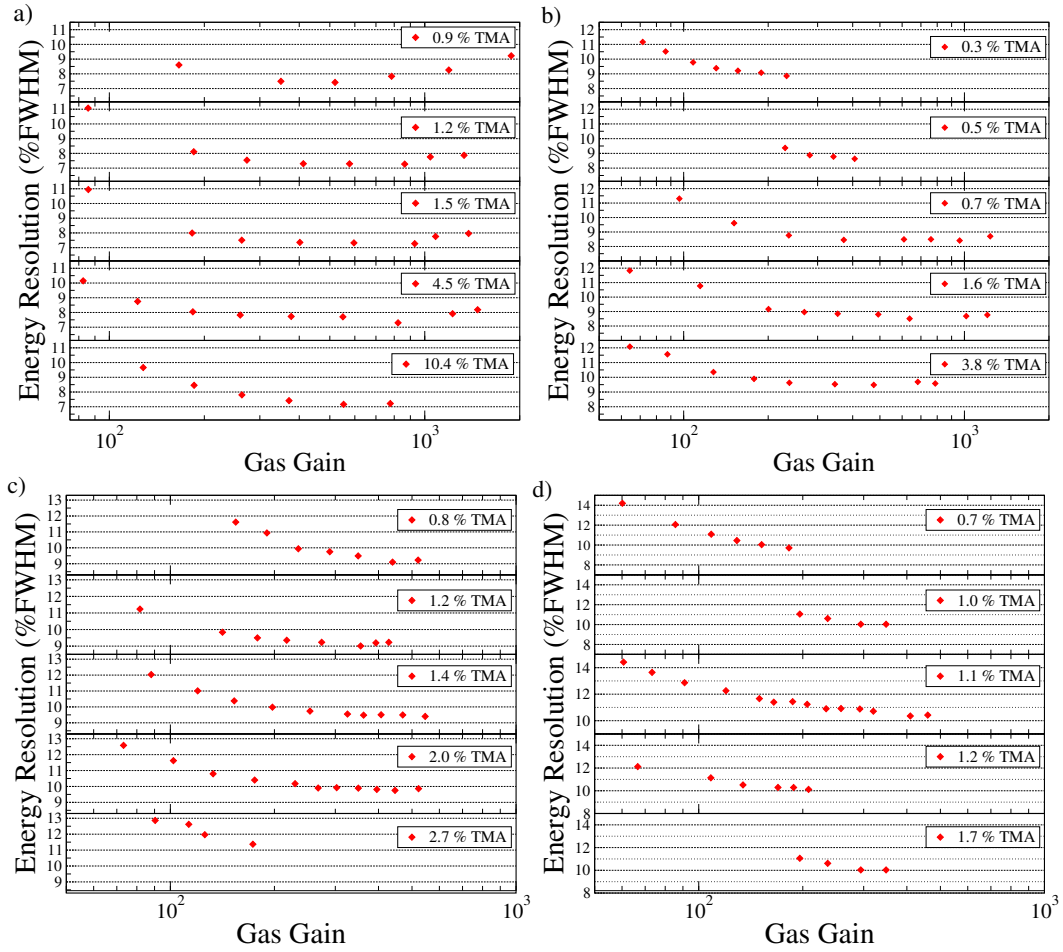


Fig. 4.9: Energy resolution at 22.1 keV as a function of gain for different TMA concentrations at 1 bar (a), 5 bar (b), 8 bar (c) and 10 bar (d). The TMA concentration for each data set is indicated.

For mixtures at which it was possible to get gains larger than 800, the energy resolution deteriorates after having achieved its minimum value, as is shown in Fig. 4.9. This occurs for mixtures within the optimal range for Penning transfer (0.9%-2%). Degradation at greater gains could be explained by secondary avalanches induced by UV photons or space charge effects; the worsening in energy resolution caused by these effects it is well known. Moreover, it is seen an over exponential behaviour of gain curves at 1 bar (see Fig.4.7a), for mixtures between 0.9% and 4.5% TMA, which is an evidence that secondary avalanches could be the most important effect. In addition, gains achieved are significantly lower than values reached in previous works in Ar+2% C_4H_{10} where the feedback effect has been clearly seen. The reason why this degradation is not observed at high pressures (8 bar and 10 bar), is that sparks did not allowed to reach higher gains. The same trend would be expected in case of having a good Micromegas that allows to apply higher amplification fields.

The best energy resolution values obtained for each mixture are listed in Ta-

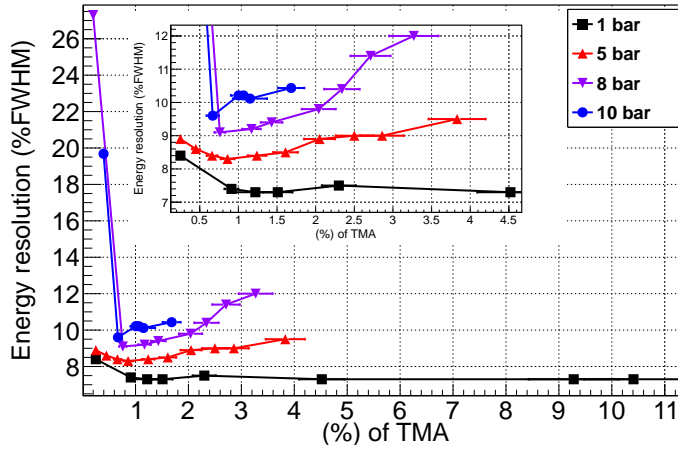


Fig. 4.10: Best energy resolution for each mixture against the TMA concentration at different pressures. For each pressure, an optimum region of TMA is observed where the best energy resolutions are achieved.

ble 4.2, together with the gain at which they were measured, and in Fig. 4.10 all values are plotted. At each pressure, the energy resolution improves adding TMA, reaching minimum values between 1% and 2% TMA and deteriorating at higher concentrations. For instance, at 1 bar, the energy resolution goes from a value of 8.4% (0.3 % TMA) to 7.4% FWHM (0.9% TMA); then it takes a stable value of 7.3%(FWHM), between 1.2% and 10.4% TMA. However, for 2.3% TMA mixture the value is slightly higher because the radioactive source was uncollimated. All the best energy resolutions are reached for gains above 500. These values are consistent with measurements performed on a cylindrical proportional counter using 95% Xe + 5% TMA at 1 bar [50].

It must be noted that energy resolution presents more variations within optimum range as pressure increases. In particular this fact is more marked at 10 bar, where the energy resolution is more sensitive to small changes in oxygen because attachment is stronger at high pressures. This is likely the reason why larger variations in energy resolution are observed for mixtures between 0.7% and 1.0% TMA. The level of oxygen measured with the mass spectrometer for 0.7% TMA mixture confirms this fact, being much less than for higher concentrations.

On the other hand, it could be seen that the energy resolution increases with pressure; the best values of energy resolution are 7.3%, 8.3%, 9.0 % and 9.6% FWHM for 1 bar, 5 bar, 8 bar and 10 bar, respectively. The energy resolution dependence on pressure will be discussed in detail the next section.

4.3.3 Variation with Pressure

In this section, results of gain and energy resolution are presented for pressure values from 1 bar to 10 bar, using TMA concentrations between 0.9 % and 1.2%.

This range was established as the optimum in terms of gain and energy resolution (see section 4.3.1). The values of TMA used for each pressure are specified in Table 4.3.

Pressure (bar)	TMA (%)	Pressure (bar)	TMA (%) $\pm 10_{stat}$
1	1.22 ± 0.22	6	1.24 ± 0.03
2	1.01 ± 0.03	7	1.26 ± 0.03
3	0.92 ± 0.02	8	1.17 ± 0.03
4	0.99 ± 0.02	9	1.17 ± 0.03
5	1.24 ± 0.03	10	1.71 ± 0.03

Table 4.3: Values of TMA concentration used for each pressure to study the gain and energy resolution. The TMA concentrations are within the range that was established as optimum for Penning transfer (see section 4.3.1). For each TMA concentration measured was estimated a 10% of systematic error, and a statistic error that does not exceed 2% for all cases.

The gain curves are shown in Fig. 4.11 (top). It is seen that the amplification field necessary to reach any given gain, increases with pressure, as already observed in pure Xe [38, 176]. The slope of gain curves decreases with pressure, which means that: at high pressures for a given change in the amplification field, the absolute change in gain is lower, in agreement with what has been observed in pure Xe and Xe+methane mixtures [176]. On the other hand, the maximum gain drops nearly exponentially with pressure for pressures above 2 bar; a value down to ~ 400 was obtained at 10 bar. However, the maximum gain at any pressure is still at least a factor 3 higher than for Micromegas operated in pure Xe [38]. This behaviour is probably caused by photons in the avalanche generated from molecular Xe excitations [176].

Energy resolution (Fig. 4.11 (bottom)) shows a rapid improvement with the amplification field, reaching a minimum value and then degrading at high fields. As mentioned before, the poor signal-to-noise ratio at low fields explains the high values, while the degradation at high fields is presumably caused by secondary avalanches or space charge processes.

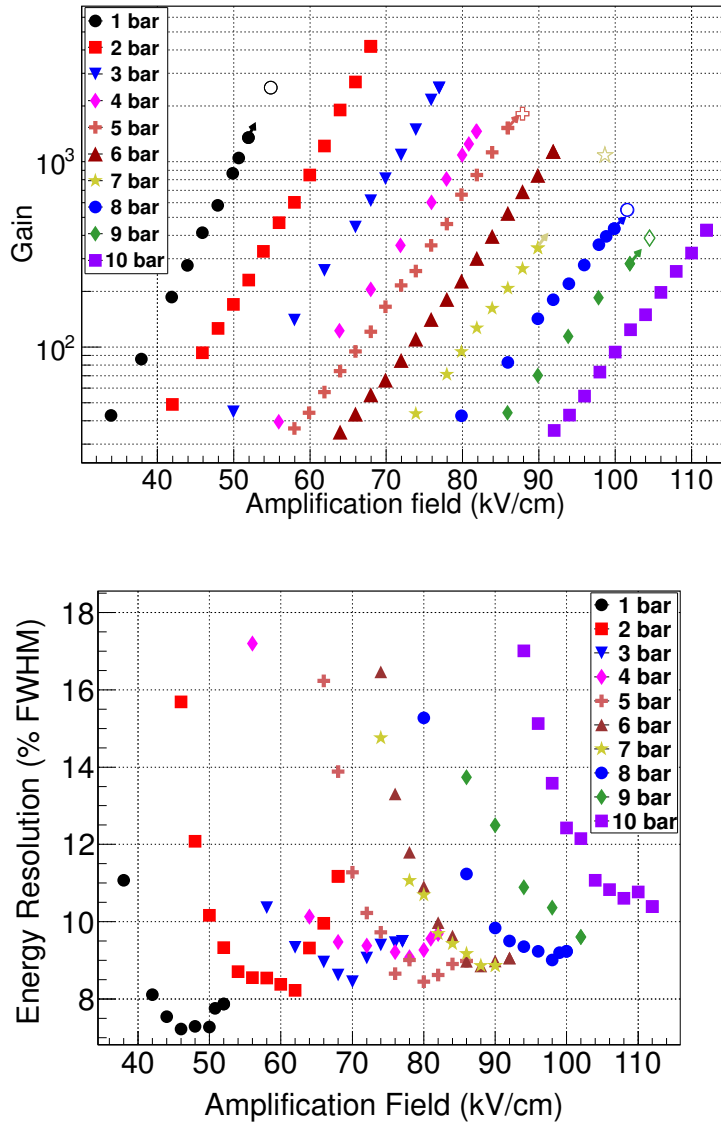


Fig. 4.11: Dependence of gain (top) and the energy resolution at 22.1 keV (bottom) on the amplification field for a pressures ranging from 1 bar to 10 bar, at optimal TMA concentrations within the range 0.9%-1.2%. Empty markers in gain curves represents the maximum gain reached for each pressure, in cases where higher gains were obtained using a slightly different gas mixture around the optimum.

The best energy resolution measured at each pressure, selected for gains within the range from 300 to 800 is shown in Fig. 4.12(■). A slight degradation with pressure is observed, likely caused by electronegative impurities or inherent physical mechanisms [176]. Moreover, the deterioration of energy resolution with pressure has a trend compatible with measurements performed by H. Sakurai et al [176], where the estimated level of impurities was very low, below than 3 ppm. This allows to conclude that a mechanism inherent to the avalanche process in HP Xe+TMA

mixtures is responsible for the observed degradation. As it has been noted, at higher pressure the reduced amplification field is weaker, a fact resulting in the increase of the number of excitations as compared to ionizations; hence it is expected to have more avalanche fluctuations and the subsequent degradation in the energy resolution [176, 177].

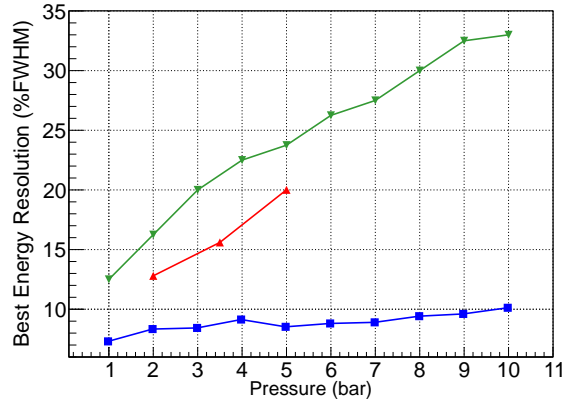


Fig. 4.12: Dependence of the best energy resolution at 22.1 keV on pressure, for data from [38] (▼), and data at 59.54 keV in section 2.3 extrapolated to 22.1 keV (▲) in pure Xe, as well as in this work (■) for Xe+TMA mixtures.

Results of this work are compared in Fig. 4.12 with previous measurements using Micromegas detectors in pure Xe: with the same setup used in this study, but at an energy of 59.54 keV and extrapolated to 22.1 keV (▲) (see section 2.3) [180] and with a different one (▼) [38]. The energy resolution achieved at 22.1 keV is substantially better in this work, going down to 7.3% (9.7%) FWHM at 1 (10) bar. This fact translates into an improvement of a factor 2 (3) at 1 (10) bar as compared to previous measurements in pure Xe. Therefore, it is evident that the addition of TMA to Xe reduces the avalanche fluctuations; this is likely due to transfer reactions from the Xe excited states to TMA molecules (Penning effect).

Figure 4.13 shows the value of $(\ln(\ln(G)/P))$ against (S^{-1}) , for all pressures measured. Under the assumptions implicit in the model of equations 4.2 and 4.3 it is expected that all data points follow the same straight line. However, deviations from the model expectation are observed for pressures below 5 bar, something that is more clearly observed in Fig. 4.14, where the parameters A (left) and the ratio B/A (right) are plotted as a function of pressure.

Both A and B were determined from linear fits of the curves showed in Fig. 4.13. As seen, A drops with increasing pressure up to 5 bar, remaining at a relatively constant value for higher pressures, while B/A increases with pressure, but at a slower rate from 5 bar on. In contrast, measurements performed in cylindrical proportional detectors in the same pressure range, both in pure Xe and in Xe-methane mixtures [176], as well as measurements performed with Micromegas up to 2.5 bar in Xe-methane [175] have shown that the parameters A and B are independent of the pressure, and thus the model of equations 4.2 and 4.3 represents a good de-

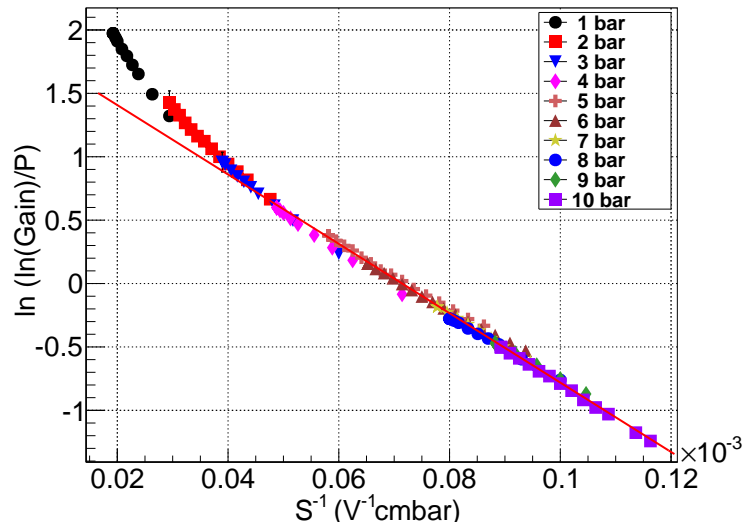


Fig. 4.13: Natural logarithm of the reduced gain as a function of the inverse of the reduced amplification field. The red line is a linear fit made for all data with pressure above 5 bar. This representation emphasizes the deviations from the expected behaviour for data below this pressure.

scription of those mixtures. The departure of data from the expected model trends may be caused by the presence of Penning effect. This fact needs further study, in particular using detailed Monte Carlo simulation of the avalanche microphysics it could be confirmed.

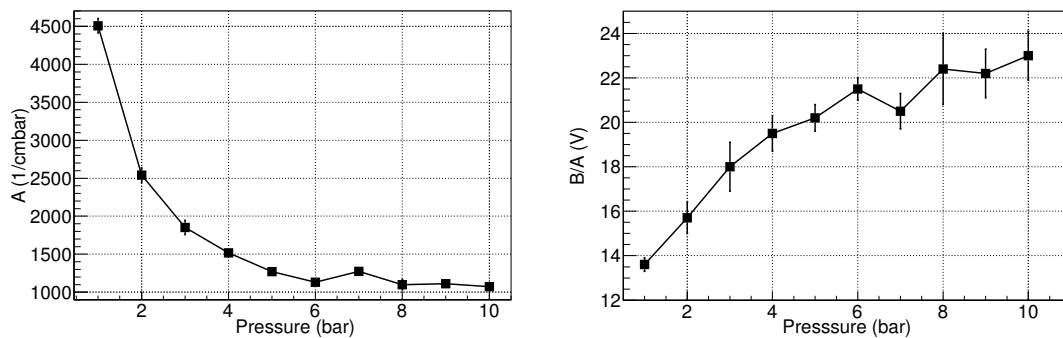


Fig. 4.14: Parameter A (left) and the ratio of B to A (right) as a function of pressure. Parameters have been obtained from gain curves at each pressure fitted to Eq. 4.3, considering a semi-empirical formula of the first Townsend coefficient.

4.3.4 Drift velocity

The small-TPC setup was modified by F. J. Iguaz to measure drift velocity and attachment in Xe+TMA mixtures. A schematic view of the setup used for these measurements is shown in Fig. 4.15. A silicon photo-diode detector together with an ^{241}Am source were encapsulated into a plastic piece made of POM (polioxymethylene) with low outgassing, and then installed inside the NEXT-0-TPC. The ^{241}Am source emits in coincidence an α -particle and a γ -ray which are detected by the silicon diode and the Micromegas readout, respectively. Both signals are pre-amplified and registered by a Tektronix oscilloscope, allowing to select the coincidences.

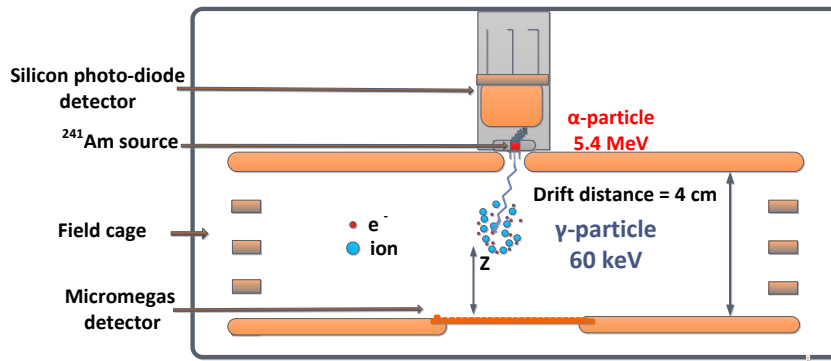


Fig. 4.15: Modified setup for measuring the drift velocity and attachment in Xe+TMA mixtures (Setup commissioned by F.J. Iguaz). The system is formed by a microbulk Micromegas readout and a silicon detector that allow the measurement of the coincidence of an α -particle and γ -ray, emitted by an ^{241}Am source.

With this configuration a coincidence system is obtained which provides the t_0 for each event, hence the drift time and the drift velocity can be obtained. The drift time of each event is calculated from the temporal difference between the α and γ signals. The drift velocity is then obtained from the overall range of drift times (ΔT), that spans the full drift region, and the (fixed) drift distance (Δx) as $v_e = \Delta x / \Delta T$. In this way, the drift velocity was determined for various Xe+TMA mixtures and pressures. Preliminary measurements are illustrated in Fig. 4.16 (no error bars are included yet) are compared with the Magboltz calculations [28]. The drift velocity for Xe+2.2%TMA mixture is larger than for pure Xe from 100 V/cm/bar, reaching to be one order of magnitude at 100 V/cm/bar. Measurements are in good agreement with Magboltz calculations.

4.4 Towards Fano factor measurement in NEXT-0-MM

The measurement of Fano factor in Xe+TMA mixture is very important, since it gives the intrinsic energy resolution. Since this mixture is a Penning mixture, the Fano factor should be lower than the value for pure Xe. With this aim an experiment with an InGrid readout in Xe+TMA mixtures was carried by the Zaragoza group

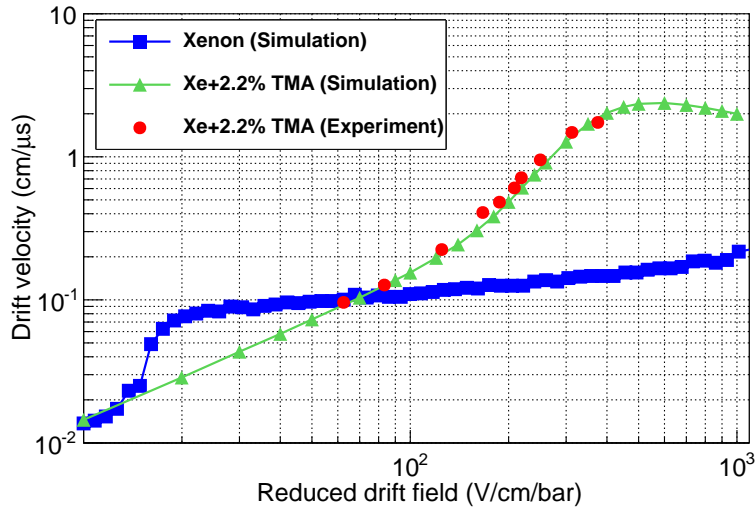


Fig. 4.16: Drift velocity measurements together with calculations with Magboltz-10 as a function of E_d/P in a Xe+2.2%TMA mixture. The measurements were performed with a system formed by Micromegas and a silicon readout that allows the measurement of the coincidence of an α -particle and γ -ray, emitted by an ^{241}Am source. In addition, calculated drift velocities with Magboltz-10 in pure Xe are included.

and collaborators of the Bonn University, which is detailed in Appendix B.

The measurement of Fano factor and the mean energy per ion pair W in $\text{Ar}+i\text{C}_4\text{H}_{10}$ using InGrids readouts was demonstrated in [19]. The Fano factor measurement consists in the direct counting of the primary electrons produced by the absorption of a given energy in the gas. The Fano factor is determined through the measurement of the single electron spectrum and its related dispersion, The major requirement is obtaining a multiplicity equal to one, which is difficult, mainly because the multiplicity increases with the gain due to the amorphous (SiProt) silicon layer [19]. In addition, a large diffusion gas media and a low number of primary electrons are necessary to decrease the probability of having larger multiplicities. On base of these aspects and the preliminary results presented in Appendix B, the following requirements should be taken in consideration in a future experiment:

1. A larger diffusion in Xe+TMA mixtures would be necessary to increase the diffusion, less than 1% are recommended, thus the diffusion can be reduced by a factor $\times 1.5$.

On the other hand, the drift distance should be increased as much as possible; taking into account the dimensions of the NEXT-0-MM TPC, it is considered that drift distance of 6 cm can be implemented.

2. A radioactive source with low energy should be used, and with higher activity than the used for the first tests; a ^{55}Fe source would be ideal.
3. An InGrid readout with a lower threshold would be necessary, reducing the

4.5. Comparison between Ingrid and microbulk Micromegas readouts 15

probability of obtaining multiplicities larger than 1.

4.5 Comparison between Ingrid and microbulk Micromegas readouts

Measurements of gain and energy resolutions with InGrid readout presented in Appendix B are compared to measurements with microbulk Micromegas (showed in the first part of this chapter) in similar conditions TMA concentrations in Fig. 4.17. Gain curves of InGrid are a factor 4 above than those the Micromegas, being the maximum gains achieved 7500 for InGrid and 1500 for microbulk.

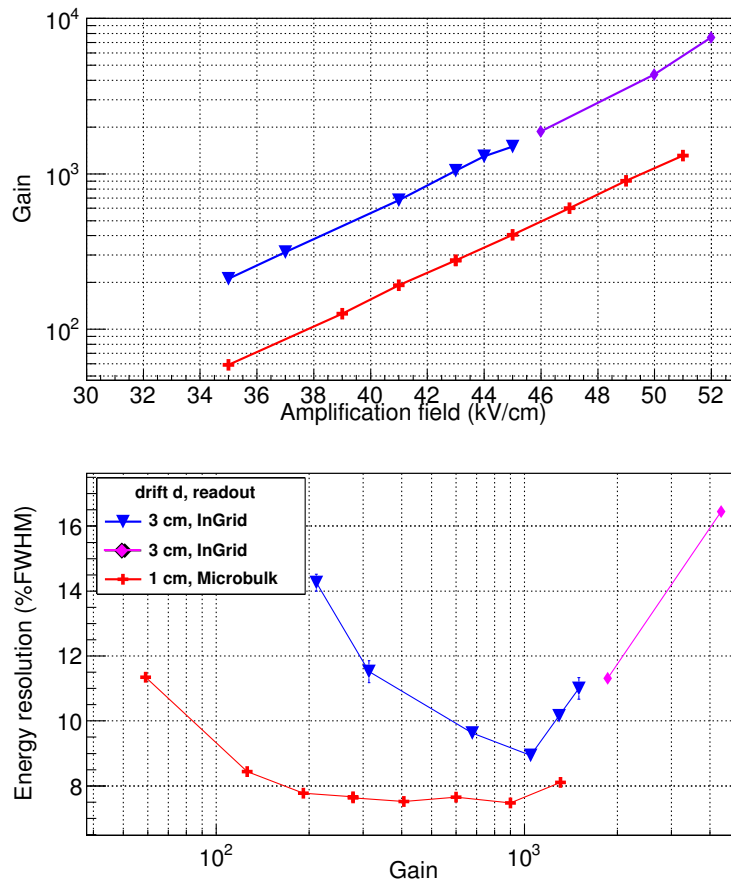


Fig. 4.17: Dependence of the gain on the amplification field (top) and energy resolution at 22.1 keV %FWHM as function of gain (bottom) for a Xe+2.8%TMA mixture, from the grid signal of an InGrid and the mesh signal of a microbulk Micromegas readouts. The drift distance used for each experiment is indicated in the legend.

On the other hand, the best energy resolution for Micromegas is slightly better than for the grid signal of InGrid, a value above 8% FWHM (InGrid) against 7% FWHM (microbulk). It is noticeable that the signal-to-noise ratio for InGrid read-

outs is much higher than for Micromegas, which is observed by the fact that energy resolution reaches stable value rapidly for Micromegas, while the improvement for InGrid is slower. The energy resolution get worse with gain for both readouts, however it seems that for InGrid the degradation is more rapid. This result may be due to the fact that feedback for InGrid is higher than for microbulk.

4.6 Conclusions

The operation of microbulk Micromegas detectors in high pressure Xe+TMA Penning gas mixtures was performed, obtaining very good performance in terms of gain and energy resolution. Systematic measurements of gain and energy resolution have been presented for a variety of TMA concentrations ranging from 0.2% to 10.41% and for gas pressures from 1 to 10 bar. An optimum range for TMA concentration between 0.9% and 1.7% was found, in which the Penning effect is maximum, requiring amplification fields at least 40% lower than for pure Xe for the same gain; similarly, gains up to a factor ~ 100 higher have been obtained for the same amplification field. On the other hand, maximum workable gains are superior by a factor at least $\times 3$ with respect to pure Xe, reaching in particular gains above 400 at 10 bar.

For appropriate TMA fractions, energy resolutions down to 7.3% (9.6%) FWHM at 1 (10) bar for the 22.1 keV ^{109}Cd peak have been achieved. This implies an improvement of about a factor 2 (3) with respect to values obtained by microbulks in pure Xe [38]. This result extrapolates into an energy resolution of 0.7% (0.9%) FWHM at the $Q_{\beta\beta}$ value of Xe for 1 (10) bar, and therefore opens very good prospects for double-beta decay experiments.

In addition, a modification of the setup was performed to measure the drift velocity and attachment. First measurements of the drift velocity in Xe+TMA mixtures have been made and show good agreement with Magboltz calculations.

In general, the performance of a TPC detector based on Xe+TMA admixtures is comparable to optimum values typically obtained with benchmark Micromegas mixtures (e.g. optimized Ar-isobutane mixtures). This result proves that Xe+TMA may be a mixture of choice in applications envisaging the use of Xe as conversion gas, especially at high pressures.

Study of Recombination in Xe+TMA Mixtures

Contents

5.1	Recombination Theory	118
5.2	Experimental Setup and Procedure	120
5.2.1	Overview	120
5.2.2	Drift field cage	120
5.2.3	Micromegas readouts	122
5.2.4	Gas mixture	122
5.2.5	Data acquisition	123
5.2.6	Measurements	124
5.3	Analysis and Results for the Coincidence Mode	125
5.3.1	Electron lifetime	127
5.4	Analysis for the Independent Mode	128
5.4.1	^{241}Am γ energy spectrum in Xe+TMA mixtures	128
5.4.2	PSA for α signals: charge and track angle	129
5.4.3	Ion mobility	135
5.5	Electronic Properties	136
5.5.1	Drift Velocity and Longitudinal Diffusion Coefficient	136
5.5.2	Gain for α -particles and γ -rays	137
5.6	Recombination Dependence on Drift Field	138
5.7	Columnar Recombination of Charge Collected from α-particles	139
5.7.1	Charge vs. $\cos\varphi$	139
5.7.2	Figure of merit: Q_0/Q_{90}	140
5.7.3	Discussion	144
5.8	Conclusions and Outlook	145

As explained in Sec. 1.4.3 the Earth's rotational motion with respect to the galactic rest frame yields variations in the mean direction of incidence of WIMPs at the Earth's surface, that in the laboratory frame translate to a day-night modulation of the nuclear recoil direction. This signal is more robust than the annual

modulation, since there is not known background that can mask it. A new concept based on columnar recombination in a HPXe TPC could provide the direction of the nuclear recoil on an event-by-event analysis, relying on the dependence of charge collection on the track angle prior to drifting the track ionization produced by WIMP interaction [6, 7]. In particular, the addition of Penning molecular additives (e.g. TMA) may improve the directional sensitivity because excitations of Xe translate to ionizations of TMA [102], and the diffusion is reduced.

In this chapter, a systematic study of recombination for charge collected from α -particles and γ -rays on pressure and drift field is carried out, focusing on the dependence of the recombination on the track angle for α -particles. A description of theoretical models of recombination is given in Sec. 5.1, followed by the experimental setup and procedure presented in Sec. 5.2, then by the data analysis in Secs. 5.3 and 5.4. The measurement of electronic properties: drift velocity, longitudinal diffusion coefficient, and gain for α -particles and γ -rays are shown in Sec. 5.5. The study of recombination is given in Secs. 5.6 and 5.7. Finally, in Sec. 5.8 the conclusions and outlook are drawn.

5.1 Recombination Theory

The recombination can be separated in two contributions: the initial and the columnar. The initial refers to the recombination with the parent ion by the effect of the Coulomb field, Onsager proposed the first theory for initial recombination in 1938 [181]. On the other hand, the columnar recombination involves all ions generated by the ionizing particles [182], Jaffé was the first in developing a theory for columnar recombination in 1913 [183].

Theory of initial recombination reduces to a problem of Brownian motion of one particle under the action of an electric field together with the Coulomb field [181]. The two primary assumptions of this theory are: i) the ion and electron are spatially separated, and ii) the ions and electrons interact by an infinite range Coulomb force. The theory predicts that the electron has a finite probability of being captured back by the ion Coulomb field, probability that reduces when an external field is applied. A simple expression for the recombination for relatively low electric fields is [184]:

$$\frac{Q}{Q_0} = e^{-r_{KT}/r_0} \left(1 + \frac{E}{E_{KT}} \right) \quad (5.1)$$

where $r_{KT} = e^2/\varepsilon kT$ is the Onsager length, that is the radius at which the electron thermal energy equals the Coulomb potential energy, and E_{KT} is such that satisfies $eE_{KT}r_{KT} = kTE_{KT}$ which is also the limit of application of the Eq. 5.1. The parameter r_0 is the average electron-ion distance at the end of thermalization process, this parameter is frequently fitted as a free parameter and ε the dielectric constant of the gas. As in Onsager's theory is assumed a single electron-ion pair, the dependence on the ionization density is not accounted [184].

The Jaffé theory adopts a different approach. This theory considers that the initial ionization is distributed in a column around the trajectory of the track from

ionizing particle. Jaffé carried out an approximate computation of all the ions in the track left by an ionizing particle. He assumed that the electric field separates the intensely ionized column into two parts, one of positive and the other of negative ions. The columns broaden by effect of diffusion during separation and wherever they may overlap, hence there is a probability of recombination given by the recombination coefficient [182, 185]. The theory parts from the following diffusion equations proposed by Jaffé:

$$\begin{aligned}\frac{\partial N_+}{\partial t} &= -u_+ E \cdot \nabla N_+ + d_+ \nabla^2 N_+ - \alpha N_+ N_- \\ \frac{\partial N_-}{\partial t} &= -u_- E \cdot \nabla N_- + d_- \nabla^2 N_- - \alpha N_+ N_-\end{aligned}$$

where N_{\pm} are the ion and electron charge distributions, u_{\pm} are the mobilities, d_{\pm} , and α are the coefficients related to the diffusion and recombination, respectively, and E is the external electric field. In particular, Jaffé solved this model, including the recombination term as a perturbation, considering as boundary condition that the initial distribution is a column of charge around the primary track. It must be noted that the Jaffé assumptions are related to the gas phase.

The columnar recombination leads to a nonlinear system of differential equations, and the solutions give the ratio of ions collected to those formed. The Jaffé solution includes a formula for parallel tracks, an another for tracks with $\varphi \gg 0$. A simplified formula could be written as [184]:

$$\frac{Q}{Q_0} = \frac{1}{1 + q_0 F(E \sin \varphi)} \quad (5.2)$$

where q_0 is the initial density of electron-ion pairs, F is a function that depends on the diffusion and mobility coefficients, and φ is the angle between the track and the electric field. Most of the recent works have shown that the predicted dependence of charge collected on the track angle by the Jaffé model is stronger than the observed experimentally. In 1952 Kramers [186] gave a modified version of the columnar theory. The theory considers that under the application of an electric field, the diffusion term is smaller than the drift or recombination terms; this implies that a perturbative solution is not possible. In this way, the equations were solved ignoring the diffusion terms, and including the columnar boundary conditions as well as assuming that electron and ion mobilities are equal. In addition the diffusion was added later as a perturbation term [187, 186].

More recently, the initial electron-ion recombination was studied for liquid argon and liquid xenon [187] by J. Thomas and D. Imel in 1987, and where a more accurate model based on a single-parameter model was developed, the so-called Box model, in which assumptions related to liquid phase are performed. As a result it was observed good agreement between the measured electric field dependence on the electron-ion recombination and the model. They assert that the second assumption performed by Onsager is not valid, because Onsager's theory neglects the effects

of high coefficient of polarization on the effective charge of an ion. Consequently the effective charge of an ion reduces within a few atomic spacings. In Box model -developed for liquid Ar and Xe- the diffusion is considered very small, the box model starts from the diffusion equations proposed by Jaff e, thus diffusion terms in Eq. 5.2 are dropped and the positive ion mobility set to zero. This assumption simplifies the problem allowing to obtain a model depending on a unique parameter

$$\frac{Q}{Q_0} = \frac{1}{\xi} \ln(1 + \xi), \quad \xi = \alpha_{Box} \frac{N_0}{4a^2 u E} \quad (5.3)$$

where Q/Q_0 is the fraction of charge collected, and ξ is the parameter of the model. The quantity $N_0/(4a^2)$ represents the charge density in a microscopic box of size a , E the electric field and μ the movility, and α_{Box} the recombination factor. This model has been used successfully to model data for liquid Ar and Xe [187, 184].

It must be noted that up to now, the most appropriated theory for gas phase is the Jaff e theory, however, for a correct interpretation of experimental data within the Jaff e model, the complete solutions should be used.

5.2 Experimental Setup and Procedure

5.2.1 Overview

The goal of these measurements is to study the electron-ion recombination of α -particles and γ -rays, in Xe+TMA mixtures using a HP TPC. For this purpose, a modification of the experimental setup described in chapters 2 and 4 was performed, in order to measure the coincidence of an α -particle and a γ -ray emitted by an ^{241}Am radioactive source. The main change applied was the modification of the drift field cage. The experimental procedure to work with Xe+TMA mixtures follows the one explained in chapter 3; however, minor changes were introduced on the bases of the experience gained in previous measurements. Summarizing, the 2.41 TPC, NEXT-0-MM, was connected to a high purity gas system. The gas system enabled operation with very low levels of outgassing, down to 10^5 mbar l/s, recirculation of the gas at high pressure to filter out impurities, and gas recovery and storage by means of cryopumping. Below the new drift field cage configuration is described in detail, and the setup together with the experimental procedure are drawn.

5.2.2 Drift field cage

The drift field cage consists of two symmetric drift regions of 3 cm, formed by three circular copper plates together with a field cage defined by five copper rings and six $33\text{ M}\Omega$ resistors. The entire structure is supported by means of three PEEK pillars. The drift field cage is shown in Fig. 5.1.

The middle plate constitutes the cathode for the α and γ drift regions, being applied a negative HV to it. A specific cable able of withstanding voltages up to 10 kV is used. This plate was thinned by 1 mm over a 2 cm diameter circle, in order

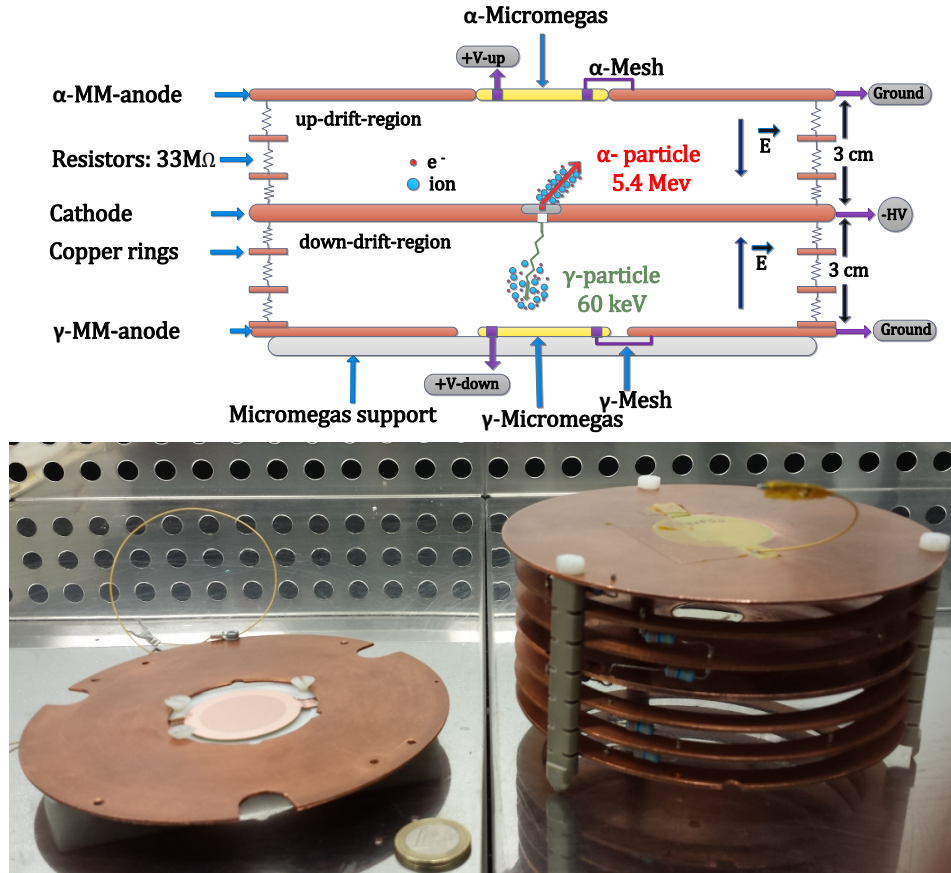


Fig. 5.1: Schematic representation of the drift field cage used to measure the coincidence of α -particles and γ -rays emitted by an ^{241}Am source, the microbulk-Micromegas and the voltage configuration (top). A picture of the drift structure is also shown (bottom); the bottom copper plate is at the left side of the picture, and the rest of the structure at the right side.

to gently place the ^{241}Am source, so as to form a coplanar surface. The advantage of this configuration is that the angular distribution of α tracks is covered completely; this is a very important aspect, considering that one of the objectives of this work is the study of the electron-ion recombination dependence on the track angle of the α -particles. In addition, a centered through-hole of 2 mm in diameter was drilled, allowing the coincidence 59.5 keV γ -rays from the Np daughter to reach the down drift region (γ drift region).

The top and the bottom copper plates are the corresponding anodes for the α and γ drift regions. In each plate a microbulk Micromegas readout of 35 mm in diameter is housed. For the top copper plate, the geometry form of the Micromegas was drilled; and for the bottom one, a circular hole with a larger diameter than that of the Micromegas was made (see Fig. 5.1). The fact that γ -Micromegas anode surfaces are non-contiguous, may produce drift field inhomogeneities; on the contrary for α drift region, the mesh together with the anode form a coplanar contiguous surface.

However, these inhomogeneities can be considered negligible, because measurements of electron transmission of several Micromegas readouts with this configuration did not show evidences of strong border effects.

For the voltage configuration, the mesh of each Micromegas is connected to the corresponding anode (top and bottom copper plates), which in turn is grounded to the vessel, and the back-electrode of each Micromegas is fed to a positive HV to allow the amplification. In this way, the interaction of the α -particles is produced in the up drift region, and in the down drift region for the γ -rays. The electrons from each interaction are drifted to the corresponding Micromegas, in the gap the amplification takes place; finally the charge on the back-electrode is read out by means of an appropriate preamplifier.

5.2.3 Micromegas readouts

The microbulk-Micromegas used in these measurements were built by CERN, two batches of 10 readouts each one and with different geometrical parameters were characterized in Ar+2%C₄H₁₀ at 1 bar; description of these measurements can be found in Appendix C. The study showed that the readouts with 50-90-40 μ m, corresponding to gap-pitch-hole diameter, had better energy resolution; thus the measurements were performed with Micromegas of this batch. Maximum gains above 10^4 and energy resolution below 7%(FWHM) at 22.1 keV were obtained, moreover, all readouts of the batch showed at same conditions similar energy resolutions and gains. This fact is very important, because it allows to do direct comparison between the recombination of charge collected from α -particles and γ -rays.

5.2.4 Gas mixture

The experimental procedure followed to obtain the appropriate conditions of the gas mixture for data acquisition is similar to the one carried out for measurements presented in chapter 4. However, some changes were introduced, on the basis of experience previously acquired. Initially, it was planned to work with a 98%Xe+2%TMA mixture, because this mixture implies a TMA concentration near to the that optimizes for Penning transfer [103]. However, given that the TMA vapor pressure is strongly dependent on temperature at ambient conditions (boiling point $\sim 3-7^\circ$) the chamber refilling from recovery bottle showed some variability. For some of the measurements, this resulted in working TMA concentrations of 1.2% and 1.5%TMA. A systematic concentration scan is currently envisaged. It should be noted that once the mixture is formed, the TMA concentration can be known with a high accuracy, by measuring at the end of each data acquisition with an Omnistar mass spectrometer previously calibrated, following the procedure explained in chapter 3. The procedure carried out before starting the data acquisition is accounted below:

1. The pumping process was started together with a bake-out. In cases where the chamber had been opened to apply necessary changes inside -without

open the chamber, the bake-out was extended to 2 h. Otherwise, when the gas had been recovered completely after a data acquisition, the bake-out was performed for about 1 h.

The pumping process was stopped when the values of vacuum and outgassing were below 5×10^{-6} mb and 5×10^{-5} mb/l/s, respectively.

2. The gas was introduced from the sample bottle through bypass valve, filling the chamber until the desired pressure was reached; values of pressure between 3 and 8 bar were set. Afterwards, the recirculation process through the SAES filter was started, most of the times, the night previous to the data acquisition or a couple of hours before. This allows a complete homogenization of the mixture.
3. Just before to the data acquisition a determined voltage configuration was set, then the α -peak position and the FWHM/E ratio on the MCA spectrum were monitored. Typically the time for the stabilization was 30 minutes.

5.2.5 Data acquisition

For this study, two configurations for the data acquisition were used: the coincidence and the independent modes. The setup allows a coincident measurement of α 's and γ 's (59.5 keV γ branching ratio=36%), allowing the measurement of electron lifetime (τ_e) to determine the level of attachment. Each signal from the Micromegas back-electrode is fed to a CANBERRA preamplifier (model 2004) and then to an oscilloscope (model TDS5054B) (see Fig. 5.2). In order to avoid fortuitous coincidence the trigger is set in the γ -signal, hence the event rate for this mode is very low, approximately 1 Hz, reaching greater values as the pressure is increased.

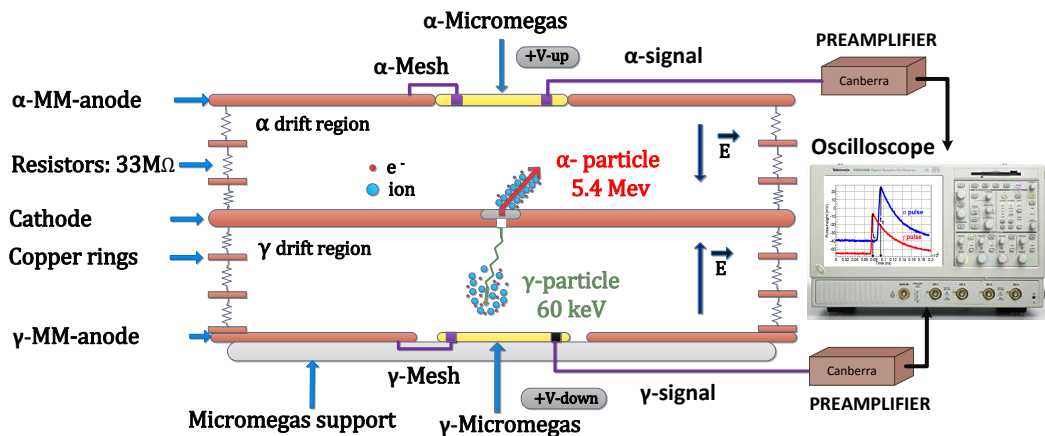


Fig. 5.2: Schematic representation of the coincidence mode configuration. With this mode the electron lifetime can be determined, providing the level of attachment, as well as the drift velocity for electrons generated by the γ -interaction.

On the other hand, signals from the two Micromegas could be read independently (see Fig. 5.3), providing i) the relative recombination for the charge collected from α -particles and γ -rays; and ii) the dependence of the recombination on the track angle, by analyzing the correlation of the pulse-height (charge) on its rise-time (track angle). For this, the output of the α -signal was fed into an ORTEC[®] preamplifier (142C) and then to an oscilloscope (TDS5054B) for pulse digitization. Meanwhile the γ -signal was fed into a CANBERRA preamplifier+amplifier electronic chain, model 2004 and 2022, respectively. The amplified signal was connected to a multichannel analyzer (AMTEK MCA 8000A) and then to a computer where the pulse-height distribution was stored.

As the activity for the ^{241}Am source is 500 Bq, the event rate for α -Micromegas should be around 250 Bq. This is because from 2 bar, the α -tracks are completely contained in the α drift region (3 cm), because the range at this pressure is lower than 1.1 cm. Thus high statistics can be obtained for α -particles in short period of time using this configuration. It must be noted that during the data acquisition the signal-to-noise ratio was initially very high, therefore the trigger was set higher to suppress the pulse noises, thus giving a net rate above 100 Hz. Meanwhile the rate from the γ -rays is very low, strongly depending on the mean free path of γ -rays, which in turn depends on pressure. The event rate measured at 3 bar was ≈ 1 Hz, increasing with pressure.

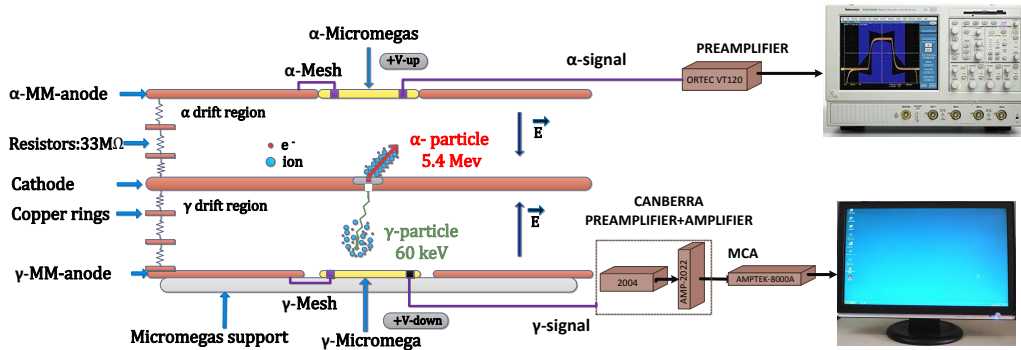


Fig. 5.3: Scheme of the independent mode configuration to provide i) the relative recombination for the charge collected of α -particles and γ -rays is measured, and ii) the dependence of the recombination on the track angle. As seen, signals of the two Micromegas are readout independently.

5.2.6 Measurements

Measurements with the coincidence mode allows to determine the electron lifetime. This configuration was used mainly to verify the level of impurities in the mixture during the data acquisition. Systematic measurements were not taken due to the low rate of this type of measurement (below 1 Hz). Therefore, electron lifetime measurements were performed before having started or after having finished the measurements with the independent mode.

Pressure (bar)	TMA (%)	E_d/P range (V/cm/bar)	Electron lifetime	E_d/P (V/cm/bar)
3	2.2	3 – 450	✓	
4	2.2	10 – 400	✓	
5	1.2	10 – 375	✓	
6	1.5	10 – 350	✓	
6	2.2	10 – 350	✓	30, 50
8	2.2	10 – 325		
10	2.2	10 – 300		

Table 5.1: Description of the measurements taken for the electron-ion recombination study in Xe+TMA mixtures. For each pressure, the TMA concentration and E_d/P values used for the acquisition are shown. In addition, it is specified by a checkmark when the measurement of electron lifetime was performed, and the E_d/P at which was acquired.

Typically, the reduced drift field was changed from 10 to 300 V/cm/bar. A scan of the drift field was performed, fixing the amplification voltage for the α -Micromegas in such a way that the pulse-height was above 100 mV. For each voltage configuration, more than of 15000 pulses were acquired from the α -signal, while the energy spectrum from the γ interaction was stored during 10 min.

After the drift field scan, a common range of full transmission for α - and γ -Micromegas was established. In this range the maximum pulse-height for α -particles and peak position on MCA for γ -rays is obtained. From this information is selected a ratio of $E_d/E_{a,\alpha}$ ($E_{a,\alpha}$ is the amplification field for the α -Micromegas), within the full transmission region. Afterwards, both amplification fields, for α and γ , were varied in such a way that this ratio remained constant for α -particles.

In Table 5.1 are summarized all the measurements taken. The TMA concentration and the E_d/P values for each data acquisition are drawn. It is also specified by a checkmark when the attachment measurement was carried out and it is given the corresponding E_d/P value for the acquisition.

5.3 Analysis and Results for the Coincidence Mode

A ROOT application was used to analyze the coincidence pulses digitized by the oscilloscope. This application was developed by F.J. Iguaz for analyzing events with only one pulse [30], therefore an extension for two pulses was done. In the first step, both pulses are smoothed; for each point of one pulse is generated a new point, obtained from the mean value of the closer n points at the right and the left side, including the original point. The value of smoothing, n , was changed depending on the time bin of the measurement, typically values between 20 and 40 were used. Examples of α (red) and γ (blue) smoothed pulses are shown in Fig. 5.4.

In the second step the values of the pulse baseline, the minimum (min PP), and

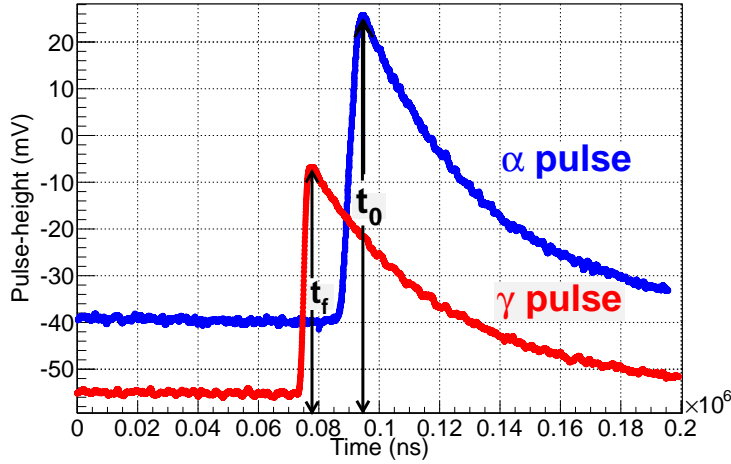


Fig. 5.4: Example of α and γ smoothed pulses obtained from the coincidence acquisition. In this mode, the t_0 of each event is given by the maximum point of the α pulse, because this point is independent of the track angle.

the maximum position of the pulse (max PP), the risetime (t_{rise}) and the pulse-height (H_p) for each pulse are calculated by means of mathematical algorithms. Since the pulse parameters values are slightly dependent on the definition, this is described below:

- **baseline:** It is the offset voltage calculated as the mean value of the first 100 points of the pulse.
- **max PP :** Time position at which the maximum height is obtained.
- **pulse-height:** The amplitude of the pulse, obtained subtracting the pulse baseline from the height the at max PP.
- **min PP :** Time position at which the pulse starts to rise, defined as the point at which the height reaches the 0.05 % of the pulse-height.
- **risetime:** The temporal difference between the time position at which the height reaches 90% and 10% of the pulse-height.

The main objective of these measurements is to calculate the electron lifetime (τ_e) for electron clouds generated by the γ interactions. For this purpose, the pulse-height of the γ -pulses as a function of the drift time of electrons from the γ interaction was studied. The drift time of electrons was determined as the temporal difference between the γ -signal and α -signal ($t_{0,\alpha} - t_{f,\gamma}$) (see Fig. 5.4). The $t_{0,\alpha}$ of each event was taken to be as the max PP of α -particles signal, this point is independent of the track angle, because corresponds to electrons traveling the complete drift region (3 cm); while the min PP depends on the track angle respect to the drift field.

5.3.1 Electron lifetime

The passage of γ -rays by the drift region yields electrons that drift under the influence of an applied electric field; in absence of impurities the charge collected for each interaction should be independent on the drift time, otherwise it shows an exponential behaviour. Therefor the electron lifetime of the mixture used can be measured with this setup by studying the correlation between the pulse-height and the drift time of γ -rays. From the data collected with the coincidence mode this information is obtained, the drift time is measured through the temporal difference between γ and α signal.

Plotting the logarithm of the pulse-height against the drift time, the electron lifetime is determined as the inverse of the slope. The dependence of the logarithm of the pulse-height on the drift time at 6 bar for $E_d/P = 30$ and 50 V/cm/bar is depicted in Fig. 5.5. It can be seen that the logarithm of the pulse-height is independent of the drift for both configurations. A profile for 29 keV events is performed and fitted to a linear function, as a result for the two cases the slope is compatible with zero, providing lower limits of $\tau_e > 2$ ms ($E_d/P = 30$ V/cm/bar) and $\tau_e > 1$ ms at ($E_d/P = 50$ V/cm/bar) with 90% C.L. Even though more measurements at several pressures and drift fields were done showing similar behaviour, the statistics for them is very low, and they are not presented. It must be noted that the initial purpose of measuring the electron life was to discard the attachment at low drift fields, for this reason measurements at higher drift fields were not done, but in a next experiment it should be included.

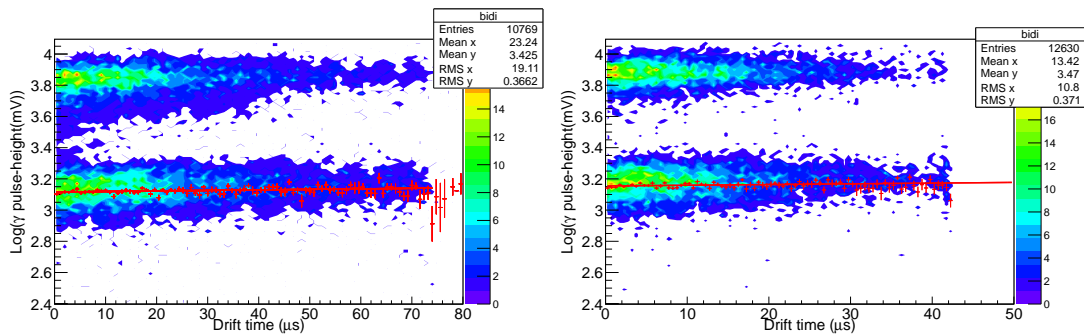


Fig. 5.5: Logarithm of the pulse-height vs the drift time for electrons generated by the γ interaction (lower drift region), acquired at 6 bar with $E_d/P = 30$ V/cm/bar (left) and $E_d/P = 50$ V/cm/bar (right). The two bands in the contour plot correspond to the Xe K_α escape peak (29 keV, lower band) and the photo-peak (59.5 keV, upper band). The mean values and error bars for Xe K_α escape peak events are shown together with a linear fit whose slope is compatible with zero in both cases.

5.4 Analysis for the Independent Mode

Data acquired with the not coincident configuration (see setup in Fig.5.3) consist of an array of α -pulses digitized by the Tektronix Oscilloscope and a γ energy spectrum, produced by the interaction of the γ -rays and α -particles from the ^{241}Am radioactive source. Fig. 5.6 shows one of the α -pulse digitized and a γ energy spectrum acquired at 6 bar. The voltage configuration for the acquisition is shown in the top of each figure. The description of the offline analysis carried out with each data information is presented below.

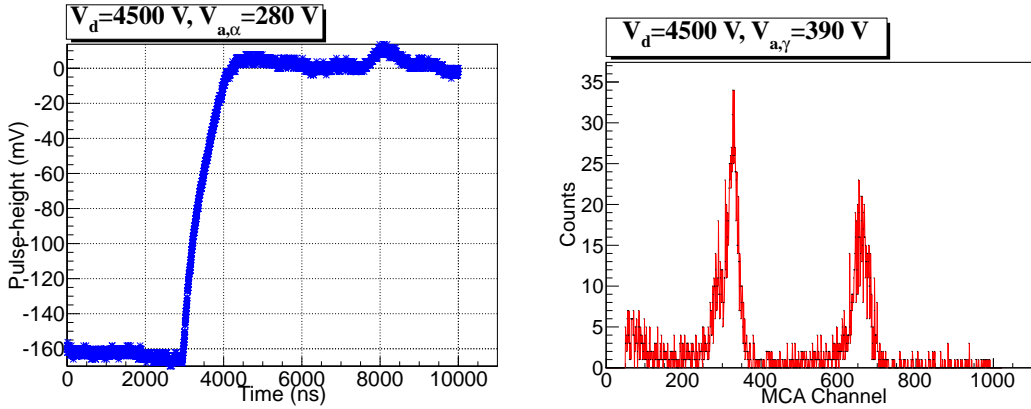


Fig. 5.6: Typical digitized α -pulse from ORTEC[®] preamplifier (left) and γ energy spectrum (right), both signals produced by the interaction of the γ -rays and α -particles from the ^{241}Am radioactive source.

5.4.1 ^{241}Am γ energy spectrum in Xe+TMA mixtures

The energy spectrum produced by the γ emission from the ^{241}Am source, in a HPXe TPC, was explained in detail in Sec. 2.3. Using Xe+TMA as filling gas the expected lines are the same as in a Xe HP TPC. The energy spectrum for γ -rays emitted by the ^{241}Am source, in Xe+1.5%TMA at 6 bar, is plotted in Fig. 5.7 together with the corresponding fits for each peak. Three peaks are distinguished on the spectrum. The first one placed around 26.0 keV is the sum of Xe K_β -EP and the 26.34 keV γ -ray emission, being the γ -rays the minor contribution. The second, the highest one, corresponds to the 29.87 keV Xe K_α -EP. The last one represents the signal from the most intense γ -rays (59.54 keV). The procedure for fitting the energy range where γ -rays (26.34 keV), Xe K_α -EP and Xe K_β -EP are located, was also described in Sec. 2.3.

The determination of the relative recombination of charge collected from γ -rays was done by studying the dependence of the peak position for Xe K_α -EP (29.87 keV) on the drift field; this peak was selected because it provides higher statistics, thus less error in its determination. The change of the peak position with drift field, gives the dependence of collected charge on drift field. It must be noted that the

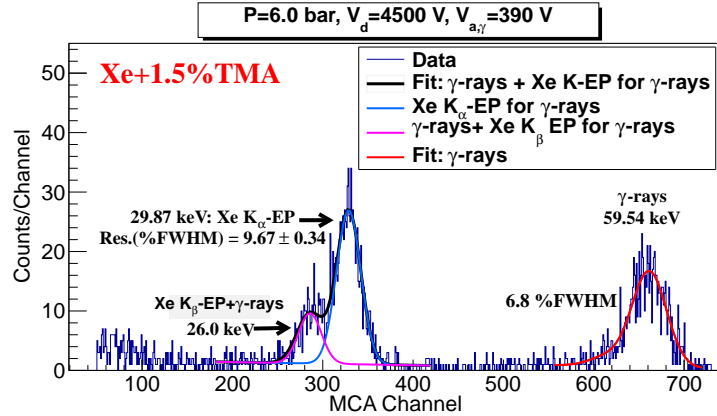


Fig. 5.7: γ energy spectrum emitted by an ^{241}Am radioactive source. The γ interaction takes place in the drift region of 3 cm of the NEXT-1-MM chamber, using a Xe+1.5%TMA mixture at 6 bar. A three-step root routine was used to fit the energy range where the Xe K_{α} -EP (29.87 keV), Xe K_{β} -EP and γ -rays (26.34 keV) are located. A simple Gaussian fit is done for 59.54 keV γ -rays. The values of energy resolution at FWHM are indicated for the two major contributions.

study of the energy resolutions was not the focus of this work, mainly because the event rate for γ -rays is very low, hence long periods of data acquisition would be required. However, the values of the energy resolution at FWHM for γ -rays (59.54 keV, 6.8%) and Xe K_{α} -EP (29.87 keV, 9.7%) have been evaluated for the energy spectrum plotted. These values should be taken as guideline values due to the low statistics. The gain of γ -rays was measured using the peak position of the Xe K_{α} -EP (29.87 keV) for the same reasons as outlined above.

5.4.2 PSA for α signals: charge and track angle

For the current study, it was only digitized the rise of the signal generated by the α interaction, as shown in Fig. 5.6-left. On the one hand, this part of the signal provides enough information for this study: the charge collected and the track orientation respect to the drift field for each event, obtained from the pulse-height and the risetime of the signal, respectively. On the other hand, storing only the rise of the signal allows to determine with more precision the risetime, which implies that the track angle of the α -particle is evaluated with more resolution.

The first estimation of the risetime and the pulse-height was done using the application that was used for the coincident data, in which the output pulse is smoothed through a simple algorithm (see Sec. 5.3). However, on the risetime distributions peaks caused by the noise fluctuations on the signal were observed. This happens especially for data acquired at low drift fields and high pressures where the signal-to-noise ratio is worse. For this reason, a new PSA was developed in order to improve the estimation of pulse-height and risetime. The PSA consists in two-steps:

1. First-step:

The pulse is smoothed via Fast Fourier Transform analysis (see section 2.2.2), in which high frequencies related to noise fluctuations are eliminated. From the smoothed FFT pulse, the pulse parameters -risetime, the pulse-height and the baseline- are calculated using the algorithms for the definitions outlined in section 5.3. In addition, a new parameter is also determined, t_{half} that corresponds to the time position at which the half height of the pulse-height is reached.

2. Second-step:

The smoothed FFT pulse is fitted to a sigmoid function given by:

$$H(t) = -\frac{H_p}{1 + \exp[(t - t_{half})/s]} + C \quad (5.4)$$

where H_p , t_{half} , s and C are the pulse-height, time at half of the pulse-height, the shape parameter of the sigmoid function and the baseline offset, respectively. In order to achieve a rapid convergence for the fit, the pulse parameters calculated in the first-step (risetime, pulse-height, baseline, and t_{half}) are introduced as input parameters, thus best estimates of the pulse parameters are obtained. Meanwhile the pulse-height H_p is obtained directly from the fit, the risetime is calculated from the time difference between the time at 90% and 10% of the pulse-height (H_p), hence the risetime is given by $t_r = H^{-1}(90\%H_p) - H^{-1}(10\%H_p)$.

The results of application of the PSA are shown in Fig. 5.8, for two configurations: one at 3 bar (left) and the other at 8 bar (right). In each plot the raw pulse together with the smoothed pulse (FFT analysis, first-step), and the fitted pulse (fit to a sigmoid function, second-step) are depicted. As it can be seen, the application of the FFT analysis to the raw pulse generates pulses with less noise fluctuations; however the smoothed pulses still show large noise fluctuations, which is increasingly clear at 8 bar (Fig. 5.8-right), because the signal-to-noise ratio is higher. This is the reason why it was necessary to go one step further in the analysis; fitting the smoothed pulse to a sigmoid function allows to model very well the rise of the signal for α -particles, as viewed for the two configurations.

Comparison of histograms of pulse parameters calculated from raw, smoothed and fitted pulse, is viewed in Fig. 5.9 -risetime (left) and pulse-height (right)- for the two same configurations that in the previous figure, at 3 bar (top) and 8 bar (bottom). It is seen that the statistical distribution of the pulse parameters determined from raw, smoothed, and fitted pulse presents similar form for risetime and pulse-height.

Typically the risetime distribution show a narrow peak and then a flat region as clearly seen at 3 bar. This distribution is the expected considering that by solid angle properties, there are more tracks in an element of solid angle with larger φ ¹,

¹As the risetime for α signals corresponds to the temporal projection of the track, hence a

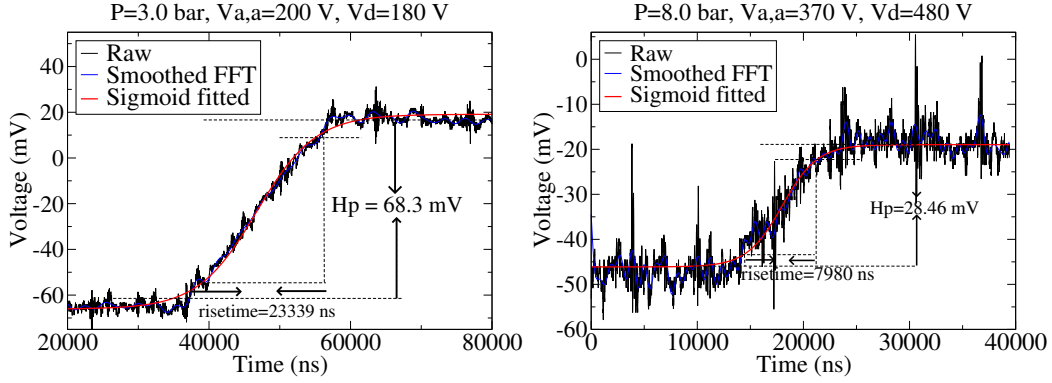


Fig. 5.8: Raw pulse together with smoothed FFT pulse and sigmoid fit pulse are plotted at 3 bar (left) and 8 bar (right). The raw pulse is the output signal from the preamplifier for the interaction of an α -particle in Xe+2.2%TMA; the smoothed FFT pulse is obtained after applying a cut frequency ($w_t < 40\text{MHz}$) to remove the high frequency noise to the raw pulse; and the fit pulse is obtained fitting the smoothed pulse to a sigmoid function. The voltages for each configuration are indicated on the top of each plot.

which implies that tracks with lower values in risetime are higher. This fact accounts for the peak in the risetime distributions. It must be noted that $\cos\varphi$ should have an uniform distribution, as will be shown latter. The high noise fluctuations of the signals for the configuration at 8 bar, produces that the risetime can not be properly calculated. This is evidenced from the peaks aside of the first peak in the risetime distributions for the raw and smoothed FFT pulses. However, the histogram of risetime obtained from the sigmoid fitted pulses shows the expected distribution.

On the other hand, the pulse-height distributions (Fig. 5.9-right) for sigmoid fitted pulses seem to have a very well defined peak, allowing a best estimation of the peak position and the energy resolution.

5.4.2.1 Charge

The pulse-height of α signal is proportional to the total charge generated in an α interaction. The factor of proportionality is given by the amplification factor of the ORTEC[®] preamplifier, which was obtained following the calibration procedure explained in Sec. 2.2.7. The result of the calibration provides a value of $R_{pre} = 0.4\text{mV/fC}$ ($6.4 \times 10^{-5}\text{mV/e}^-$), thus the charge is obtained as $Q = H_p/R_{pre}$.

5.4.2.2 Track angle

The risetime (t_r) represents the temporal projection of the α track on the drift field direction. As a first approach the track length l_α can be estimated as the product between the drift velocity and the maximum risetime, $l_\alpha = v_d t_{r,max}$, as

transformation can be done to obtain the track angle (φ) for each event.

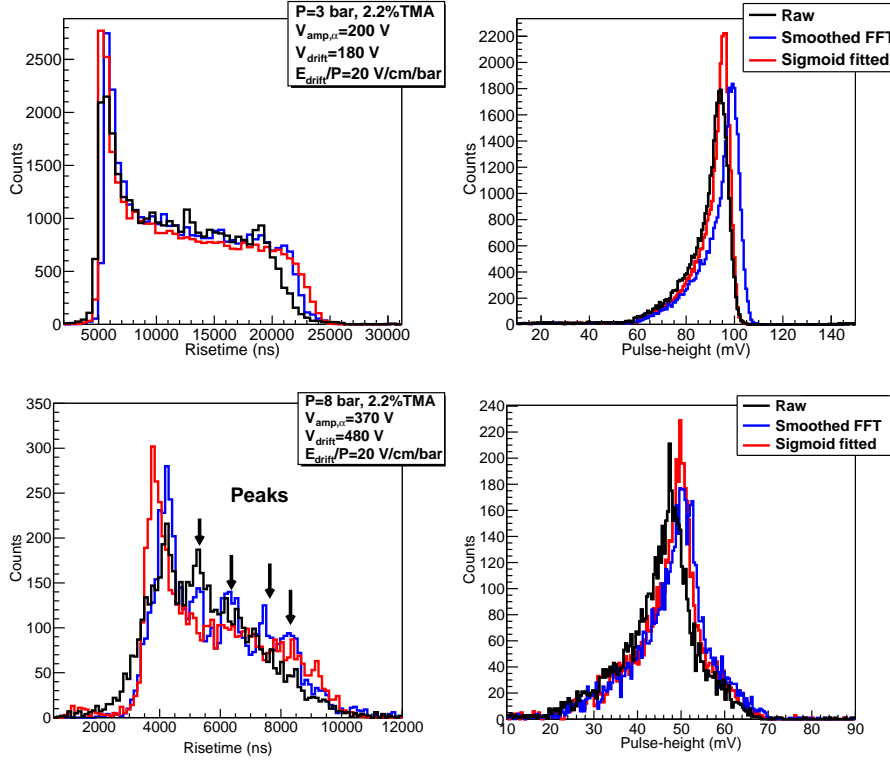


Fig. 5.9: Risetime (left) and pulse-height (right) distributions obtained from the raw pulse (black), smoothed FFT pulse (blue) and sigmoid fitted pulse (red) at 3 bar (top) and 8 bar (bottom). The legend and the text with the experimental details apply for both plots.

was explained in sec. 2.2.6. The cosine of the track angle ($\cos \varphi$) can therefore be written as:

$$\cos \varphi = \frac{\sqrt{t_r^2 - t_{r,min}^2}}{\sqrt{t_{r,max}^2 - t_{r,min}^2}} \quad (5.5)$$

where the $t_{r,min}$ is subtracted in quadrature to take into account the diffusion suffered by electrons and the electronic time response. Thus the track angle can be determined for each α interaction, by estimating $t_{r,min}$ and $t_{r,max}$ for each pressure and drift field. The $t_{r,min}$ and $t_{r,max}$ are defined and calculated as follows:

- $t_{r,min}$: the peak at the left side of the risetime distribution is fitted to a Gaussian function; $t_{r,min}$ is the risetime at which the height of the Gaussian function is $90\%H_G$, where H_G corresponds to the maximum height of the Gaussian. The error associated is given by the standard deviation of the Gaussian function, σ .
- $t_{r,max}$: the flat region of the distribution is fitted to a sigmoid function (see Eq. 5.4). The $t_{r,max}$ is calculated as the risetime for which the sigmoid

function reaches the $50\%H_s$, where H_s is the sigmoid function's height. The error associated is defined as the difference between the risetime at $60\%H_s$ and $40\%H_s$.

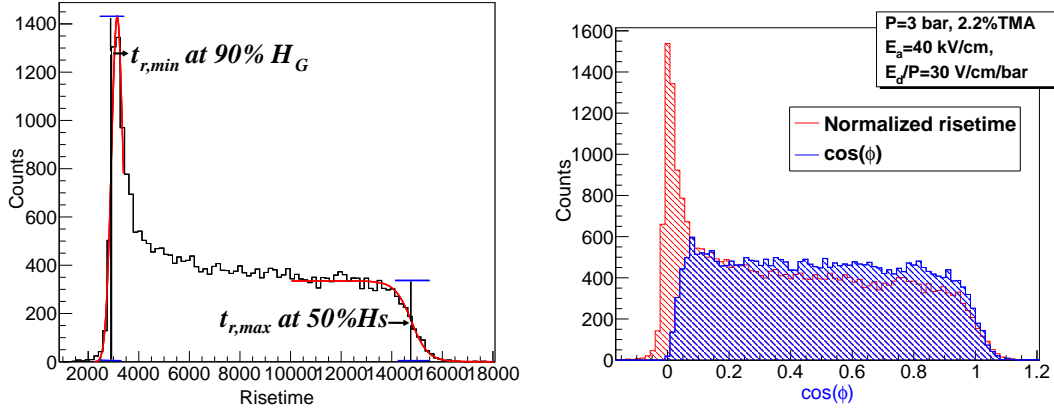


Fig. 5.10: Right: risetime distribution for α -particles, the definition of $t_{r,min}$ and $t_{r,max}$ are shown. Left: distribution of the cosine of the track angle ($\cos \varphi$) together with the normalized risetime distribution for the same pressure and drift field. As it is seen after the transformation of the risetime to $\cos \varphi$ the distribution becomes uniform as it is expected. The text with the experimental details of the measurement on the right plot also applies for the left one.

Risetime distribution for α -particles at 3 bar and a mixture of Xe+2.2%TMA is shown in Fig. 5.10-left, together with the definition of $t_{r,min}$ and $t_{r,max}$. The results of the transformation between risetime and $\cos \varphi$ by applying the Eq. 5.5 are shown in the Fig. 5.10-right; the $\cos \varphi$ distribution is depicted together with the normalized risetime distribution. As it can be seen after the transformation of the risetime to $\cos \varphi$, the distribution becomes uniform as expected.

The procedure explained to determine $t_{r,min}$ and $t_{r,max}$, cannot be applied for all pressures and drift fields, because risetime distribution changes its form as the drift field increases. The risetime distributions for different drift fields at 4 bar and 8 bar are depicted in Fig. 5.11. For both pressures at low E_d/P values, the histograms show similar form, a peak at the left side followed by a flat region. However, at higher E_d/P values, the flat region becomes narrower and eventually disappears at the largest values. This may happen because the ion transit in the amplification gap starts to dominate at higher E_d/P values; the risetime becomes smaller (drift velocity increases), reaching values below of the ion transit.

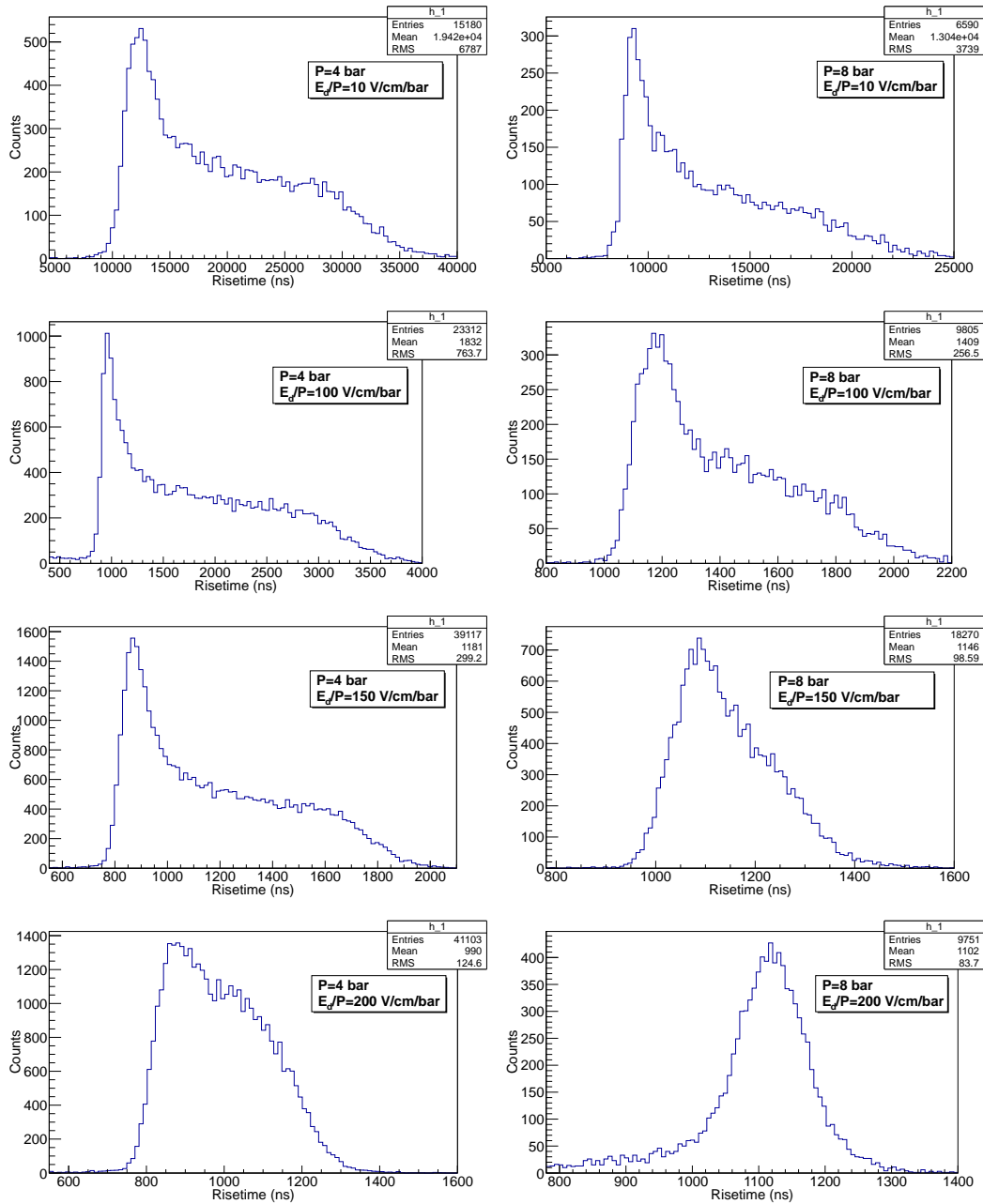


Fig. 5.11: Risetime distributions for several E_d/P values at 4 bar (left) and 8 bar (right). As the pressure increases, the determination of the $t_{r,min}$ and $t_{r,max}$ can not be done with the defined method.

5.4.3 Ion mobility

Accordingly, the minimum value of $t_{r,min}$ -for a fix pressure and mixture- denoted hereinafter by $T_{r,min}$ must be related with the ion drift velocity ($v_{d,I}$) in the amplification gap, so that:

$$v_{d,I} = k \frac{g}{T_{r,min}} \quad (5.6)$$

where g is the gap distance of the Micromegas ($g = 0.005$ cm) and $k = 0.8$ is a constant related with the definition of the risetime. The $T_{r,min}$ is obtained as the $t_{r,min}$ for the highest drift field configuration, acquired for a fix pressure and mixture. The ion mobility coefficient μ is defined as $\mu = v_{d,I}/E_a/P$, where E_a corresponds to the amplification field; this relation together with the Eq. 5.6 lead to:

$$\mu = k \frac{g^2}{V_a T_{r,min} P} \quad (5.7)$$

The Eq. 5.7 is obtained taking into consideration the relation between the amplification field (E_a) and the amplification voltage (V_a). Results of ion mobility for experimental data acquired in a Xe+2.2%TMA mixture in this study, are shown in Fig. 5.12 as a function of E_a/P . The values of ion mobilities are in the range 0.41-0.48 cm²/Vs/bar. Contrary to the expectations the ion mobility seems to increase systematically with the reduced amplification field (E_a/P).

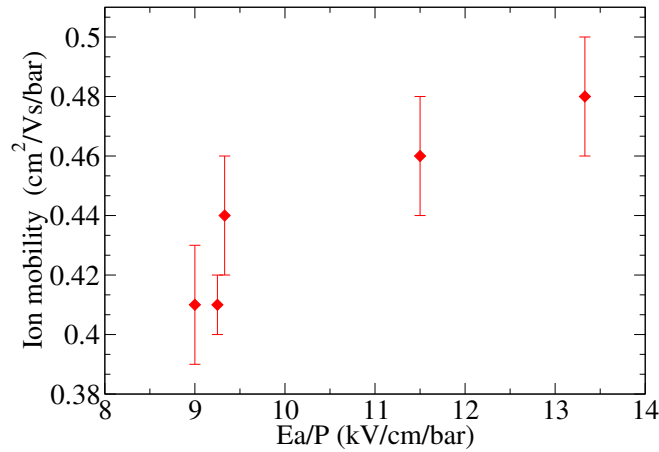


Fig. 5.12: Results of ion mobility (μ) as a function of E_a/P in a mixture of Xe+2.2%TMA and pressure ranged from 3 to 8 bar. Even though there is no knowledge about the identity of the migrating ions, the TMA ions (e.g. TMA^+ and TMA^{++}) are likely to be those moving toward the mesh.

It must be noted that so far, there is no knowledge about what ion or ions are migrating toward the mesh. It is plausible that between Xe^+ ion and TMA molecules occur charge exchange process, because the ionization potential of the

TMA is smaller than the energy available in the Xe^+ ion, hence through collision the Xe^+ would neutralize creating new ions e.g. TMA^+ and TMA^{++} .

In the literature there is not any available data of the ion mobility for ions of TMA. On the contrary, there are many experimental measurements of the ion mobilities of Xe^+ in Xe, the average measured value is $0.57 \pm 0.05 \text{ cm}^2/\text{Vs}$ at normal conditions [25]. The values for other ions in Ar or other gases are between $0.26\text{--}1.87 \text{ cm}^2/\text{Vs}$. The estimated values in this study are therefore of the same order of magnitude than the typical values of ion mobilities of Xe^+ in Xe and other molecular ions in different gases. These results for the ion mobilities are consistent with the interpretation that at higher drift fields the ion transit dominate, explaining the form of the risetime distribution at high drift fields.

In this way, the track length and the track angle cannot be reliably determined at higher drift fields. Thus for these configuration it is considered that the transformation is not appropriated, hence only a qualitative interpretation was done.

5.5 Electronic Properties

Even though the main goal of this chapter is the study of the recombination, measurements taken with the two modes provide enough information to determine some electronic properties. In this section, the results of measurements of drift velocity, diffusion coefficient and gain are presented. The measurements of drift velocity and diffusion coefficient allow to validate the PSA, and the measurement of gain of α -particles and γ -rays provides a direct comparison of the recombination for the charge collected from both interactions.

5.5.1 Drift Velocity and Longitudinal Diffusion Coefficient

The drift velocity (v_d) and longitudinal diffusion coefficient pressure-independent (D_L^*) were determined and compared with previous experimental results as well as with Magboltz calculations.

The drift velocity was determined with Eq. 2.3, and then the result was multiplied by a factor $k = 0.8$, a constant associated with the definition of risetime. The value of the track length at 1 bar, l_α^1 was also taken as 2.2 cm, value for pure Xe; since the values of TMA concentrations are very small, therefore the effect would be negligible.

The scatter of a point-like cloud drifting a distance d at a pressure P can be obtained as:

$$\sigma_L = D_L^* \frac{\sqrt{d}}{\sqrt{P}} \frac{1}{v_d} \quad (5.8)$$

where D_L^* is the pressure-independent longitudinal diffusion coefficient (divided by \sqrt{P}). As explained in Sec. 2.2.6, $t_{r,min}$ is proportional to the diffusion, thus $t_{r,min} = \sigma_L/k_2$, substituting D_L^* is given by:

$$D_L^* = k_2 \frac{\sqrt{P}}{\sqrt{d}} t_{r,min} v_d, \quad k_2 = 0.36 \quad (5.9)$$

where $d = 3$ cm is the drift distance and k_2 is a factor related to the convolution with the electronic response function.

In Fig. 5.13, v_d (left) and D_L^* (right) are plotted as a function of E_d/P , for pressures between 3 and 8 bar in a mixture of Xe+2.2%TMA (top) and varying the TMA concentration (bottom). Specially for the variation with pressure (top), the experimental values of this work are compatible among them at a given value of E_d/P , and compatible with previous experimental measurements acquired with different setups [103, 101]. The behaviour with pressure is expected considering that these electronic properties are to first order dependent on the E_d/P ratio only. It must be noted that in the case of D_L^* a slight dependence with pressure is observed. In addition, Magboltz calculations of the electronic properties are also plotted [28], showing to be compatible in the case of the v_d and to follow the trend with deviations up to 50% for D_L^* . These results validate the PSA and the transformation between risetime and $\cos(\varphi)$, for cases where the track can be well defined, that is when the flat region of the risetime distribution can be well distinguished.

5.5.2 Gain for α -particles and γ -rays

With the independent mode systematic variations of the amplification field for both α - and γ -Micromegas were carried out. The gain for α -particles was determined through Eq. 2.4, substituting H_p by the peak position at 5.4 MeV, E/w by $2.4 \times 10^5 e^-$ and R_{pre} by 6.4×10^{-5} mV/ e^- (see Sec. 5.4.2.1). Concerning γ -rays, the Eq. 4.1 was used, where P is the peak position at 29.87 keV, $f_{mca} = 4.88$ mV/channel, $E/w = 1351.6 e^-$ and $R_{pre+amp} = 3.15 \times 10^{-4}$, 9.71×10^{-4} , 3.03×10^{-3} , 8.09×10^{-3} for amplifier factors of 10, 30, 100, 300, respectively. Gain curves for α -particles and γ -rays as a function of the amplification field are shown in Fig. 5.14. Systematic gain measurements for γ -rays were not taken at 8 bar because the γ -Micromegas failed at 8 bar, likewise at 10 bar.

For both α -particles and γ -rays, the gain follows an exponential function with the amplification field. The gain for a fix pressure fits on a same line, this implies that the quenching factor for both interactions is the same, allowing a direct comparison of the recombination of the charge collected from both interactions (see in Sec. 5.6.) . The onset of breakdown for α -particles remain constant, around 10, for all pressures studied (3-10 bar). However, for γ -rays it seems to drop exponentially with the amplification field.

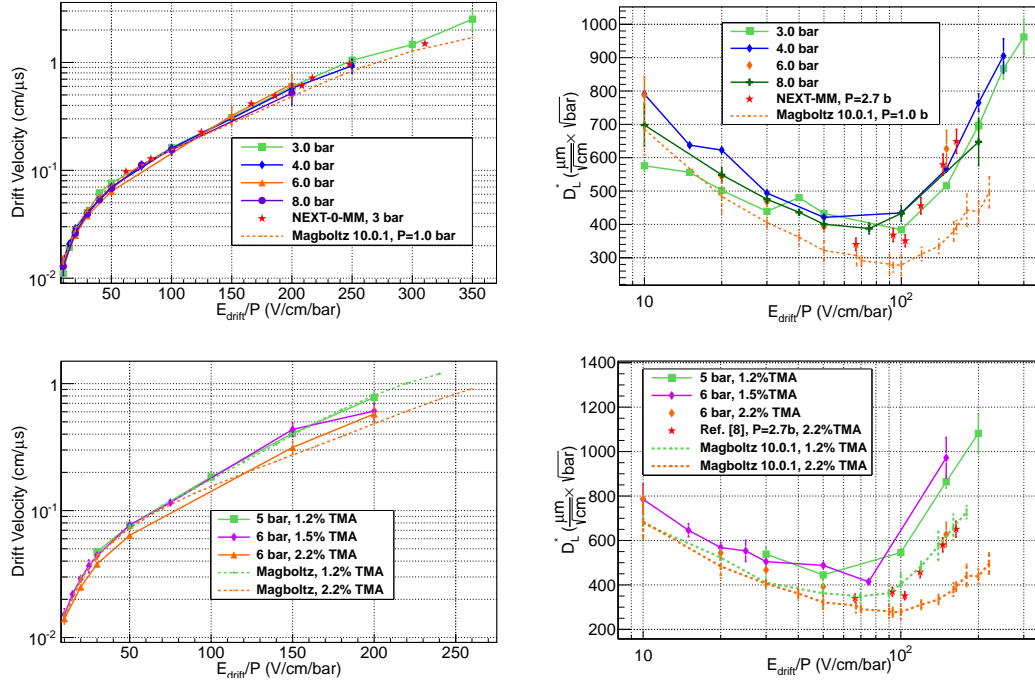


Fig. 5.13: Drift velocity (left) and longitudinal diffusion coefficient D_L^* (divided by \sqrt{P}) (right) as a function of E_d/P , for pressures between 3 and 8 bar in a mixture of 2.2%TMA (top) and varying the TMA concentration (bottom). Previous experimental results are plotted, obtained in the same TPC but with other drift configuration for the drift velocity (see [103]) and using the NEXT-MM TPC for D_L^* (see Ref. [101]). Magboltz calculations [28] are also plotted.

5.6 Recombination Dependence on Drift Field

The relative recombination of charge of α -particles and γ -rays has been studied with this setup by measuring the pulse-height charge spectrum for both interactions. With this aim, the peak position at 29 keV (Xe K_α escape peak) from the γ -rays spectrum, and the position for α -particles spectrum at 5.4 MeV were determined and divided by the maximum value obtained for each configuration. This ratio represents the fraction of charge that survives to recombination.

The Q/Q_{max} ratio is depicted in Fig. 5.15 for γ -rays and α -particles as a function of E_d/P at 5 (left) and 6 bar (right). In both cases, the values of the ratio for γ -rays are above those values for α -particles. It is also seen that at a given E_d/P value, Q/Q_{max} ratio is lower at 6 bar, for α and γ interaction. These results imply that the recombination is stronger at higher pressures and for the charge collected from α -particles. The latter is partially explained by the fact that α -particles would suffer more columnar recombination for being highly ionizing radiation, as will be shown in the next section.

5.7. Columnar Recombination of Charge Collected from α -particles 139

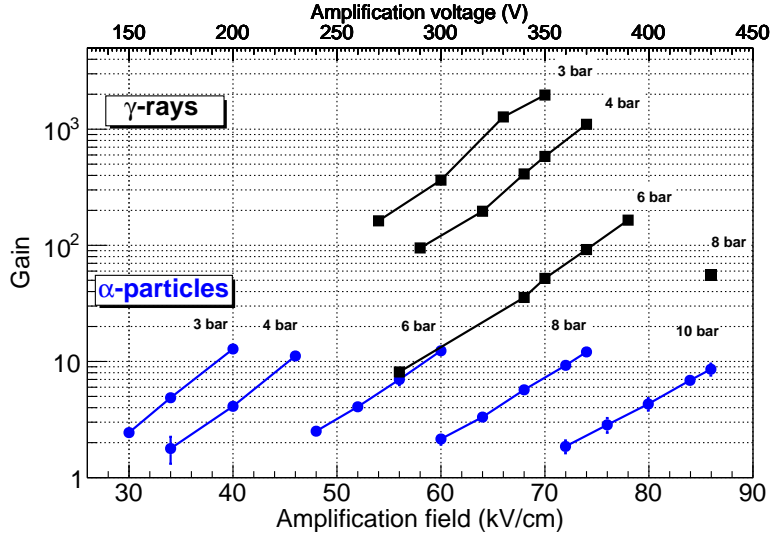


Fig. 5.14: Dependence of gain on the amplification field for α -particles (\circ) and γ -rays (\blacksquare) Micromegas using Xe+2.2%TMA.

5.7 Columnar Recombination of Charge Collected from α -particles

5.7.1 Charge vs. $\cos \varphi$

The columnar recombination for α -particles is studied through the dependence of the charge collected on track angle respect to the drift field. The determination of these parameters was explained in Sec. 5.4.2. Charge plotted against $\cos \varphi$ for α -particles in a Xe+2.2%TMA mixture at different drift fields ($E_d/P = 10, 100, 150$ V/cm/bar), is shown in Fig. 5.16 at 4bar (left) and

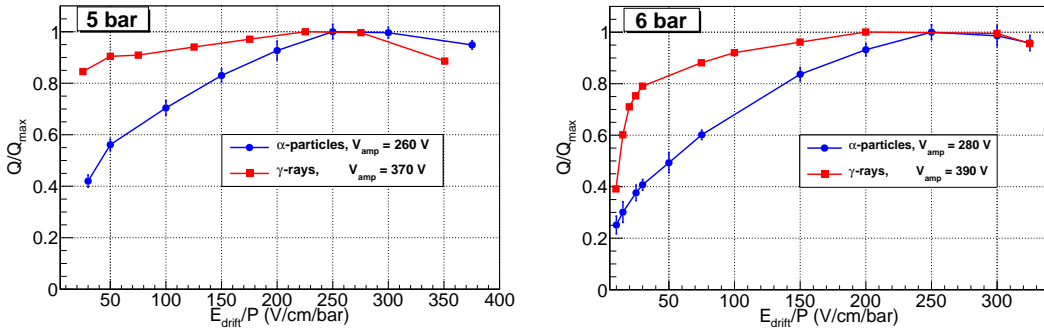


Fig. 5.15: Dependence of the relative recombination of the charge collected from α -particles and γ -rays on E_d/P at 5 (left) and 6 bar (right).

8 bar (right).

For both pressures, events with track angles near to the perpendicular direction ($\cos \varphi \approx 0$) have larger charge than events with track angles close to the parallel direction ($\cos \varphi \approx 1$). This result is in agreement with columnar recombination: ionization charge of parallel tracks in its drifting way has larger probability of recombination.

To study the dependence of the columnar effect on the drift field for a fix pressure, profile plots of the charge collected against the φ were done from the scatter-plot of the charge vs track angle. The percentage of charge is obtained as the ratio of the mean value of charge for each angle bin to the maximum value for any pressure and mixture. The result is shown in Fig. 5.17 at 4 (left) and 8 bar (right) for several drift fields in a Xe+2.2%TMA mixture. In both plots, at very low E_d/P values, the dependence of the charge on the track angle (φ) is very low, increasing with E_d/P , but again decreasing at higher E_d/P values. It must be noted that this behaviour is observed for all the pressures and mixtures studied.

5.7.2 Figure of merit: Q_0/Q_{90}

The dependence of columnar recombination on the track angle for all pressures and E_d/P values was studied through a figure of merit, defined as Q_0/Q_{90} , where Q_0 and Q_{90} are obtained from the charge distributions formed from events with track angles between 0° - 25° and 85° - 90° , respectively. These ranges were selected since the $\cos(\varphi)$ distributions are uniform, and therefore similar statistics for both distributions can be obtained. The corresponding charge distributions obtained at 4 bar are shown in Fig. 5.18 at $E_d/P = 10, 100, 200$ V/cm/bar. In each plot, the risetime distribution for all events is also depicted. Each charge distribution is fitted to a Gaussian function, thus Q_0 and Q_{90} values are the peak's positions of the corresponding distribution. The energy resolution at FWHM for distributions is also shown.

These three plots represent the behavior observed for all the pressure and mixtures studied. As it can be seen the peak's positions - Q_0 and Q_{90} - stay away as the E_d/P increases, becoming close again at high values. The overlap of the distributions at high values could be due to a bad transformation between risetime and φ rather than to a physical process, considering that the flat region of the risetime distribution is very narrow. However, the analysis at 3 bar confirms that this is a physical process, as shown in Fig. 5.19, where the overlap of the distributions is also observed for a same E_d/P value; in this case the transformation is well performed as in the risetime distribution the peak and the flat region can be distinguished clearly.

5.7. Columnar Recombination of Charge Collected from α -particles 141

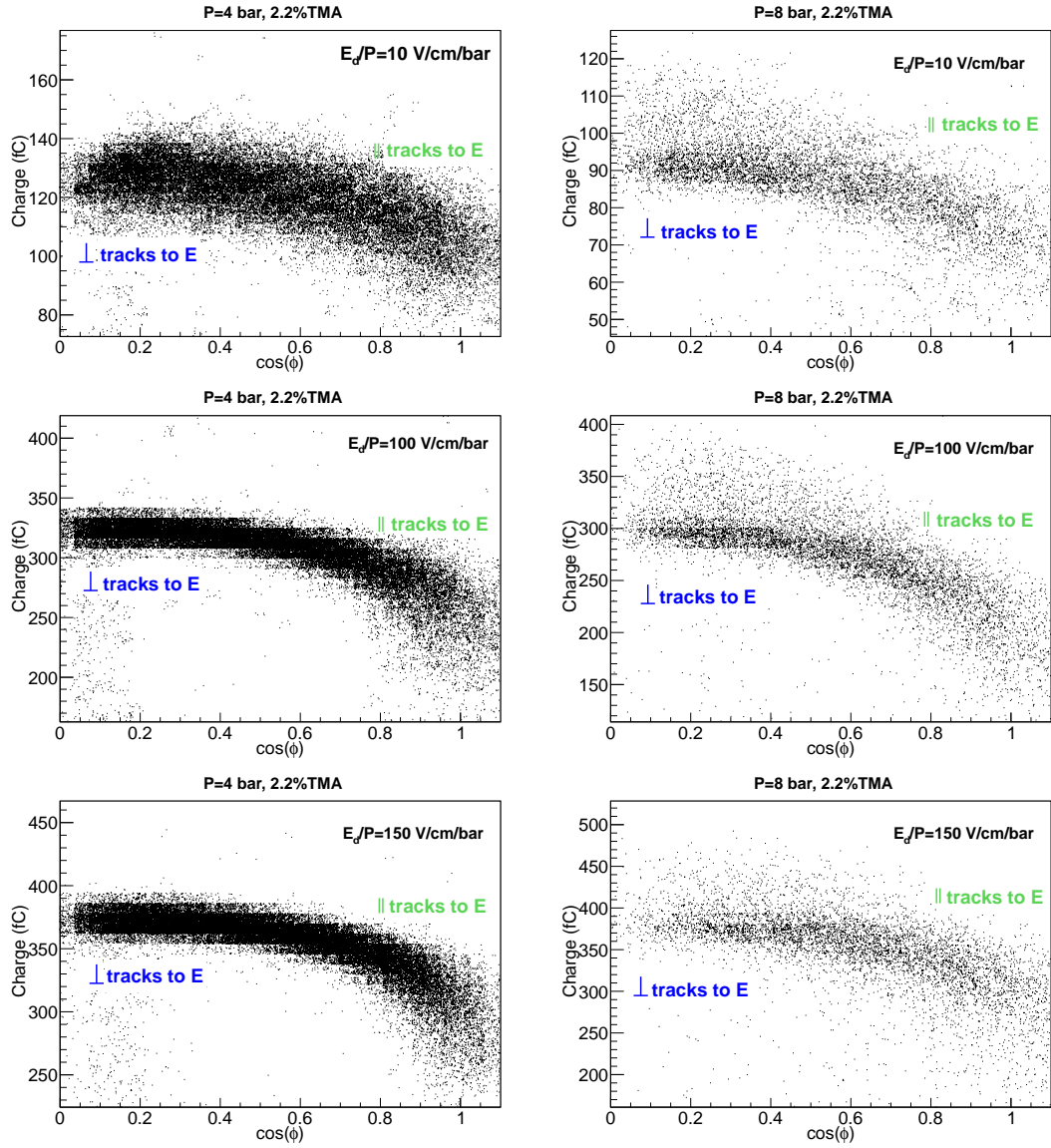


Fig. 5.16: Charge versus $\cos \varphi$ for α -particles in different drift fields, at 4 bar ($E_a = 46$ kV/cm) (left) and 8 bar ($E_a = 74$ kV/cm) (right). The dependence of the charge on the $\cos \varphi$ is compatible with the columnar recombination.

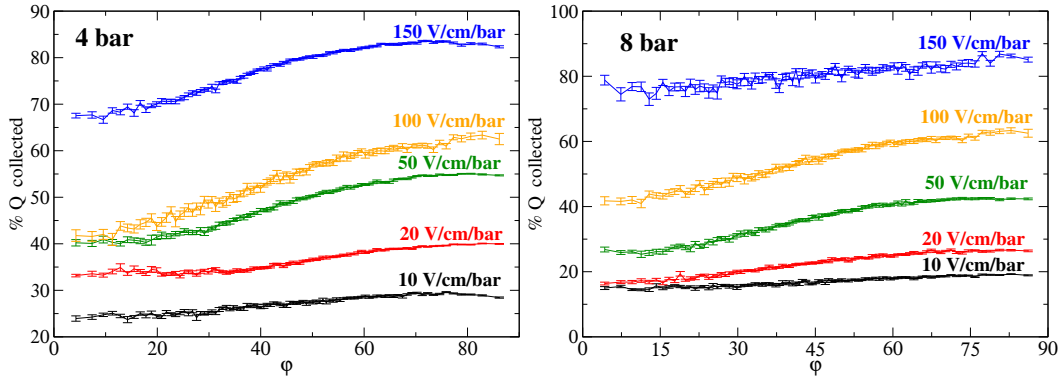


Fig. 5.17: Dependence of the percentage of charge collected on the track angle (φ) at 4 bar (left) and 8 bar (right). This is a profile plot obtained from the scatter-plot of the charge vs track angle, in which the percentage of charge obtained is the ratio of the mean value of charge for each angle bin to the maximum value for any pressure and mixture.

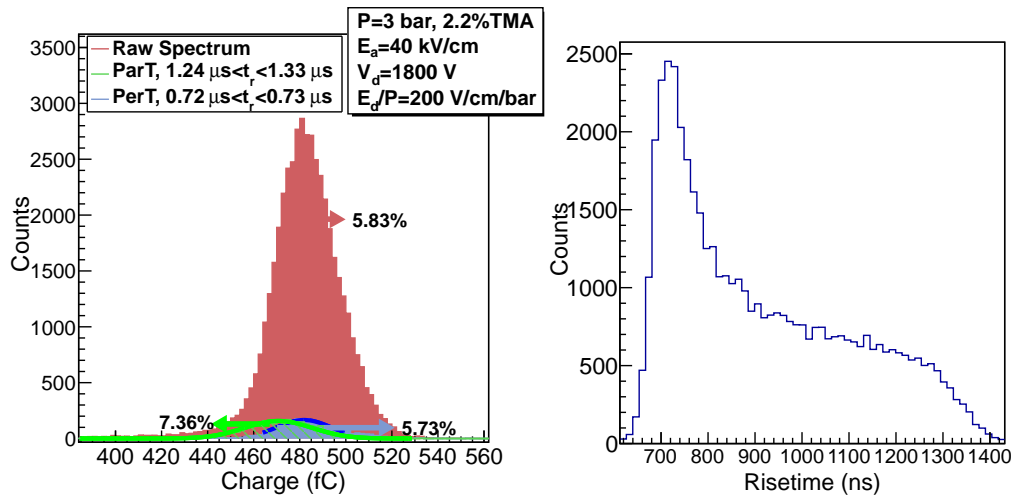


Fig. 5.19: As for previous figure, but for data at 3 bar. The distributions of Q_0 and Q_{90} overlap at high E_d/P showing that columnar recombination is negligible at these conditions.

Finally, the quantity Q_0/Q_{90} is plotted against E_d/P in Fig. 5.20. The systematic variation with pressure in a mixture of Xe+2.2%TMA is depicted in Fig. 5.20-left, and the variation with the TMA concentration is given in Fig. 5.20-right.

From these observations it seems that the columnar effect on the track angle at very low drift fields may not be important, increasing with drift field up to its maximum strength at about 40-50 V/cm/bar, from where the dependence on the angle becomes increasingly smaller. The overall drop of Q_0/Q_{90} with the increase of pressure and TMA concentration points to the importance of the accelerated electron thermalization and the reduced diffusion in this study, which helps to

5.7. Columnar Recombination of Charge Collected from α -particles¹⁴³

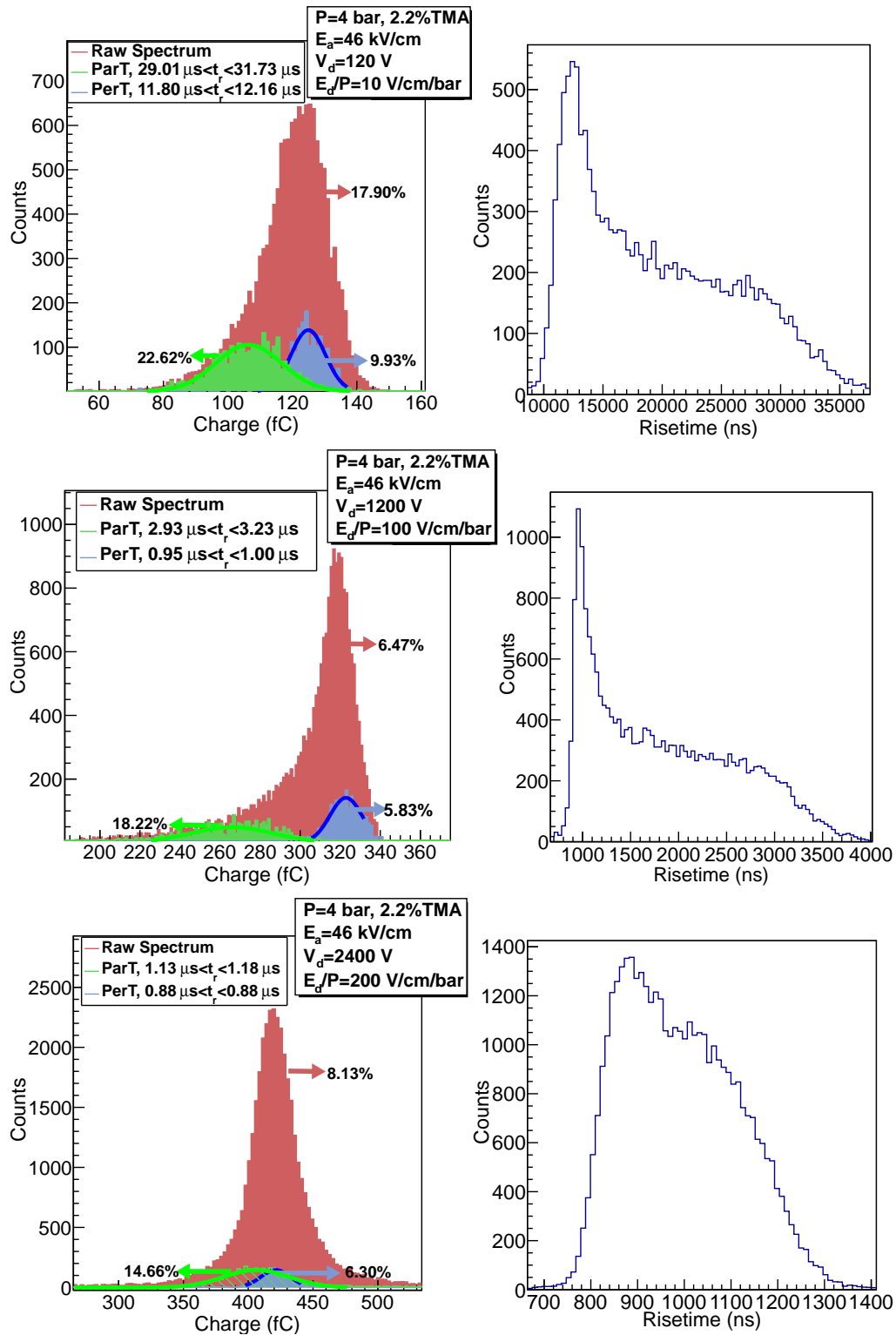


Fig. 5.18: Left: Charge distribution for all tracks together with the distribution for tracks near to parallel direction (Q_0) respect to drift field and closer (Q_{90}) to perpendicular one. Energy resolution at FWHM is given for each distribution. The cut applied on risetime for each distribution is indicated. Right: Risetime distribution for all tracks corresponding to the same configurations considered on the left plots.

maintain the initial track geometry in the reconstructed ionization footprint. A more thorough modeling is currently in progress.

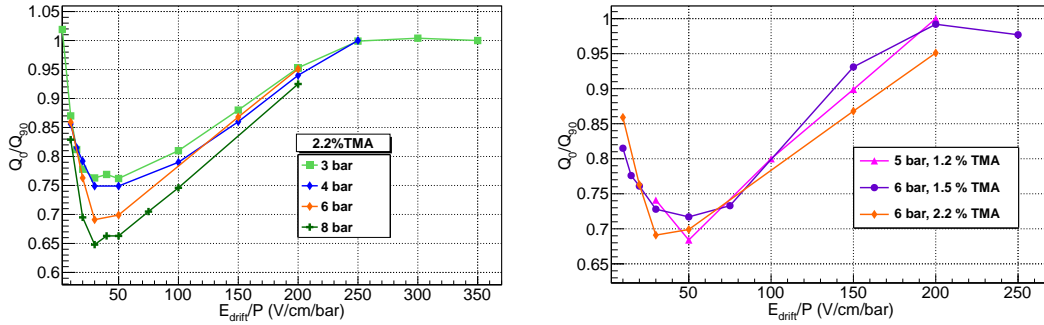


Fig. 5.20: Dependence of Q_0/Q_{90} on E_d/P for different pressures in a mixture of Xe+2.2%TMA (left) and for two concentrations at 5 and 6 bar (right).

5.7.3 Discussion

The dependence of collected charge on the track angle may be produced by recombination in the amplification region instead of by columnar recombination in the drift region. Electrons traveling toward anode may recombine with ions of an earlier avalanche, and this would be more likely for parallel tracks than for perpendicular ones. A schematic representation of this process is illustrated in Fig. 5.21. This type of recombination would have a similar behaviour with pressure and E_d/P than the recombination in the drift region. In order to discard this process, a new campaign of experimental measurements is being prepared, taking data at several amplification fields at a fix pressure and E_d/P . At different amplification fields it should be seen the same Q_0/Q_{90} ratio if the recombination is taking place in the drift instead the amplification region.

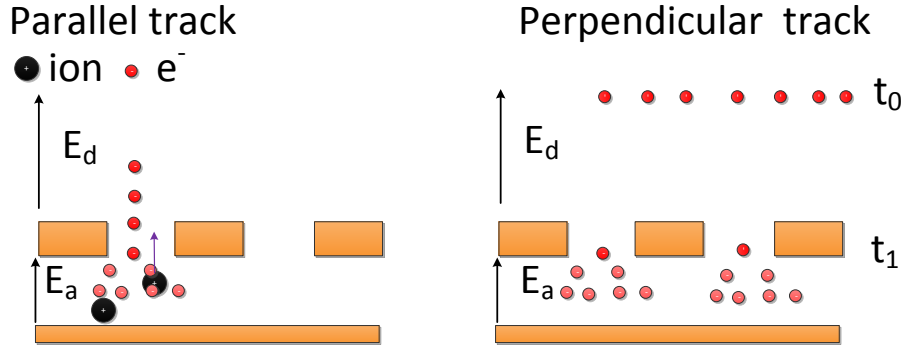


Fig. 5.21: Representation of the recombination that would have place in the amplification region. Left scheme represents a parallel track to the drift field and right scheme a perpendicular one. For parallel tracks this type of recombination -recombination in the amplification region- is stronger as the probability to find ions of an earlier avalanche is larger.

5.8 Conclusions and Outlook

Recombination for charge collected from α -particles and γ -rays has been studied in high pressure Xe+TMA mixtures using a double drift configuration of a Micromegas-TPC. The dependence of the relative recombination on the reduced drift field increases with the pressure and it is stronger for the charge collected from α -particles, as expected. The columnar effect on the track angle was observed for α -particles, which is reflected in a decrease of the collected charge for small angles relative to the electric drift field direction.

The definition of a figure of merit as Q_0/Q_{90} , representing the charge relation between tracks with small and large track angles, permitted to evaluate the dependence of the effect with E_d/P , pressure and TMA concentration. The columnar recombination increases with the reduced drift field, reaching a maximum around 40 V/cm/bar, and becomes increasingly smaller thereafter. At a given value of E_d/P , Q_0/Q_{90} ratio shows that the columnar recombination increases with pressure, and a slight increase is observed with the TMA concentration. The electron life time was also measured for $E_d/P > 20$ V/cm/bar, setting lower limits $\tau_e > 1$ ms which allowed to discard attachment for the measurements.

In addition, some electronic properties were measured: drift velocity, longitudinal diffusion coefficient, and gain for α -particles and γ -rays. Drift velocity and longitudinal diffusion coefficient allowed to validate the PSA, since results are compatible with previous experimental measurements and show a reasonable agreement with Magboltz, yet showing up to 50% deviations in case of the diffusion coefficient. Gains for α -particles and γ -rays fall on the same straight line for a fix pressure and mixture, showing that both interactions have similar quenching factor.

These results represent a first step toward the evaluation of the idea to use Xe+TMA mixture as medium gas for directional Dark Matter searches on virtue of the columnar recombination effect. Next steps will focus on modeling the experimental data within the Jaffé theory. Apart from this, possible electron-ion recombination in the amplification region is being studied; measurements at different amplification will be done to discard any recombination effect in the amplification region.

Conclusions

In this thesis was studied the performance of a microbulk Micromegas High Pressure Time Projection Chamber (HP TPC) filled with Xe-based Penning mixtures towards Rare Event Searches. During the last years Gaseous Xe detectors have become in a competitive option mainly due to its improved energy resolution and pattern recognition capabilities. The use of an admixture in Gaseous Xe detectors -specially an additive with a closer ionization potential to the first metastable level of Xe- allows to enhance the gain and improve the energy resolution respect to the pure Xe; there are the so-called Penning mixtures. Two Xe-based Penning mixtures were studied experimentally in a small TPC prototype of 2.4 l of volume: a xenon+neon (Xe+Ne) and a xenon+trimethylamine (Xe+TMA) mixture. Measurements of electronic drift and multiplication properties were performed in view of possible application for the observation of the neutrinoless double beta decay and the identification of galactic dark matter. The conclusions drawn in the study are described below:

- A complete characterization of Xe+TMA mixtures was carried out, measuring drift and multiplications properties, as well as energy resolution for X- and γ -rays. In general, the performance of a TPC detector based on Xe+TMA mixtures is comparable to optimum values typically obtained with benchmark Micromegas mixtures (e.g. optimized Ar-isobutane mixtures). Results presented in this work demonstrate that Xe+TMA mixtures may be a mixture of choice, specially at high pressures, in applications envisaging the use of Xe as conversion gas and Micromegas as readout plane.
- We conclude that a mixture of Xe (which should be enriched in ^{136}Xe) with TMA concentration between 1-2% is very attractive for neutrinoless double decay searches. The most important advantage of this mixture is the improvement in energy resolution, reaching values that fulfill the requirements of an experiment of this type. In particular, values of energy resolution of 7.3% (9.6%) FWHM at 1(10) bar for 22.1 keV were attained, which extrapolate into 0.7% (0.9%) FWHM at $Q_{\beta\beta}$. Gains up to a factor ~ 100 higher and required amplification fields at least 40% lower than in pure Xe were achieved. On the other hand, the drift velocity in Xe+TMA mixtures is higher than in pure Xe in the range 50-400 V/cm/bar, reaching values up to an order of magnitude superior; for instance, for a reduced drift field (E_d/P) of 300 V/cm/bar the drift velocity in a Xe+2.2%TMA mixture is 1.3 cm/ μs and for pure Xe 0.14 cm/ μs .

A reduction of the longitudinal diffusion coefficient by a factor about 3 respect to pure Xe was also observed. This result validates a theoretical study in this mixture performed in [178], and it implies that with this mixture the

topological cut to discriminate between $0\nu\beta\beta$ signal and background will be more efficient.

The evidence that this mixture acts as wavelength-shifter may allow to collect more efficiently the electroluminescence signal in a TPC working in both modes electroluminescence and charge.

The characterization of Xe+TMA mixtures in a small TPC (2.4 l), allowed to improve the performance of a larger prototype operated also with microbulk-Micromegas readout plane (70 l, active volume ~ 25 l) by using TMA as admixture, with concentrations within the optimum found in this work. Results from that prototype so far at 10 bar showed to be compatible from those obtained in the small one. This reinforces our conclusion - use of Xe+TMA mixtures for neutrinoless double beta decay searches is very competitive option - extending it to a larger scale with conditions similar to a real experiment for double beta decay searches.

- A novel configuration formed by two symmetric drift regions equipped with two microbulk Micromegas readouts was launched, by this the recombination of the collected charge from α -particles and γ -rays -emitted in coincidence by an ^{241}Am source- is studied. With this setup the longitudinal diffusion coefficient and the drift velocity were measured, as well as the electron lifetime. Results of drift velocity and longitudinal diffusion coefficient are compatible with previous experimental measurements and show a reasonable agreement with Magboltz, although with up to 50% deviations in case of the diffusion coefficient. Gains curves of α -particles and γ -rays are compatible for a fix pressure and mixture, which implies a quenching factor near to 1. On the other hand, electron life time was also measured for $E_d/P > 20$ V/cm/bar, setting a lower limit of $\tau_e > 1$ ms which allowed to discard attachment for the measurements.

The dependence of the collected charge ratio generated by α -particles and γ -rays on the reduced drift field shows that the recombination is stronger for α -particles, as expected considering that α -particles are highly ionizing radiation.

Columnar recombination effect was observed for α -particles, for pressures between 3 and 8 bar. For small angles the charge is less than for large angles. The definition of a figure of merit as Q_0/Q_{90} , representing the charge relation between tracks with small and large track angles, permitted to evaluate the dependence of the effect with E_d/P , pressure and TMA concentration. The columnar recombination increases with the reduced drift field, reaching a maximum around 40 V/cm/bar, and becomes increasingly smaller thereafter. A slight increase of columnar effect with pressure is observed with the TMA concentration. This should be confirmed in future measurements. These results are qualitatively in agreement with the existent theory for columnar recombination, next steps will focus on modeling the experimental data within

the Jaffé theory. Apart from this, possible electron-ion recombination in the amplification region is being studied; in this way further experimental work is needed, measurements at different amplification will be done to discard any recombination effect in the amplification region.

These results represent a first step towards the evaluation of the idea to use Xe+TMA mixture as medium gas for directional dark matter searches on virtue of the columnar recombination effect. To validate this idea for WIMP searches measurements with particles such as neutrons or pions, which produce nuclear recoils as WIMPs, should be done.

- Measurements in Xe+Ne mixtures with α -particles of 5.4 MeV, indicate that a microbulk Micromegas High Pressure TPC with Ne concentration between 20 and 30% may be optimum; in these conditions improvements in gain by a factor 2-3, and in energy resolution at high pressure are obtained ($\sim 2\%$ FWHM at 7 bar). In addition, drift velocity for Xe+Ne mixtures is also larger than for pure Xe in the range 10-300 V/cm/bar. For instance at 100 V/cm/bar, the value is 0.16 cm/ μ s for a Xe+20%Ne mixture, which implies a factor 1.6 above than in pure Xe (0.10 cm/ μ s). Although with this admixture substantial Ne concentrations ($>20\%$) should be added to improve the performance respect to pure Xe, this mixture may be specially recommended for application at low energy as for axions and dark matter searches, where the presence of a lighter noble gas is of interest.
- Optimum conditions to quantify the concentration of TMA components of mixtures were obtained by successfully installing of a Quadrupole Mass Spectrometer into the gas system of the HP Xe-based TPC. A calibration procedure was established -specially for Xe+TMA mixtures- for which mixtures at several concentrations were prepared and the calibration factor was calculated. It was observed that quantification of oxygen -essential for Xe gas detector- can not be done at order of ppm due to the high irreducible background of the instrument.

Resumen y Conclusiones

Resumen

La búsqueda de la desintegración doble beta sin neutrinos y la detección de materia oscura son de gran interés en Física de Partículas y Astrofísica, porque el resultado positivo de alguna de estas dos búsquedas tiene grandes implicaciones en los dos campos [4, 2, 3]. La detección de la desintegración doble beta sin neutrinos ($\beta\beta 0\nu$) permitiría determinar la masa del neutrino y su naturaleza, y la detección de materia oscura conduciría a explicar la composición e influencia del 26.8% del universo que ocupa esta materia. A pesar de que para los dos procesos se han realizados grandes esfuerzos experimentales, no se han tenido resultados positivos concluyentes.

El proyecto europeo T-REX surge con el objetivo de desarrollar detectores gaseosos de última generación para la detección de sucesos poco probables, en base a la utilización de Micromegas de tipo microbulk como planos de lectura de carga. Desde la invención de estos dispositivos, la Física en detectores gaseosos ha ganado importancia en diversas aplicaciones; astronomía, instrumentación médica y en los últimos años ha adquirido gran relevancia en la Física de Partículas. Actualmente el proyecto trabaja en dos líneas principales: la primera para la detección de axiones -rayos-X de baja energía- para el experimento CAST (CERN Axion Solar Telescope) y el futuro IAXO, y la segunda para la desintegración doble beta dentro del proyecto NEXT (Neutrino Experiment with a Xe TPC) así como la detección de WIMPs de baja masa (prototipo TREX-DM).

Principalmente en esta tesis se estudió la posibilidad de adicionar un gas secundario al Xe -en particular un gas cuyo potencial de ionización (PI) esté por debajo del primer nivel metaestable del gas principal, conformando las denominadas mezclas Penning- esto permite que la energía de desexcitación del gas principal se transforme en ionización del gas secundario. De esta forma se obtiene un incremento de ganancia y además mejora en la resolución de energía. En particular, se estudiaron dos mezclas Penning formadas a partir del Xenon. En la primera mezcla xenon+neon (Xe+Ne), la energía de desexcitación del Ne es transferida en ionizaciones del Xe, debido a que el PI del Xe (12.12 eV) está por debajo del primer nivel metaestable del Ne (15.1 eV). Además la adición de un gas noble más ligero como lo es el Ne, permite la reducción de la radiación de frenado (*bremsstrahlung*) y de la dispersión múltiple. La segunda mezcla estudiada es xenon+trimetilamina (Xe+TMA), este aditivo molecular fluorescente, forma una mezcla Pennig con el Xe; en este caso la energía de desexcitación de Xe (primer nivel metaestable 8.3 eV) se transfiere al TMA (PI= 8.32 eV). Estudios experimental previos de varios aditivos Penning, mostraron que con el TMA se obtenía la mayor ganancia a campo fijo y la mejor resolución en energía. Además esta molécula absorbe energía del Xe y luego la emite con una longitud onda de mayor (*wavelength-shifting*), lo que permite que la recolección de luz se haga de una forma más eficiente en un detector

que mida electroluminiscencia. Además la adición de TMA reduce la difusión e incrementa la velocidad de deriva de los electrones.

Introducción

Desintegración Doble Beta sin Neutrinos

La desintegración doble beta sin neutrinos ($\beta\beta 0\nu$) es relevante porque es el método más sensible para determinar la denominada masa efectiva del neutrino y además su naturaleza, Dirac ($\nu \neq \bar{\nu}$) o Majorana ($\nu = \bar{\nu}$). La desintegración $\beta\beta$ es un proceso de segundo orden que se produce solamente en núcleos con número par de neutrones y protones, para los cuales la desintegración β está prohibida energéticamente o fuertemente suprimida por el cambio de momento angular. Esta desintegración puede tener tres modos, de los cuales son conocidos dos principalmente. El primer modo, la *Desintegración Doble Beta con Emisión de Neutrinos* ($\beta\beta 2\nu$) conserva el número leptónico y está dentro del Modelo Estándar; las vidas medias se encuentran en un rango de $10^{18} < T_{1/2}^{2\nu} < 10^{25}$ años. Por el contrario, en el segundo modo, la *Desintegración Doble Beta sin Neutrinos* ($\beta\beta 0\nu$), el número leptónico no se conserva y está por fuera del Modelo Estándar, su observación implica que el neutrino es una partícula de Majorana masiva ($\nu = \bar{\nu}$, $m_\nu \neq 0$) y las vidas medias podrían estar por encima de $T_{1/2}^{0\nu} > 10^{25}$ años. En el primer modo la energía disponible en la transición (Q) se reparte entre los electrones y los dos neutrinos, siendo la señal un espectro continuo centrado en $Q/3$ finalizando en Q . Por el contrario en el segundo modo la energía se la llevan completamente los dos electrones, así la señal es un pico con energía Q y su anchura depende de la resolución de energía del detector.

Los esfuerzos experimentales de la primera generación de experimentos para la detección directa de la desintegración doble beta, solo han permitido medir el primer modo para una decena de núcleos, utilizando masas de hasta unos kg de isotopo $\beta\beta$, llegando a explorar vidas medias para el segundo modo entre 10^{23} - 10^{25} años, que equivale explorar masas efectivas del neutrino entre 250-1000 meV. El principal reto de la nueva generación de experimentos es mejorar la sensibilidad, poniendo en marcha detectores con masas del isótopo $\beta\beta$ del orden de 100 kg y reducir al máximo el fondo radiactivo, con el objetivo de explorar masas efectivas del neutrino del orden de decenas de meV. La mayoría de experimentos de nueva generación se encuentran en etapa de I+D, otros en construcción y pocos tomando medidas.

Las cámaras de proyección temporal (TPCs) basadas en Xe son una opción muy competente que ha venido cobrando importancia, su principal ventaja respecto a otras técnicas es que se logra una identificación topológica que permite discriminar la señal buscada del fondo y una excelente resolución de energía. El experimento EXO utiliza 175 kg de Xe líquido, y fue el primero en medir la desintegración $\beta\beta 2\nu$ en ^{136}Xe ($T_{1/2}^{2\nu} = 2.17 \times 10^{21}$ años), y para el modo $\beta\beta 0\nu$ ha obtenido un límite de $T_{1/2}^{0\nu} > 1.6 \times 10^{25}$ años. Sin embargo, la principal desventaja de utilizar Xe líquido es que la resolución de energía es limitada por las fluctuaciones primarias, así como también, la identificación topológica por la alta densidad. Así que una

solución es utilizar una TPC en Xe gas a alta presión lo que permitiría obtener una excelente resolución de energía y al mismo tiempo una identificación topológica. El experimento NEXT planea construir una TPC de 100 kg trabajando a 10 bar, con plano electroluminiscente [5]. Una de las líneas que se han venido estudiando en la fase de I+D es utilizar como plano de lectura detectores Micromegas; estos detectores han mostrado ser una tecnología competente desde su invención en el año 1996 [11]. Principalmente la resolución de energía, y el bajo contenido radiactivo hacen que esta tecnología sea atractiva para ser usada en experimentos $\beta\beta 2\nu$ [188, 189].

Detección de Materia oscura direccional

La materia oscura compone el 26.8% de la masa total del universo, su presencia fue postulada desde 1933 al estudiar la luminosidad de los cúmulos de galaxias. Diversas observaciones evidencian desde entonces la necesidad de la existencia de materia oscura, como las curvas de rotación planas de las galaxias espirales o el efecto de lente gravitacional. La composición de la materia oscura se desconoce; se ha propuesto como constituyentes a los neutrinos, los axiones o los genéricamente denominados WIMP's ("Weakly Interacting Massive Particles"). Para su detección se han propuesto métodos directos (registrando la interacción de las partículas en un detector) e indirectos (registrándose los productos de la aniquilación de las partículas de materia oscura). Para la identificación inequívoca de la materia oscura galáctica en un experimento de detección directa se ha propuesto la búsqueda de señales distintivas, como la modulación anual de los ritmos producida por el movimiento de la Tierra en torno al sol o la direccionalidad.

Una TPC basada en tecnología Micromegas en Xe+TMA podría ser utilizada para la detección direccional de materia oscura. El hecho de que en una mezcla de Xe+TMA la recombinación columnar permita la identificación de la dirección del retroceso nuclear producido por la interacción de un WIMP², permitiría confirmar el origen de una señal positiva de materia oscura [6, 7]. En el grupo de Zaragoza como parte de trabajos de I+D se empezó a explorar esta opción, en base al estudio de la recombinación de partículas α en mezclas de Xe+TMA.

Medidas de partículas α en Xe puro y mezclas de Xe+Ne

Las primeras medidas que se realizaron fueron en Xe puro, estas medidas fueron hechas para 2, 4, 6 y 8 bares. Después se realizaron medidas con mezclas de Xe+Ne, para presiones entre 2 y 7 bar. En los dos casos se trabajó sin recircular el gas, lo que implicaba tener más oxígeno en el sistema; liberado por los materiales de las paredes de la cámara y de la deriva (*outgassing*). Este efecto produce pérdidas de carga, sufridos durante el proceso de deriva de los electrones por la captura de electrones por parte de átomos o moléculas electronegativas (*attachment*)

²La recombinación columnar ocurre para electrones que escapan a la recombinación inicial asociada a los iones padre.

-principalmente oxígeno.

Las medidas con mezclas de Xe+Ne se realizaron recuperando el gas después de cada medida, lo que disminuyó de forma considerable el efecto producido por el *attachment*. Esto fue posible gracias a la incorporación de un sistema de recuperación de Xe, que consiste en condensar el Xe en una botella que se enfría a temperaturas criogénicas a través del uso de Nitrógeno líquido. Este sistema actúa como una bomba de vacío, y permite recuperar el Xe desde el sistema de gas y la TPC, una vez finalizadas las medidas.

Para estas medidas se utilizó una fuente de ^{241}Am que emite partículas alfa de 5.4 MeV. En estas medidas se varió el voltaje de deriva y el de amplificación, lo que permitió estudiar la transmisión, la ganancia del gas la resolución en energía y la velocidad de deriva. Para las medidas en Xe, como era esperado se observó un efecto de *attachment* bastante mayor, evidente en la correlación obtenida entre la carga y el ángulo de la traza de la partícula. Sin embargo para las mezclas de Xe+Ne, el efecto de *attachment* fue prácticamente despreciable, sobre todo para presiones por debajo de 5 bares.

Para las medidas con Xe+Ne, se utilizaron concentraciones entre 10-50% (volumen). Los resultados obtenidos de la medida de velocidad de deriva están en acuerdo con los obtenidos en simulaciones con Magboltz dentro de un 20% de desviación. Para un dado campo eléctrico, la adición de Ne produce incremento en la ganancia. En particular, se observó que para una mezcla de Xe+50%Ne se obtienen ganancias de un orden de magnitud superiores comparadas con las de Xe puro. En la figura 5.1 se observan las curvas de ganancia, obtenidas para diferentes concentraciones de Ne, así como curvas de ganancia con Xe.

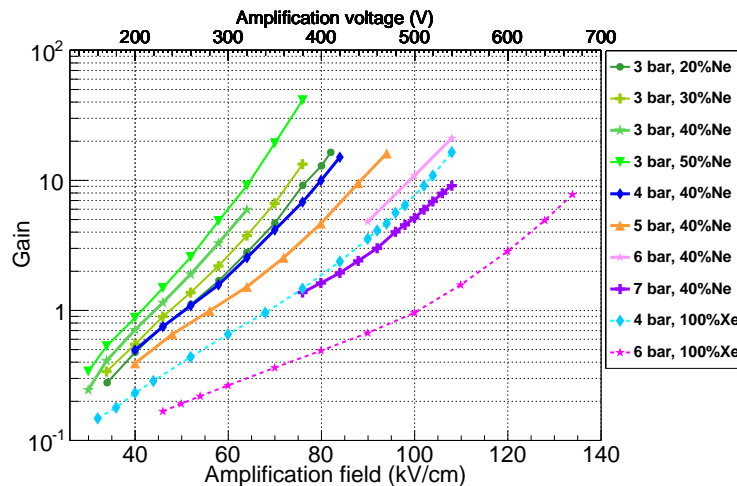


Fig. 5.1: Dependencia de la ganancia con el voltaje de amplificación para diferentes presiones en Xe puro y mezclas de Xe+Ne

Por otra parte los resultados de la resolución de energías se muestran en la figura 2.17. Se observa que al adicionar concentraciones de Ne (figura 5.2-izquierda),

mayores de 20%, la resolución en energía mejora; pasando de valores $\sim 3\%$ a valores por debajo del $\sim 2.5\%$. El comportamiento con la presión es observado en la figura 5.2 (derecha). En el caso de Xe puro la degradación en la resolución de energía es bastante considerable, mientras que para la mezclas de Xe+Ne se presenta una ligera degradación. En principio esta degradación de energía, puede ser generada por el efecto de *attachment*, o por un aumento en las fluctuaciones primarias con la presión.

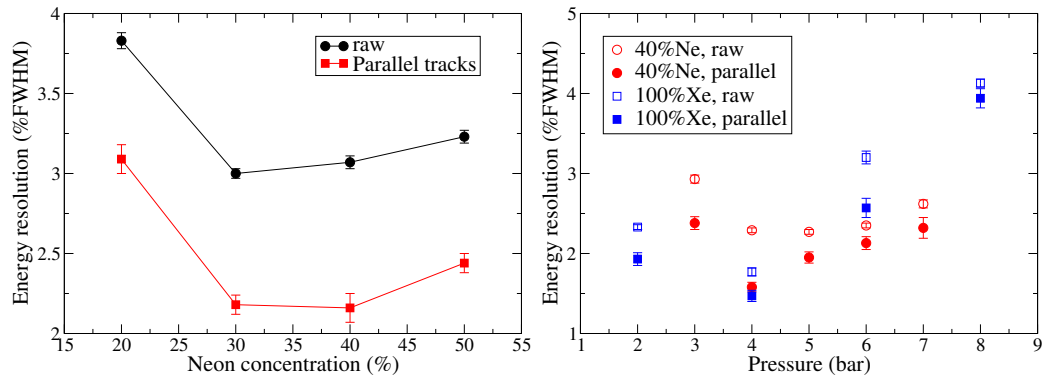


Fig. 5.2: Mejores valores de resolución de energía (%FWHM) para partículas- α de 5.4 MeV, en diferentes mezclas de Xe+Ne a 3 bares (izquierda), y en una mezcla de 60%Xe+40%Ne y Xe puro para diferentes presiones (derecha).

Medidas de rayos-X y rayos- γ en mezclas de Xe+TMA

La caracterización de la mezcla de Xe+TMA fue posible gracias a la instalación de un espectrómetro de masas al sistema de gas. Medidas del comportamiento de la presión de vacío, y de los gases residuales del instrumento fueron realizadas para determinar las condiciones óptimas de medida. Además un proceso de calibración para mezclas de Xe+TMA fue establecido, lo que permitió determinar la concentración de TMA con un nivel de error dentro del 10%.

De esta forma medidas de ganancia y resolución de energía para rayos X de 22.1 keV fueron realizadas para diferentes concentraciones de TMA y presiones entre 1 y 10 bares (1, 5, 8 y 10 bares). En la figura 5.3 (izquierda) se observa la variación de la ganancia para un valor fijo del campo de amplificación para cada presión estudiada, y en la figura 5.3 (derecha) el comportamiento de la resolución de energía en función de la concentración de TMA. Apartir de estos resultados se concluye que dentro del rango entre 1-2% la ganancia es máxima y los mejores valores de resolución de energía son obtenidos.

Por otra parte, la presión fue variada sistemáticamente entre 1 y 10 bares utilizando una mezcla dentro del rango óptimo determinado previamente (1-2%). Los resultados de los mejores valores de resolución de energía son mostrados en la figura 5.4. Además en esta figura se han introducidas medidas en Xe puro con rayos- γ , realizadas antes de empezar a trabajar con mezclas de Xe+TMA.

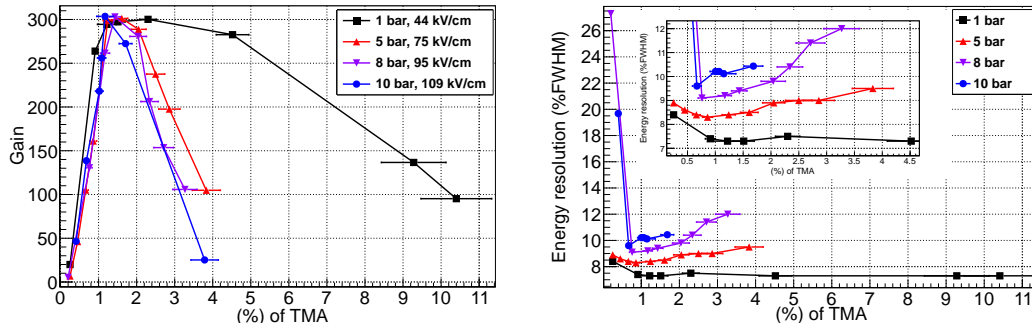


Fig. 5.3: Ganancia para valores fijos del campo de amplificación (izquierda) y mejores valores de resolución de energía en función de la concentración de TMA (derecha). En el rango entre 1-2% la ganancia es máxima y los mejores valores resolución de energía son obtenidos.

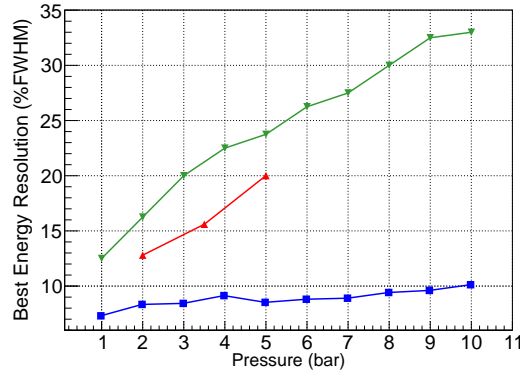


Fig. 5.4: Mejores valores de resolución de energía para rayos-X de 22.1 keV en función de la presión, para datos tomados de [38] (▼), para rayos- γ de 59.54 keV de este trabajo extrapolados a 22.1 keV (▲) en Xe puro, y para datos tomados en este trabajo (■) para mezclas de Xe+TMA.

Estudio de la recombinación en mezclas de Xe+TMA

Motivados por el posible uso de la señal de recombinación columnar en la determinación de la dirección de retroceso nuclear producida por la interacción de un WIMP en el detector [6, 7], fue puesta en marcha una novedosa configuración de deriva con el fin de estudiar la recombinación columnar de la carga producida por partículas- α . Esta configuración está basada en dos regiones de deriva simétricas con planos de lectura Micromegas en cada una de ellas para medir la coincidencia entre partículas- α y rayos- γ generadas por una fuente de ^{241}Am . Esta configuración permite medir la recombinación de la carga producida por rayos γ , así como medir las propiedades de deriva y multiplicación de los electrones. Y una de sus ventajas es que medidas de la vida media del electron pueden realizarse, y de esta forma determinar el attachment.

La medida de recombinación columnar para la carga generada por partículas-

α , fue realizada a través del estudio de la carga en función del ángulo de la traza respecto a la dirección del campo eléctrico. Experimentalmente se guardan los pulsos generados por las señales α , los cuales son analizados con una aplicación desarrollada en ROOT [160]. Para cada señal se obtiene la altura y risetime, y estos a su vez son transformados a carga y a ángulo. Como resultado se observa una dependencia de la carga con el ángulo de la traza: para trazas paralelas la carga es menor que para trazas perpendiculares. Esta dependencia fue observada para las presiones estudiadas en el rango de 3-6 bares y para las concentraciones de TMA estudiadas. En la figura 5.5 se muestra para presiones de 4 y 8 bares, y para varios campos eléctricos reducidos.

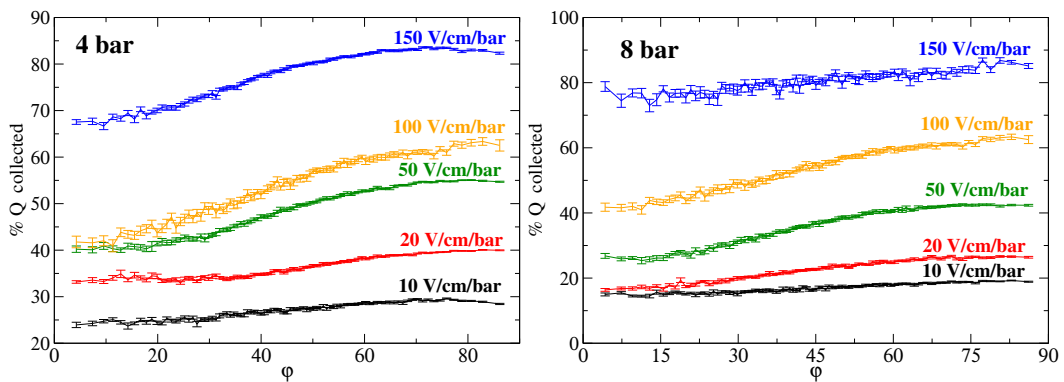


Fig. 5.5: Dependencia del porcentaje de carga como función del ángulo de la traza respecto al campo eléctrico (φ) a 4 bar (izquierda) y 8 bar (derecha). Esta dependencia es compatible con los modelos existentes de la recombinación columnar.

Con el fin de cuantificar el efecto, se definió una figura de mérito, dada por Q_0/Q_{90} ; valores bajos implican un efecto mayor de recombinación columnar, debido a que la carga generada por partículas con trazas cercanas a la dirección del campo es mucho menor que las generadas por trazas perpendiculares a la dirección del campo. Los resultados para todas las configuraciones se encuentran en la figura 5.6. Para valores bajos de E_d/P , Q_0/Q_{90} es alto, la dependencia con el ángulo es menor; en cuanto incrementa E_d/P se observa un mayor efecto columnar que llega a ser máximo para valores entre 30–40 V/cm/bar y a partir de este valor la dependencia con el ángulo vuelve a disminuir.

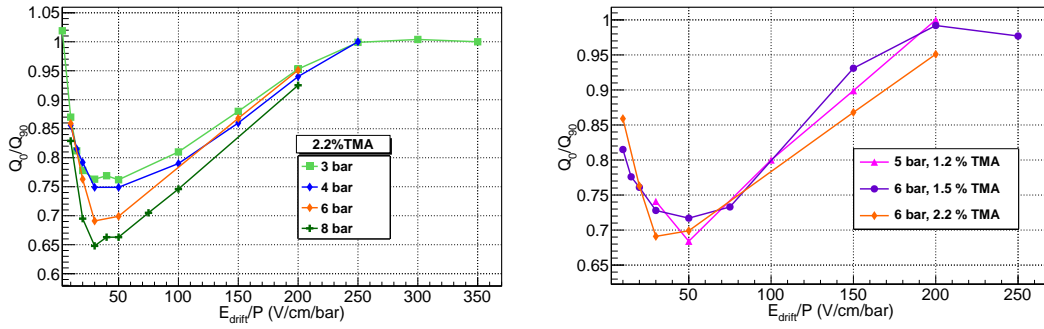


Fig. 5.6: Dependencia de Q_0/Q_{90} con E_d/P para diferentes presiones en una mezcla de Xe+2.2%TMA (izquierda) y para dos concentraciones a 5 y 6 bar (derecha).

Conclusiones

En esta tesis fue estudiada la respuesta de una Cámara de Proyección Temporal a alta presión, utilizando como medio de detección mezclas Penning con Xe como gas principal y planos de lectura Micromegas de tipo microbulk con el fin de detectar sucesos poco probables. Durante los últimos años los detectores gaseosos se han convertido en una opción competitiva, principalmente debido a su buena resolución en energía y capacidad de de reconstruir la topología de los eventos. La utilización de un aditivo en detectores gaseosos de Xe -específicamente un aditivo cuyo potencial de ionización esté muy cercano al primer nivel metaestable de Xe permite incrementar la ganancia y mejorar la resolución en energía respecto al Xe puro. Se han estudiado experimentalmente dos mezclas Penning en un prototipo pequeño (TPC de 2.4 l): mezclas de xenon+neon (Xe+Ne) y xenon+trimetilamina (Xe+TMA). Se realizaron medidas de las propiedades electrónicas de deriva y de multiplicación, en vistas a la aplicación en la búsqueda de la desintegración doble beta sin neutrinos y detección de materia oscura galáctica. Las conclusiones son descritas a continuación:

- Una completa caracterización de la mezcla Xe+TMA fue realizada, para la cual se midieron las propiedades electrónicas de deriva y de multiplicación, además de la resolución en energía de rayos X y γ . En general, el funcionamiento de una TPC utilizando mezclas de Xe+TMA como gas de llenado, es comparable al observado en mezclas de referencia (como Ar+isobutano). Los resultados presentados en este trabajo demuestran que mezclas de Xe+TMA pueden ser utilizadas en detectores gaseosos que utilicen Xe y Micromegas como planos de lectura.
- Se concluye que un detector gaseoso en Xe (adecuadamente enriquecido con ^{136}Xe), al adicionar concentraciones de TMA en el rango 1-2% es una opción muy atractiva para la búsqueda de la desintegración doble beta sin neutrinos. La ventaja principal que presenta esta mezcla es la mejora en la resolución en

energía, la cual llega a cumplir los requerimientos de un experimento de este tipo. Específicamente, valores de resolución de energía de 7.3% (9.6%) FWHM a 1(10) bar para 22.1 keV fueron obtenidos, estos valores extrapolan a 0.7% (0.9%) FWHM para el valor $Q_{\beta\beta}$. Se han medido valores de ganancia por encima de un factor ~ 100 , aplicando campos de amplificación por lo menos un 40% más bajos que en Xe puro. Por otra parte, la velocidad de deriva de mezclas de Xe+TMA medida es superior que en Xe puro en el rango 50-400 V/cm/bar, llegando a ser hasta un orden de magnitud mayor; por ejemplo para un campo de deriva reducido (E_d/P) de 300 V/cm/bar la velocidad en una mezcla de Xe+2%TMA la velocidad medida es 1.3 cm/ μ s y para Xe puro 0.14 cm/ μ s.

Una reducción del coeficiente de difusión por un factor 3 respecto a Xe puro fue obtenida. Este resultado experimental valida el estudio teórico [178], e implica que con esta mezcla los cortes topológicos para discriminar entre la señal buscada y eventos de fondo serán más eficientes.

La evidencia experimental de que el TMA puede cambiar la longitud de onda de los fotones emitidos (wavelength-shifter) permitiría recoger más eficientemente la señal de luz (electroluminescencia) en una TPC trabajando en modo carga y luz.

La caracterización de mezclas de Xe+TMA en el prototipo pequeño (2.4 l) permitió mejorar el funcionamiento de un prototipo de mayor tamaño, también equipado con Micromegas tipo microbulk como plano de lectura (70 l, volumen activo ~ 25 l) por medio del uso de esta mezcla. Los resultados obtenidos con el prototipo de mayor tamaño hasta el momento muestran ser compatibles con los medidos en el pequeño. Este resultado refuerza nuestra conclusión -el uso de mezclas de Xe+TMA son una opción muy competitiva- que los extiende a escalas en las cuales hay condiciones similares a las de un experimento real de búsqueda de la desintegración doble beta sin neutrinos.

- Una novedosa configuración formada por dos regiones de deriva simétricas, equipada cada una con plano de lectura de tipo microbulk Micromegas fue puesta en marcha. Con esta configuración se pudo estudiar la recombinación de la carga producida por partículas α y rayos γ emitidos en coincidencia por una fuente de ^{241}Am . Los resultados obtenidos de velocidad de deriva y el coeficiente de difusión longitudinal presentan valores compatibles con previas medidas experimentales en el mismo gas en similares condiciones (prototipo de 70 l), y concuerdan con valores obtenidos por Magboltz, aunque muestran hasta un 50% de desviación para el caso de la difusión. Las curvas de ganancias medidas, para una presión y mezcla fijas, de partículas α y rayos γ fueron compatibles, lo que implica un *quenching* cercano a 1. Por otro lado, la vida media del electron para $E_d/P > 20$ V/cm/bar fue también medida, lo que permitió establecer un limite inferior de $\tau_e > 1$ ms, este límite es compatible con valores muy bajos de oxígeno; esto permite descartar que las medidas

estén dominadas por *attachment*.

La fracción de carga generada por partículas- α y rayos- γ mostró que la recombinación para partículas- α es que para rayos- γ , como era esperado dado que estas partículas son altamente ionizantes.

El efecto de recombinación columnar fue observado para partículas- α , en el rango de presiones entre 3 y 8 bares. Para trazas paralelas la carga es menor que para trazas perpendiculares. La definición de la figura de mérito, dada por Q_0/Q_{90} , permitió evaluar el efecto para diferentes condiciones. Para valores bajos de E_d/P el efecto columnar es menor; en cuanto E_d/P incrementa se observa una mayor dependencia que llega a ser máxima para valores entre 30-40 V/cm/bar y a partir de este valor la dependencia con el ángulo vuelve a disminuir. La utilización de dos mezclas diferentes permitió observar una ligera dependencia con la concentración de TMA. Aparte de esto, un posible efecto de recombinación en la zona de amplificación está siendo estudiado; este efecto podría generar el mismo comportamiento que estamos observando. Este efecto será analizado en futuras medidas para diferentes campos de amplificación. Es importante notar, que el efecto observado está cualitativamente en acuerdo con los modelos existentes de recombinación columnar, el paso siguiente sería intentar modelar nuestros resultados teóricamente.

En vista a una posible aplicación para búsqueda de la direccionalidad en la detección de materia oscura será necesario medir con partículas que induzcan retrocesos nucleares como los WIMPs, y de esta forma observar si el efecto se mantiene y es tan fuerte como para permitir la discriminación angular de los retrocesos nucleares.

- Medidas con mezclas de Xe+Ne con partículas- α fueron llevadas a cabo en la TPC, de las cuales se concluye que una mezcla con concentraciones de Ne entre el 20 y el 30% puede ser óptima; en estas condiciones se obtuvieron mejoras en la ganancia por un factor entre 2-3 y en la resolución de energía a alta presión ($\sim 2\%$ FWHM at 7 bar). Además los valores de la velocidad de deriva de diferentes mezclas, mostraron ser superiores a los obtenidos para Xe puro en el rango de 10-300 V/cm/bar. Por ejemplo para 100 V/cm/bar, un valor de 0.16 cm/ μ s para una mezcla de Xe+20%Ne, lo que implica un factor 1.6 por encima de Xe puro (0.10 cm/ μ s). A pesar de que para esta mezcla es necesario adicionar cantidades considerables de Ne para mejorar las condiciones de operación ($>20\%$), sin embargo, una mezcla de Xe+Ne podría ser utilizada para aplicaciones de baja energía como en el caso de la detección de axiones o materia oscura, en las cuales la presencia de un gas ligero es de interés.
- Condiciones óptimas de medida para la cuantificación de la concentración de TMA fueron obtenidas por medio de la puesta en marcha de un espectrómetro de masas dentro del sistema de gas. Un procedimiento de calibración fue establecido para mezclas de Xe+TMA, en el que se prepararon mezclas con

diferente concentración determinando el factor de calibración para cada una de ellas. Fue observado que la cuantificación de oxígeno no puede ser realizada con este sistema en el orden de ppm, debido a que el fondo del instrumento es muy alto.

Appendices

Assessment of material Radiopurity for Rare Event Experiments by γ -spectrometry

A screening program based on gamma-ray spectrometry using an ultra-low background HPGe detector in the Canfranc Underground Laboratory is being developed for several years, with the aim to measure the activity levels of materials used in the Micromegas planes and also in other components involved in a plausible experimental setup: gas vessel, field cage, electronic boards, calibration system or shielding. The results obtained have been published in [57]. The γ -spectrometry system will be described and the main results will be presented and discussed.

A.1 Overview

All germanium spectroscopy measurements described here were carried out using a ~ 1 kg detector from the University of Zaragoza named Paquito and operated at LSC. Since the laboratory is located at a depth of 2450 m.w.e., the cosmic muon flux is about 5 orders of magnitude lower than at sea-level surface. Radon activity in the air is between 50 and 80 Bq/m³ in the underground halls [190]. The detector is a p-type close-end coaxial High Purity germanium detector, with a crystal of 190 cm³ and a copper cryostat. It is operated inside a shield made of 10 cm of archaeological lead plus 15 cm of low activity lead, enclosed in a plastic bag continuously flushed with boil-off nitrogen to avoid radon intrusion (see Fig. A.1, a). The electronic chain for the data acquisition is based on standard Canberra 2020 Linear Amplifier and Canberra 8075 Analog-to-Digital-Converter modules. This detector has been used for radiopurity measurements at Canfranc for some years (details can be found in [42]).

The background of the detector, produced by the shielding and the surrounding materials, is characterized by taking data with no sample for periods of time of at least one month, due to the low counting rates.

The activity A of nuclei producing a gamma emission of a certain energy can be estimated as:

$$A = \frac{S}{\varepsilon IT} \quad (\text{A.1})$$

being S the number of events at the gamma line due to the sample, ε the full-energy peak detection efficiency at the corresponding energy, I the intensity of the

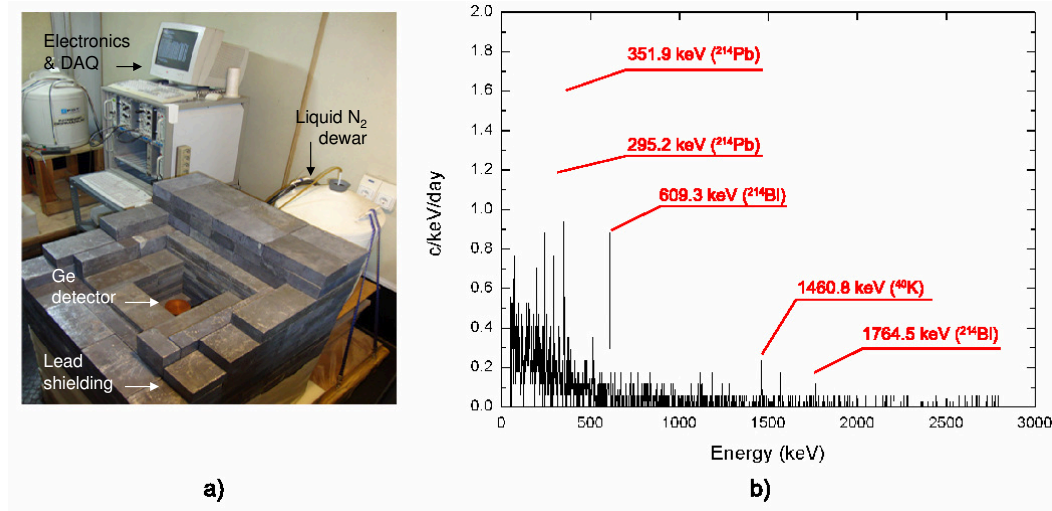


Fig. A.1: a) The germanium detector used for material screening inside its lead shielding at LSC. b) Energy spectrum registered by the detector in a background measurement; the main gamma lines from isotopes of the ²³⁸U and ²³²Th chains and from ⁴⁰K are marked.

emission and T the time of the measurement. When several gamma emissions from the same isotope are available, activities from each line are properly averaged taking into account their uncertainties. Upper limits at 95% C.L. are derived if the gross signal does not statistically differ from the background signal [191, 192]. Detection efficiency is determined by Monte Carlo simulations based on the Geant4 [158] code for each sample, accounting for intrinsic efficiency, the geometric factor and self-absorption at the sample. Special care is taken to reproduce the dimensions, composition and density of the samples in the simulation code. Validation has been made by comparing the efficiency curve of the detectors measured with a ¹⁵²Eu reference source of known activity located at 25 cm from the detector with the simulated one (see Fig. A.2). A safe, overall uncertainty of 30% is considered for the deduced efficiency and properly propagated to the final results.

Activities of different sub-series in the natural chains of ²³⁸U, ²³²Th and ²³⁵U as well as of common primordial, cosmogenic or anthropogenic radionuclides like ⁴⁰K, ⁶⁰Co and ¹³⁷Cs are typically evaluated by analyzing the most intense gamma lines of different isotopes. Outgassing and chemical procedures in materials can make secular equilibrium in radioactive chains break, so information provided by germanium detectors at the different stages is very important. For ²³⁸U, emissions from ²³⁴Th and ^{234m}Pa are searched to quantify the activity of the upper part of the chain and lines from ²¹⁴Pb and ²¹⁴Bi for the sub-chain starting with ²²⁶Ra down to ²¹⁰Pb. For ²³²Th chain, emissions of ²²⁸Ac are analyzed for the upper part and those of ²¹²Pb, ²¹²Bi and ²⁰⁸Tl for the lower one. Concerning ²³⁵U chain, only emissions from the parent isotope are taken into account.

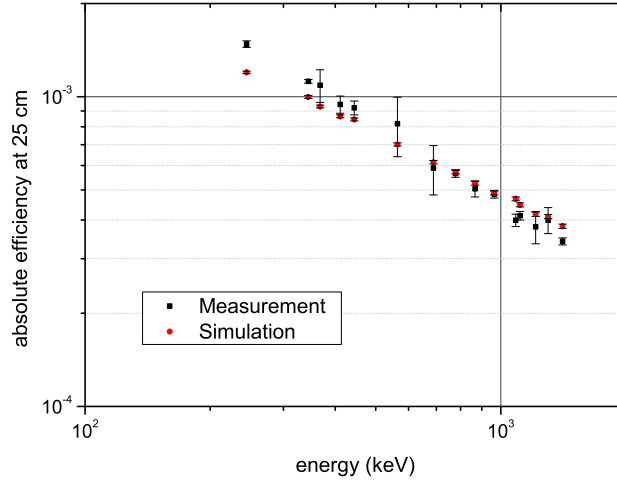


Fig. A.2: Comparison of the absolute efficiency curve measured for Paquito detector with a ^{152}Eu reference source located at 25 cm and the one deduced from the corresponding Geant4 simulation.

In addition to the germanium measurements, some samples have been analyzed by Glow Discharge Mass Spectrometry (GDMS). Similarly to other techniques also based on mass spectrometry, it is fast and requires only a small sample of the material. The GDMS analysis was made by Evans Analytical Group in France.

A.2 Measurements and results

A wide range of materials and components related to Micromegas readout planes and the whole setup of TPCs have been taken into consideration. They make part of vessel, field cage, radiation shielding or electronic acquisition system. Massive elements and those in contact with the sensitive volume of the detector are in principle the most relevant. Pictures of some of the samples are collected in Fig. A.3. Table A.1 shows the results deduced by GDMS. For the measurements using the germanium detector, details concerning the size of the sample and the time of data taking are presented in Table A.2 and the activity values obtained are summarized in Table A.2; reported errors correspond to 1σ uncertainties including both statistical and efficiency uncertainties.



Fig. A.3: Selection of pictures of some the samples screened with the germanium detector in LSC. Identifying numbers used in Tables 2-4 are indicated.

Table A.1: Activities derived for different Pb and Cu metal samples from GDMS measurements.

#	Material	Supplier	Units	^{238}U	^{232}Th	^{40}K
1	Pb	Mifer	mBq/kg	<1.2	< 0.41	0.31
2	Pb	Mifer	mBq/kg	0.33	0.10	1.2
3	Pb	Tecnibusa	mBq/kg	0.73	0.14	0.91
4	Cu (ETP)	Sanmetal	mBq/kg	<0.062	<0.020	
5	Cu (C10100, hot rolled)	Luvata	mBq/kg	<0.012	<0.0041	0.061
6	Cu (C10100, cold rolled)	Luvata	mBq/kg	<0.012	<0.0041	0.091

Table A.2: Information for the measurements performed with the germanium detector: material, samples size (mass, area or number of pieces) and screening time.

#	Material, Supplier	Sample size	Screening time (d)
7	Cu, Luvata	681 g	39.17
8	304L Stainless Steel, Pfeiffer	347 g	19.55
9	Al cathode, CAST	55 g	25.90
10	Cu cathode, CAST	176 g	33.23
11	PEEK, Sanmetal	459 g	24.27
12	Teflon, Sanmetal	945 g	37.99
13	Teflon tube, RS	91 g	35.33
14	Stycast, Henkel	551 g	17.67
15	Epoxy Hysol, Henkel	245 g	39.64
16	SMD resistor, Farnell	50 pc	18.15
17	SM5D resistor, Finechem	100 pc	31.45
18	Connectors, Samtec	10 pc (2.2 g/pc)	13.76
19	Connectors, Panasonic	15 pc (0.67 g/pc)	7.58
20	Solder wire, Multicore	91 g	7.74
21	Kapton-Cu PCB, LabCircuits	260.15 cm ²	35.28
22	PTFE circuit, LabCircuits	49 g	6.75
23	InGrid chip, U. Bonn	0.4 g	30.11
24	InGrid + PCB, U. Bonn	4.6 g	12.34
25	Classical Micromegas, CAST	2.6 g	32.
26	Microbulk Micromegas, CAST	2.8 g	34.
27	Kapton-Cu foil,CERN	5.9 g	34.48
28	Cu-Kapton-Cu foil,CERN	4.7 g	37.17
25	Vacrel, Saclay	65 g	32.38

Appendix A. Assessment of material Radiopurity for Rare Event Experiments by γ -spectrometry

#	Material	Supplier	Unit	^{238}U	^{226}Ra	^{232}Th	^{228}Th	^{235}U	^{40}K	^{60}Co	^{137}Cs
7	Cu (C10100)	Luvata	mBq/kg	<7.4	<0.8	<4.3	<18	<0.8	<1.2	<0.8	<1.2
8	304L Stainless Steel	Pfeiffer	mBq/kg	14.3 \pm 2.8	9.7 \pm 2.3	16.2 \pm 3.9	3.2 \pm 1.1	11.3 \pm 2.7	<1.6	<0.013	<0.018
9	Al cathode	CAST	Bq/kg	<0.08	0.42 \pm 0.09	0.33 \pm 0.06	0.49 \pm 0.13	<30	<85	<5.6	<6.4
10	Cu cathode	CAST	mBq/kg	<728	<27	<22	<7.8	8.3 \pm 3.0	<3.3	<1.2	<8.0
11	PEEK	Sanmetal	mBq/kg	36.3 \pm 4.3	14.9 \pm 5.3	11.0 \pm 2.4	<4.8	<19	510 \pm 170	<7.6	<4.5
12	Teflon	Sanmetal	mBq/kg	<157	<4.1	<6.6	<31	<0.006	<83	<4.2	<0.03
13	Teflon tube	RS	mBq/kg	<943	<21	<37	0.32 \pm 0.11	<0.05	0.19 \pm 0.08	<0.02	<0.005
14	Stycast	Henkel	Bq/kg	3.7 \pm 1.4	0.052 \pm 0.010	0.044 \pm 0.012	0.038 \pm 0.009	1.5 \pm 0.4	12.2 \pm 4.1	<0.6	<1.3
15	Epoxy Hysol	Henkel	mBq/kg	<273	<16	<14	<8	<0.95	4.1 \pm 1.5	<0.2	<0.8
16	SMD resistor	Farnell	mBq/pc	2.3 \pm 1.0	0.16 \pm 0.03	0.30 \pm 0.06	<8	<2	<257	<30	<36
17	SM5D resistor	Finechem	mBq/pc	0.4 \pm 0.2	0.022 \pm 0.007	<0.023	<0.016	<0.50	<40	<2	<2
18	Connectors	Samtec	mBq/pc	<77	9.2 \pm 1.1	19.6 \pm 3.6	18.5 \pm 2.2	<0.50	4.5 \pm 1.5	<0.16	<0.54
19	Connectors	Panasonic	mBq/pc	<42	6.0 \pm 0.9	9.5 \pm 1.7	9.4 \pm 1.4	<0.86	<5.7	<0.37	<0.37
20	Solder wire	Multicore	mBq/kg	<4900	770 \pm 120	<147	<14	<82	26 \pm 11	<1.3	<3.7
21	Kapton-Cu PCB	LabCircuits	$\mu\text{Bq}/\text{cm}^2$	<160	<14	<12	<8	<0.19	4.6 \pm 1.9	<0.10	<0.14
22	PTFE circuit	LabCircuits	Bq/kg	<36	4.7 \pm 0.6	5.0 \pm 1.1	6.2 \pm 0.9	<6.2	<46	<3.1	<3.1
23	InGrid chip	U. Bonn	mBq/pc	<46	<1.2	<1.8	<0.52	<14	57 \pm 25	<3.1	<1.6
24	InGrid chip + PCB	U. Bonn	mBq/pc	<407	47.7 \pm 7.0	57 \pm 11	45.0 \pm 7.0	<82	<7.7	<1.6	<1.6
25	Vacrel	Saclay	$\mu\text{Bq}/\text{cm}^2$	<19	<0.61	<0.63	<0.72	<0.19	<3.1	<3.1	<1.6
26	Classical Micromegas	CAST	$\mu\text{Bq}/\text{cm}^2$	<40	4.6 \pm 1.6	<9.3	<0.72	<6.2	<46	<3.1	<1.6
27	Microbulk cromegas	CAST	$\mu\text{Bq}/\text{cm}^2$	26 \pm 14	<9.3	<4.6	<4.6	<14	57 \pm 25	<3.1	<1.6
28	Kapton-Cu foil	CERN	$\mu\text{Bq}/\text{cm}^2$	<11	<4.6	<4.6	<4.6	<3.1	<7.7	<1.6	<1.6
29	Cu-kapton-Cu foil	CERN	$\mu\text{Bq}/\text{cm}^2$	<11	<4.6	<4.6	<4.6	<3.1	<7.7	<1.6	<1.6

Table A.3: Results obtained using the germanium detector for the activity of the natural chains and some common radioactive isotopes. Values reported for ^{238}U and ^{232}Th correspond to the upper part of the chains and those of ^{226}Ra and ^{228}Th give activities of the lower parts (see text).

A.3 Summary

Micromegas readouts used in TPCs offer appealing features for Rare Event searches, like a powerful background rejection thanks to the recording of topological signals. But a thorough material radiopurity control is always a must in these experiments. A program started years ago and will go on screening materials used in Micromegas setups, related to different experiments and projects like T-REX, NEXT, CAST and IAXO. This program relies mainly on activity measurements performed with a 1-kg, ultra-low background, HPGe detector named Paquito operated in the Canfranc Underground Laboratory. GDMS measurements have been also performed for metals.

The activity information of the screened materials is useful not only to guide in the selection of components in the design of Rare Event experiments but also to develop models capable of reproducing their experimental data with the help of Monte Carlo simulations. In particular, some of the performed measurements have compelled us to disregard the use of some kind of resistors, connectors, solder wire, adhesives or PCB materials due to their high intrinsic activities; radiopure enough alternatives have been found in most cases.

First assessment of the activity levels of microbulk Micromegas readouts produced at CERN indicate that they are already comparable to the cleanest readout systems in low background experiments; further improvements seem possible after careful selection of materials and procedures.

Measurements with InGrid Micromegas readout

With the aim of evaluating the performance of an InGrid (see Chapter 1) readout in Xe+TMA mixtures, an experimental setup was commissioned by the Zaragoza group (D. González-Díaz) in collaboration with the University of Bonn (Johel Kaminski and Michael Lupberger). Measurements of the stability, electron transmission, gain and energy resolution were carried out at several voltages configurations, here a very preliminary analysis is presented.

B.1 Experimental Setup

For this experiment, the NEXT-0-MM TPC was used together with its gas system (see in Sec. 2.1). A new drift field cage was designed and built, consisting of three copper foils -the cathode, the anode and the readout support- and three PEEK columns. The InGrid was encapsulated into a plastic POM piece which is adjusted to the copper support foil. The structure is joined by means of the three PEEK columns, as shown in Fig. B.1. The anode and support copper plates were electrically isolated using kapton sheets. Two sets of peek-plastic columns were done, one of 1-cm and the another of 3-cm-long; this allowed to take measurements with two drift distances.

The cathode, grid and anode are connected to a negative HV supply and the back electrode of the InGrid was set at ground potential. Since the anode surface is a little higher -by about 1 mm- than the grid surface, the voltage applied to it was always adjusted to be slightly above the grid voltage.

B.2 Experimental Procedure

The first measurements were carried out to test the operation of the InGrid readout in Xe+TMA mixtures, thus the signal was only readout from the grid, without connecting the chip. The grid signal is connected to a CANBERRA preamplifier +amplifier electronic chain (models 2005 and 2022, respectively), with a shaping time of $4\mu\text{s}$ for the amplifier. The output is fed to a PC-controlled Amptek portable Multi Channel Analyzer. The calibration constant of the electronic chain was previously calibrated using the procedure described in Sec. 2.2.7.

For these measurements, the electron transmission, gain and energy resolution for the grid signal was studied, varying systematically the drift and amplification



Fig. B.1: Pictures of the drift structure together with the InGrid readout installed inside the NEXT-0-MM chamber. Left: InGrid readout on a copper circular structure used as support. Right: Drift field cage together the InGrid readout. The image shows a drift with 3 cm of distance, however, most of the measurements were performed for a drift distance of 1 cm.

voltage. The two first tests were done with a drift distance of 1 cm, which was increased for the next measurements to 3 cm. After that, once a good performance was verified of the InGrid readout, the last measurements were focused on the acquisition of the single electron spectra at several gains, for which the chip was connected. The amplification voltage was varied systematically, acquiring data from the grid signal as well as from the chip. All the measurements were carried out with a ^{109}Cd source. A ^{55}Fe source was tested but its use was discarded due to its low activity.

For all measurements a Xe+2.8%TMA mixture was used. The experimental procedure performed before the data acquisition is similar to the one explained in Sec. 4.1.4. The gas system together with the TPC were pumped, with a previous bake-out of the chamber. Some measurements were carried out without recirculation of the mixture, because by accident one of the valves of the recirculation line remained closed during the experiment.

The energy spectrum generated by the ^{109}Cd source in a Xe+2.8%TMA mixture, acquired with an InGrid readout is depicted in Fig. B.2. As expected, the energy spectrum is similar to the acquired with Micromegas readouts (see Sec. ??). The K_α (22.1 keV) and K_β (25.0 keV) Ag X-rays peaks are well distinguished, as well as the corresponding Xe L_α -EP. The procedure for fitting these peaks is also described in Sec. ?. On the spectrum, it appears also the contribution of 8.1 keV Cu X-rays, which are produced by the interaction with the copper cathode of the source emissions.

B.3 Electron Transmission

The electron transmission curves and energy resolution measurements at 22.1 keV are presented in Fig. B.3 for three different configurations: two of them with a drift

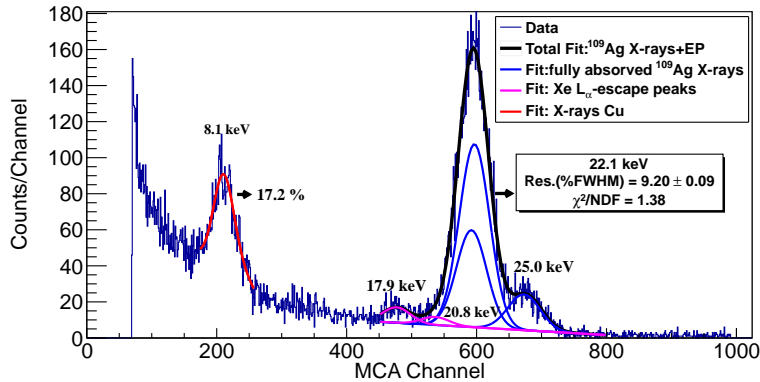


Fig. B.2: X-rays energy spectrum generated by a ^{109}Cd source in a Xe+2.8%TMA mixture at 1 bar, recorded with an InGrid readout where the signal is taken from the grid. The procedure for fitting the K_{α} (22.1 keV) and K_{β} (25.0 keV) Ag X-rays together with the corresponding Xe L_{α} -EPs is the one described in Sec. ???. The contribution of the X-rays Cu (8.1 keV) is also observed, produced by interaction in the cathode. Energy resolution (% FWHM) for 22.1 and 8.1 keV peaks is indicated.

distance of 1 cm but carried out in consecutive days, and the other one with 3 cm. The three sets of measurements were performed without recirculation. Electron transmissions larger than 98% are reached for field ratios above 0.003, being the region of full transmission between this value and 0.012.

On the other hand, the energy resolution reaches a plateau region rapidly, for field ratios above 0.002 for the three curves, being around 11% FWHM for measurements with a drift distance of 1 cm and around 9% FWHM with 3 cm. The degradation of energy resolution is only observed below field ratios of 0.015, for measurements acquired with a drift distance of 1 cm; because for the other drift distance the voltage was not increased for higher values. The energy resolution for the red curve is a little better than for the green curve, which is attributed to the larger level impurities in this mixture, because the gas was stored for longer time. It is interesting to note that the energy resolution improves when the drift distance is increased from 1 (11%FWHM) to 3 cm (8.5% FWHM). This fact can be due to the inhomogeneities in the drift field, caused by the fact that around the InGrid readout there is an empty space.

B.4 Gain Measurements

Gain measurements were done selecting a drift field ratio within the region of full transmission (transmission above 99%). For the first two tests, the amplification voltage was increased up to 230 V (46 kV/cm), while in the third until 260 V (52 kV/cm). During this last test (260 V) a spark produced the loss of communication with the chip, which was not possible to restore. Results of measurements are shown in Fig. B.4: two of them taken with a drift distance of 1 cm, and no

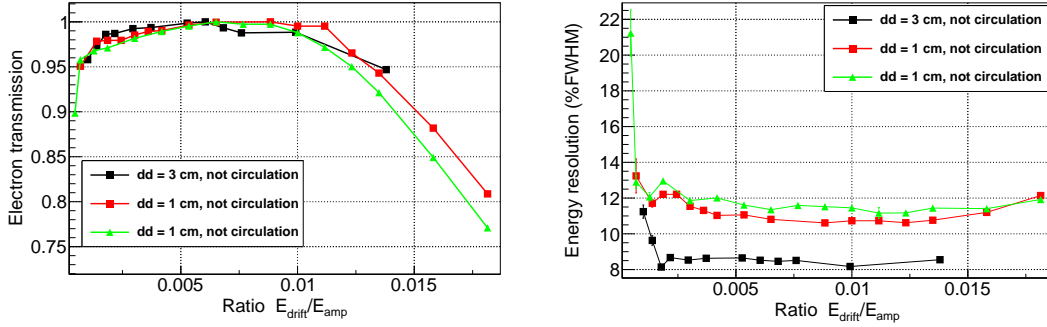


Fig. B.3: Electron transmission curves (left) and energy resolution (22.1 keV) against the fields ratio (E_{drift}/E_{amp}) (right) for InGrid readout in a Xe+2.8%TMA mixture at 1 bar. Three set of measurements are presented, two of them with a drift distance of 1 cm but performed in consecutive days, and the other one with drift distance of 3 cm.

recirculation of the gas (not RC); three sets with 3 cm of drift distance, one of them without recirculation and the other two with recirculation. The difference between the two measurements taken with drift distance of 1 cm is the level of impurities, being for the red curve (■) lower than for the green one (▲). In addition, in this figure are also plotted results for Micromegas readouts; this is discussed in Sec. ??.

Results of gain (Fig. B.4-top) show that all the gain curves acquired with the InGrid readout are compatible among each other, however, the curves for the measurements with a drift distance of 1 cm are slightly below the others. This result is attributed to the fact that for these measurements the gas was not recirculated, therefore, the attachment should be larger, causing the lower gains.

The energy resolution at 22.1 keV versus the gain is shown in Fig. B.4-bottom. Energy resolution improves slowly as gain increases for all the configurations. As for the variation with the drift voltage, the energy resolution for measurements with a drift distance of 1 cm is worse than for drift distance of 3 cm. The best values are achieved for gains above 900, being 11% FWHM for 1 cm) and 8.5% FWHM for 3 cm of drift distance. As was mentioned previously, this fact could be due to the inhomogeneities of the drift field.

B.5 Single electron spectra

Here only a very preliminary analysis is reported, results of the data acquired with InGrid in a Xe+2.8% TMA mixture at 1 bar are shown in Fig. B.5 [193]); scatter-plot with the number of occupancy for each pixel (left) and the single electron spectra (right) are presented for a systematic variation of the amplification voltage which are indicated together with the corresponding gain. The best behaviour is observed for an amplification voltage $V_{mm} = 250$ V corresponding to a gain of 4500. On the single electron spectrum in these conditions (middle-row) is observed the Cu X-rays (8.1 keV) peak with ≈ 200 activated pixels and the K_{α} Ag X-rays

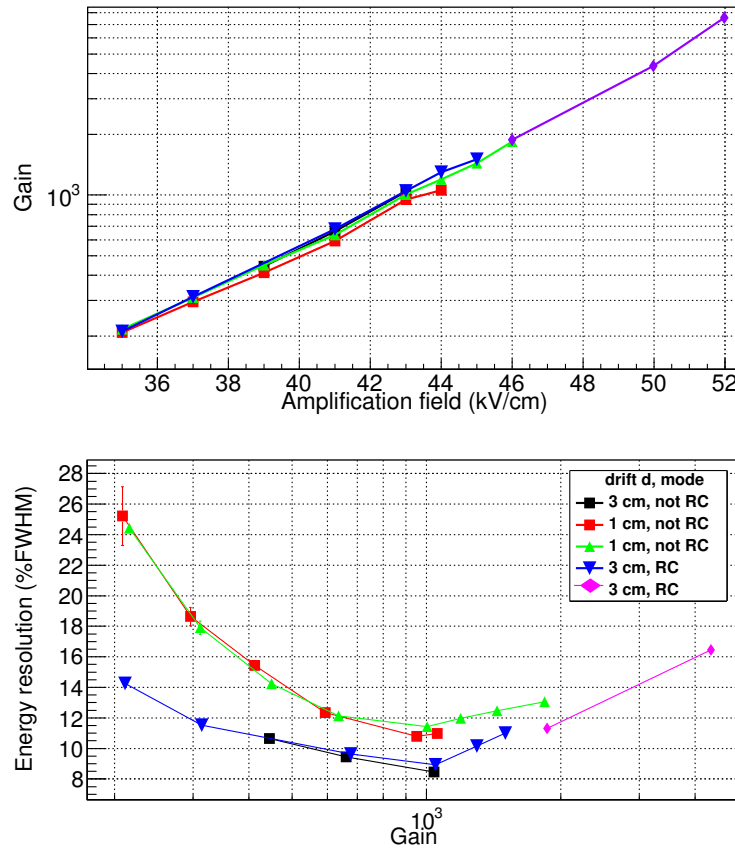


Fig. B.4: Dependence of the gain on the amplification field (top) and energy resolution at 22.1 keV (%FWHM) as function of gain (bottom) for a Xe+2.8%TMA mixture, from the grid signal of InGrid (50 μm gap thickness). For InGrid Micromegas readout, different sets of measurements were performed, varying the drift distance and in some cases without recirculation (not RC) of the gas, this is indicated in each case. Legend for the bottom plot applies for the top one.

(22.1 keV) peak with ≈ 500 ; these values are below the expected values -366 and 1000 respectively- which are the number of primary electrons for these energies E/W . Even for the highest gains acquired (up-row) the number activated pixel reaches to ≈ 750 for the 22.1 keV line, quantity still lower than the expected.

Both the scatter plot and the single electron spectrum for $V_{mm} = 260$ V evidence the bad behavior of the InGrid at these conditions. At higher gains the feedback process takes place, evidenced in the worsening of the energy resolution from gains above 1000 (see Fig. B.4-bottom).

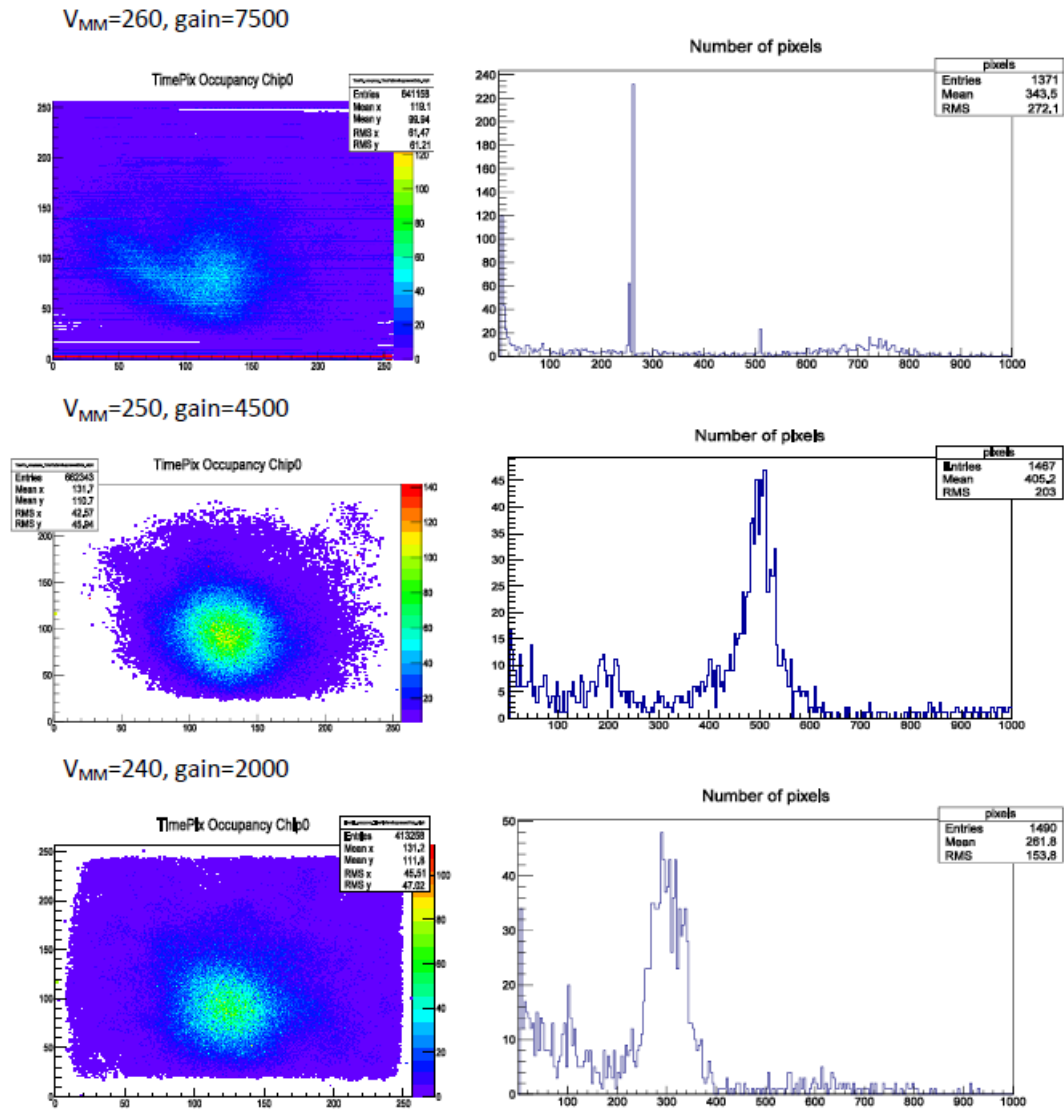


Fig. B.5: Data acquired with an InGrid readout in a Xe+2.8%TMA mixture at 1 bar, for different amplification voltages which are indicated together with the corresponding gain: scatter-plot with the number of occupancy for each pixel (left) and single electron spectra (right) [193].

Characterization of Micromegas readouts in Ar+2%*i*C₄H₁₀ mixtures.

A description of the experimental procedure and results of measurements of gain and energy resolution for several geometries of microbulk Micromegas readouts in Ar+2%*i*C₄H₁₀ is presented. These measurements were carried out in collaboration with F.J Iguaz.

C.1 Experimental Setup and Procedure

The setup consists of a TPC of 2l of volume working at atmospheric pressure in Ar+2%*i*C₄H₁₀. Four different batches of microbulk Micromegas were characterized, the geometrical parameters are summarized in Table C.1. The Micromegas with gap thickness of 50 μm were built at CERN, and the readouts with 25 μm are in total 4; two fabricated in CERN with the latest technology and the other ones from Saclay. In fig. C.1 can be seen the microbulk detectors installed and in Fig. C.2 are shown pictures taken with a microscope.

Batch	Reference	gap-pitch-holes diameter (μm)	active area diameter (cm)
1	01-11	50-90-40	30
2	06,03,11,12	50-100-55	30
3	01-02	25-100-30	35
4	06-07	25-50-25	35

Table C.1: Geometrical parameters of the microbulk Micromegas used in these measurements.

The gas was constantly recirculated in open loop, thus the gas was evacuated by an overpressure in the gas line to the atmosphere. The characterization of every readout started when the gain and energy resolution were stable for a determined voltage configuration. This situation was reached after approximately 30 minutes, by high inlet flow (≈ 9 l/h). Thereafter the flow rate was decreased down to 4l/h. For all measurements a ¹⁰⁹Cd source was used, encapsulated in stainless steel; the

source was located outside of the chamber on a metacrilate thin window just above the center of each microbulk measured.

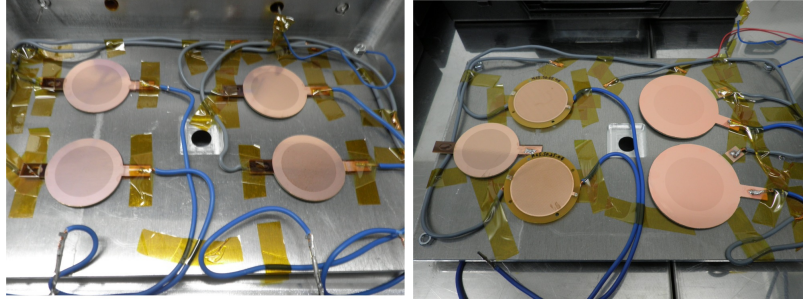


Fig. C.1: Pictures of the Micromegas readouts installed at the test-bench TPC. Left: Micromegas of 50 μm gap. Right: those of 25 μm gap, two of old type from Saclay (left) and two new ones from CERN (right). As a comparison, a new detector of 50 μm gap was placed between the old type ones.

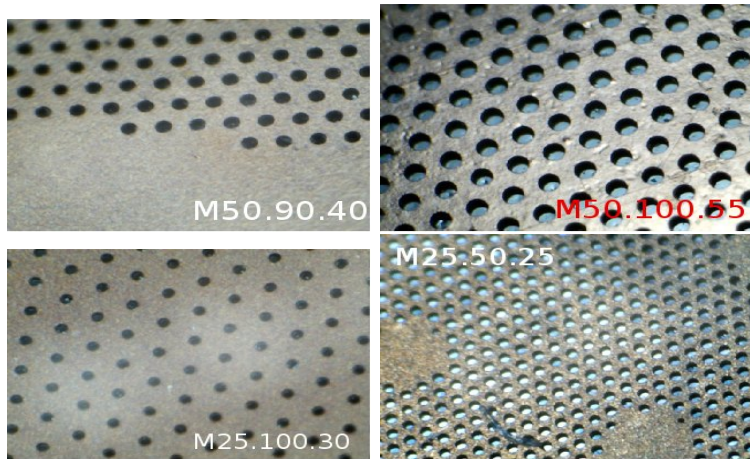


Fig. C.2: Microscopic pictures of the microbulk Micromegas readouts tested with a gap of 50 μm (top images) and 25 μm (bottom ones). In each picture there is a label with the geometrical parameters in microns (gap-pitch-hole diameter). The first number is the gap, the second one the pitch and the last one indicates the hole diameter.

C.2 Results

C.2.1 Gain

Measurements of gas gain and energy resolutions were realized using the $K\alpha$ line of the X-rays from ^{109}Ag at 22.1 keV emitted by the ^{109}Cd radioactive source. The total electronic amplification due to the preamplifier plus the amplifier was evaluated using a pulse generator adapting a capacitor of 10 pF, thus the total gain

of the electronic was obtained with the ratio between the output signal produced by the Multi Channel Analyzer (MCA) and the initial charge.

Gains were calculated using the Eq. 2.4. The 22.1 keV peak was used for the analysis. The number of primary electrons, N_e , used for the calculations was $N_e = 850 e^-$, which is the value for pure Ar. This assumption can introduce an overestimation of the gain not higher than 10%.

The typical energy spectrum can be seen in Fig. C.3 with the fit used in the analysis. The X-rays from ^{109}Ag , the Ar X-rays escape peaks (shifted ~ 3 keV) are observed. At low energy, it is also observed the X-rays produced by Cu (from Micromegas' mesh and Cu drift structure), Fe and Cr (from source encapsulate or cathode structure). Moreover, the peak located at ≈ 3 keV is likely originated by the sum of the Ar X-rays escape peaks from the Fe and Cr material.

The gas gain curves for the microbulk detectors of $50 \mu\text{m}$ of gap are presented in Fig. C.4. There is a slight dispersion in the gain between similar detectors, more important for the first batch. This fact may be attributed to changes in the gas flow rate, yielding different levels of impurities in the gas between measurements. The detector M11 of the batch 1 has systematically less gain as the detector suffered a strong spark affecting its normal performance. On the other hand, the gain curves of the batch 2 present less dispersion probably because we had more control in the flow rate of the gas.

On the other hand, measurements of gain for microbulk of $25 \mu\text{m}$ are depicted in Fig. C.4. The microbulk detectors M01 and M02 belong to the same batch, built with the latest technology, while the M06 and M07 detectors are older. The detector M06 shows a higher gain than the detector M07, even more the maximum amplification field is also higher, reaching values above 500 while the other detector has a maximum gain around 300. Although the new detectors have less gain for a given amplification field, the maximum gain is above 1000 before the spark limit, which represents a factor 2 higher respect the other detectors.

C.2.2 Energy resolution

Energy resolution dependence with the gain is shown in Fig. C.5, for the two characterized batches of microbulk readouts of $50 \mu\text{m}$. The energy resolution presents more dispersion for Micromegas of the batch 1, as mentioned above for the gain. The bad energy resolution at low gains is caused by noise contribution of the electronic chain. For gains above 100, the energy resolution remains stable up to 4000, thereafter it degrades likely due to feedback. The best energy resolution at 22.1 keV for the detectors of the batch 1 is around 7% FWHM, and for the other detectors is above of 7.5% FWHM.

The energy resolution dependency with gain for microbulk of $25 \mu\text{m}$ gap is shown in Fig. C.5-bottom. Values for M01 and M02 are different, finding bad performance for the M01 detector. The M06 and M07 detectors have compatible values of energy resolution at low gains.

C.3 Conclusions

Results of measurements of gain for microbulk Micromegas show that the readouts with 50 μm of gap have higher maximum gains ($\approx 10^4$) than the readouts with 25 μm of gap ($\approx 10^3$). On the other hand, the best values of energy resolution were obtained for the Micromegas with gap thickness of 25 μm , with a value above 6.2% (FWHM) for X-rays of 22.1 keV. The best value of energy resolution for Micromegas with gap thickness of 50 μm was 7(%FWHM).

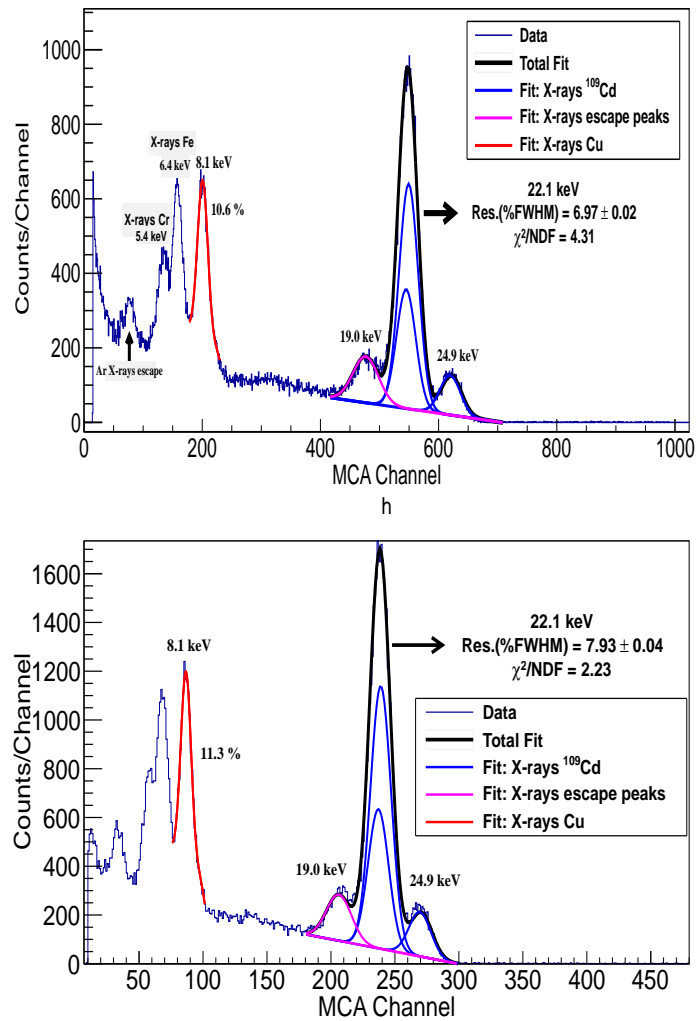


Fig. C.3: Energy spectra registered by a ^{109}Cd source for Micromegas of 50 μm gap (top, M01) and of 25 μm gap (bottom, M02). The K_α and K_β lines emitted by Ag are clearly distinguished, as well as the X-rays generated by the detector's mesh and cathode plate (copper line at 8.1 keV), the source encapsulate (Fe & Cr lines, at 6.4 and 5.4 keV) and their corresponding Ar EP. K_α and K_β from Ag, as well as the copper lines have been fitted to Gaussian functions and the obtained energy resolution ($\%FWHM$) is indicated on the plots.

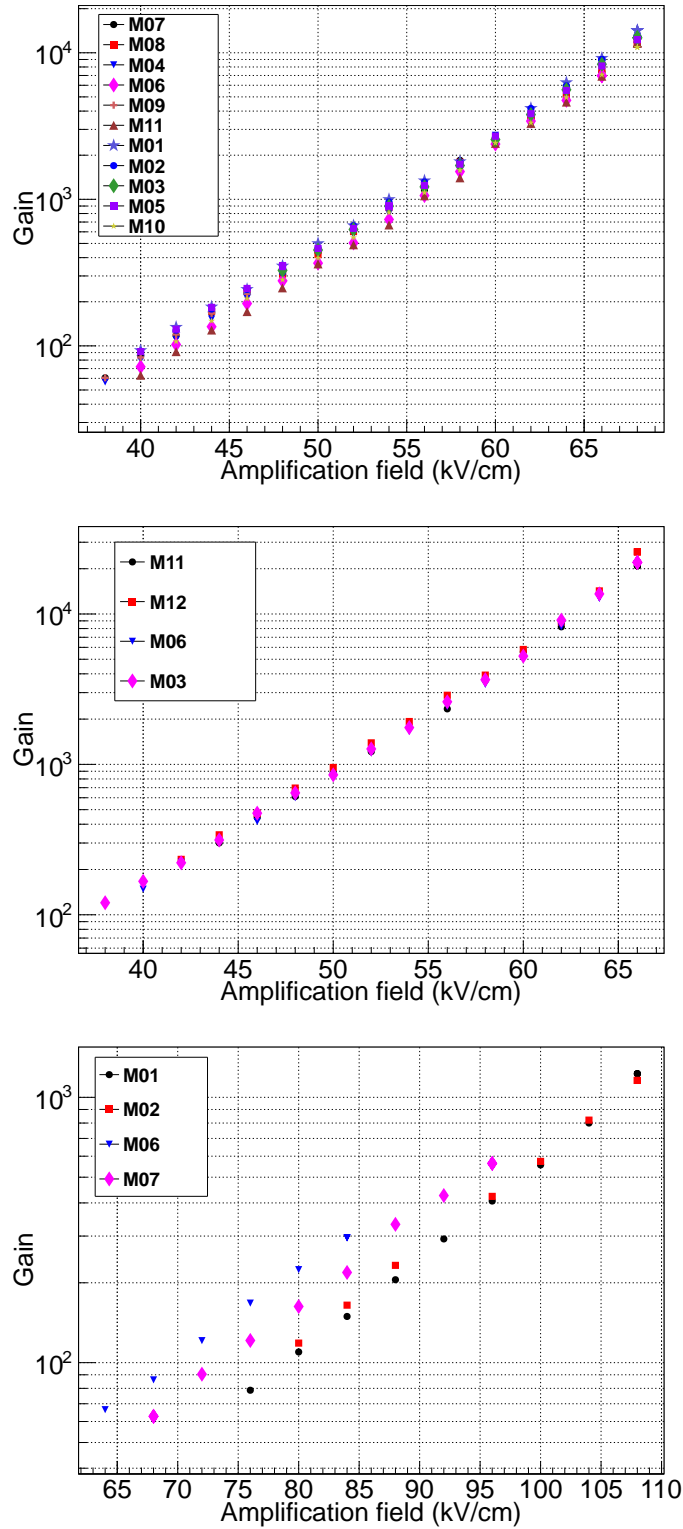


Fig. C.4: Dependence of the gain on the amplification field. For Micromegas of batch 1 (50 μm gap, top), batch 2 (50 μm gap, middle) and for batch 3 and 4 (25 μm gap, bottom). For geometric details see Table C.1.

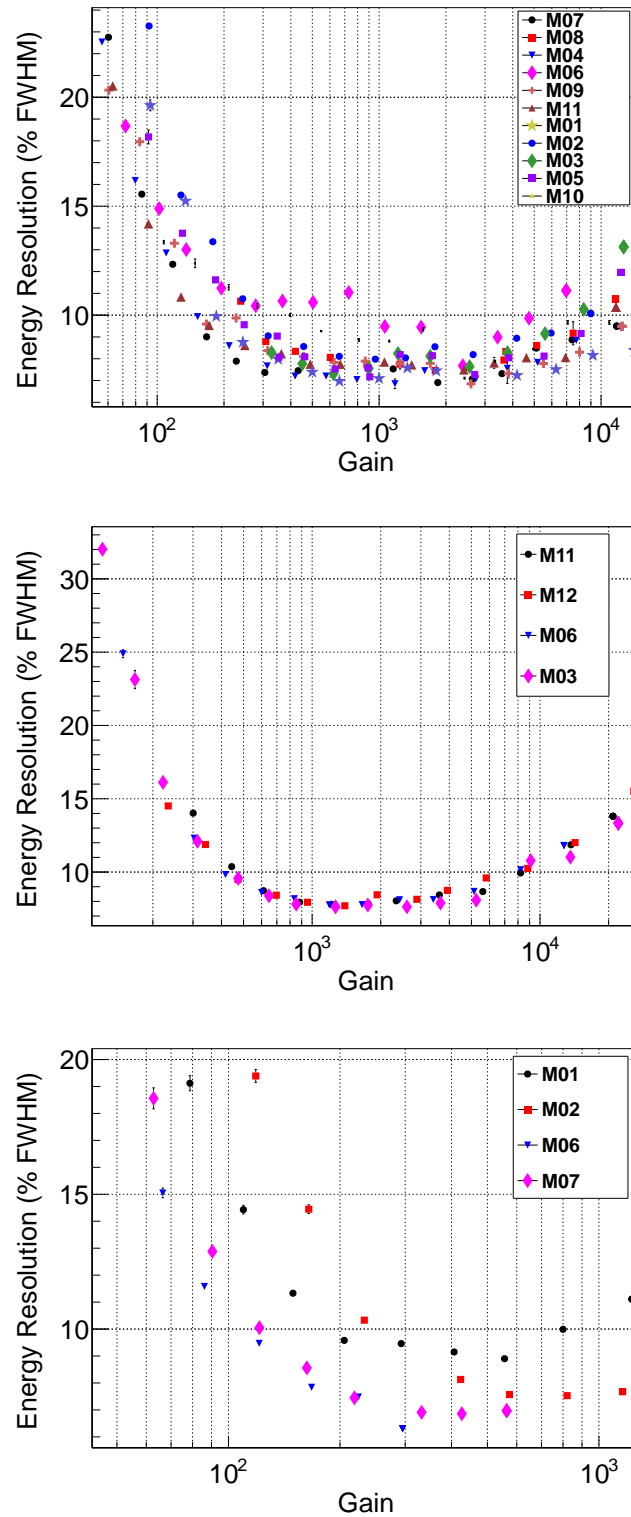


Fig. C.5: Dependence of the energy resolution on the gain. For microbulk of the batch 1 (50 μm gap, top), batch 2 (50 μm gap, middle) and for batch 3 and 4 (25 μm gap, bottom). For geometric details see Table C.1.

Bibliography

- [1] I. G. Irastorza et al. (2012). “Status of R&D on Micromegas for Rare Event Searches: The T-REX project”. *EAS Publications Series*, **53**, 147. (Cited on pages [vii](#) and [27](#).)
- [2] F. T. Avignone et al. (2008). “Dou Beta Decay, Majorana Neutrinos, and Neutrino Mass”. *Rev. Mod. Phys.*, **80**, 481. DOI:[10.1016/S0031-8914\(34\)80298-4](https://doi.org/10.1016/S0031-8914(34)80298-4) (Cited on pages [vii](#), [19](#) and [151](#).)
- [3] G. Bertone, D. Hooper, and J. Silk (2005). “Particle dark matter: evidence, candidates and constraints”. *Physics Reports*, **405**. (Cited on pages [vii](#) and [151](#).)
- [4] L. Baudis (2014). “WIMP Dark Matter Direct-Detection Searches in Noble Gases”. *arXiv:1408.4371v1 [astro-ph.IM]*. (Cited on pages [vii](#), [18](#) and [151](#).)
- [5] V. Álvarez et al. (2012). “NEXT-100 Technical Design Report (TDR). Executive summary”. *JINST*, **7**, T06001. (Cited on pages [vii](#) and [153](#).)
- [6] D. Nygren (2013). “Columnar recombination: a tool for nuclear recoil directional sensitivity in a xenon-based direct detection WIMP search”. *J. Phys.: Conf. Ser.*, **460**, 012006. <http://doi:10.1088/1742-6596/460/1/012006> (Cited on pages [vii](#), [33](#), [118](#), [153](#) and [156](#).)
- [7] V.M. Gehman, A. Goldschmidt, D. Nygren, C.A.B. Oliveira, and J. Renner (2013). “A plan for directional dark matter sensitivity in high-pressure xenon detectors through the addition of wavelength shifting gaseous molecules”. *JINST*, **8**, C10001. <http://doi:10.1088/1748-0221/8/10/C10001> (Cited on pages [vii](#), [118](#), [153](#) and [156](#).)
- [8] A. Bolotnikov and B. Ramsay (1997). “The spectroscopic properties of high-pressure xenon”. *Nucl. Instr. and Meth. A*, **396**, 360. DOI:[10.1016/S0168-9002\(97\)00784-5](https://doi.org/10.1016/S0168-9002(97)00784-5) (Cited on pages [1](#) and [14](#).)
- [9] D. Nygren (1975). “A Time Projection Chamber-1975”. *PEP1975 proceedings*, **198**, 20. (Cited on page [2](#).)
- [10] D. Nygren and J. N. Marx (1978). “The Time Projection Chamber”. *Physics Today*, **31**, 46. (Cited on page [2](#).)
- [11] Y. Giomataris, P. Rebourgeard, J. Robert, and G. Charpak (1996). “MicroMEGAS: a high-granularity position-sensitive gaseous detector for high particle flux environments”. *Nucl. Instr. and Meth. A*, **376**, 29. [http://dx.doi.org/10.1016/0168-9002\(96\)00175-1](http://dx.doi.org/10.1016/0168-9002(96)00175-1) (Cited on pages [2](#), [10](#) and [153](#).)

- [12] Kaixuan Ni (2006). “Development of a Liquid Xenon Time Projection Chamber for the XENON Dark Matter Search”. Ph.D. thesis, Columbia University. (Cited on page 2.)
- [13] E. Aprile and A. E. Bolotnikov (2006). “Noble Gas Detectors” edition. (Cited on page 2.)
- [14] G. F. Knoll (1992). “Radiation Detection and Measurement” edition. (Cited on page 3.)
- [15] XCOM: Photon Cross Sections Database (2014, Oct 15). [http://dx.doi.org/10.1016/0029-554X\(70\)90818-9](http://dx.doi.org/10.1016/0029-554X(70)90818-9) (Cited on page 5.)
- [16] U. Fano (1947). “Ionization Yield of Radiations. II. The Fluctuations of the Number of Ions”. *Phys. Rev.*, **72**, 26. (Cited on page 6.)
- [17] A. Hashiba, K. Masuda, T. Doke, T. Takahashi, and Y. Fujita. (1984). “Fano factor in gaseous argon measured by the proportional scintillation method”. *Nucl. Instr. and Meth. A*, **227**, 305. (Cited on page 6.)
- [18] M. Kase, T. Akioka, H. Mamyoda, J. Kikuchi, and T. Doke (1984). “Fano factor in pure argon”. *Nucl. Instr. and Meth. A*, **227**, 311. (Cited on page 6.)
- [19] M. A. Chefdeville (2009). “Development of Micromegas-like gaseous detectors using a pixel readout chip as collecting anode”. Ph.D. thesis, Universiteit van Amsterdam. http://www.nikhef.nl/pub/services/biblio/theses_pdf/thesis_MA_Chefdeville.pdf (Cited on pages 6, 10 and 114.)
- [20] I. Krajcar Bronic (1992). “The Fano factor for electrons in gas mixtures”. *Nucl. Instr. and Meth. B*, **71**, 366. (Cited on page 6.)
- [21] T.H.V.T. Dias et al (1997). “Fano factor in mixtures”. *Appl. Phys.*, **82**, 2742. (Cited on page 6.)
- [22] A. J. P. L. Policarpo et al. (1974). “Detection of soft X-rays with a xenon proportional scintillation counter.” *NIM*, **118**, 221-226. (Cited on page 6.)
- [23] T. H. V. T. Dias et al. (1999). “Xenon-neon gas proportional scintillation counters: Experimental and simulation results”. *J. Appl. Phys.*, **85**, 6303. <http://dx.doi.org/10.1063/1.370131> (Cited on pages 6, 17, 18 and 63.)
- [24] E. G. D. Cohen and W. Thirring (1973). “The Boltzmann equation and applications” edition. (Cited on page 6.)
- [25] W. Blum (2008). “Particle Detection with Drift Chambers” edition. (Cited on pages 6 and 136.)
- [26] Robert E. Robson (2006). “Introductory Transport Theory for Charged Particles in Gases” edition. (Cited on page 6.)

- [27] F. Sauli and A. Peisert (1984). “Drift and diffusion of electrons in gases a compilation”. Technical report. (Cited on pages 6 and 55.)
- [28] Magboltz: Transport of electrons in gas mixtures. <http://magboltz.web.cern.ch/magboltz/> (Cited on pages 7, 113, 137 and 138.)
- [29] S. F. Biagi (1999). “Monte Carlo simulation of electron drift and diffusion in counting gases under the influence of electric and magnetic fields”. *Nucl. Instrum. Meth. A*, **421**, 1999. (Cited on page 7.)
- [30] F.J. Iguaz (2010). “Development of a Time Projection Chamber prototype with Micromegas technology for the search of the Double Beta Decay of ^{136}Xe ”. Ph.D. thesis, Universidad de Zaragoza. (Cited on pages 7, 8, 38, 55, 58 and 125.)
- [31] C.A.B. Oliveira (2011). “Monte Carlo study of electroluminescence in gaseous detectors”. Ph.D. thesis, Universidad de Aveiro. http://next.ific.uv.es/DocDB/0000/000071/001/thesis_COliveira.pdf (Cited on pages 8 and 11.)
- [32] A. Oed (1988). “Position-sensitive detector with microstrip anode for electron multiplication with gases”. *Nucl. Instr. and Meth. A*, **263**, 351. (Cited on page 9.)
- [33] R. Bouclier et al. (1996). “High rate operation of micro-strip gas chambers on diamond-coated glass”. *Nucl. Instr. and Meth. A*, **369**, 328. (Cited on page 9.)
- [34] R. Bouclier et al. (1995). “On some factors affecting discharge conditions in micro-strip gas chambers”. *Nucl. Instr. and Meth. A*, **365**, 65. (Cited on page 9.)
- [35] F. Sauli (1997). “GEM: A new concept for electron amplification in gas detectors”. *Nucl. Instr. and Meth. A*, **386**, 531. (Cited on page 10.)
- [36] D. Attié (2009). “TPC review”. *Nucl. Instr. and Meth. A*, **598**, 89. (Cited on page 10.)
- [37] F. Sauli (2010). “Recent topics on gaseous detectors”. *Nucl. Instr. and Meth. A*, **623**, 29. (Cited on page 10.)
- [38] C. Balan et al. (2011). “Micromegas operation in high pressure xenon: charge and scintillation readout”. *JINST*, **6**, P02006. doi:10.1088/1748-0221/6/02/P02006 (Cited on pages 11, 67, 109, 111, 116 and 156.)
- [39] Y. Giomataris et al. (2006). “MICROMEAS in a bulk”. *Nucl. Instr. and Meth. A*, **560**, 405. (Cited on page 10.)
- [40] S. Andriamonje et al. (2010). “Development and performance of Microbulk Micromegas detectors”. *JINST*, **5**, P02001. (Cited on page 10.)

- [41] M. Chefdeville et al. (2006). “An electron-multiplying ‘Micromegas’ grid made in silicon wafer post-processing technology”. *Nucl. Instr. and Meth. A*, **556**, 490. (Cited on page 10.)
- [42] S. Cebrian et al. (2011). “Radiopurity of micromegas readout planes”. *Astropart. Phys.*, **34**, 354. <http://dx.doi.org/10.1016/j.astropartphys.2010.09.003> (Cited on pages 11, 18, 27 and 165.)
- [43] H. Schindler, R. Veenhof, et al. “Garfield++: Simulation of gaseous detectors”. (Cited on page 11.)
- [44] C. Geuzaine. “Gmsh: a three-dimensional finite element mesh generator with built-in pre- and post-processing facilities Simulation of gaseous detectors”. (Cited on page 11.)
- [45] Elmer. <https://csc.fi/web/elmer> (Cited on page 11.)
- [46] J. Renner (2009). “Detector Simulation in Garfield++ with Open-Source Finite Element Electrostatics”. *Garfield Examples*. (Cited on page 12.)
- [47] E. Ruiz-Chóliz (2014). “Simulación de la dinámica de transmisión y Amplificación de carga en micro-agujeros”. *6ª Jornadas de Jóvenes Investigadores en Aragón*. (Cited on page 12.)
- [48] F. M. Penning (1927). “Über Ionisation durch metastabile Atome”. *Die Naturwissenschaften*, **15**, 818. (Cited on pages 14 and 15.)
- [49] H. Hotop and A. Niehaus (1969). “Reactions of Excited Atoms and Molecules with Atoms and Molecules II. Energy Analysis of Penning Electrons”. *Z. Phys.*, **228**, 68. (Cited on page 15.)
- [50] B. Ramsey and P. Agrawal (1989). “Xenon- based Penning mixtures for proportional counters”. *Nucl. Instr. and Meth. A*, **278**, 576. [http://dx.doi.org/10.1016/0168-9002\(89\)90882-6](http://dx.doi.org/10.1016/0168-9002(89)90882-6) (Cited on pages 15, 16, 93 and 108.)
- [51] K. White et al. (1987). “Gas gain in xenon +2,3 dimethyl-2-butene filled proportional counters”. *Nucl. Instr. and Meth. A*, **260**, 443. [http://dx.doi.org/10.1016/0168-9002\(87\)90114-8](http://dx.doi.org/10.1016/0168-9002(87)90114-8) (Cited on pages 15 and 104.)
- [52] D. Nygren (2011). “Can the intrinsic energy resolution in xenon be surpassed”. *J. Phys.: Conf. Ser.*, **309**, 012006. <http://doi:10.1088/1742-6596/309/1/012006> (Cited on page 15.)
- [53] D. Nygren (2009). “High-pressure xenon gas electroluminescent TPC for $0-\nu\beta\beta$ -decay search”. *Nucl. Instr. and Meth. A*, **603**, 337. DOI:10.1016/j.nima.2009.01.222 (Cited on page 15.)
- [54] F. I. G. M. Borges et al. (2003). “XenonâNeon Gas Proportional-Scintillation Counters for X-Rays Below 2 keV: Experimental Results”. *IEE Trans. Nucl. Sci.*, **50**, 4. DOI:10.1109/NSSMIC.2002.1239294 (Cited on page 17.)

- [55] F. I. G. M. Borges et al. (2003). “XenonâNeon Gas Proportional-Scintillation Counters for X-Rays Below 2 keV: A Monte Carlo Simulation Study”. *IEE Trans. Nucl. Sci.*, **50**, 4. DOI:10.1109/NSSMIC.2002.1239294 (Cited on page 17.)
- [56] G. Heusser (1995). “Low-radioactivity background techniques”. *Ann. Rev. Nucl. Part. Sci.*, **45**, 543. (Cited on page 18.)
- [57] F. Aznar et al. (2013). “Assessment of material purity for Rare Event experiments using Micromegas”. *JINST*, **8**, C11012. (Cited on pages 18 and 165.)
- [58] S. Fukuka et al. (Super-Kamiokande Collab.) (2001). “Solar ^8B and hep Neutrino Measurements from 1258 Days of Super-Kamiokande Data”. *Phys. Rev. Lett.*, **86**, 5651. (Cited on pages 19 and 20.)
- [59] Q. R. Ahmad et al. (SNO Collab.) (2002). “Direct Evidence for Neutrino Flavor Transformation from Neutral-Current Interactions in the Sudbury Neutrino Observatory”. *Phys. Rev. Lett.*, **89**, 1. (Cited on page 19.)
- [60] T. Araki et al. (KamLAND Collab.) (2005). “Measurement of Neutrino Oscillation with KamLAND: Evidence of Spectral Distortion”. *Phys. Rev. Lett.*, **94**, 081801. (Cited on page 19.)
- [61] J. J. Gómez-Cadenas et al. (2012). “The search for neutrinoless double beta decay”. *Riv. Nuovo Cim.*, **35**, 29-98. (Cited on page 19.)
- [62] W. Rodejohann (2011). “Neutrino-less double beta decay and Particle Physics”. *Int. Mod. Phys. E*, **20**, 1833. (Cited on pages 19, 21 and 23.)
- [63] F. Reines and C. L Cowen (1956). “The Neutrino”. *Nature*, **178**, 446. (Cited on page 20.)
- [64] H. Arason et al. (1992). “Renormalization-group study of the standard model and its extensions: The standard model”. *Phys. Rev. D*, **46**, 3945. (Cited on page 20.)
- [65] B. Pontecorvo (1957). “Mesonium and Antimesonium”. *J. Exptl. Theoret. Phys.*, **33**. (Cited on page 20.)
- [66] and S. Sakata Z. Maki, M. Nakagawa (1962). “Remarks on the unified model of elementary particles”. *Prog. Theor. Phys.*, **28**, 870. (Cited on page 20.)
- [67] S. Dell’Oro, S. Marcocci, and F. Vissan (2014). “New expectations and uncertainties on neutrinoless double beta decay”. *Phys. Rev. D*, **90**, 033005. (Cited on page 20.)
- [68] H. V. Klapdor-Kleingrothaus (2002). “First Evidence for Lepton Number Violation and of the Majorana Character of Neutrinos”. *Mod. Phys. Let. A*, **16**, 092007. (Cited on pages 21 and 24.)

- [69] J. Kotila and F. Iachello (2012). “Phase-space factors for double- β decay”. *Phys. Rev. C*, **85**, 034316. (Cited on page 22.)
- [70] J. M. Yaoa et al. (2014). “Nuclear matrix elements in neutrinoless double β decay: beyond mean-field covariant density functional theory”. *arXiv:1410.6326 [nucl-th]*. (Cited on pages 22 and 23.)
- [71] A. Neacsu and S. Stoica (2012). “Fast, efficient calculations of the two-body matrix elements of the transition operators for neutrino double- β decay”. *Phys. Rev. C*, **86**, 067304. (Cited on page 23.)
- [72] M. Horoi and B. A. Brown (2013). “Shell-Model Analysis of the ^{136}Xe Double Beta Decay Nuclear Matrix Elements”. *Phys. Rev. Lett.*, **110**, 222502. (Cited on page 23.)
- [73] M. T. Mustonen and J. Engel (2013). “Large-scale calculations of the double- β decay of ^{76}Ge , ^{130}Te , ^{136}Xe , and ^{150}Nd in the deformed self-consistent Skyrme quasiparticle random-phase approximation”. *Phys. Rev. C*, **87**, 064302. (Cited on page 23.)
- [74] J. Barea, J. Kotila, and F. Iachello (2013). “Nuclear matrix elements for double- β decay”. *Phys. Rev. C*, **87**, 014315. (Cited on page 23.)
- [75] P. K. Rath et al. (2013). “Neutrinoless $\beta\beta$ decay transition matrix elements within mechanisms involving light Majorana neutrinos, classical Majorons, and sterile neutrinos”. *Phys. Rev. C*, **88**, 064322. (Cited on page 23.)
- [76] A. S. Barabash (2010). “Precise half-life values for two-neutrino double- β decay”. *Phys. Rev. C*, **81**, 035501. (Cited on pages 24 and 26.)
- [77] The EXO-200 Collaboration (2014). “An improved measurement of the $2\nu\beta\beta$ half-life of Xe-136 with EXO-200”. *Phys. Rev. C*, **89**, 015502. (Cited on page 24.)
- [78] A. Gando et al. (KamLAND-Zen) (2013). “Limit on Neutrinoless $\beta\beta$ Decay of ^{136}Xe from the First Phase of KamLAND-Zen and Comparison with the Positive Claim in ^{76}Ge ”. *Phys. Rev. Lett.*, **110**, 062502. (Cited on page 24.)
- [79] M. Agostini et al. (GERDA) (2013). “Results on Neutrinoless Double- β Decay of ^{76}Ge from Phase I of the GERDA Experiment”. *Phys. Rev. Lett.*, **111**, 122503. (Cited on page 24.)
- [80] M. Redshaw et al. (2007). “Mass and Double-Beta-Decay Q Value of ^{136}Xe ”. *Phys. Rev. Lett.*, **98**, 053003. (Cited on page 24.)
- [81] E. Aprile (2010). “Liquid xenon detectors for particle physics and astrophysics”. *Rev. Mod. Phys.*, **82**, 2053. (Cited on pages 24, 29 and 31.)

- [82] O. Cremonesi and M. Pavan (2014). “Challenges in Double Beta Decay”. *Advances in High Energy*, **2014**, 951432. (Cited on page 25.)
- [83] N. Abgrall et al. (2014). “The MAJORANA Demonstrator Neutrinoless Double-Beta Decay Experiment”. *Advances in High Energy Physics*, **2014**. (Cited on page 24.)
- [84] H. V. Klapdor-Kleingrothaus et al. (2001). “Latest Results from the Heidelberg-Moscow Double-Beta-Decay Experiment”. *Eur. Phys. J. A*, **12**, 147. (Cited on page 24.)
- [85] C. E. Aalseth et al. (IGEX Collab.) (2002). “IGEX 76Ge neutrinoless double-beta decay experiment: Prospects for next generation experiments”. *Phys. Rev. Lett. D*, **65**, 092007. (Cited on page 24.)
- [86] R. Arnold et al. (NEMO Collab.) (2005). “First Results of the Search for Neutrinoless Double-Beta Decay with the NEMO 3 Detector”. *Phys. Rev. Lett.*, **95**, 182302. (Cited on page 24.)
- [87] J. Argyriades et al. (NEMO-3 Collab.) (2010). “Measurement of the two neutrino double beta decay half-life of Zr-96 with the NEMO-3 detector”. *Nucl. Phys. A*, **847**, 168. (Cited on page 24.)
- [88] C. Arnaboldi et al. (2004). “CUORE: a cryogenic underground observatory for rare events”. *Nucl. Instr. and Meth. A*, **518**, 775. (Cited on page 24.)
- [89] EXO collaboration (2012). “Search for Neutrinoless Double-Beta Decay in ^{136}Xe with EXO-200”. *Phys. Rev. Lett.*, **109**, 032505. (Cited on page 24.)
- [90] EXO collaboration (2011). “Observation of Two-Neutrino Double-Beta Decay in Xe-136 with EXO-200”. *Phys. Rev. Lett.*, **107**, 212501. (Cited on page 24.)
- [91] M. G. Marino (2014). “Search for Majorana neutrinos with the first two years of EXO-200 data”. *Nature*, **510**, 229. (Cited on page 24.)
- [92] KamLAND-Zen Collaboration (2012). “Measurement of the double-beta decay half-life of ^{136}Xe with the KamLAND-Zen Experiment”. *Phys. Rev. Lett. C*, **85**, 045504. (Cited on page 24.)
- [93] V. Álvarez et al. (NEXT Collab.) (2012). “NEXT-100 Technical Design Report (TDR). Executive Summary”. *JINST*, **06**, T06001. (Cited on page 25.)
- [94] The NEXT collaboration (2014). “Present status and future perspectives of the NEXT experiment”. *Advances in High Energy Physics*, **2014**, 907067. <http://dx.doi.org/10.1155/2014/907067> (Cited on page 25.)
- [95] V. Álvarez (NEXT Collab.) (2012). “SiPMs coated with TPB: Coating protocol and characterization for NEXT”. *JINST*, **7**, P02010. (Cited on page 25.)

- [96] V. Álvarez et al. (NEXT Collab.) (2014). “Near-intrinsic energy resolution for 30-662 keV gamma rays in a high pressure xenon electroluminescent TPC”. *Nucl. Instr. and Meth. A*, **708**, 101. (Cited on page 27.)
- [97] J. Renner et al. (NEXT Collab.) (2014). “Ionization and scintillation of nuclear recoils in gaseous xenon”. *arXiv:1409.2853 [physics.ins-det]*. <http://arxiv.org/abs/1409.2853> (Cited on page 27.)
- [98] L. Serra et al. (NEXT Collab.) (2014). “Latest results of NEXT-DEMO, the prototype of the NEXT 100 double beta decay experiment”. *arXiv:1410.6700 [physics.ins-det]*. (Cited on page 27.)
- [99] S. Cebrián et al. (2010). “Micromegas readouts for double beta decay searches”. *JCAP*, **10**, 010. (Cited on page 27.)
- [100] V. Alvarez et al. (2014). “Description and commissioning of NEXT-MM prototype: first results from operation in a Xenon-Trimethylamine gas mixture”. *JINST*, **9**, P03010. (Cited on page 27.)
- [101] V. Álvarez et al. (NEXT Collab.) (2014). “Characterization of a medium size Xe/TMA TPC instrumented with microbulk Micromegas, using low-energy γ rays”. *JINST*, **9**, C04015. <http://doi:10.1088/1748-0221/9/04/C04015> (Cited on pages 27, 28, 137 and 138.)
- [102] S. Cebrián et al. (2013). “Micromegas-TPC operation at high pressure in xenon-trimethylamine mixtures”. *JINST*, **8**, P01012. (Cited on pages 27, 85 and 118.)
- [103] D. C. Herrera (2013). “Micromegas-TPC operation at high pressure in Xenon-trimethylamine mixtures”. *J. Phys.: Conf. Ser.*, **460**, 012012. <http://doi:10.1088/1742-6596/460/1/012012> (Cited on pages 27, 122, 137 and 138.)
- [104] F. Zwicky (1933). “Spectral displacement of extra galactic nebulae”. *Helv. Phys. Acta*, **6**, 110. (Cited on page 28.)
- [105] V. C. Rubin and W. K. Ford (1970). “Rotation of the Andromeda Nebula from a Spectroscopic Survey of Emission Regions”. *Astrophys. J.*, **159**, 379. (Cited on page 28.)
- [106] A. Bosma (1978). “The distribution and kinematics of neutral hydrogen in spiral galaxies of various morphological types”. Ph.D. thesis, Groningen Univ. (Cited on page 28.)
- [107] A. Refregier (2003). “Weak Gravitational Lensing by Large-Scale Structure”. *Ann. Rev. Astron. Astrophys.*, **41**, 645. (Cited on page 28.)
- [108] J. A. Tyson, G. P. Kochanski, and I. P. Dell’Antoni (1998). “Detailed Mass Map of CL0024+1654 from Strong Lensing”. *Astrophys. J.*, **498**, L107. (Cited on page 28.)

- [109] A. D. Lewis, D. A. Buote, and J. T. Stocke (2003). “Chandra Observations of Abell 2029: The Dark Matter Profile at $< 0.01R_{vir}$ in an Unusually Relaxed Cluster”. *Astrophys. J.*, **586**, 135. (Cited on page 28.)
- [110] D. Clowe et al. (2006). “A direct empirical proof of the existence of dark matter”. *Astrophys. J.*, **648**, L109. (Cited on page 28.)
- [111] B. D. Fields and S. Sarkar (Particle Data Group Collab.) (2008). “Big Bang nucleosynthesis”. *Phys. Lett. B*, **667**, 228. (Cited on page 28.)
- [112] G. Hinshaw et al. (2013). “Nine-year Wilkinson Microwave Anisotropy Probe (WMAP) observations: Cosmological Parameters Results”. *Astrphys. J. Sumpp. Ser.*, **208**, 19. (Cited on page 28.)
- [113] P. A. R. Ade et al. (2013). “Planck 2013 results. XVI. Cosmological parameters”. *arXiv:1303.5076 [astro-ph.CO]*. (Cited on page 29.)
- [114] J. L. Feng (2010). “Dark Matter Candidates from Particle Physics and Methods of Detection”. *Annu. Rev. Astro.*, **48**, 495-545. (Cited on page 29.)
- [115] and K. Griest G. Jungman, M. Kamionkowski (1996). “Supersymmetric Dark Matter”. *Phys. Rept.*, **267**, 195. (Cited on page 29.)
- [116] D. Hooper and S. Profumo (2007). “Dark Matter and Collider Phenomenology of Universal Extra Dimensions”. *Phys. Rept.*, **453**, 29. (Cited on page 29.)
- [117] G. Raffelt (2002). “Axions”. *Space Sci. Rev.*, **100**, 153. (Cited on page 29.)
- [118] G. Rybka (2014). “Direct Detection Searches for Axion Dark Matter”. *Phys. Dark Univ.*, **4**, 14. (Cited on page 29.)
- [119] I. G. Irastorza et al. (2011). “Towards a new generation axion helioscope”. *JCAP*, **1106**, 013. (Cited on page 29.)
- [120] E. Armengaud et al. (2014). “Conceptual Design of the International Axion Observatory (IAXO)”. *JINST*, **9**, T05002. (Cited on page 29.)
- [121] G. Kane and S. Watson (2008). “Dark Matter and LHC: What is the connection”. *Mod. Phys. Lett. A*, **23**, 26. (Cited on page 29.)
- [122] O. Adriani et al. (PAMELA Collab.) (2009). “An anomalous positron abundance in cosmic rays with energies 1.5-100 GeV”. *Nature*, **458**, 07942. (Cited on page 29.)
- [123] M. Ackermann et al. (Fermi-LAT Collab.) (2014). “Dark Matter Constraints from Observations of 25 Milky Way Satellite Galaxies with the Fermi Large Area Telescope”. *Phys. Rev. D*, **89**, 042001. (Cited on page 29.)
- [124] D. Hooper and T. Linden (2011). “Origin of the gamma rays from the Galactic Center”. *Phys. Rev. D*, **84**, 123005. (Cited on pages 29 and 31.)

- [125] and P. Mertsch D. Hooper, T. Linden (2014). “What Does The PAMELA Antiproton Spectrum Tell Us About Dark Matter?” *arXiv:1410.1527 [astro-ph.HE]*. (Cited on page 29.)
- [126] S. Ahlen et al. (2010). “The case for a directional dark matter detector and the status of current experiments efforts”. *Int. J. Mod. Phys.*, **25**, 1. (Cited on pages 29, 30, 32 and 33.)
- [127] K. Freese (1988). “Signal modulation in cold dark matter detection”. *Phys. Rev. D*, **27**, 3388. (Cited on page 30.)
- [128] R. Bernabei et al. (DAMA Collab.) (2013). “Final model independent result of DAMA/LIBRA-phase1”. *Eur. Phys. J.*, , 73:2648. (Cited on page 30.)
- [129] J. Amaré et al. (2014). “Preliminary results of ANAIS-25”. *Nucl. Ins. Meth. A*, **742**, 187. (Cited on page 30.)
- [130] R. Agnese et al. (CDMS Collab.) (2013). “Silicon Detector Dark Matter Results from the Final Exposure of CDMS II”. *Phys. Rev. Lett.*, **111**, 251301. (Cited on page 30.)
- [131] C. E. Aalseth et al. (CoGeNT Collab.) (2013). “CoGeNT: A search for low-mass dark matter using p-type point contact germanium detectors”. *Phys. Rev. D*, **88**, 012002. (Cited on page 30.)
- [132] G. Angloher et al (2013). “Results from 730 kg days of the CRESST-II Dark Matter search”. *Eur. Phys. J. C*, **72**, 1971. (Cited on page 30.)
- [133] E. Aprile et al. (XENON100 Collab.) (2012). “Dark Matter Results from 225 Live Days of XENON100 Data”. *Phys. Rev. Lett.*, **109**, 181301. (Cited on pages 30 and 31.)
- [134] D. Akimov et al. (ZEPLIN-III Collab.) (2012). “WIMP-nucleon cross-section results from the second science run of ZEPLIN-III,”. *Phys. Lett. B*, **709**, 14. (Cited on pages 30 and 31.)
- [135] D. S. Akerib et al. (LUX Collab.) (2013). “First results from the LUX dark matter experiment at the Sanford Underground Research Facility”. *Phys. Rev. Lett.*, **112**, 091303. (Cited on pages 30 and 31.)
- [136] K. Abe et al. (The XMASS Collab.) (2014). “Search for Bosonic Superweakly Interacting Massive Dark Matter Particles with the XMASS-I Detector”. *Phys. Rev. Lett.*, **113**, 121301. (Cited on page 30.)
- [137] J. Angle et al. (XENON100 Collab.) (2008). “First Results from the XENON10 Dark Matter Experiment at the Gran Sasso National Laboratory”. *Phys. Rev. Lett.*, **100**, 021303. (Cited on page 31.)

- [138] E. Aprile et al. (XENON100 Collab.) (2013). “Limits on spin-dependent WIMP-nucleon cross sections from 225 live days of XENON100 data”. *Phys. Rev. Lett.*, **111**, 021301. (Cited on page 31.)
- [139] R. Agnese et al. (SuperCDMS Collab.) (2014). “Search for Low-Mass Weakly Interacting Massive Particles with SuperCDMS”. *Phys. Rev. Lett.*, **112**, 241302. (Cited on page 31.)
- [140] D. N. Spergel (1988). “Motion of the Earth and the detection of weakly interacting massive particles”. *Phys. Rev. D*, **37**, 6. (Cited on page 32.)
- [141] and L. M. Krauss C. J. Copi, J. Heo (2010). “Directional sensitivity”. *Phys. Lett. B*, **461**, 43. (Cited on page 32.)
- [142] A. J. O’Hare and A. M. Green (2014). “Directional detection of dark matter streams”. *arXiv:1410.2749v1 [astro-ph.CO]*. (Cited on page 32.)
- [143] J. Macias-Perez and D. Santos J. Billard, F. Mayet (2010). “Directional detection as a strategy to discover Galactic Dark Matter”. *Phys. Lett. B*, **691**, 156. (Cited on page 32.)
- [144] S. Ahlen et al. (DMTPC Collab.) (2011). “First Dark Matter Search Results from a Surface Run of the 10-L DMTPC Directional Dark Matter Detector”. *Phys. Lett. B*, **695**, 124-129. (Cited on page 33.)
- [145] J. B. R. Battat et al. “First background-free limit from a directional dark matter experiment: results from a fully fiducialised DRIFT detector”. *arXiv:1410.7821 [hep-ex]*. (Cited on page 33.)
- [146] D. Santos et al. (2009). “MIMAC: Micro-tpc MAtrix of Chambers for dark matter directional detection”. *arXiv:1311.0616 [physics.ins-det]*. (Cited on page 33.)
- [147] K. Miuchi et al. (2010). “First underground results with NEWAGE-0.3a direction-sensitive dark matter detector”. *Phys. Lett. B*, **686**, 11-17. (Cited on page 33.)
- [148] S. Burgos et al. (2009). “Astropart. Phys.” *Phys. Rev. D*, **31**, 261. (Cited on page 33.)
- [149] D. C. Herrera et al. (2014). “Study of Columnar Recombination in Xe+trimethylamine Mixtures using a Micromegas-TPC”. *PoS(TIPP2014)*, **057**. (Cited on page 33.)
- [150] F. J. Iguaz et al. (2009). “Energy resolution of alpha particles in a Micromegas detector at high pressure”. *J. Phys. Conf. Ser.*, **179**, 012007. (Cited on page 38.)

- [151] T. Dafni et al. (2009). “Energy resolution of alpha particles in a microbulk Micromegas detector at high pressure argon and xenon mixtures”. *Nucl. Instr. and Meth. A*, **608**, 259. <http://dx.doi.org/10.1016/j.nima.2009.06.099> (Cited on page 38.)
- [152] ISO 3529/1-3 (1981). “Vacuum Technology: Vocabulary (International Organization for Standardization)”. Technical report. (Cited on page 43.)
- [153] C. Day. “Basics and applications of cryopumps”. Technical report. <http://cds.cern.ch/record/1047069/files/p241.pdf> (Cited on page 43.)
- [154] NIST. “NIST Mass Spectrometry Data Center”. <http://www.nist.gov/> (Cited on pages 43 and 86.)
- [155] M. Frigo and S.G. Johnson (2005). “The design and implementation of FFTW3”. volume 93(2):216-231. Proceedings of the IEEE. (Cited on page 45.)
- [156] M. Chefdeville et al. (2008). “Pulse height fluctuations of integrated micromegas detectors”. *Nucl. Instr. and Meth. A*, **591**, 147. <http://dx.doi.org/10.1016/j.nima.2008.03.045> (Cited on page 48.)
- [157] Private communication with F. J. Iguaz. (Cited on page 58.)
- [158] S. Agostinelli et al. (2003). “GEANT4: A simulation toolkit”. *Nucl. Instrum. Meth. A*, **506**, 250. (Cited on pages 65 and 166.)
- [159] A. Tomás (2013). “Development of Time Projection Chambers with Micromegas for Rare Event Searches”. Ph.D. thesis, Universidad de Zaragoza. http://jinst.sissa.it/jinst/theses/2013_JINST_TH_001.jsp (Cited on pages 65 and 66.)
- [160] ROOT: A Data Analysis Framework. <http://root.cern.ch> (Cited on pages 66 and 157.)
- [161] K. Jousten and J. Kim (2010). “A simple high-sensitivity technique for purity analysis of xenon gas”. *Nucl. Instr. and Meth. A*, **621**, 678. (Cited on page 73.)
- [162] H. Kienitz (1968). “Massenspektrometrie” edition. (Cited on page 74.)
- [163] E. Hoffmann et al. (2003). “Mass Spectrometry: Principles and Applications” edition. (Cited on pages 74, 75 and 79.)
- [164] Balzers document. “Partial pressure measurement in vacuum technology”. Technical report. (Cited on pages 74, 75, 78, 79 and 86.)
- [165] P. Dawson (1976). “Quadrupole Mass Spectrometry” edition. (Cited on pages 75 and 80.)

- [166] J. H. Batey (2014). “The physics and technology of quadrupole spectrometer”. *Vacuum*, **101**. DOI:10.1016/j.vacuum.2013.05.005 (Cited on pages 75 and 79.)
- [167] P. Turner et al. (2004). “Calibration effects during natural gas analysis using a quadrupole mass spectrometer”. *Trends in Anal. Chem.*, **23**, 4. [http://DOI:10.1016/S0165-9936\(04\)00403-0](http://DOI:10.1016/S0165-9936(04)00403-0) (Cited on page 80.)
- [168] K. Jousten (2014). “The work of ISO TC 112 towards standardization for specification and calibration of quadrupole mass spectrometers”. *Vacuum*, **101**. (Cited on page 86.)
- [169] Mass Bank Project. “High Quality Mass Spectral Database”. <http://www.massbank.jp/?lang=en> (Cited on page 86.)
- [170] G. Hvistendahl and K. Undheim (1970). “High resolution mass spectrometry of trimethylamine”. *J. of Mass. Spec.*, **3**, 821. (Cited on page 87.)
- [171] P. J. B. M. Rachinhas et al. (2000). “Simulation and experimental results for the detection of conversion electrons with gas proportional scintillation counters”. *Nucl. Instr. and Meth. A*, **441**, 468. [http://dx.doi.org/10.1016/S0168-9002\(99\)00978-X](http://dx.doi.org/10.1016/S0168-9002(99)00978-X) (Cited on pages 94 and 95.)
- [172] S.Y.F. Chu¹, L.P. Ekström^{1,2} and R.B. Firestone. “The Lund/LBNL Nuclear Data Search”. *LBNL, Berkeley, USA*. <http://nucleardata.nuclear.lu.se/toi/index.asp> (Cited on pages 95 and 96.)
- [173] F.J. Iguaz (2012). “Characterization of microbulk detectors in argon-and neon-based mixtures”. *JINST*, **7**, P04007. <http://iopscience.iop.org/1748-0221/7/04/P04007/> (Cited on page 102.)
- [174] F. Sauli (1991). “Principles of operation of multiwire proportional and drift chambers”. Technical report. <http://cdsweb.cern.ch/record/117989/files/CERN-77-09.pdf> (Cited on page 104.)
- [175] P. K. Lightfoot et al. (2005). “Development of a double-phase Xenon cell using micromegas charge readout for applications in dark matter physics”. *Nucl. Instr. and Meth. A*, **554**, 266. [http://dx.doi.org/10.1016/0168-9002\(91\)90224-E](http://dx.doi.org/10.1016/0168-9002(91)90224-E) (Cited on pages 104 and 111.)
- [176] H. Sakurai et al. (1991). “High pressure xenon proportional counter up to 10 bar”. *Nucl. Instr. and Meth. A*, **307**, 504. [http://dx.doi.org/10.1016/0168-9002\(91\)90224-E](http://dx.doi.org/10.1016/0168-9002(91)90224-E) (Cited on pages 104, 109, 110 and 111.)
- [177] H. Sakurai and B.D. Ramsey (1992). “Dependence of energy resolution on anode diameter in xenon proportional counters”. *Nucl. Instr. and Meth. A*, **313**, 155. (Cited on pages 104 and 111.)

- [178] S. Cebrian et al. (2013). “Pattern recognition of ^{136}Xe double beta decay events and background discrimination in a high pressure xenon TPC”. *J. Phys. G: Nucl. Part. Phys*, **40**, 125203. <http://doi:10.1088/0954-3899/40/12/125203> (Cited on pages 106, 147 and 159.)
- [179] L. Seguí (2013). “Pattern Recognition in a high pressure time projection chamber prototype with a Micromegas readout for the ^{136}Xe double beta decay”. Ph.D. thesis, Universidad de Zaragoza. (Cited on page 106.)
- [180] T. Dafni et al. (NEXT Collab.) (2011). “Micromegas planes for the neutrinoless double beta decay search with NEXT”. *J. Phys.: Conf. Ser*, **309**, 012009. <http://doi:10.1088/1742-6596/309/1/012009> (Cited on page 111.)
- [181] L. Onsager (1938). “Initial Recombination”. *Phys. Rev.*, **54**, 554. DOI:<http://dx.doi.org/10.1103/PhysRev.54.554> (Cited on page 118.)
- [182] G. Jaffé (1929). “On the theory of ionization in columns”. *Ann. Phys.*, **30**, 977. (Cited on pages 118 and 119.)
- [183] G. Jaffé (1913). “On the theory of ionization in columns”. *Ann. Phys.*, **42**, 303. (Cited on page 118.)
- [184] S. Amoruso et. al. (2004). “Study of electron recombination in liquid argon with the ICARUS TPC”. *Nucl. Instr. and Meth. A*, **523**, 275. DOI:[10.1016/j.nima.2003.11.423](https://doi.org/10.1016/j.nima.2003.11.423) (Cited on pages 118, 119 and 120.)
- [185] W. R. Kanne and J. A. Bearden (1936). “Columnar Ionization”. *Phys. Rev.*, **50**, 935. DOI:<http://dx.doi.org/10.1103/PhysRev.50.935> (Cited on page 119.)
- [186] H. A. Kramers (1952). “On a modification of jaffés theory of column-ionization”. *Physica*, **18**, 10. DOI:[10.1016/S0031-8914\(52\)80255-1](https://doi.org/10.1016/S0031-8914(52)80255-1) (Cited on page 119.)
- [187] J. Thomas and D. A. Imel (1987). “Recombination of electron-ion pairs in liquid argon and liquid xenon”. *Phys. Rev. A*, **36**, 2. DOI:<http://dx.doi.org/10.1103/PhysRevA.36.614> (Cited on pages 119 and 120.)
- [188] I. G. Irastorza, T. Dafni, and E. Ferrer-Ribas (1-9). “Micromegas in the rare event searches field”. *Mod. Phys. Lett., A*, **2**. (Cited on page 153.)
- [189] S. Cebrián et al. (2010). “Micromegas readouts for double beta decay searches”. *JINST*, **5**, P02001. doi:[10.1088/1475-7516/2010/10/010](https://doi.org/10.1088/1475-7516/2010/10/010) (Cited on page 153.)
- [190] A. Bettini (2011). “Underground laboratories”. *Nucl. Instrum. Meth. A*, **626-627**, S64. (Cited on page 165.)

-
- [191] Ll. A. Currie (40). “Limits for qualitative detection and quantitative determination. Application to radiochemistry”. *Anal. Chem.*, **40**, 586. (Cited on page 166.)
- [192] Ch. Hurtgen et al. (2000). “Revisiting Currie: how long can you go?” *Appl. Rad. Isot.*, **53**, 45. (Cited on page 166.)
- [193] D. González-Díaz. “Private communication”. (Cited on pages 176 and 178.)

